Grains vibrés, frottement et perception tactile

Alexis Michel Prevost

Alexis Michel Prevost. Grains vibrés, frottement et perception tactile. Matière Molle [cond-mat.soft]. Université Pierre & Marie Curie, 2015. tel-02421651

HAL Id: tel-02421651
https://hal.science/tel-02421651

Submitted on 20 Dec 2019

Université Pierre et Marie Curie
Paris

Habilitation à Diriger des Recherches

Grains vibrés, frottement et perception tactile

ALEXIS PREVOST

Soutenance le 12 Février 2015
devant le jury composé de :

M. Axel Buguin
M. Jean-Marc Di Meglio (rapporteur)
M. Jay Fineberg
M. Yoël Forterre (rapporteur)
M. Benoît Ladoux (rapporteur)

Laboratoire Jean Perrin – UMR 8237 – CNRS – UPMC
4, place Jussieu 75005 Paris

Résumé :

Ce manuscrit décrit l'ensemble de mes activités de recherche depuis mon postdoctorat jusqu'à ce jour. Il y est tout d'abord question de milieux granulaires vibrés, thématique que nous avons abordée en combinant expériences et simulations de dynamique moléculaire. Nous décrivons ensuite le développement d'un outil tribologique, analogue du fonctionnement de l'extrémité du doigt humain, pour étudier les mécanismes de transduction de l'information tactile, en s'attardant notamment sur un rôle possible des empreintes digitales pour la discrimination de textures fines. Nous montrons ensuite comment utiliser ce senseur pour mesurer des contraintes sous un film d'élastomère et relier nos mesures aux propriétés du contact interfacial. Ce manuscrit se poursuit avec la description de la mise au point de méthodes d'imagerie de contact résolues spatialement, utilisées pour étudier la mise en glissement d'une sphère contre un plan. Enfin, nous concluons en présentant une étude consacrée à la mécanique du contact et le frottement de surfaces texturées à des échelles mésoscopiques, permettant une mesure optique des contraintes de pression et de cisaillement à l'échelle des micro-aspérités. Nous l'appliquons au problème de la mise en glissement d'un contact plan-plan et à la mécanique d'un contact normal sphère-plan.

Abstract :

This manuscript describes my research activity during my postdoc and since then. Emphasis is first made on vibrated liquid and granular gases, using a combination of experiments and molecular dynamics simulations. We then describe the development of a tribological sensor, which mimics the functioning of the human fingertip, to study the mechanical transduction mechanisms of tactile perception. We particularly focus on a possible role of the fingerprints in discriminating fine textures. We then show how the use of this sensor can allow measuring stresses below an elastomer film and we relate such measurements to the interfacial contact properties. We continue with the description of spatially resolved contact imaging techniques, to probe the transition from static to dynamic friction in a sphere-on-plane contact. Finally, we conclude this manuscript with a study centered on the contact mechanics and friction of engineered textured surfaces that allow optical measurements of both pressure and shear stresses at the scale of the micro-asperities. We use this system to probe, first, the transition from static to dynamic friction in a plane-plane contact, second, the contact mechanics at a sphere-on-plane normal contact.

SOMMAIRE

CURRICULUM VITÆ

Alexis Prevost

Chargé de Recherches 1ère classe au CNRS

Laboratoire Jean Perrin CNRS/UPMC UMR 8237, Tour 32-33, 4 Place Jussieu, 75005 Paris
Tél : +33 1 44 27 77 72 - *Fax* : +33 1 44 27 47 16
alexis.prevost@upmc.fr
http://www.labos.upmc.fr/ljp/?people4

Né le 04 Février 1972. Nationalité française.
Marié, 3 enfants.

Formation

- *Décembre 1999*: Doctorat de l'Université Paris XI (Spécialité : Champs-Particules-Matières). Thèse au LPS-ENS sous la direction d'Etienne Rolley, Professeur Paris 7.
- *1997-1998* : Service National (10 mois) : Scientifique du Contingent au LPS-ENS.
- *1995* : Magistère de Physique de l'Université Paris XI Orsay.
  DEA Champs-Particules-Matières.

Parcours professionnel

- *Depuis le 1er Janvier 2009* : Chargé de Recherches 1ère classe au CNRS au Laboratoire Jean Perrin dirigé par Didier Chatenay.

- *Janvier 2005 - Janvier 2009*: Chargé de Recherches CNRS 2nde classe, puis 1ère classe au LPS-ENS dans le groupe de Didier Chatenay.

- *Décembre 2002-Décembre 2004*: Chargé de Recherches CNRS 2nde classe au Laboratoire des Fluides Organisés du Collège de France, Paris, France, dans le groupe de Liliane Léger.

- *Février 2000-Novembre 2002*: Post-doctorat au Département de Physique de l'Université de Georgetown à Washington DC, USA, dans le groupe de Jeffrey S. Urbach.

Domaines scientifiques

- Physique de la perception tactile. Approches biomimétiques.
- Frottement solide et mécanique du contact.
- Physique des milieux granulaires.
- Mouillage. Physique des basses températures (Hélium 4 superfluide).

ACTIVITE DE RECHERCHE

INTRODUCTION

Après une thèse qui portait sur la dynamique de la ligne de contact d'un ménisque d'hélium-4 liquide sur un substrat désordonné de césium, j'ai effectué un post-doctorat de 2 ans et 10 mois au **Département de Physique de l'Université de Georgetown**, à Washington DC, USA (2000-2002). Je m'y suis intéressé aux milieux granulaires vibrés qui constituent un exemple de systèmes dissipatifs stationnaires hors d'équilibre, en développant une expérience consistant à faire vibrer verticalement une couche de billes horizontale. J'ai étudié et caractérisé les analogies frappantes que présente ce système avec un gaz ou un liquide moléculaire en fonction de la densité de la couche, de sa composition (mono- ou bi- disperse) et du type d'injection d'énergie (support lisse ou rugueux).

Recruté au CNRS, j'ai rejoint le 1er Décembre 2002 le **Laboratoire des Fluides Organisés (LFO)** dirigé par Pierre-Gilles de Gennes, au Collège de France, où j'ai développé une activité centrée autour de la mécanique du contact et du frottement solide avec G. Debrégeas. Il s'agissait en particulier de comprendre le rôle de la micro-texturation des surfaces (rugosité) lors du frottement macroscopique entre deux objets solides. Ce travail s'est poursuivi au **Laboratoire de Physique statistique (LPS) de l'ENS** à Paris, que j'ai rejoint en Janvier 2005 lors de la fermeture du LFO, puis au **Laboratoire Jean Perrin (LJP)** de l'UPMC depuis le 1er septembre 2012. J'y ai développé des méthodes d'imagerie des interfaces rugueuses de type élastomère/verre permettant d'extraire optiquement par corrélation d'images les champs de déplacements de l'interface. Combinées à des méthodes d'inversion, ces mesures ont permis de remonter au champ des contraintes interfaciales dans un contact étendu de type Hertz et d'étudier en particulier la transition vers le glissement.

L'une des motivations initiale de ces études était de comprendre, dans le cadre de la thèse de J. Scheibert, la transduction mécanique de l'information tactile dans le toucher humain. La perception tactile par le doigt repose en effet sur une exploration dynamique des surfaces au cours de laquelle l'information de texture est transmise, via la peau, à des terminaisons nerveuses mécano-réceptrices sous-cutanées. Pour comprendre ce processus, j'ai mis au point, parallèlement à mes expériences sur le frottement, un capteur biomimétique du fonctionnement de l'extrémité du doigt humain. Il consistait en un micro-capteur de force de type MEMS simulant son analogue vivant, recouvert d'un film d'élastomère en guise de peau, d'épaisseur millimétrique. Ce senseur frotté contre des substrats solides lisses et micro-texturés, a permis de comprendre les propriétés de filtrage mécanique de l'organe tactile, notamment le rôle essentiel de la texturation de la peau (les empreintes digitales) pour la transduction de l'information tactile. Grâce à un financement européen NEST (projet MONAT, dont j'étais le responsable pour le LPS), et dans le cadre d'une collaboration avec le CEA-LETI, des réseaux 1x10 de capteurs MEMS de dimensions réduites et sensibilité accrue ont été développés et ont permis de montrer que la fonction de transfert qui caractérise la transduction tactile dépend non seulement des caractéristiques intrinsèques du capteur mais aussi des conditions d'exploration tactile, telles que la force normale appliquée et la position d'un micro-capteur par rapport à la zone de contact.

Récemment, dans le cadre d'une ANR (projet DYNALO, dont j'étais le responsable pour le LPS-LJP), je me suis intéressé aux fluctuations de la force de frottement induites quand on frotte une sphère texturée (empreintes digitales) sur un substrat rugueux à des échelles microscopiques. J'ai montré l'existence d'un mécanisme de sélection spectrale analogue à celui observé avec le système MEMS. Ce travail a permis d'une part, de comprendre comment l'amplitude des modulations induites était reliée aux caractéristiques topographiques et d'autre part, de montrer que leur existence dépendait du caractère non-linéaire de la loi de frottement.

Depuis Septembre 2012, je développe dans le cadre de la thèse de N. Claverie le même type d'approche biomimétique pour étudier la perception tactile chez les rongeurs. Ces derniers utilisent leurs moustaches faciales pour sonder tactilement leur environnement et il s'agit ici d'en mimer le fonctionnement. J'étudie également la mécanique du contact d'interfaces multi-contacts en développant des surfaces modèles (collaboration A. Chateauminois et C. Frétigny, Laboratoire SIMM-ESPCI) permettant une mesure optique des champs de contraintes à l'échelle des aspérités. Il s'agit de faire le lien entre le frottement à l'échelle d'une aspérité et le comportement frictionnel collectif de quelques milliers d'aspérités.

Dans ce manuscrit, je détaille chacune des activités, sous la forme d'un chapeau introductif aux articles les plus significatifs attachés au document. Chaque chapeau est constitué d'un résumé, suivi d'une description des principaux résultats et de la liste intégrale des publications qui concernent la thématique.

La liste de l'ensemble de mes publications est également donnée en fin de ce manuscrit (voir le sommaire).

THEME 1 : MILIEUX GRANULAIRES VIBRES

Résumé: Nous avons étudié la dynamique d'une couche granulaire vibrée qui constitue un exemple de systèmes dissipatifs hors-équilibre. Nous avons mis en évidence que la forme des distributions et des corrélations spatiales de vitesses dépend fortement du mécanisme d'injection d'énergie dans la couche granulaire et n'est pas uniquement déterminée par la dynamique de collisions inélastiques entre billes. Nous avons également observé et caractérisé une transition de phase de type liquide-solide quand la couche granulaire est confinée. Enfin, pour une couche confinée bi-disperse, nous avons mis en évidence et caractérisé l'effet de forces de déplétion qui tendent à favoriser une ségrégation des grosses billes.

J'ai étudié cette thématique au cours de mon post-doctorat dans le groupe de Jeffrey Urbach à l'Université de Georgetown située à Washington DC, USA.

Les milieux granulaires vibrés constituent un exemple de systèmes dissipatifs loin de l'équilibre pour lesquels il n'existe toujours pas de description théorique satisfaisante : la difficulté tient essentiellement au fait que les collisions entre grains de taille macroscopique sont dissipatives, et qu'il faut donc constamment injecter de l'énergie dans le milieu granulaire *via* une agitation externe. On obtient alors un état stationnaire, mais qui est toujours hors-équilibre. Dans certains cas, les similitudes de comportements sont cependant si proches de ce qui est observé pour un gaz ou un liquide moléculaire, que l'on peut se demander jusqu'à quel point les outils de la physique statistique d'équilibre peuvent s'appliquer à ce type de système. Pour essayer de répondre à ces questions, une des approches naturelles est d'utiliser des systèmes expérimentaux modèles, constitués par exemple de grains « identiques » dont les tailles sont bien calibrées, dans le but de réduire la complexité du système et permettre une comparaison directe avec des modèles théoriques et des simulations.

L'expérience que j'ai développée consistait à faire vibrer verticalement et sinusoïdalement une couche de billes d'acier mono-disperse de taille millimétrique au contact d'un plateau horizontal. Il s'agissait d'étudier les organisations spatiales et dynamiques en régime stationnaire d'un système granulaire quasi-2D, permettant ainsi un suivi complet des trajectoires des particules au cours du temps avec une caméra rapide. Pour contraindre le système dans une configuration quasi-2D à forte amplitude d'excitation, nous pouvions confiner le système granulaire au moyen d'un couvercle épais de Plexiglas.

Des travaux antérieurs[1] dans le groupe de J. Urbach avaient permis de mettre en évidence pour le système non-contraint un diagramme de phase très riche qui dépend à la fois de l'amplitude d'excitation et de la densité de billes sur le plateau. En particulier, à relativement faible amplitude d'excitation et faible densité des billes, la couche est dans un état dit de « gaz granulaire » caractérisé par un libre parcours moyen des billes qui est grand devant leur diamètre. A plus haute densité et relativement faible amplitude d'excitation, les billes s'arrangent quasi-spontanément pour former un réseau hexagonal dynamique qui persiste tant que le système est excité périodiquement. En mesurant les trajectoires individuelles des billes dans la phase granulaire, J. Urbach et ses collaborateurs avaient notamment observé que dans la phase de gaz granulaire, les distributions des vitesses instantanées des billes n'étaient pas maxwelliennes, mais présentait des queues exponentielles. Ces mesures étaient contraires à ce qu'on aurait eu pour un gaz moléculaire en équilibre thermodynamique, et traduisaient directement le caractère hors-équilibre d'un milieu granulaire vibré.

---

[1] J. S. Olafsen, J. S. Urbach, *Phys. Rev. Lett.* **81**, 4369 (1998); *Phys. Rev. E* **60**, R2468 (1999).

Pour ce système, on s'attendait de plus à ce que l'hypothèse de « chaos moléculaire » ne soit pas vérifiée et que les corrélations spatiales de vitesses soient donc non-nulles. Des travaux théoriques et numériques prédisaient en effet qu'elles devaient être à longue portée, décroissant en loi de puissance, et résultantes de la compétition entre l'excitation de modes hydrodynamiques par le forçage extérieur et leur dissipation par diffusion dans la couche granulaire. Peu d'expériences n'avaient cependant cherché ni à les mesurer, ni à caractériser leur dépendance avec la manière dont l'énergie était injectée dans la couche granulaire. De plus, d'une expérience à l'autre, les modes d'injection étaient très différents et restaient très éloignés du type de forçage homogène utilisé dans les modèles, ne permettant pas ainsi une comparaison facile avec les prédictions théoriques.

Nous disposions cependant d'un système plan pour lequel l'injection d'énergie dans la couche granulaire était très proche d'un forçage homogène. Ma première contribution a donc été de développer une méthode expérimentale d'imagerie stroboscopique permettant de mesurer les corrélations spatiales des vitesses et de montrer que leur signe et leur forme dépendaient fortement des mécanismes d'injection d'énergie dans la couche granulaire. Nous avons d'abord mesuré les corrélations spatiales des vitesses des billes pour une couche granulaire excitée par un plateau lisse, et contrairement à toute attente, les avons mesurées négatives **(Fig. 1a)**. Ces mesures ont été confirmées grâce à une simulation du système par la méthode de dynamique moléculaire. Les billes, qui sont soumises à la gravité, y sont assimilées à des sphères molles qui peuvent s'interpénétrer légèrement lors de collisions binaires. La composante normale de la force d'interaction de contact (le long de la ligne qui joint les centres des deux billes) s'écrit comme la somme d'un terme élastique répulsif et d'un terme dissipatif, respectivement proportionnels à la distance d'interpénétration et à la vitesse normale relative au point de contact. La composante tangentielle (normale à la ligne qui joint les centres des deux billes) de la force d'interaction est, quant à elle, proportionnelle à la vitesse relative tangentielle entre les billes. Enfin, l'interaction avec le plateau est modélisée en considérant ce dernier comme un plan de masse infinie qui bouge avec la vitesse du plateau.

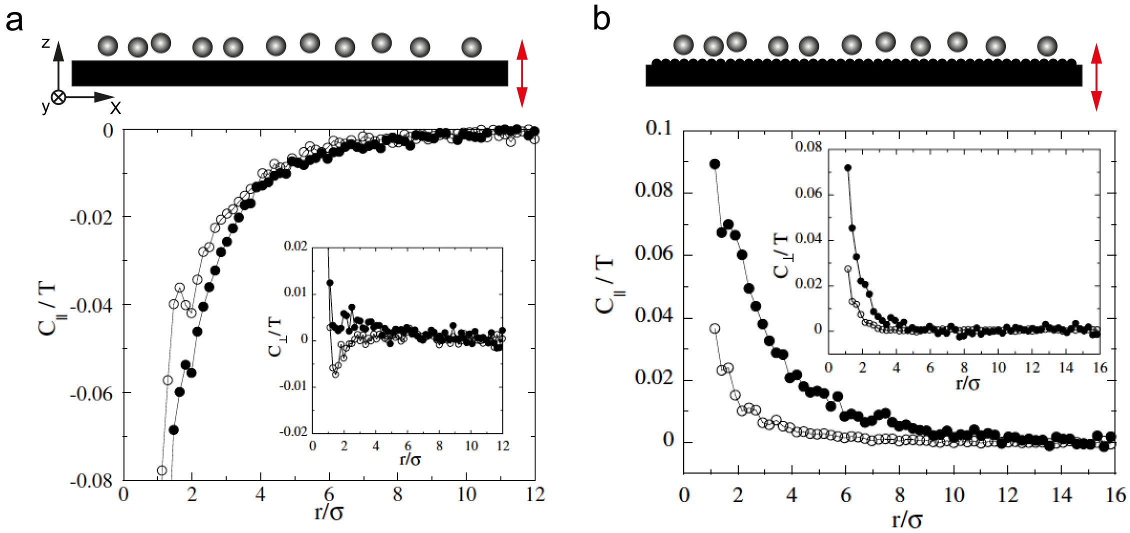

Figure 1 – *Corrélations spatiales des vitesses, longitudinales* $C_\parallel$ *et transverses* $C_\perp$ *(insert), divisées par la température granulaire* $T = \langle \vec{v}^2 \rangle$*, avec* $\vec{v}$ *la vitesse instantanée des billes dans le plan* xy *du plateau. Résultat obtenu pour une couche granulaire excitée sinusoïdalement le long de l'axe* z *avec* **(a)** *le plateau lisse et* **(b)** *le plateau rugueux. Les corrélations spatiales des vitesses sont définies par la relation* $C_{\parallel,\perp} = \frac{1}{N_r}\sum_{i\neq j}^{N_r} v_i^{\parallel,\perp}\, v_j^{\parallel,\perp}$*, où* N_r *est le nombre total de paires de billes séparées d'une distance* r*,* $v_i^{\parallel}$ *la projection de* $\vec{v}_i$ *le long de la ligne qui relie les centres des billes* i *et* j*, et* $v_i^{\perp}$ *la projection de* $\vec{v}_i$ *perpendiculaire à cette ligne. Pour* **(a)** *et* **(b)***,* r *est divisé par le diamètre des billes* σ*.*

Grâce à cette simulation, nous avons compris que l'anti-corrélation résultait du fait que l'énergie est injectée par le plateau dans la direction verticale et est transférée horizontalement lors des collisions entre billes.

Cette interprétation a été confirmée en remplaçant le plateau lisse par un plateau rugueux qui permet d'injecter de l'énergie directement dans la direction horizontale. Nous avons ainsi retrouvé des corrélations spatiales des vitesses positives, proches des prédictions théoriques **(Fig. 1b)**. Nous avons ainsi montré que la forme et le signe de ces corrélations ne dépendaient pas seulement de la dynamique de collisions inélastiques entre billes mais étaient intiment liés au type de mécanisme d'injection d'énergie. Ces observations montraient pour la première fois l'importance d'inclure une modélisation appropriée de l'interaction bille-substrat dans les modèles théoriques qui considéraient toujours le terme de forçage comme un bruit blanc gaussien.

Sur plateau rugueux, nous avons également caractérisé les distributions des vitesses des billes et trouvé qu'elles étaient d'autant plus gaussiennes que la densité de billes était faible. Là encore, nous avons pu interpréter ces mesures comme résultant de la compétition entre le forçage stochastique induit par le plateau rugueux et l'effet combiné de la dynamique de collisions inélastiques entre billes et du frottement des billes avec le plateau **[1]**.

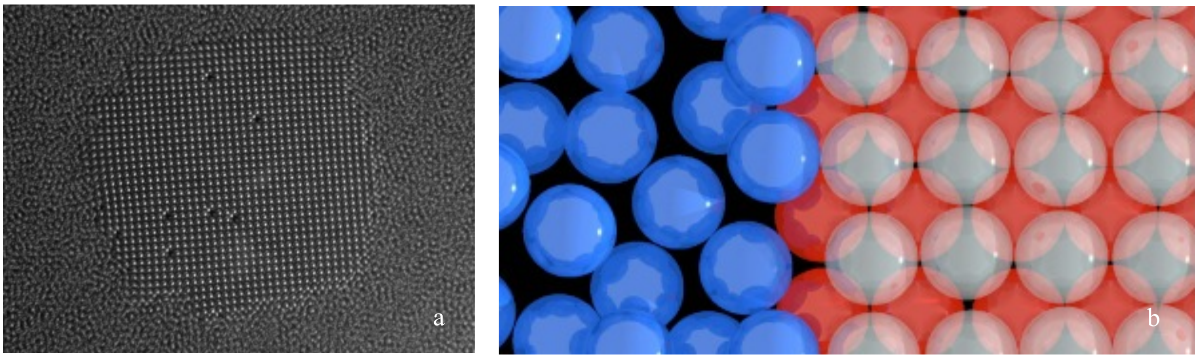

Figure 2 – *Coexistence de phase dans l'état stationnaire entre un cristal de symétrie cubique et un liquide granulaire.* **(a)** *Expérience: le système est agité verticalement sinusoïdalement (amplitude A, fréquence ν) et visualisé par le dessus. Les billes ont un diamètre* $\sigma = 1.59\ mm$ *et l'espacement entre plateau et couvercle est de* $1.75\,\sigma$. *Sur cette image moyennée sur 1 s, seule la couche supérieure est visible et le cristal présente quelques lacunes* $(A = 0.085\,\sigma, \nu = 80\ Hz, \rho = N/N_{max} = 0.9\ avec\ N\ (resp. N_{max})$ *le nombre de billes présentes dans la couche (resp. le nombre maximal de billes sous forme d'un réseau hexagonal compact)).* **(b)** *Simulation: vue 3D du dessus des positions instantanées des billes à la frontière du cristal. Les billes dans le cristal sont colorées en rouge, celles dans le gaz en bleu. La couche supérieure est représentée en transparence* $(A = 0.13\,\sigma, \nu = 60\ Hz, \rho = 0.89)$.

J'ai souhaité ensuite explorer le diagramme de phase de la couche granulaire pour des amplitudes d'excitation plus élevées que ce que nous avions considéré jusqu'alors. Au delà d'une certaine amplitude seuil, la couche ne pouvait cependant plus être assimilée à un système quasi-2D, puisque les billes avaient suffisamment d'énergie pour explorer la direction verticale sur des distances bien supérieures à leur diamètre. Pour conserver le caractère bidimensionnel du système et toujours permettre le suivi optique des trajectoires des billes, nous avons donc fermé la cellule d'observation par un plateau transparent en Plexiglas.

Pour des densités de billes relativement dense et un espacement de moins de deux diamètres de billes, nous avons mis en évidence de façon inattendue la nucléation d'une phase cristalline stable, de symétrie cubique, et qui coexiste avec une phase de liquide granulaire. Tant que l'amplitude d'excitation est faible, cette phase cristalline n'existe pas et le mouvement des billes est désordonné, s'apparentant à celui des molécules d'un liquide à l'équilibre. Si on augmente un peu plus l'amplitude d'excitation, on observe alors la formation de structures cristallines indépendantes et instables. Au-dessus d'une amplitude critique dite de nucléation, celles-ci deviennent stables et finissent par coalescer en un unique cristal qui, tant que l'amplitude et la fréquence d'excitation sont maintenues constantes, coexiste avec le liquide granulaire environnant. Ces structures cristallines sont formées de 2 couches de billes superposées avec une symétrie cubique **(Fig. 2)**. Celles-ci disparaissent si l'on diminue l'amplitude d'excitation en dessous d'une amplitude critique dite d'évaporation.

Nous avons déterminé le diagramme de phase (courbes de nucléation et d'évaporation obtenues en traçant l'amplitude critique fonction de la fréquence d'excitation) pour cette transition. Nous avons également caractérisé la coexistence de phase en mesurant la température granulaire (définie comme la moyenne du carré des vitesses instantanées des billes) et la pression dans les deux phases. De façon surprenante, la température granulaire au sein du cristal est beaucoup plus faible que dans le liquide, contrairement à ce que l'on observe pour un système à l'équilibre, alors que la pression est identique dans les deux phases. Ces mesures, complétées par des simulations numériques de dynamique moléculaire, ont permis de confirmer l'existence de cette transition et de ses principales caractéristiques.

Cette transition ordre/désordre présente des similitudes frappantes avec les transitions de phase qu'on observe dans des suspensions colloïdales confinées à l'équilibre thermique. Ceci suggère que les outils de la mécanique statistique d'équilibre pourraient être utiles pour décrire le comportement des systèmes granulaires. Cependant, la coexistence de phase diffère par bien des aspects (température granulaire non uniforme, dépendance de l'amplitude critique avec la fréquence d'excitation) de celle obtenue avec un système à l'équilibre et montre que les effets liés au caractère hors d'équilibre doivent être pris en compte pour avoir une description complète des systèmes granulaires **[2]**.

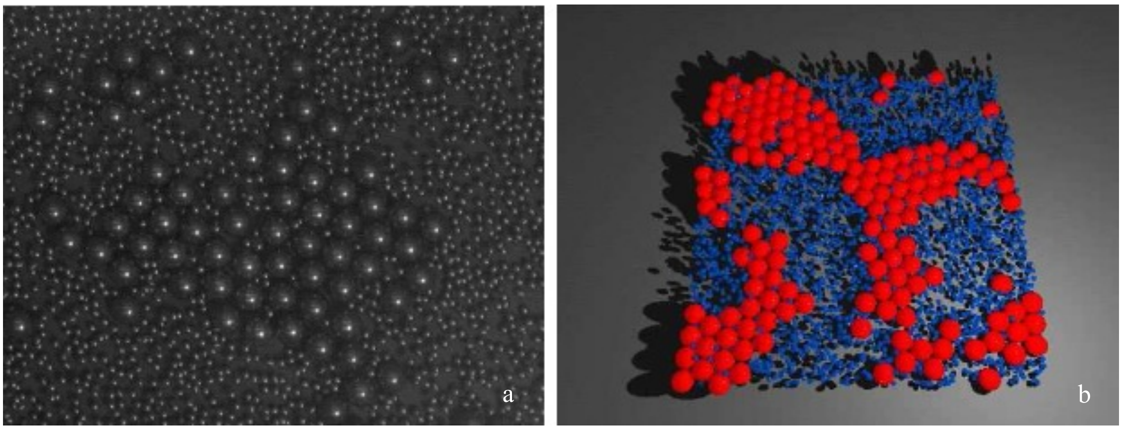

Figure 3 – *Ségrégation des grosses billes résultant des forces de déplétion.* **(a)** *Expérience avec* $\rho_p = 0.036$ *et* $\rho_G = 0.066$ *(*$\rho_{p,G} = N_{p,G}V_{p,G}/V$*, avec* V *le volume du système,* $N_{p,G}$ *et* $V_{p,G}$ *respectivement les nombres et volumes des petites et grosses billes).* **(b)** *Simulation avec* $\rho_p = 0.080$ *et* $\rho_G = 0.132$*. Pour* **(a)** *et* **(b)***, les grosses et petites billes ont été initialement disposées aléatoirement sur le plateau (*$\nu = 30\,Hz$*, accélération maximale* $3.5\,g$*, rayon des grosses billes* $r_G = 4\,mm$*, rapport des rayons grosses billes/petites billes* $r_G/r_p = 3.33$*, espacement entre le plateau et le couvercle égal à* $2.3\,r_G$*).*

Nous avons enfin mis en évidence expérimentalement, pour la première fois à notre connaissance, l'effet des forces de déplétion dans le même type de couche granulaire confinée, formée cette fois-ci d'un mélange bi-disperse de petites et grosses billes de rapport de diamètres 3.33 **[3]**. Dans l'état stationnaire, nous avons observé une ségrégation de taille, se caractérisant, à haute densité de grosses billes, par un regroupement de celles-ci en un réseau hexagonal excluant les petites billes **(Fig. 3)**, et à basse densité, par une augmentation importante de la fonction de corrélation de position des grosses billes pour les courtes distances **(Fig. 4)**.

Après mon départ de Georgetown University, ces effets ont été confirmés par des simulations numériques de dynamique moléculaire réalisées avec P. Melby, alors chercheur postdoctoral dans le groupe de J. Urbach. Les fonctions de corrélation de position des grosses billes mesurées et simulées sont bien décrites par la combinaison d'un potentiel de déplétion utilisé pour les systèmes colloïdaux à l'équilibre et d'un facteur de Boltzmann qui définit une température effective du système **(Fig. 4)**.

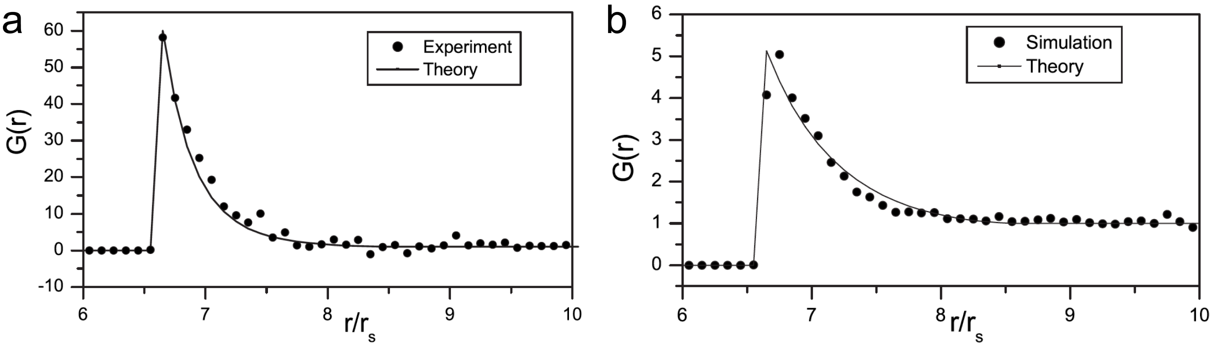

Figure 4 – *Fonction de corrélation de position* $G(r)$ *des grosses billes (points noirs) et meilleur ajustement (ligne continue) dérivé de la forme du potentiel de déplétion d'équilibre.* **(a)** *Expérience* ($\rho_p = 0.071, \rho_G = 0.007$) **(b)** *Dynamique moléculaire* ($\rho_p = 0.08, \rho_G = 0.03$). *Pour* **(a)** *et* **(b)**, r_S *est le diamètre des petites billes.*

Nous n'avons en revanche pas trouvé de relation simple entre cette température effective et d'autres mesures de température effective dans le système.

Comme dans le cas de la nucléation d'un cristal cubique précédemment décrite, ces résultats suggèrent une fois de plus que les outils de la mécanique statistique d'équilibre pourraient être utiles pour décrire le comportement des systèmes granulaires vibrés, tout en incluant nécessairement dans la description des ingrédients supplémentaires pour rendre compte de leur caractère hors équilibre.

Une partie de ces résultats a été synthétisée dans un article de revue donné en référence **[4]**.

Références

[1]. “Forcing and velocity correlations in a vibrated granular monolayer”, A. Prevost, D.A. Egolf, J.S. Urbach, *Phys. Rev. Lett.* **89**, 084301 (2002).

[2]. “Nonequilibrium two-phase coexistence in a confined granular layer”, A. Prevost, P. A. Melby, D. A. Egolf, J. S. Urbach, *Phys. Rev. E* **70**, 050301(R) (2004).

[3]. “Depletion force in a bidisperse granular layer”, P. Melby, A. Prevost, D. A. Egolf, J. S. Urbach, *Phys. Rev. E.* **76**, 051307 (2007).

[4]. “The dynamics of thin vibrated granular layers”, P. Melby, F. Vega Reyes, A. Prevost, R. Robertson, P. Kumar, D. A. Egolf, J. S. Urbach, *J. Phys.: Condens. Matter* **17** S2689-S2704, (2005).

Forcing and Velocity Correlations in a Vibrated Granular Monolayer

Alexis Prevost,* David A. Egolf, and Jeffrey S. Urbach
Department of Physics, Georgetown University, Washington, D.C., 20057

(Received 14 March 2002; published 2 August 2002)

The role of forcing on the dynamics of a vertically shaken granular monolayer is investigated. Using a flat plate, surprising negative velocity correlations are measured. A mechanism for this anticorrelation is proposed with support from both experimental results and molecular dynamics simulations. Using a rough plate, velocity correlations are positive, and the velocity distribution evolves from a Gaussian at very low densities to a broader distribution at high densities. These results are interpreted as a balance between stochastic forcing, interparticle collisions, and friction with the plate.

DOI: 10.1103/PhysRevLett.89.084301 PACS numbers: 45.70.Mg, 05.20.Dd, 05.20.Jj, 83.10.Rs

Granular gases, systems of large numbers of macroscopic grains in rapid motion and interacting through dissipative collisions, appear in a wide range of industrial applications and natural phenomena. Energy must be supplied externally to compensate for the inelastic collisions, so granular gases are necessarily systems out of equilibrium. As a result, they may display dramatic nonequilibrium effects such as non-Gaussian velocity distributions [1–6] and long-range spatial velocity correlations [7–10]. Non-Gaussian velocity distributions are a direct demonstration of the inapplicability of the Gibbs distribution, and significant velocity correlations indicate the absence of "molecular chaos," which is a crucial approximation normally used to solve the Boltzmann equation and to calculate other fundamental quantities in kinetic theory. Recent theoretical work has focused on the nonequilibrium steady state obtained when the energy supplied by spatially homogeneous random external forcing is balanced by the dissipation due to the collisions such that the average energy of the system remains constant [4,7,8]. Non-Gaussian velocity distributions and algebraically decaying velocity correlations arise as a direct consequence of the energy injection. Non-Gaussian velocity distributions and velocity correlations have been observed in a number of experiments [1–3,10], but in each case the forcing is sufficiently different from that of the theoretical models that a direct comparison is difficult. In this Letter, we provide a direct demonstration of the determining role that the forcing plays on the spatial velocity correlations in a homogeneously forced granular gas. We will also show how the framework of kinetic theory can provide a coherent description of the origin of the observed velocity distributions and correlations.

We have investigated a quasi-2D granular system consisting of a layer of a large number of spherical particles partially covering a vertically driven horizontal plate. Two plates with different surface properties were used in the experiments: a smooth circular plate (20 cm in diameter) made of black anodized aluminum, and a rough hexagonally shaped plate (30 cm between opposite corners). The roughness of the latter is provided by a close-packed lattice of blackened steel balls (1.19 mm diameter) glued to a flat plate. The granular gas is made of uniform stainless steel spheres with diameter $\sigma = 1.59$ mm (smooth plate) or $\sigma = 3.97$ mm (rough plate). On the smooth plate, the layer is constrained from above by an antistatic coated Plexiglas lid, 1.7σ above the plate. Using an electromagnetic shaker, the plate is driven sinusoidally, and the granular layer is brought to a nonequilibrium steady state. The strength of the shaking $\Gamma = A\omega^2/g$ is directly measured with a fast response accelerometer (A is the amplitude, ω the frequency of the plate oscillation, and g the acceleration due to gravity).

A high resolution camera (Pulnix TM1040) placed above the plate records the bright spots on the tops of the balls produced by a stroboscopic LED array. Instantaneous horizontal velocities $\mathbf{v}_i$ are obtained from the displacements between strobe pulses. The strobe is synchronized with the camera so that the first pulse occurs at the end of the exposure of one frame, and the next pulse occurs at the beginning of the subsequent frame. The time interval between pulses (~ 1 ms) is chosen to be significantly smaller than the mean collision time. The width of both pulses is typically less than 0.05 ms. Displacements of the centers of the bright spots are measured with 0.1 pixel accuracy. To eliminate systematic errors in the velocity correlations, snapshots are taken at a fixed phase relative to the driving signal corresponding to the maximum average position of the layer.

The general behavior of the granular layer on the smooth plate has been reported previously [1], and a rich phase diagram depending on both Γ and ω was found. Here we focus mainly on the fluidized regime, obtained for $\Gamma \geq 1$. All results presented in this Letter were obtained with $\Gamma = 1.5$ and $\omega/2\pi = 60$ Hz.

The longitudinal and transverse velocity correlations, $C_{\|}$ and $C_{\perp}$, respectively, are calculated by

$$C_{\|,\perp}(r) = \sum_{i \neq j}^{N_r} v_i^{\|,\perp} v_j^{\|,\perp} / N_r,$$

where the sum runs over the N_r pairs of particles separated by a distance r, $v_i^{||}$ is the projection of $\mathbf{v}_i$ along the line connecting the centers of particles i and j, and $v_i^{\perp}$ is the projection perpendicular to that line.

Figure 1 shows $C_{||}$ (inset: $C_{\perp}$) normalized by the granular temperature $T = \langle \mathbf{v}_i^2 \rangle / 2$ obtained on the smooth plate for $\rho = 0.4$ and 0.5, and $\Gamma = 1.5$ [11]. Surprisingly, the longitudinal velocity correlations are strongly negative for all r and all accessible densities: the velocities are anticorrelated. $C_{||}$ decays slower than exponentially, and in the range $r = [2\sigma, 16\sigma]$ can be reasonably well described by $C_{||}(r) \propto r^{-2}$. The structure visible between 1σ and 2σ is stronger at high density, and its origin is not understood. The transverse component $C_{\perp}$ is much smaller and has a shorter range than $C_{||}$ (note the difference in vertical scale). Nearly identical correlations were observed without the lid in place. We have performed molecular dynamics simulations that closely match the conditions of the experiment [12] and find qualitatively similar correlations.

The existence of long-range velocity correlations in a randomly forced granular gas has been explained theoretically using a hydrodynamic approach [7]. The velocity correlations result from the balance between the excitation of hydrodynamic modes by the random external forcing and their dissipation through diffusion. At shorter range, velocity correlations arise from an increased probability of recollision due to the forcing [8]. This suggests that the correlations could be quite sensitive to the particular mechanism of energy injection, and we believe that this is the origin of the dramatic difference between the negative correlations observed in our experiment and the positive correlations observed in the randomly forced model systems [4,7–9]. In those systems, energy is injected through white noise forcing of each particle independently, while on the smooth plate energy is injected only into the vertical motion of the spheres and is then transferred to the horizontal motion through interparticle collisions. As a result of this transfer, collisions will result, on average, in an increase in the magnitude of the relative horizontal velocities $\mathbf{v}_r$ of pairs of particles. This effect can be measured directly in the molecular dynamics simulations, and at $\rho = 0.5$ we find that the average value of $\langle \mathbf{v}_r^2 \rangle$ for pairs of particles leaving a collision is 13% higher than for pairs entering a collision. Experimental support for this scenario can be found in Fig. 2, which shows a calculation of $\langle \mathbf{v}(0)\mathbf{v}(r) \rangle$, where the average includes only particles restricted to a narrow band along the direction of motion of the particle at the origin, either ahead (for positive r) or behind (for negative r). There is a clear asymmetry with respect to zero, showing that balls moving away from each other contribute significantly more to the velocity anticorrelation than do particles moving towards each other. The velocity anticorrelations would presumably dissipate through diffusion as the momentum gets transferred to surrounding particles through collisions; thus it is not surprising that the observed correlations extend over several mean free paths. This mechanism for the generation of anticorrelated velocities may also operate in inhomogeneously forced granular media when the average kinetic energy of the grains is anisotropic.

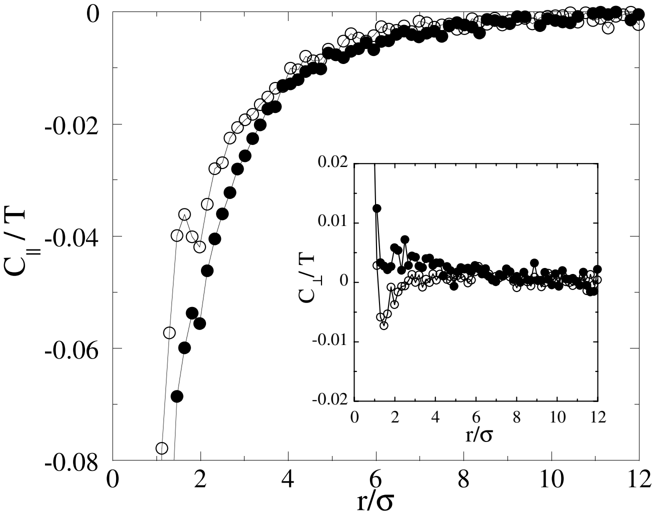

FIG. 1. Longitudinal velocity correlations normalized by the granular temperature T on the smooth plate: $\Gamma = 1.5$, $\rho = 0.4$ (•), and $\rho = 0.5$ (∘). Inset: transverse velocity correlations. Data represent averages over approximately 8000 pairs of images with about 180 balls per image.

To test our hypothesis about the origin of the correlations, we have changed the forcing by using a rough surface, so that the vibrating plate also injects energy directly into the horizontal motion of the spheres. This energy input mechanism is closer to the white noise forcing of Ref. [7], and allows for a more direct comparison between experiment and theory [13].

The velocity correlations measured on the rough plate are shown in Fig. 3 for $\Gamma = 1.5$ [14] and two extremal densities. We find that both $C_{||}$ and $C_{\perp}$ are positive for all measured ρ. $\langle \mathbf{v}(0) \cdot \mathbf{v}(r) \rangle$, calculated as described above, is positive everywhere and is roughly symmetric about zero. Molecular dynamics simulations of the layer on the rough plate [12] show similar correlations, and the effect of the

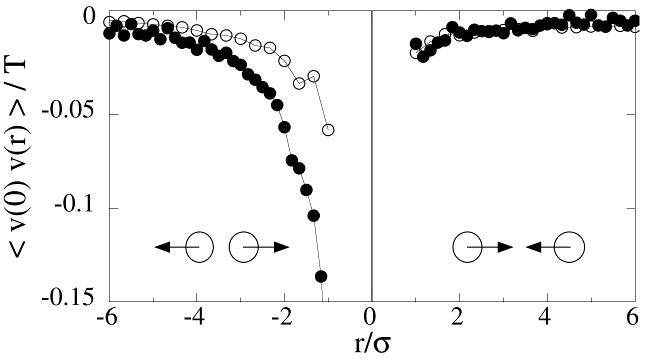

FIG. 2. $\langle \mathbf{v}(0) \cdot \mathbf{v}(r) \rangle$ (as described in the text) normalized by T for $\Gamma = 1.5$, $\rho = 0.4$ (•), and $\rho = 0.5$ (∘).

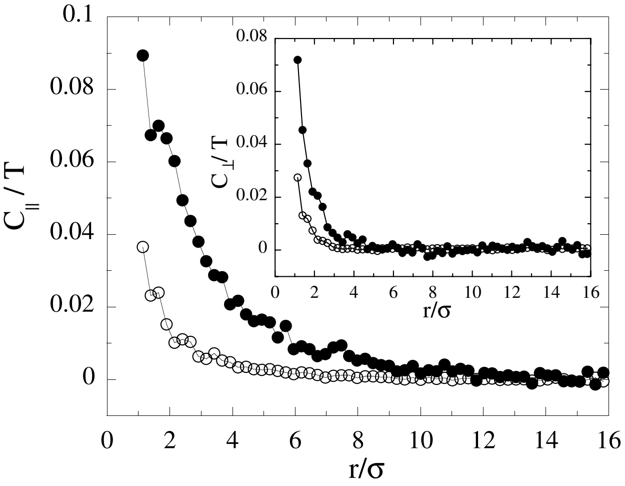

FIG. 3. Longitudinal velocity correlations normalized by the granular temperature on the rough plate: $\Gamma = 1.5$, $\rho = 0.125$ (•), and $\rho = 0.6$ (∘). Inset: transverse velocity correlations. Data are averaged over 16 000 pairs of images (~ 80 balls per image) for $\rho = 0.125$ and 8000 pairs (~ 420 balls) for $\rho = 0.6$.

collisions is to decrease the average value of $\langle \mathbf{v}_r^2 \rangle$ by 3.7% at $\rho = 0.5$. Thus in the absence of large vertical to horizontal collisional energy transfer, the velocity anticorrelations are replaced by positive velocity correlations, presumably arising from the random forcing as described in Refs. [7,8]. The dramatic difference in the correlations between the smooth and rough plates is a clear indication that the forcing, rather than the inelastic interparticle collisions, determines the velocity correlations.

Interestingly, we find that $C_{\|}$ and $C_{\perp}$ can be roughly scaled on two different curves of the form $C_{\|,\perp} = T\alpha(\rho) f_{\|,\perp}(r)$ (Fig. 4). The functions $f_{\|}$ and $f_{\perp}$ have different r dependence, but the function $\alpha(\rho)$ is the same for both $C_{\|}$ and $C_{\perp}$. $f_{\|}$ and $f_{\perp}$ are reasonably well described by $f(r) \propto e^{-r/r_o}$, with $r_o = 2\sigma$ for $f_{\|}$ and 0.6σ for $f_{\perp}$. It is surprising that this decay length has little density dependence, despite the fact that the mean free path estimated from Enskog-Boltzmann kinetic theory varies from 2.3σ for $\rho = 0.125$ to 0.16σ for $\rho = 0.6$. A similar scaling relation is predicted in the randomly forced model at large r [7], but the scaling is the same for both $C_{\|}$ and $C_{\perp}$, and $f(r)$ decays algebraically.

An important difference between our experiment and the randomly forced model is revealed by the velocity distributions $P(v)$ of the balls on the rough plate. Figure 5 shows the normalized $P(v_x)$ obtained for $\Gamma = 1.5$, and ρ ranging from 0.014 to 0.6. At the lowest density, $P(v_x)$ is well described by a Gaussian. As ρ increases, the tails of the distribution rise significantly above a Gaussian. At high density, the velocity distribution resembles those reported previously on flat plates [1,2]. To better understand the effect of density on $P(v)$, we have followed the trajectories of individual balls using a fast camera (838 frames/s [1]), measured the time-dependent velocity autocorrelation function $C_v(t) = \langle \mathbf{v}(0) \cdot \mathbf{v}(t) \rangle$, and found that $C_v(t) \approx e^{-t/\tau(\rho)}$ at all densities. The scattering length defined by $l \equiv \sqrt{T}\tau(\rho)$ varies from about 0.1σ at $\rho = 0.6$ to about 2.5σ at $\rho = 0.014$. At the lowest density, l is much smaller than the mean free path for ball-ball scattering ($\sim 20\sigma$) obtained from kinetic theory. This suggests that it is ball-plate scattering that is responsible for the

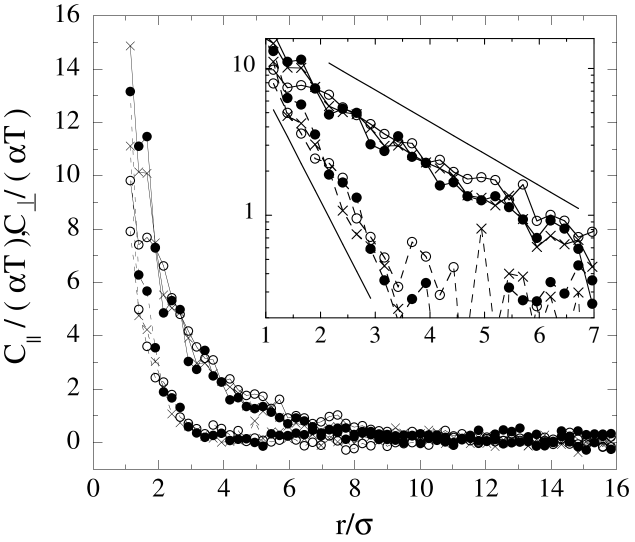

FIG. 4. Scaled longitudinal and transverse velocity correlations normalized by T. $C_{\|}/(\alpha T)$ (symbols with solid lines) and $C_{\perp}/(\alpha T)$ (symbols with dashed lines) for $\Gamma = 1.5$, $\rho = 0.125$ (∘), $\rho = 0.5$ (×), and $\rho = 0.6$ (•). Inset: Log-linear plot of the scaled velocity correlations (the straight lines are exponentials with decay lengths of 2σ and 0.6σ).

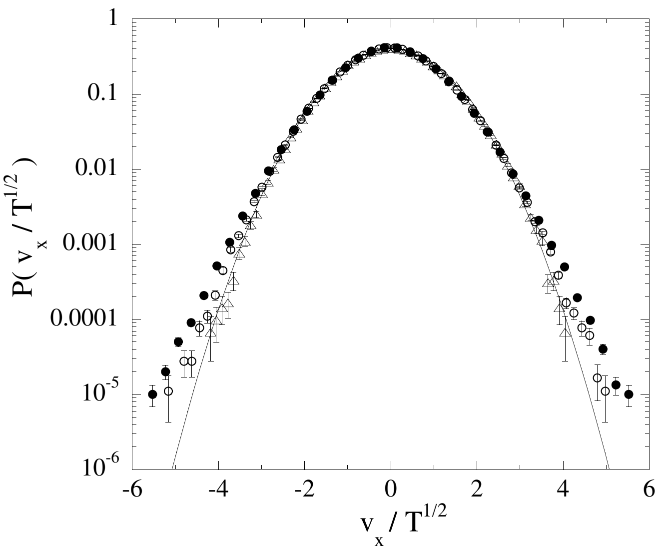

FIG. 5. Normalized velocity distributions $P(v_x)$, on the rough plate for $\Gamma = 1.5$, $\rho = 0.014$ (△), $\rho = 0.125$ (∘), and $\rho = 0.6$ (•). The solid line is a Gaussian. [Results for $P(v_y)$ are identical.]

decay of the velocity autocorrelation function, and that the scattering must therefore have a viscous component. The evolution of $P(v)$ for a single ball on the rough plate can thus be very likely modeled with an equation including only random white noise forcing and a viscous term, such as the Fokker-Plank equation for Brownian motion, which produces a Gaussian $P(v)$. When the random forcing is instead balanced by ball-ball scattering in a modified Boltzmann equation, there is an overpopulation of the tails of the distributions, $P(v) \sim \exp(-|v|^{3/2})$ [4]. This is consistent with the experimentally measured $P(v)$ at high densities, where the scattering is dominated by ball-ball collisions. At intermediate densities both scattering processes contribute, and the evolution of $P(v)$ with density can likely be described with a Boltzmann equation consisting of random white noise forcing, collisional scattering, and a density independent viscous drag. This model has been recently investigated [15], although primarily at higher inelasticities, where significant clustering is observed.

The ball-plate scattering may also explain the lack of significant density dependence of the decay length of the velocity correlations. We speculate that the density independent scattering with the plate, which unlike ball-ball collisions does not conserve momentum, is more effective at destroying the long-range velocity correlations, and therefore controls the observed decay. Support for this scenario is provided by the fact that the decay length for the exponentially decaying $C_{||}(r)$ at *all* measured densities is close to the ball-plate scattering length deduced from the individual trajectories at very low densities (2σ vs 2.5σ). However, a full quantitative understanding of the velocity correlations observed on the rough plate will require a theoretical analysis along the lines of Ref. [7], including the effect of viscous drag. Our results provide a clear experimental demonstration that the velocity distribution and correlations in a granular gas are not determined exclusively by internal dynamics (inelastic ball-ball collisions) but by a balance between internal dynamics and external forcing.

The authors gratefully acknowledge Mickey Moore for providing us with the rough plate and Rae Robertson for assistance with measurements of the velocity autocorrelation functions. This work was supported by grants from the Research Corporation, the Petroleum Research fund, and Grants No. DMR-9875529 and No. DMR-0094178 from the NSF. J. S. U. acknowledges support from the Sloan Foundation.

---

*Email address: prevost@physics.georgetown.edu

[1] J. S. Olafsen and J. S. Urbach, Phys. Rev. Lett. **81**, 4369 (1998); Phys. Rev. E **60**, R2468 (1999).
[2] W. Losert, D. G. W. Cooper, J. Delour, A. Kudrolli, and J. P. Gollub, Chaos **9**, 682 (1999).
[3] F. Rouyer and N. Menon, Phys. Rev. Lett. **85**, 3676 (2000).
[4] T. P. C. van Noije and M. H. Ernst, Granular Matter **1**, 57 (1998).
[5] C. Bizon, M. D. Shattuck, J. B. Swift, and H. L. Swinney, Phys. Rev. E **60**, 4340 (1999).
[6] X. Nie, E. Ben-Naim, and S. Y. Chen, Europhys. Lett. **51**, 679 (2000).
[7] T. P. C. van Noije, M. H. Ernst, E. Trizac, and I. Pagonabarraga, Phys. Rev. E **59**, 4326 (1999).
[8] I. Pagonabarraga, E. Trizac, T. P. C van Noije, and M. H. Ernst, Phys. Rev. E **65**, 011303 (2002).
[9] S. J. Moon, M. D. Shattuck, and J. B. Swift, Phys. Rev. E **64**, 031303 (2001).
[10] D. L. Blair and A. Kudrolli, Phys. Rev. E **64**, 050301(R) (2001).
[11] $\rho = N/N_c$, where N is the number of balls and N_c the number in a full close-packed monolayer.
[12] The interaction rules and parameters for the molecular dynamics simulation were taken from Ref. [6]. The roughness was simulated by adding a layer of close-packed spheres rigidly attached to the plate. The values for σ, ω, and A are taken from the experiment.
[13] Although the roughness of the plate is periodic, its wavelength is considerably less than the measured scattering length, and the motion of the balls on the surface is presumably chaotic, so stochastic forcing and scattering are likely to be a good approximation.
[14] At $\Gamma = 1.5$, the layer is fully fluidized. Clustering, due to trapping of the balls by the lattice, is present for values of Γ below 1.2.
[15] A. Puglisi, V. Loreto, U. Marini Bettolo Marconi, and A. Vulpiani, Phys. Rev. E **59**, 5582 (1999).

PHYSICAL REVIEW E **70**, 050301(R) (2004)

Nonequilibrium two-phase coexistence in a confined granular layer

Alexis Prevost,* Paul Melby, David A. Egolf, and Jeffrey S. Urbach†
Department of Physics, Georgetown University, 37th & O Streets, Washington, DC 20057, USA

(Received 9 December 2003; published 24 November 2004)

We report the observation of the homogenous nucleation of crystals in a dense layer of steel spheres confined between two horizontal plates vibrated vertically. Above a critical vibration amplitude, two-layer crystals with square symmetry were found to coexist in steady state with a surrounding granular liquid. By analogy to equilibrium hard-sphere systems, the phase behavior may be explained through entropy maximization. However, dramatic nonequilibrium effects are present, including a significant difference in the granular temperatures of the two phases.

DOI: 10.1103/PhysRevE.70.050301 PACS number(s): 45.70.Mg, 05.70.Fh, 05.70.Ln, 83.10.Rs

Statistical mechanics provides a powerful formalism for predicting the behavior of systems at or near equilibrium. Many natural phenomena, however, occur far from equilibrium, and extensions of the machinery of statistical mechanics to situations where significant energy flows are present would have a wide range of potential applications. Some success has been achieved in extending statistical mechanics to far-from-equilibrium situations. For example, techniques for calculating the relative probabilities of different configurations have been successfully developed for nonequilibrium steady states in a few restricted situations [1–3]. Also, effective temperatures based on the fluctuations in nonequilibrium steady states have been developed recently and, in some cases, have been found to equilibrate across different fluctuating quantities [4–10]. To generalize these initial successes to a broader spectrum of phenomena, and to develop insights into other facets of a statistical theory of far-from-equilibrium systems, new model systems for investigating nonequilibrium steady states must be developed and studied. Here we report our investigations of a simple, far-from-equilibrium granular system that shows that some mechanisms that operate in equilibrium appear to persist into situations far from equilibrium, whereas other basic tenets of equilibrium statistical mechanics must be substantially modified.

Granular materials are ubiquitous in nature and show a remarkable range of nonequilibrium behavior [11–13]. Dynamic steady states, achieved when energy input from an external source balances energy lost through inelastic collisions, provide an ideal testing ground for extensions of equilibrium statistical mechanics [4–6,10]. Here we report experimental measurements and computer simulations of the dynamics of spherical particles confined between two horizontal vibrating parallel plates. We observe a freezing transition from a homogeneous, disordered liquid to an ordered solid with square symmetry coexisting with a surrounding liquid. An essentially identical transition is observed in confined hard-sphere colloidal suspensions in equilibrium [14–18], where it is driven by entropy maximization. The presence in both the granular and the colloidal system of a solid phase with the same unexpected symmetry which occurs under the same geometric constraints and at similar densities strongly suggests a common mechanism. Unlike the equilibrium system, however, we find that the coexisting phases have dramatically different granular temperatures, demonstrating that the "zeroth law" of thermodynamics is not followed by the granular temperature. Taken together, these results show that the driving mechanism behind an equilibrium phase transition may still operate far from equilibrium, but that a thermodynamic theory must account for the absence of equipartition in the kinetic energy of the particles.

The granular system is sketched in Fig. 1(a). Previous studies which used a similar geometry at lower shaking amplitude and lower density than what is presented here found a range of complex nonequilibrium phenomena including inelastic collapse [19,20], hexagonal ordering [19,21], non-Gaussian velocity distributions [19,20,22], and velocity correlations [23]. In our experiment, stainless-steel spheres of diameter $\sigma=1.59$ mm were placed between a smooth anodized aluminum plate and an 11-mm-thick Plexiglas lid with an antistatic coating. A gap spacing of 1.75σ between the plate and the lid was maintained by circular rings of aluminum and Mylar spacers. Using an electromagnetic shaker, the system was driven sinusoidally in the vertical direction with frequency ν and amplitude A. The motion of the balls was imaged from above using a high-resolution camera (Pulnix TM1040). The results presented here were obtained for densities $\rho=N/N_{\mathrm{max}}$ ranging from 0.8 to 0.9, where N is the number of balls in the system and $N_{\mathrm{max}}=11\,377$ is the maximum number of balls that can fit in a single hexagonally close-packed layer at rest on the bottom plate. For modest vibration amplitude, the system appears liquidlike. As the vibration is increased, small independent unstable crystalline structures form. Increasing the vibration amplitude further causes the crystallites to become stable and eventually coalesce to form a single crystal which coexists with a surrounding granular liquid [see Fig. 1(b) and supplemental movie [24]]. The crystal consists of two layers, each with a square symmetry. The balls in the second layer are above the centers of the squares formed by the balls in the bottom layer. The

---

*Present address: Laboratoire des Fluides Organisés, CNRS-UMR 7125, Collège de France, 11 place Marcelin Berthelot 75231 Paris cedex 05, France.

†Corresponding author. urbach@physics.georgetown.edu

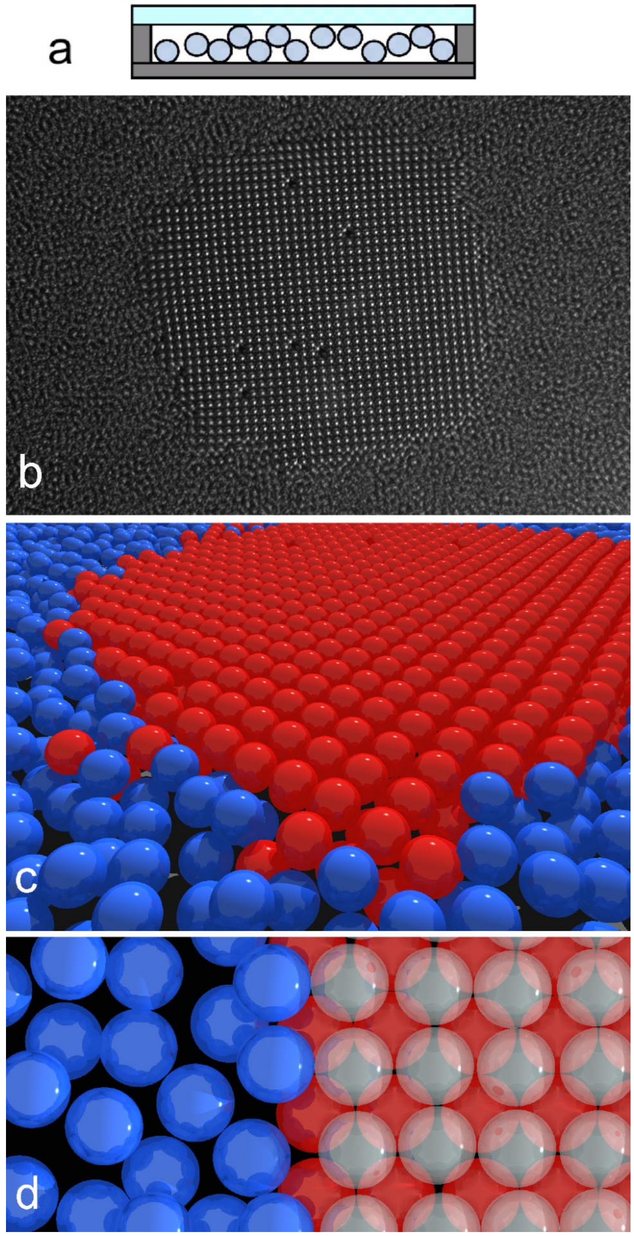

FIG. 1. Two-phase coexistence in steady state. (a) Side view of experimental setup. The system is shaken vertically and imaged from above. (b) Experiment: time-averaged image of ball positions. Only the top layer of the crystal is visible and there are several vacancies ($A=0.085\sigma, \rho=0.9, \nu=80$ Hz, averaged over 1 s). See also supplemental movie [24]. (c, d) Simulation: 3D rendering of instantaneous ball positions. In (c), balls in the crystal are colored red, balls in the liquid are colored blue. In (d) a closeup of the crystal is shown with the top layer transparent. ($A=0.13\sigma, \rho=0.89, \nu=60$ Hz, and 5000 balls.)

crystals are not densely packed and the balls constantly jitter around in the cage formed by their neighbors and the confining plates. Rearrangements continually occur at the interface, but the average size of the crystal does not change as long as the shaking amplitude and frequency are held constant.

In order to verify that the coexistence was not due to nonuniformities in the experimental apparatus, and to measure quantities not readily accessible in the experiment, we performed molecular-dynamics simulations using a model that has accurately reproduced many of the phenomena observed in a similar system [23,25]. Ball-ball, ball-plate, and ball-lid interactions are characterized by three forces: an elastic restoring force, a dissipative normal force which produces a velocity-independent coefficient of restitution, and a dissipative tangential friction. Periodic boundary conditions in the horizontal plane were used. The simulations reproduced the phase coexistence [Figs. 1(c) and 1(d)] and all of the general features of the observed phenomena, such as the existence of a critical threshold to nucleation and evaporation.

Perhaps the most surprising aspect of the transition we observe, the presence of a square symmetry instead of the hexagonal ordering naively expected for hard-sphere interactions, appears to be closely related to the phase behavior of suspensions of hard-sphere colloidal particles at similarly high densities in similar confining geometries [14–16]. For hard spheres the equilibrium configuration is determined by entropy maximization. For a range of gap spacings, including the spacing used in our system, two square layers pack more efficiently than two hexagonal layers, thereby maximizing the free volume available for each particle and therefore the entropy of the system [17,18]. The observation of a transition that closely matches an equilibrium, entropy driven phase transition suggests that a generalized free-energy functional might be found which describes the behavior of some driven granular materials.

Equilibrium two-phase coexistence requires that the two phases have equal temperatures, pressures (apart from surface-tension corrections), and chemical potentials. Recent work has focused on extending the concept of the chemical potential to nonequilibrium coexistence in which the first two conditions are satisfied [26,27]. To test whether these two conditions are met in this system, we measured the granular temperature $T_g=\langle \boldsymbol{v}_i^2 \rangle$, where $\boldsymbol{v}_i$ is a horizontal component of the rapidly fluctuating velocity of a particle. In the experiment, particle displacements were measured using the particle imaging velocimetry technique described in Ref. [23]. Using the method described in Ref. [22], we verified that the temporal resolution was sufficient to accurately measure instantaneous velocities. In both the experiments and simulations, we investigated whether the granular temperature equilibrated to the same value in the two phases. As shown in Figs. 2(a) and 2(b), T_g is dramatically lower in the crystal than in the surrounding liquid, both in the experiments and in the simulations. The spontaneous separation into phases of different temperatures in a homogeneous system of identical particles is a striking effect that will have to be incorporated into models of nonequilibrium phase coexistence. It is somewhat reminiscent of "inelastic collapse" [19], but in that case the absence of any significant granular temperature in the solid phase arises from the bistability of the ball-plate dynamics at low vibration amplitudes [28,29]. The results described here are observed at high vibration amplitudes where there is continuous energy input from the plate into both coexisting phases. The pressures of the two

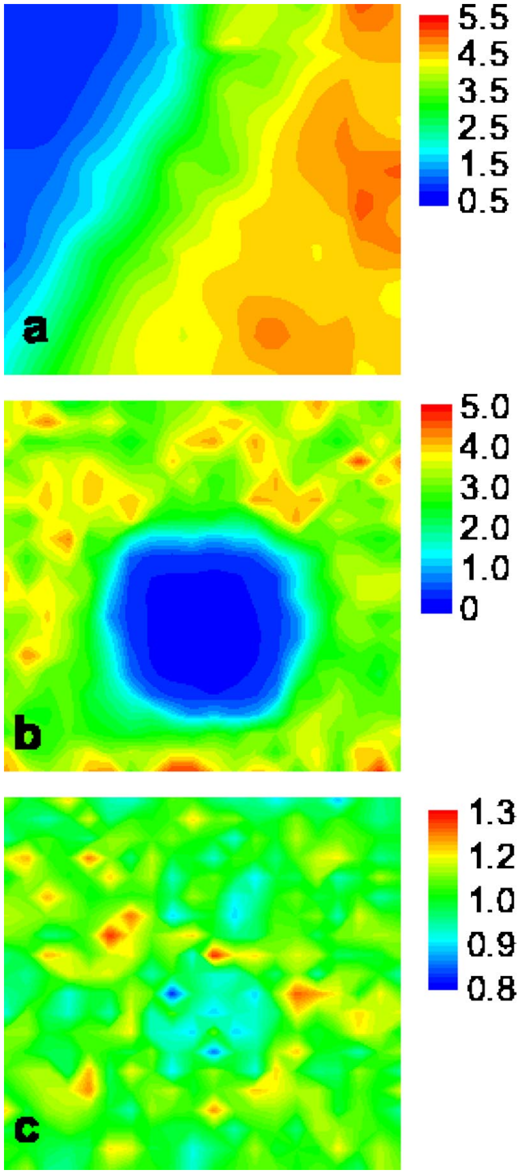

FIG. 2. Temperature and pressure fields. (a) Temperature field near the liquid-solid interface, measured in the experiment, averaged over about 40 s. The crystal is in the upper left. ($\rho=0.85, \nu=60$ Hz, $A=0.154\sigma$, displacements measured over 0.33 ms.) (b) Temperature field and (c) pressure field from the simulation shown in Fig. 1(c), averaged over 2.5 s. The crystal is in the center. The pressure was calculated using the virial expression, as described in Ref. [30].

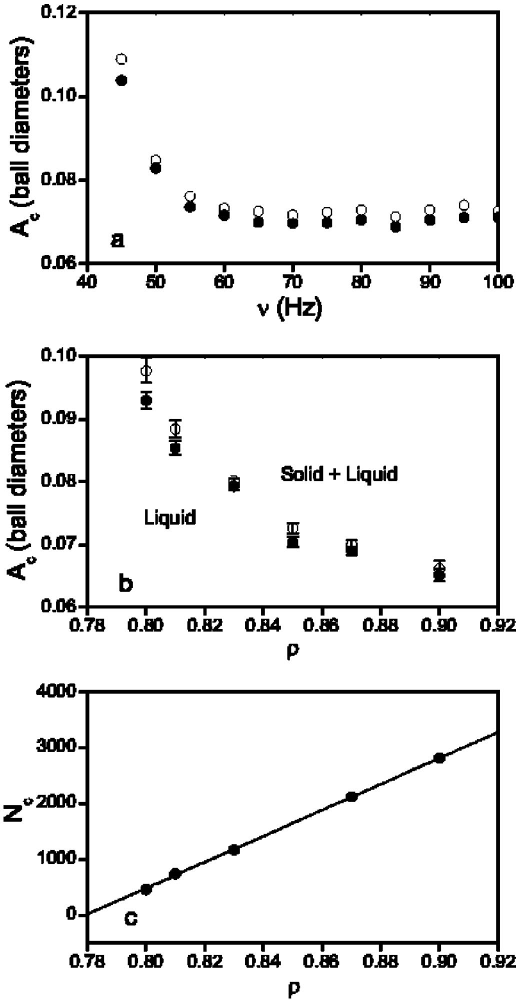

FIG. 3. (a) Frequency dependence of the critical amplitudes A_C for nucleation (open circles) and evaporation (black disks) at $\rho=0.85$. (b) High-frequency plateau value of A_C as a function of ρ. (c) Average number of balls of the crystal, N_C, as a function of ρ ($\nu=60$ Hz, $A=0.145\sigma$). Each point represents the average of 10 measurements well separated in time. The solid line is a linear fit to the points.

phases calculated in the simulations have nearly the same value, but the pressure is slightly smaller in the solid phase [Fig. 2(c)].

To further study the properties of the phase coexistence, we investigated the nucleation of the crystalline phase. Starting with the vibration amplitude at a low value, we slowly increased the intensity of shaking and measured the amplitude at which the crystalline phase first nucleates. This procedure was repeated for several densities between $\rho=0.8$ and 0.9, and for frequencies between $\nu=45$ and 100 Hz. A typical curve of the frequency dependence is displayed in Fig. 3(a) for $\rho=0.85$. In addition to this “nucleation line,” we also determined an “evaporation line” by slowly decreasing the amplitude until the crystal disappeared. For ν greater than 60 Hz, we found that the critical amplitudes were roughly independent of frequency. This high-frequency behavior was found at all densities, but the cutoff frequency increased as the density increased. One possible explanation for a frequency-independent critical amplitude is that the vibration may effectively compress the layer. If the balls are moving slowly compared to the plate and lid, then they will be mostly confined between the maximum plate height and minimum lid height. This increase in the density of the system favors nucleation of the crystal. This frequency-independent behavior cannot persist to low frequencies, however, because the acceleration, which is proportional to ν^2, must be significantly larger than that due to gravity for the balls to have enough kinetic energy to reach the second layer. We used the average value of the amplitude in the high-frequency plateau (60–100 Hz) to define a critical amplitude, A_C, and we constructed a "phase diagram" of A_C versus ρ [Fig. 3(b)]. A_C varies from roughly 0.06σ at $\rho=0.9$ to 0.1σ at $\rho=0.8$.

We measured the dependence of the crystal size on the number of particles in the system by analyzing the images to extract N_C, the number of spheres in the crystal [31]. As shown in Fig. 3(c), N_C varies linearly with ρ and extrapolates to zero at $\rho=0.78$. In steady-state coexistence, the edge of the crystal is "in equilibrium" with the surrounding liquid of density ρ_L. Assuming that the densities of the coexisting crystal and liquid are independent of the size of the crystal, the area A occupied by the crystal of density ρ_C should satisfy the relation $A/A_T=(\rho-\rho_L)/(\rho_C-\rho_L)$, where A_T is the total surface area of the plate, so that $N_C \propto (\rho-\rho_L)$. The value of ρ_L found by extrapolating to $N_C=0$ agrees with direct measurements of the density of the granular liquid in the coexistence region.

No formalism exists for incorporating the entropy into a predictive theory on nonequilibrium phase transitions, but our results indicate which parts of the equilibrium framework need modification. The large difference in the granular temperature of the coexisting phases demonstrates that the "zeroth law" of thermodynamics is not satisfied by the granular temperature. An effective temperature that does meet this requirement is probably a necessary ingredient of a quantitative theory of the phase coexistence. By comparing the system described here with the analogous and well-understood equilibrium system, new approaches for incorporating the effects of forcing and dissipation into a statistical mechanics of nonequilibrium phase transitions can be developed and tested.

This work was supported by The National Science Foundation under Grants No. DMR-9875529 and No. DMR-0094178 and by NASA under Grant No. NNC04GA63G. D.A.E. is also supported by the Alfred P. Sloan Foundation.

---

[1] L. Onsager and S. Machlup, Phys. Rev. **91**, 1505 (1953).
[2] B. Derrida, J. L. Lebowitz, and E. R. Speer, Phys. Rev. Lett. **87**, 150601 (2001).
[3] D. A. Egolf, Science **287**, 101 (2000).
[4] G. D'Anna, P. Mayor, A. Barrat, V. Loreto, and F. Nori, Nature (London) **424**, 909 (2003).
[5] H. A. Makse and J. Kurchan, Nature (London) **415**, 614 (2002).
[6] S. F. Edwards, in *Granular Matter: An Interdisciplinary Approach*, edited by A. Mehta (Springer, New York, 1994), p. 121.
[7] I. K. Ono *et al.*, Phys. Rev. Lett. **89**, 095703 (2002).
[8] G. Gallavotti and E. G. D. Cohen, Phys. Rev. Lett. **74**, 2694 (1995).
[9] W. I. Goldburg, Y. Y. Goldschmidt, and H. Kellay, Phys. Rev. Lett. **87**, 245502 (2001).
[10] S. Aumaître, S. Fauve, S. McNamara, and P. Poggi, Eur. Phys. J. B **19**, 449 (2001).
[11] H. M. Jaeger, S. R. Nagel, and R. P. Behringer, Rev. Mod. Phys. **68**, 1259 (1996).
[12] L. P. Kadanoff, Rev. Mod. Phys. **71**, 435 (1999).
[13] *Granular Gases*, Lectures Notes in Physics, Vol. 564 edited by T. Pöschel and S. Luding (Springer-Verlag, Berlin, 2001).
[14] B. Pansu, P. Pieranski, and L. Strzelecki, J. Phys. (France) **44**, 531 (1983).
[15] P. Pieranski, L. Strzelecki, and B. Pansu, Phys. Rev. Lett. **50**, 900 (1983).
[16] B. Pansu, P. Pieranski, and P. Pieranski, J. Phys. (France) **45**, 331 (1984).
[17] M. Schmidt and H. Löwen, Phys. Rev. Lett. **76**, 4552 (1996).
[18] M. Schmidt and H. Löwen, Phys. Rev. E **55**, 7228 (1997).
[19] J. S. Olafsen and J. S. Urbach, Phys. Rev. Lett. **81**, 4369 (1998).
[20] J. S. Olafsen and J. S. Urbach, Phys. Rev. E **60**, R2468 (1999).
[21] P. Pieranski, J. Malecki, W. Kuczynski, and K. Wojciechowski, Philos. Mag. A **37**, 107 (1978).
[22] W. Losert, D. G. W. Cooper, J. Delour, A. Kudrolli, and J. P. Gollub, Chaos **9**, 682 (1999).
[23] A. Prevost, D. A. Egolf, and J. S. Urbach, Phys. Rev. Lett. **89**, 084301 (2002).
[24] See EPAPS Document No. E-PLEEE8-70-R15410 for a supplemental movie of Fig. 1. A direct link to this document may be found in the online article's HTML reference section. The document may also be reached via the EPAPS homepage (http://www.aip.org/pubservs/epaps.html) or from ftp.aip.org in the directory /epaps/. See the EPAPS homepage for more information.
[25] X. Nie, E. Ben-Naim, and S. Y. Chen, Europhys. Lett. **51**, 679 (2000).
[26] A. Baranyai and P. T. Cummings, Phys. Rev. E **60**, 5522 (1999).
[27] S. Butler and P. Harrowell, Nature (London) **415**, 1008 (2002).
[28] W. Losert, D. G. W. Cooper, and J. P. Gollub, Phys. Rev. E **59**, 5855 (1999).
[29] J.-C. Géminard and C. Laroche, Phys. Rev. E **68**, 031305 (2003).
[30] D. C. Rapaport, *The Art of Molecular Dynamics Simulation* (Cambridge University Press, Cambridge, England, 1995), p. 20.
[31] N_C is taken as twice the number of balls in the top layer of the crystal, averaged over several snapshots well separated in time. An algorithm based on a fourfold symmetry order parameter and related criteria was employed in determining which balls were in the crystal.

THEME 2 : PHYSIQUE DE LA PERCEPTION TACTILE

Résumé: Nous avons développé un capteur MEMS biomimétique du fonctionnement de l'extrémité du doigt humain pour étudier les mécanismes de transduction de l'information tactile. Nous avons mis en évidence un rôle possible des empreintes digitales pour la discrimination de textures fines. Les empreintes filtrent mécaniquement les vibrations induites par le passage d'une texture de type bruit blanc, et ce filtrage s'opère à une fréquence optimisée à la fréquence de réponse des mécanorécepteurs impliqués dans la détection de textures fines. En combinant des mesures sur vrai doigt et de l'imagerie de contact de doigts biomimétiques, nous avons également montré que l'amplitude des réponses dépendait fortement de la rugosité du substrat. Enfin, à l'aide d'un système multi-capteurs MEMS, nous avons caractérisé la fonction de transfert mécanique du système biomimétique aux conditions exploratoires (vitesse relative, charge normale appliquée, coefficient de frottement).

Grâce à nos mains, nous sommes capables d'une dextérité extraordinaire qu'aucun robot n'est actuellement en mesure d'égaler. Cette dextérité résulte d'une coordination entre le système moteur qui contrôle l'activité des muscles, et le système tactile qui informe en permanence le système nerveux central des contraintes s'exerçant à la surface de la peau des doigts. La sensibilité tactile cutanée des doigts de la main nous permet ainsi d'extraire une grande quantité d'informations sur les objets que nous manipulons, telles que leur poids et leur courbure, la dureté du matériau dont ils sont constitués ou encore les propriétés de rugosité ou d'adhésion de leur surface.

Comme dans tout système sensoriel, la perception tactile met en jeu une étape de transduction de l'information par un organe périphérique qui assure l'interface entre le monde extérieur et le système nerveux central. La nature de l'information finale traitée par le système nerveux central, dépend intimement des propriétés biomécaniques de cet organe, qui contrôlent la façon dont l'information physique est filtrée, mise en forme puis traduite en activité nerveuse. Dans le cas du toucher digital humain, c'est la peau qui constitue cette interface: l'information tactile est entièrement contenue dans la séquence des déformations et des vibrations de la peau induites par le contact entre les doigts et l'objet. Ces déformations cutanées sont converties en potentiels d'action par des terminaisons nerveuses mécano-sensibles, encore appelées mécanorécepteurs, situées jusqu'à quelques millimètres sous la surface de la peau pour les plus profondes.

Afin d'obtenir une description complète de la perception tactile, il est donc nécessaire de comprendre comment les différentes caractéristiques physiques d'un substrat comme sa forme, sa dureté, sa rugosité de surface ou encore ses propriétés adhésives se traduisent mécaniquement au niveau sous-cutané dans des conditions d'exploration naturelles. Par conditions naturelles, on entend les conditions de vitesse relative et de pression impliquées quand on frotte ses doigts sur une surface. Typiquement, les vitesses relatives varient de 1 à 10 cm/s et les charges normales appliquées sont de l'ordre de un à quelques Newtons.

Pour étudier ces questions, nous avons choisi de développer une approche dite *biomimétique* qui consiste à reproduire le fonctionnement de l'extrémité du doigt humain en nous limitant à un nombre restreint de paramètres qui le caractérise **(Fig. 5)**. Cette approche contraste avec les méthodes de microneurographie utilisées plus traditionnellement pour enregistrer l'activité neuronale des mécanorécepteurs et qui consistent en l'insertion de microélectrodes conductrices au niveau du nerf afférent. En reproduisant le fonctionnement du doigt de manière simplifiée, il devient en effet possible d'étudier et d'identifier les contributions individuelles des paramètres physiques au filtrage mécanique de l'information tactile.

A. Transduction mécanique de l’information tactile digitale humaine

La peau est un milieu stratifié comportant une partie molle, le derme, recouverte d’une partie plus rigide d’épaisseur plus fine, l’épiderme. En première approximation, on peut cependant oublier cet assemblage et modéliser la peau par un matériau homogène élastique comme un caoutchouc. Nous avons donc choisi de modéliser l’extrémité de la peau du doigt par une calotte sphérique d’un élastomère silicone de PolyDiMéthylSiloxane (PDMS, Sylgard 184, Dow Corning) dont les propriétés élastiques sont proches de celles de l’ensemble derme-épiderme (module élastique de Young de l’ordre de quelques MPa). A la base de cette calotte sphérique d’épaisseur millimétrique, nous avons placé un ou plusieurs micro-capteurs de force qui simulent un ou plusieurs mécanorécepteurs sous-cutanés.

Chez l’humain, les mécanorécepteurs sont répartis à différentes profondeurs sous la peau, 2 millimètres pour les plus profonds. Ils peuvent être classés en deux catégories ; ceux dits à adaptation lente (disques de Merkel, organes de Rufini) qui répondent à l’intensité du stimulus, et ceux, dits à adaptation rapide (corpuscules de Pacini, corpuscules de Meissner) qui répondent au contraire aux variations de l’intensité du stimulus et sont donc sensibles aux vibrations **(Fig. 5a)**. Pour reproduire ces mécanorécepteurs en taille, en sensibilité et en distribution spatiale sous la peau, nous avons collaboré avec P. Rey (LETI - Laboratoire d’Electronique et Techniques de l’Information, CEA). P. Rey et son équipe nous ont d’abord fourni des micro-capteurs de force unique développé initialement pour d’autres applications, puis nous avons ensuite développé avec eux dans le cadre d’un projet européen MONAT (Measurement Of NATuralness - Initiative STREP-NEST) des barrettes linéaires de capteurs constituées de 10 capteurs avec un pas de 1 mm **(Fig. 5b)**.

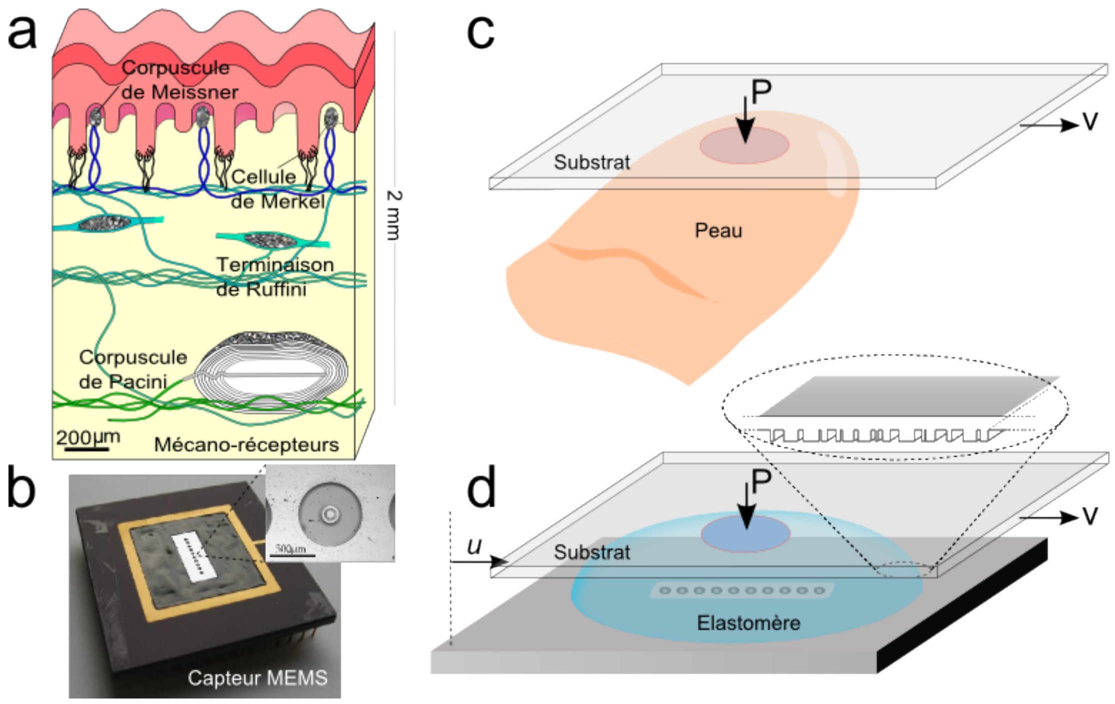

Figure 5 – *Schéma de principe de l’approche biomimétique pour étudier la perception tactile digitale humaine.* **(a)** *Coupe en profondeur de la peau du doigt permettant de localiser les 4 types de mécanorécepteurs qui participent à la perception tactile.* **(b)** *Photo d’une barrette linéaire de 10 capteurs MEMS et détail d’un capteur individuel vu du dessus (insert). Chaque capteur, entièrement réalisé en silicium, est constitué d’une membrane surmontée d’un cylindre central.* **(c)** *Exploration tactile par le doigt à vitesse V sous une charge normale P.* **(d)** *Reproduction biomimétique de ce type de mouvement avec le dispositif MEMS et un substrat de type code-barre.*

Ces capteurs, qu'ils soient individuels ou en réseau, fonctionnent sur le même principe. Ils sont entièrement réalisés en silicium grâce à la technologie MEMS (Micro-Electro-Mechanical-Systems) dérivée de la microélectronique, et consistent en une membrane circulaire suspendue, encastrée sur son périmètre. D'épaisseur 100 µm dans sa version initiale, puis 10 µm dans sa version en réseau, cette membrane est surmontée d'un cylindre en son centre, et comporte 8 jauges piézo-résistives insérées le long de deux diamètres orthogonaux et qui mesurent ses déformations. De cette mesure, on peut remonter aux forces exercées dans les 3 directions de l'espace appliquées sur l'extrémité du cylindre, à la manière d'un « joystick ».

Nous avons d'abord utilisé les capteurs individuels avec lesquels nous avons mis au point deux types de dispositifs pour explorer l'effet d'une texturation de la surface de la peau (empreintes digitales) pour détecter et discriminer des textures fines, typiquement un papier de verre de grain très petit **[1, 2]**. Nous avons ensuite utilisé les réseaux de capteurs MEMS pour mettre au point une seconde version du dispositif tactile et explorer l'effet des conditions d'exploration (vitesse relative de frottement, pression appliquée, position du capteur sous le contact, coefficient de frottement) sur la transduction mécanique de l'information tactile **[3]**.

B. Rôle d'une texturation - l'effet empreintes

La première version du senseur tactile a été déclinée en deux exemplaires, l'un avec une peau sphérique « lisse »[2], l'autre avec une peau sphérique texturée à l'image des empreintes digitales, *i.e.* recouverte d'un réseau régulier de sillons de profondeur $\sim 30\ \mu m$ et de période spatiale $\lambda \sim 200\ \mu m$. En utilisant un dispositif de mesure tribologique développé au laboratoire, nous avons frotté à vitesse constante V et sous charge normale P constante ces deux types de capteurs contre des surfaces planes rugueuses modèles. Celles-ci ont été fabriquées par photolithographie douce en résine SU8 et consistaient en des réseaux de sillons parallèles de largeur variable et dont les bords sont distribués aléatoirement selon une direction seulement (substrats dits « code-barre », dont on peut voir une représentation 3D sur la **Fig. 5d**), et présentant donc une topographie dont le spectre est celui d'un bruit blanc gaussien unidimensionnel.

---

[2] Pour atténuer les effets d'adhésion, cette peau est en réalité rugueuse à des échelles microscopiques avec une rugosité *rms* ~ 1.3 µm, caractérisée par profilométrie optique. Cette rugosité est obtenue par moulage du mélange PDMS/agent réticulant contre une surface en Plexiglas rodée avec une poudre de SiC (taille moyenne des grains 37 µm). Cette peau possède un spectre de topographie qui suit une loi de puissance.

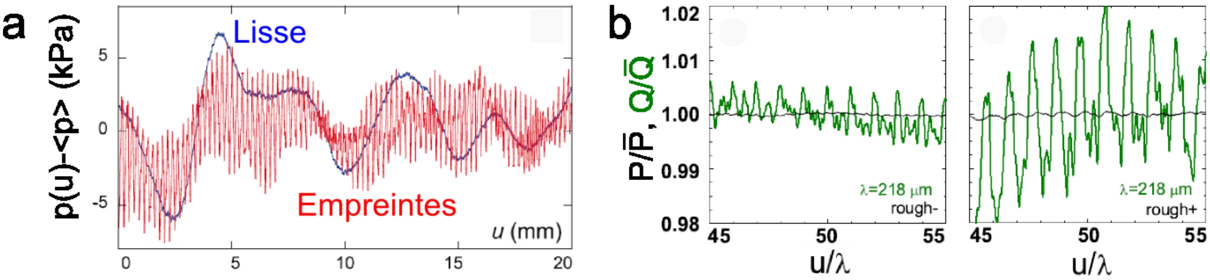

Figure 6 – **(a)** *Pression « sous-cutanée » mesurée par un capteur MEMS individuel frotté contre un substrat « code-barre », fonction du déplacement u du substrat (Fig. 5d), pour une peau lisse (ligne continue bleue) et une peau à empreintes (ligne continue rouge)* **[1]**. **(b)** *Forces normale P et tangentielle Q mesurées au cours du frottement d'une calotte sphérique recouverte d'empreintes (λ = 218 µm) contre des substrats de verre rodé (« rough – » de rugosité rms ~ 2 µm, et « rough + » avec une rugosité rms ~ 5 µm)* **[4]**.

En comparant les signaux de contraintes mesurés par le capteur MEMS pour les deux systèmes à des vitesses relatives V de quelques centaines de µm/s, nous avons montré qu'en présence d'empreintes, ceux-ci présentaient de larges fluctuations à une fréquence déterminée par le rapport V/λ **(Fig. 6a)**. La peau à empreintes se comporte donc mécaniquement comme un filtre passe-bande centré sur cette fréquence. Les conséquences pour la perception tactile de ce résultat deviennent évidentes si l'on se replace dans le contexte d'une exploration réelle chez l'humain. Dans des conditions d'exploration naturelle typiques pour le doigt humain, les vitesses de déplacement relatives sont en effet de l'ordre de 10-15 cm/s et les empreintes digitales humaines ont une longueur d'onde moyenne d'environ 500 µm. On peut ainsi construire une fréquence temporelle d'environ 200-300 Hz, qui est justement adaptée à la fréquence de réponse optimale des corpuscules de Pacini, d'environ 250 Hz. Paradoxalement, ces derniers sont situés à environ 2 millimètres sous la surface de la peau, et ont donc une faible résolution spatiale puisqu'ils intègrent les fluctuations de contraintes dans une zone en surface de taille typique ~ 2 mm². Or on sait, grâce à des expériences de psychophysique, qu'ils sont tout de même impliqués dans la détection de textures fines (théorie duale[3]). La présence d'empreintes lève le voile sur ce paradoxe en permettant la génération de vibrations qui peuvent être perçues par ces mécanorécepteurs à adaptation rapide. Cette étude a donc permis d'élucider le rôle essentiel de la texturation de la peau sous forme d'empreintes pour la transduction de l'information tactile dans le cas de textures fines **[1, 2, 5-8]**.

Nous avons pu interpréter ces résultats dans le cadre d'un modèle mécanique linéaire en montrant que les fluctuations de la contrainte s mesurée par le capteur autour de sa valeur moyenne $\langle s \rangle$ dépendaient du déplacement relatif u et étaient données par l'expression suivante

$$\delta s(u) = s(u) - \langle s \rangle = \iint [g.\bar{p}](x,y)\, T(u-x) dxdy \quad (1)$$

Dans l'équation (1), $\bar{p}(x,y)$ est typiquement le champ de pression de type Hertz obtenu en l'absence d'empreintes digitales, et $g(x,y)$ est la réponse du capteur à une indentation localisée en surface (fonction de Green, encore appelé champ récepteur intrinsèque). La fonction $T = \pm 1$ est une fonction qui prend aléatoirement les valeurs +1 ou -1 et qui caractérise la topographie binaire des substrats « code-barre » utilisés.

---

[3] La théorie duale pour la perception tactile stipule que le codage neuronal de textures grossières (caractères Braille par exemple, de tailles latérales supérieures à ~ 200 µm) est assuré par les mécanorécepteurs à adaptation lente de Merkel et est de type spatial. En revanche, pour les textures très fines (tailles latérales inférieures à ~ 200 µm), il est maintenant bien établi que le codage est de type temporel et intensif, et est assuré par les plus gros mécanorécepteurs à adaptation rapide, à savoir les corpuscules de Pacini.

Le résultat principal de ce modèle est que la transduction linéaire de l'information tactile est contrôlée par une fonction de transfert $g_1(x) = \int [g.\bar{p}](x,y)dy$, qui fait intervenir le produit du champ g, intrinsèque au capteur, et du champ de contrainte interfacial moyen $\bar{p}$ qui au contraire dépend des conditions exploratoires (charge normale P, position de la zone de contact par rapport à celle du capteur). En présence d'empreintes, la fonction g n'est modifiée que marginalement, tant que la hauteur des empreintes est faible devant l'épaisseur typique de la calotte sphérique. Par contre, le champ $\bar{p}$ est modifié significativement puisqu'il s'annule entre les empreintes. Il en résulte alors une modulation périodique de la fonction de réponse linéaire à l'origine de l'amplification spectrale du signal autour de la fréquence V/λ.

En frottant un vrai doigt contre les mêmes substrats « code-barre », nous avons ensuite mis en évidence que le même type de modulation existait dans la force de frottement macroscopique Q intégrée sur tout le contact **[2]**. Si l'on se place dans le cadre d'une description de frottement de type Amontons-Coulomb (*i.e.* la force tangentielle de frottement Q est proportionnelle à la force normale appliquée P), on s'attend à ce que la force tangentielle de frottement ne fluctue pas à force normale constante.

Pour essayer de comprendre l'origine de ces fluctuations de la force de frottement induites **[4]**, nous avons donc, avec E. Wandersman, recruté en tant que chercheur postdoctoral sur le projet ANR-DYNALO, fait frotter une calotte sphérique texturée (empreintes digitales) sur un substrat plan rugueux à des échelles microscopiques (verre rodé ou sablé de rugosité *rms* quelques µm). En combinant imagerie du contact en caméra rapide et mesures de forces macroscopiques, nous avons ainsi mis en évidence l'existence d'un mécanisme de sélection spectrale identique à celui observé avec le système MEMS **(Fig. 6b)**. Nous avons développé un modèle mécanique qui a permis d'expliquer l'origine de ces modulations comme la conséquence directe du caractère non-linéaire de la loi de frottement. Dans le cadre de ce modèle, on peut en effet montrer que les fluctuations de la force de frottement Q autour de sa valeur moyenne dépendent du déplacement relatif u entre la calotte sphérique et le substrat rugueux et s'écrivent comme

$$\delta Q(u) = \iint [\mu(p) - \langle\mu\rangle]\delta p(u-x,y)dxdy \quad (2)$$

où $\mu(p)$ caractérise la dépendance avec la pression locale du coefficient de frottement, $\langle\mu\rangle$ le coefficient de frottement moyen, et δp les fluctuations de pression induites par la rugosité microscopique du substrat. Si la loi d'Amontons-Coulomb est vérifiée localement, ce qui se traduit par $\mu(p) = C^{ste} = \langle\mu\rangle$, on ne peut donc pas observer de fluctuations de la force de frottement. En revanche, dès que la loi de frottement est non-linéaire, *i.e.* $\mu(p) \neq C^{ste}$, ceci n'est plus vrai[4]. Si de plus, le champ de pression de type Hertz du contact sphère-plan est modulé par la présence d'empreintes digitales, on observera alors des modulations de la force de frottement à la période des empreintes.

Ce modèle a également permis de prédire quantitativement comment dépendait l'amplitude des modulations induites avec la charge normale et les caractéristiques topographiques. Le mécanisme que nous avons décrit permet enfin d'expliquer nos mesures sur un vrai doigt quand on sait que la peau humaine présente aussi des dynamiques de frottement non-linéaires.

---

[4] Une telle non-linéarité est généralement observée pour tous les élastomères et l'est également pour la peau humaine.

Au-delà des enjeux propres liés à la perception tactile, ce mécanisme a également révélé que texturer une surface avec des motifs à empreintes permettait de discriminer deux surfaces rugueuses aléatoires dont la rugosité *rms* ne diffère que d'un facteur 2 (2 µm *versus* 5 µm, pour nos expériences). Ceci nous a permis de suggérer une méthode simple de caractérisation des surfaces par « spectro-tribométrie », consistant à mesurer l'amplitude du mode fondamental des fluctuations de la force de frottement, pour un réseau d'empreintes de période donnée. En variant la période de ce réseau, on peut ainsi décomposer spectralement la topographie de la surface sondée pour avoir accès à ses caractéristiques de rugosité à des échelles bien plus petites que la taille des empreintes.

Ces idées ont été soulignées dans la revue Nature par C. M. Mate et R. W. Carpick (News & Views, Materials science : « A sense for touch », Nature **480**, 189-190 (2011)). Ces derniers ont également suggéré d'utiliser ce mécanisme pour sonder les fluctuations de la force de frottement à l'échelle nanométrique en utilisant des contacts millimétriques réalisables facilement expérimentalement, et non plus nanométriques comme c'est le cas avec un AFM.

C. Rôle des conditions d'exploration

La deuxième version du senseur tactile que nous avons développé avait pour but d'être plus fidèle au doigt humain, tant du point de vue de la sensibilité des mécanorécepteurs que du point de vue de leur multiplicité sous la peau, avec une densité surfacique similaire.

En partenariat avec le LETI et grâce à un financement européen obtenu dans le cadre du projet MONAT, nous avons donc développé des réseaux 1x10 de capteurs MEMS de dimensions réduites et de sensibilité accrue, plus proches de celles des mécanorécepteurs humains, au détriment d'une fragilité accrue. Nous avons donc mis au point des protocoles permettant d'intégrer ces capteurs sans les briser sous une membrane d'élastomère sphérique d'épaisseur millimétrique. Nous avons également développé des cartes électroniques de multiplexage pour faciliter l'enregistrement simultané des 40 signaux de sortie générés par la barrette de capteurs (chaque capteur mesure 3 composantes de la force appliquée, obtenues par la combinaison de 4 tensions). Enfin, nous avons mis en place de nouveaux outils d'analyse et de gestion des données massives produites. Nous avons accompli ces différentes tâches avec R. Candelier, recruté en tant que chercheur postdoctoral sur le sujet dans le cadre du projet ANR TRANSACT.

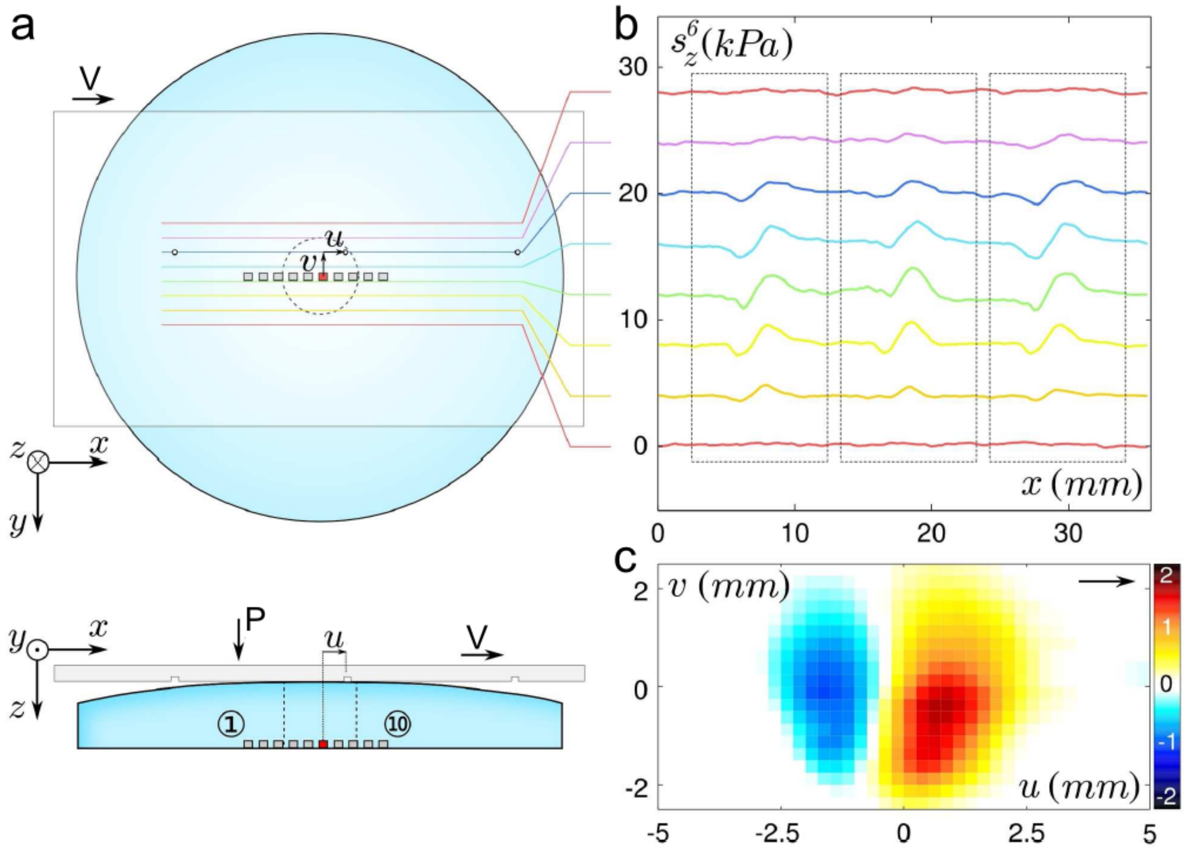

Figure 7 – *Principe de l'expérience pour mesurer pour chaque micro-capteur de forces sous le contact sa fonction de transfert au passage d'un défaut isolé. On déplace sous charge P et à vitesse constante V le long de lignes parallèles un substrat de Plexiglas à la surface duquel des trous isolés de diamètre 500 µm et de profondeur 1 mm ont été gravés par micro-fraisage.* **(a)** *Vue de dessus et de côté.* **(b)** *Fluctuations des contraintes normales enregistrées par le capteur #6 au passage des défauts le long de 8 traces parallèles.* **(c)** *Fonction de transfert 2D du capteur #6 (en KPa) déduites de 14 traces parallèles.*

Ce dispositif a permis, via la mesure simultanée des contraintes en plusieurs points sous le contact d'extraire la fonction de transfert 2D $g_1(x, y)$ pour chaque capteur individuel dans des conditions exploratoires différentes. Cette fonction, encore appelée champ récepteur exploratoire et déjà évoquée plus haut dans sa version 1D (intégrée dans la direction y), caractérise la réponse spatiale en pression ou cisaillement d'un capteur à une excitation localisée et en mouvement à la surface de la peau. Elle a d'abord été obtenue dans sa version 1D avec le premier dispositif tactile à un capteur MEMS, en utilisant une technique de corrélation inverse dite de Wiener-Voltera, dont le résultat pratique est que la réponse linéaire de tout système peut être obtenue en corrélant le signal d'entrée au signal de sortie dès lors que le premier présente les caractéristiques d'un bruit blanc gaussien **[1]**.

En utilisant le dispositif multi-capteurs frotté contre des substrats lisses présentant une série de trous microscopiques **(Fig. 7)**, il a été possible de mesurer et de caractériser complètement la fonction de transfert 2D pour des conditions exploratoires différentes. Ces mesures ont en particulier révélé que la forme de $g_1(x, y)$ dépendait fortement de la position du capteur sous le contact **(Figs. 8a-8c)**, suggérant une explication purement mécanique à la diversité des champs récepteurs neuronaux mesurés dans des expériences de neurophysiologie. Ces mesures ont été confrontées avec succès à un modèle de transduction mécanique linéaire **(Figs. 8b-8d)**, dont les ingrédients sont similaires à ceux utilisés pour dériver l'équation (1).

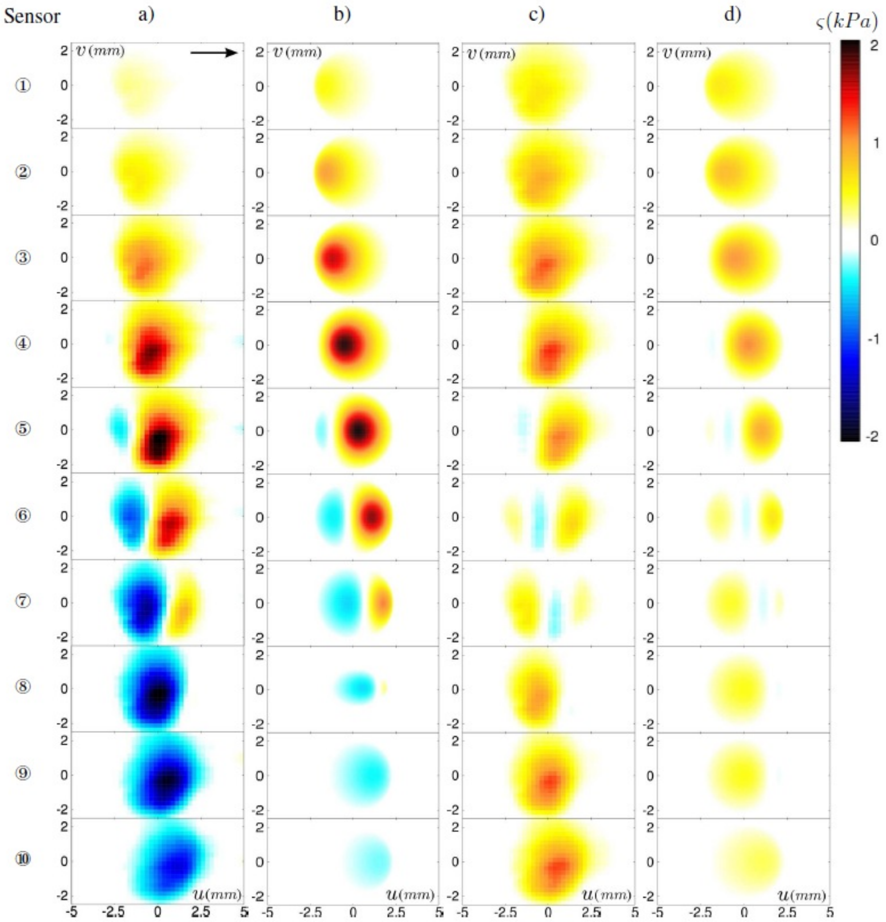

Figure 8 – *Comparaison entre les champs récepteurs exploratoires mesurés et prédits par le modèle de transduction mécanique pour les 10 capteurs qui constituent la barrette linéaire (du haut vers le bas, et pour P=0.8N). Chaque ligne correspond à un capteur. Réponse en contrainte normale mesurée* **(a)** *et prédite* **(b)***. Réponse en contrainte tangentielle mesurée* **(c)** *et prédite* **(d)***. La flèche noire indique le sens du déplacement du défaut. Les contraintes sont données en kPa sur la barre de couleur.*

Ce modèle validé sur un nombre restreint de conditions expérimentales a ensuite été utilisé pour étudier de façon plus systématique le rôle des paramètres exploratoires sur les caractéristiques de la fonction de transfert, notamment le coefficient de frottement entre l'élastomère du capteur tactile et le substrat exploré que nous avons fait varier entre 0 et 6. Il ressort de cette étude que la fonction de transfert, en plus de dépendre des caractéristiques intrinsèques du capteur (présence d'empreintes par exemple), dépend fortement du coefficient de frottement et de la position des capteurs par rapport à la zone de contact, mais peu de la charge normale appliquée.

Cette étude nous a permis d'autre part de quantifier l'hyperacuité du système, c'est-à-dire une résolution sur la prédiction de la position de défauts topologiques qui est un ordre de grandeur en dessous de l'espacement entre mécanorécepteurs.

Combinés aux travaux sur les empreintes digitales, ces résultats pourraient expliquer en grande partie les excellentes performances du système tactile digital humain **[3]**.

D. Du biomimétisme au toucher humain

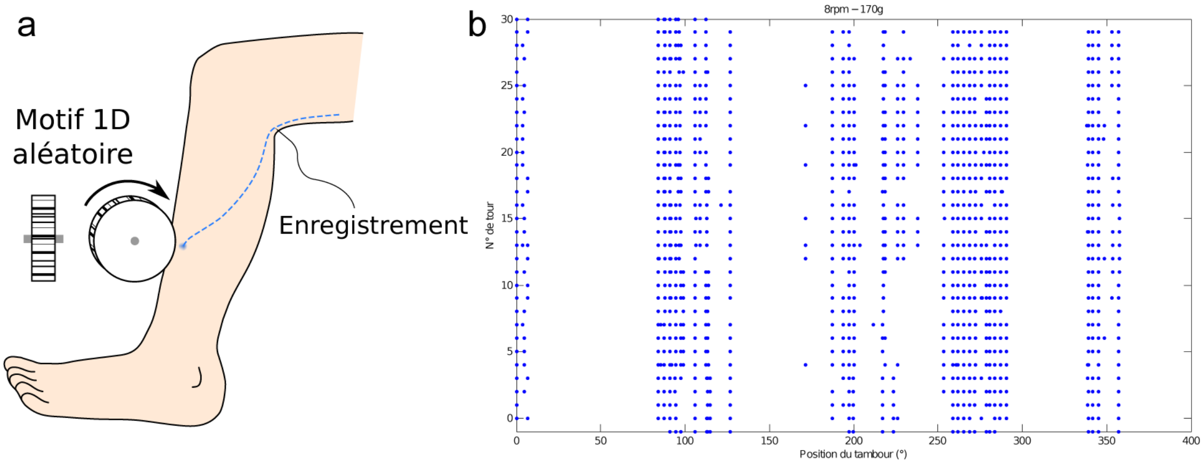

Figure 9 – **(a)** *Principe de l'expérience d'excitation et de mesure des potentiels d'action générés quand on frotte un rouleau texturé contre l'avant de la jambe sous pression et vitesse contrôlées. La mesure se fait en insérant une microélectrode de tungstène à l'arrière du genou dans le nerf poplité externe qui collecte l'ensemble des fibres nerveuses des mécanorécepteurs.* **(b)** *Raster plot sous une charge de 170 grammes et une vitesse de 8 tours par minute : chaque point bleu correspond à un potentiel d'action enregistré.*

Forts de ces résultats, nous avons entamé une collaboration avec J. P. Roll et J. M. Aimonetti (Laboratoire de Neurosciences Intégratives et Adaptatives, Université de Provence, Marseille) pour valider nos hypothèses directement chez l'humain. Cette équipe fait partie des quelques groupes au monde, spécialisés dans l'enregistrement de l'activité neuronale de mécanorécepteurs chez l'humain en utilisant la technique de microneurographie. Cette méthode consiste à insérer une ou plusieurs microélectrodes conductrices sous la peau au niveau des terminaisons nerveuses afférentes et permet en pratique de mesurer la séquence temporelle de potentiels d'action émis par un unique mécanorécepteur quand on stimule l'extrémité du doigt.

Au tout début de la thèse de T. Panier, nous avons mis au point un système de tambour frottant dont la surface est texturée par micro-fraisage soit sous forme de code-barre, soit sous forme de défauts aléatoirement répartis **(Fig. 9a)**, et qui permet d'exciter les mécanorécepteurs présents sous le contact dans des conditions de pression et de vitesse contrôlées. Ce dispositif a été testé avec succès sur l'avant de la jambe **(Fig. 9b)**, partie du corps humain sur laquelle J.P. Roll et J.M. Aimonetti avaient jusqu'à présent concentré leur recherche pour notamment étudier les mécanismes de proprioception musculaire et de perception spatiale du mouvement. Récemment, ils ont commencé à se familiariser avec l'enregistrement de potentiels d'action de mécanorécepteurs de la main.

Le dispositif de stimulation contrôlé que nous avons mis au point devra leur permettre de corréler la réponse neuronale aux caractéristiques topographiques des surfaces en contact, mesurer les champs récepteurs exploratoires et tester en conditions réelles le scénario que nous avons proposé pour le rôle des empreintes digitales.

Références

[1]. "The Role of Fingerprints in the Coding of Tactile Information Probed with a Biomimetic Sensor", J. Scheibert, S. Leurent, A. Prevost, G. Debrégeas, *Science,* Vol. **323** Issue 5920, pages 1503-1506 (2009).

[2]. "Effect of fingerprints orientation on skin vibrations during tactile exploration of textured surfaces", A. Prevost, J. Scheibert, G. Debrégeas, *Communicative & Integrative Biology* **2:5**, 1-3 (2009).

[3]. "The Role of Exploratory Conditions in Bio-Inspired Tactile Sensing of Single Topogical Features", R. Candelier, A. Prevost, G. Debrégeas, *Sensors* **11**(8), 7934-7953 (2011).

[4]. "Texture-Induced Modulations of Friction Force: The Fingerprint Effect", E. Wandersman, R. Candelier, G. Debrégeas, A. Prevost, *Phys. Rev. Lett.* **107**, 164301 (2011).

[5]. "A MEMS-based tactile sensor to study human digital touch: mechanical transduction of the tactile information and role of fingerprints", J. Scheibert, G. Debrégeas, A. Prevost, *ICEM 14: 14th International Conference on Experimental Mechanics*, **6**, 21006 (2010).

[6]. "Vers des senseurs tactiles biomimétiques", A. Prevost, G. Debrégeas, *Biofutur* **326**, 34 (2011).

[7]. "Mécanique du contact rugueux et perception tactile", J. Scheibert, G. Debrégeas, A. Prevost, *Reflets de la physique* n°**16**, octobre 2009, pp. 17-19.

[8]. G. Debrégeas, A. Prevost, J. Scheibert, "Toucher digital humain : transduction mécanique de l'information tactile et rôle des empreintes digitales", pp. 11−17, *Images de la Physique* (2009).

the interaction was greatly enhanced in the presence of SYD-1 (Fig. 4, C, D, and G), suggesting that SYD-1 facilitates binding between ELKS-1 and SYD-2. Consistent with this result, SYD-1 directly interacted with ELKS-1 (Fig. 4, E and G), and this interaction was weakened in the presence of RSY-1ΔSR (Fig. 4, F and G). Thus, one way in which RSY-1 regulates SYD-2 function is indirectly by weakening the interaction of SYD-1 with ELKS-1 and thus potentially blocking the ability of SYD-1 to facilitate SYD-2 function (Fig. 4K).

Given that the ELKS-1/SYD-2 binding is very weak in the absence of SYD-1 in our assay, we could not test whether interaction of RSY-1 with SYD-2 inhibited ELKS-1/SYD-2 binding. However, the ELKS-1/SYD-2 interaction does increase when SYD-2 contains a gain-of-function mutation, Arg^{184} → Cys^{184} (R184C) (*14*), which was verified in our cell-based assay (Fig. 4, H and J). We then tested the effect of RSY-1 on this interaction and found that the interaction between ELKS-1 and SYD-2R184C was weakened in the presence of RSY-1ΔSR (Fig. 4, I and J), suggesting that, besides acting via SYD-1, RSY-1 can also directly antagonize the ability of SYD-2 to recruit ELKS-1 (Fig. 4K).

It is increasingly clear that positive and negative regulators control synapse development at multiple levels. For example, the transcription factor MEF2 globally regulates the number of excitatory synapses (*7*). Three ubiquitin ligase complexes also regulate presynaptic development (*5*, *8*, *29*). Here, RSY-1 was shown to act as a negative regulator of synaptogenesis by counteracting SYD-1 function to inhibit SYD-2–dependent presynaptic assembly in the HSNL neuron. RSY-1 controls the amount of synaptic material recruited to presynaptic sites. RSY-1 also plays a role in establishing a balance between synapse formation and synapse elimination. RSY-1 achieves these functions by interacting with integral components of the synapse assembly machinery and by regulating a dense network of protein-protein interactions between various active-zone molecules (Fig. 4K).

References and Notes

1. M. Zhen, Y. Jin, *Nature* **401**, 371 (1999).
2. M. Zhen, Y. Jin, *Curr. Opin. Neurobiol.* **14**, 280 (2004).
3. C. L. Waites, A. M. Craig, C. C. Garner, *Annu. Rev. Neurosci.* **28**, 251 (2005).
4. Q. Chang, R. J. Balice-Gordon, *Neuron* **26**, 287 (2000).
5. P. van Roessel, D. A. Elliott, I. M. Robinson, A. Prokop, A. H. Brand, *Cell* **119**, 707 (2004).
6. K. Nakata *et al.*, *Cell* **120**, 407 (2005).
7. S. W. Flavell *et al.*, *Science* **311**, 1008 (2006).
8. M. Ding, D. Chao, G. Wang, K. Shen, *Science* **317**, 947 (2007); published online 11 July 2007 (10.1126/science.1145727).
9. M. P. Klassen, K. Shen, *Cell* **130**, 704 (2007).
10. V. Y. Poon, M. P. Klassen, K. Shen, *Nature* **455**, 669 (2008).
11. C. Desai, H. R. Horvitz, *Genetics* **121**, 703 (1989).
12. K. Shen, C. I. Bargmann, *Cell* **112**, 619 (2003).
13. M. R. Patel *et al.*, *Nat. Neurosci.* **9**, 1488 (2006).
14. Y. Dai *et al.*, *Nat. Neurosci.* **9**, 1479 (2006).
15. Materials and methods are available as supporting material on *Science* Online.
16. G. Zimowska *et al.*, *Invest. Ophthalmol. Vis. Sci.* **44**, 4715 (2003).
17. P. Ouyang, *Biochem. Biophys. Res. Commun.* **263**, 192 (1999).
18. J. H. Joo *et al.*, *Mol. Vis.* **11**, 133 (2005).
19. R. Alpatov *et al.*, *Mol. Cell. Biol.* **24**, 10223 (2004).
20. P. Wang, P. J. Lou, S. Leu, P. Ouyang, *Biochem. Biophys. Res. Commun.* **294**, 448 (2002).
21. R. Baumeister, Y. Liu, G. Ruvkun, *Genes Dev.* **10**, 1395 (1996).
22. D. H. Hall, E. M. Hedgecock, *Cell* **65**, 837 (1991).
23. D. A. Wagh *et al.*, *Neuron* **49**, 833 (2006).
24. R. J. Kittel *et al.*, *Science* **312**, 1051 (2006); published online 13 April 2006 (10.1126/science.1126308).
25. S. L. Deken *et al.*, *J. Neurosci.* **25**, 5975 (2005).
26. D. Blanchard, H. Hutter, J. Fleenor, A. Fire, *Mol. Cell. Proteomics* **5**, 2175 (2006).
27. M. D. Muzumdar, B. Tasic, K. Miyamichi, L. Li, L. Luo, *Genesis* **45**, 593 (2007).
28. J. Ko, M. Na, S. Kim, J. R. Lee, E. Kim, *J. Biol. Chem.* **278**, 42377 (2003).
29. T. A. Fulga, D. Van Vactor, *Neuron* **57**, 339 (2008).
30. We would like to thank the *Caenorhabditis* Genetics Center and the Japanese NBPR for strains; Y. Kohara (National Institute of Genetics, Japan) for Y53H1A.1 cDNAs; J. Audhya (University of California, San Diego) for *C. elegans* optimized mCherry cDNA; L. Luo (Stanford University) for vertebrate mCherry cDNA; T. Meyer (Stanford University) for eYFP-C3 plasmid; M. Park (Stanford University) for mCerulean-C1 plasmid; C. Gao for technical assistance; and members of the Shen lab, C. Bargmann, T. Clandinin, and L. Luo for critical comments on the manuscript. We would also like to thank B. Grill (Stanford University) for providing protocol and guidance for coimmunoprecipitation experiments. This work was funded by grants awarded to K.S. [from NIH (1R01NS048392), the Human Frontier Science Foundation, the Howard Hughes Medical Institute, and the W. M. Keck Foundation] and by a National Research Service Award predoctoral fellowship awarded to M.R.P. by NIH.

Supporting Online Material
www.sciencemag.org/cgi/content/full/323/5920/1500/DC1
Materials and Methods
Figs. S1 to S11
References

26 November 2008; accepted 7 January 2009
10.1126/science.1169025

The Role of Fingerprints in the Coding of Tactile Information Probed with a Biomimetic Sensor

J. Scheibert,* S. Leurent, A. Prevost,† G. Debrégeas‡

In humans, the tactile perception of fine textures (spatial scale <200 micrometers) is mediated by skin vibrations generated as the finger scans the surface. To establish the relationship between texture characteristics and subcutaneous vibrations, a biomimetic tactile sensor has been designed whose dimensions match those of the fingertip. When the sensor surface is patterned with parallel ridges mimicking the fingerprints, the spectrum of vibrations elicited by randomly textured substrates is dominated by one frequency set by the ratio of the scanning speed to the interridge distance. For human touch, this frequency falls within the optimal range of sensitivity of Pacinian afferents, which mediate the coding of fine textures. Thus, fingerprints may perform spectral selection and amplification of tactile information that facilitate its processing by specific mechanoreceptors.

The hand is an important means for human interaction with the physical environment (*1*). Many of the tasks that the hand can undertake—such as precision grasping and manipulation of objects, detection of individual defects on smooth surfaces, and discrimination of textures—depend on the exquisite tactile sensitivity of the fingertips. Tactile information is conveyed by populations of mechanosensitive afferent fibers innervating the distal fingerpads (*2*, *3*). In recent years, a breakthrough in our understanding of the coding of roughness perception has been made with the experimental confirmation of Katz's historical proposition of the existence of two independent coding channels that are specific for the perception of coarse and fine textures (*4*–*6*). The perception of coarse textures (with features of lateral dimensions larger than about 200 μm) relies on spatial variations of the finger/substrate contact stress field and is mediated by the slowly adapting mechanoreceptors (*7*). The perception of finer textures (<200 μm) requires the finger to be scanned across the surface because it is based on the cutaneous vibrations thus elicited. These vibrations are intensively encoded, principally by Pacinian fibers (*8*), which are characterized by a band-pass behavior with a best frequency (i.e., the stimulus frequency where maximum sensitivity occurs) on the order of 250 Hz (*9*). The most elaborated description of the latter coding scheme was given by Bensmaïa and Hollins, who directly measured the skin vibrations of fingers scanning finely tex-

---

Laboratoire de Physique Statistique de l'Ecole Normale Supérieure, CNRS UMR 8550, Associé aux Universités Paris 6 et Paris 7, 24 rue Lhomond, 75231 Paris Cedex 05, France.

*Present address: Physics of Geological Processes, University of Oslo, Post Office Box 1048 Blindern, N-0316 Oslo, Norway.
†Present address: Laboratoire de Physique Théorique, 24 rue Lhomond, 75231 Paris Cedex 05, France.
‡To whom correspondence should be addressed. E-mail: georges.debregeas@lps.ens.fr.

tured substrates. They were able to correlate the perceived roughness of the surface with the power of the texture-induced vibrations weighted by the Pacinian spectral sensitivity (*10*, *11*).

Among the four types of mechanoreceptors that convey tactile information, Pacinian corpuscles (PCs) have the most extended receptive field and therefore the lowest spatial resolution. This may seem paradoxical given their involvement in the tactile perception of fine features (*12*, *13*). In standard psychophysical tests, the substrates used as stimuli are made of regularly spaced dots or bars (*1*). The resulting skin vibrations are confined to a single frequency whose value can be actively tuned by the subject through the scanning velocity so that it falls within the PC optimal range of sensitivity. Such regular stimuli substrates thus favor tactile identification or classification tasks. In contrast, for natural surfaces where features are randomly distributed and exhibit a wide spectrum of size, the elicited skin vibrations are expected to be spread over a large range of frequencies, among which only a limited fraction contributes to the PC activity.

To address this question on how low-resolution receptors encode fine textural information, the present study investigates the mechanical filtering properties of the skin. It aims at characterizing how textural information at any spatial scale (less than the finger/substrate contact diameter) is converted into subcutaneous vibrations in the vicinity of the mechanoreceptors during a dynamic tactile exploration. Because there is currently no way to measure experimentally the subcutaneous stress using a human subject, our approach is based on the use of a biomimetic tactile sensor whose functioning principle and main geometrical characteristics are matched to those of the human fingertip. This allows us to test, in particular, the role of epidermal ridges (fingerprints) in this transduction process. Two distinct functional roles have been so far attributed to these characteristic structures of the digital skin. Fingerprints are believed to reinforce friction and adhesion of the fingerpads, thus improving the ability to securely grasp objects or supports (*1*, *14*). They may also be implicated in tactile perception, each of them acting as a magnifying lever, thus increasing the subsurface strain with respect to the surface deformation (*15*, *16*). Here, we show that fingerprints may have a strong impact on the spectral filtering properties of the skin in dynamic tactile exploration.

The tactile sensor aims at mimicking the operation of the PC in dynamic tactile exploration (*17*, *18*). As far as possible, the various geometrical and mechanical characteristics of the sensor are scaled to its biological counterpart (see fig. S1 for a comparison of key parameters). The sensing element consists of a microelectro mechanical system (MEMS) device that provides force measurements in a region of millimeter extension. This microforce sensor is attached to a rigid base and covered with an elastic spherical cap mimicking the fingertip skin (Fig. 1A). This cap, made of cross-linked poly(dimethylsiloxane) (PDMS), has a maximum thickness $h = 2$ mm. Its surface is either "smooth" or "fingerprinted," that is, patterned with a regular square wave grating of period $\lambda = 220$ µm and depth 28 µm. The tactile sensor is mounted on a double cantilever system, allowing one to record the normal and tangential loads using capacitive position sensors. In a typical experiment, the sensor is scanned at constant velocity across a rigid, nominally flat substrate under a constant normal load $P = 1.71$ N, yielding a contact zone of centimeter extension. This value for the load, together with the periodicity of the fingerprint-like structure, is chosen so that the number of ridges within the contact in the artificial system is close to that observed with an actual fingerpad under standard exploratory load (as illustrated in Fig. 1, B and C).

The stimuli consist of white-noise one-dimensional (1D) textured substrates (Fig. 1A,

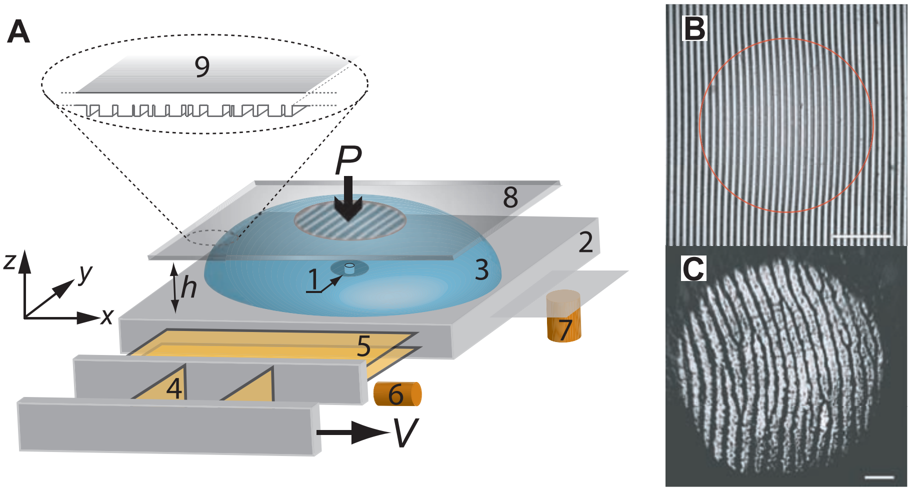

Fig. 1. (**A**) Sketch of the experimental setup. A MEMS microforce sensor (1) is mounted on a rigid base (2). It is covered with a spherical elastomer cap (3) of maximum thickness $h = 2$ mm and whose surface is smooth or patterned with parallel ridges. The resulting tactile sensor is mounted on a double-cantilever system (4, 5) allowing one to measure the total normal and tangential loads exerted on the sensor using capacitive position sensors (6, 7). In a typical experiment, the tactile sensor is scanned at constant speed v (using a linear motor) and under constant normal load P, across glass slides (8) whose surface is patterned with a 1D random square-wave grating (9). (**B**) Snapshot of the contact between the fingerprinted cap and a smooth glass slide in steady sliding. Wells between the elastomer's ridges appear bright, and the red circle, also shown on (A), defines the border of the contact. Actual contact only occurs on the ridges' summits. Ridges are slightly deformed at the periphery of the contact zone because of interfacial friction. (**C**) For comparison, this snapshot displays the contact between a human fingertip and a smooth glass surface with $P \approx 0.5$ N (a typical value in tactile exploration). Scale bars, 2 mm.

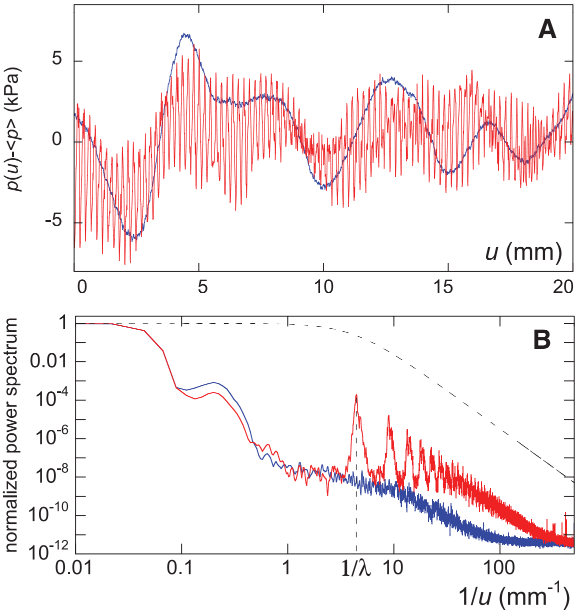

Fig. 2. (**A**) Typical pressure variation $p - \langle p \rangle$ measured with the smooth (blue) and fingerprinted (red) biomimetic fingers as a function of the substrate displacement u. The stimulus substrate used to produce these signals is a patterned glass slide exhibiting 1D random roughness. (**B**) Normalized power spectra of both signals obtained by Fourier transform averaged over four data sets, equivalent to a substrate of total length 180 mm. Shown in dashed lines is the theoretical power spectrum of the random pattern used as stimuli.

upper inset). They are obtained by patterning glass slides with a 28-μm-deep square wave grating whose edges are positioned at random positions with a mean grating width of 75 μm (*17*). The fingerprint-like ridges (when present) and substrate gratings are parallel to each other and oriented perpendicularly to the sliding direction. For moderate scanning velocities ($v <$ 0.4 mm/s) and a given normal load, the pressure signal $p(t)$ is found to be a sole function of the substrate position at time t, regardless of the scanning velocity v (figs. S2 and S3). All experiments are performed at constant v = 0.2 mm/s, well within this velocity-independent regime of friction. To facilitate the analysis, data are systematically plotted as a function of the sensor/substrate relative displacement $u = vt$, as a strict equivalence exists between time and substrate displacement in steady sliding.

Figure 2A shows the typical pressure variations $p(u) - \langle p\rangle$ (where $\langle p\rangle$ is the average pressure) measured with the microforce device as the sensor is scanned across a textured surface. The smooth sensor exhibits pressure modulations with a characteristic wavelength in the millimeter range. The fingerprinted system reveals similar long-wavelength modulations to which are superimposed rapid oscillations whose period corresponds to a displacement of the substrate over the interridge distance λ = 220 μm. A characterization of both sensors' filtering properties is given in Fig. 2B, which displays the power spectra of both signals together with that of the input stimulus, that is, the substrate topography (dashed line). The smooth sensor acts as a low-pass filter as it rapidly attenuates all pressure modulations induced by texture components of wavelength smaller than ≈1 mm. In contrast, the fingerprinted sensor exhibits band-pass filtering characteristics around the spatial frequency $1/\lambda$ (with further harmonics at integer multiples of $1/\lambda$). The presence of fingerprint-like ridges results in an amplification by a factor of 100 of the pressure modulations induced by a texture of wavelength λ (*19*).

These filtering characteristics can be interpreted to first order using a linear mechanical description of tactile sensing (*20*). Consider a small linear force sensor embedded at depth h in an elastic skin and located at ($x = 0$, $y = 0$). Its response to localized unit forces applied at various positions (x,y) on the skin surface defines its receptive field $F(x,y)$. The sensor signal p induced by any stress field $\sigma^s(x,y)$ applied at the skin surface then reads $p = \iint F(x,y)\sigma^s(x,y)\,dx\,dy$. We denote $\bar{\sigma}(x,y)$ the (time invariant) contact stress field resulting from the continuous rubbing of a smooth substrate under a given load. If the substrate exhibits a fine texture, the stress field σ^s becomes dependent on the substrate position u. As u varies, σ^s is modulated around the reference field $\bar{\sigma}(x,y)$. The use of substrates exhibiting a two-level topography and a large enough contrast prevents any contact above the wells (as optically evidenced in fig. S4). The contact pressure is thus zero over half of the apparent contact region, whereas it is expected to be about twice the time-averaged stress field $\bar{\sigma}(x,y)$ at the location of the substrate summits. As a first approximation, one may thus write the superficial stress field as a function of u in the form

$$\sigma^s(x,y) = \bar{\sigma}(x,y).(1 + T(u-x)) \qquad (1)$$

where $T(x)$ is the normalized two-level function ($T = \pm 1$), representing the topography of the surface. An exact calculation of the contact stress at a given location should take into account the local topography of the substrate and not just the average fraction of summits. The induced corrections should be important at short length-scales but become small when considering stress modulations over distances larger than the mean grating period.

With this expression, the pressure signal is then given by

$$p(u) = \langle p\rangle + \iint (F.\bar{\sigma})(x,y).T(u-x)dxdy \qquad (2)$$

The transduction of tactile information is controlled by the product of the receptive field F and the reference stress field $\bar{\sigma}$. The function F characterizes the intrinsic properties of the receptor. It is expected to have a typical lateral extension of order h and to be fairly independent of the skin topography (such as fingerprints), provided that the height of the surface features is less than h (*21*). The reference field $\bar{\sigma}$ depends on the exploratory conditions such as the normal load P, the friction coefficient, or the position of the contact zone with respect to the sensor location. Unlike F, the stress field $\bar{\sigma}$ is highly sensitive to the skin surface topography. In particular, the presence of fingerprints a few tens of micrometers deep leads to a complete extinction of $\bar{\sigma}$ along regularly spaced lines (as illustrated in fig. S6), resulting in the observed spectral amplification of the signal at the frequency $1/\lambda$.

Equation 2 can be rewritten as $p(u) = \langle p\rangle + \int g_1(x)T(u-x)dx$ where $g_1(x) = \int (F.\bar{\sigma})(x,y)dy$ now defines the linear response function of the sensor with respect to 1D two-level stimuli substrates. The use of white-noise stimuli enables us to implement a Wiener-Volterra reverse-correlation method and extract $g_1(x)$directly from the measurements, $g_1(x) = \langle p(u)T(u-x)\rangle$ (*22*, *23*). The result of this computation for both smooth and fingerprinted sensors is plotted on Fig. 3. In qualitative agreement with the linear model, both response functions exhibit an

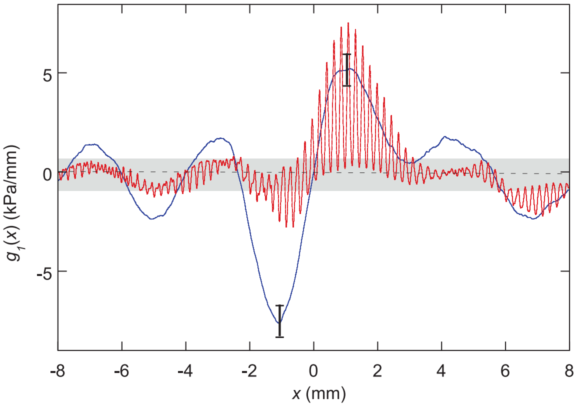

Fig. 3. Linearized stimulus-signal response functions $g_1(x)$ computed by cross-correlating the pressure signals and the stimulus topography $T(x)$, for both smooth (blue) and fingerprinted (red) systems. These data were obtained by averaging over three data sets, each one corresponding to a substrate length of 45 mm. The expected statistical deviation due to the finite length of the substrates was estimated numerically to be ±0.75 kPa/mm. This value is shown with the error bars and the shaded rectangle.

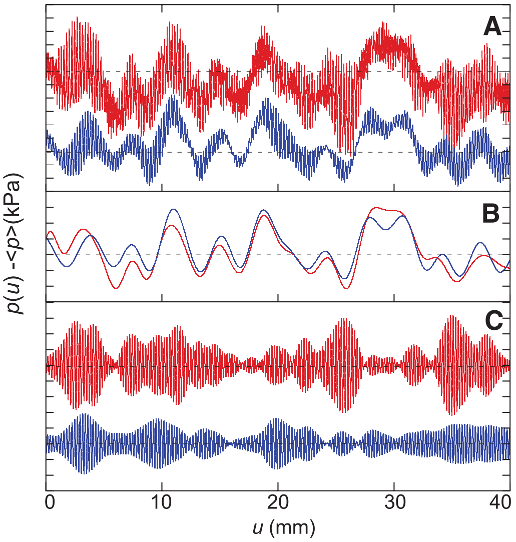

Fig. 4. (**A**) In red, pressure signal $p - \langle p\rangle$ measured with the fingerprinted sensor on a rough substrate. In blue, predicted signal obtained by convoluting the substrate topography function $T(x)$ with the linear response function $g_1(x)$. The latter was obtained independently by reverse correlation using two distinct 45-mm-long substrates. The dotted line indicates the $y = 0$ axis, and each interval along the y axis corresponds to a pressure variation of 1 kPa. For easier comparison, the same signals are plotted after applying (**B**) a low-pass filter with a cutoff frequency of $1/(2\lambda)$ and (**C**) a band-pass filter centered around the peak frequency $1/\lambda$.

envelope of lateral extension of order h, and the response function of the fingerprinted sensor is further modulated with a spatial period λ. These functions can be tested by confronting actual measurements of $p(u) - \langle p \rangle$ with the predicted signal $\int g_1(x)T(u - x)dx$ as shown in Fig. 4A for the fingerprinted system. To facilitate the comparison, Fig. 4, B and C, displays the low- and high-frequency components, respectively. The linear response function allows one to reproduce the low-frequency signal. Although it correctly predicts the maxima and minima of the high-frequency component, it fails to capture its amplitude, which indicates that nonlinear effects might not be negligible for small length-scales. These effects could be taken into account by correlating p with the successive powers of T in order to include additional terms of the Wiener-Volterra series to describe the response function. However, this computation would require using a much larger set of stimuli to provide sufficient statistics.

Although the biomimetic tactile sensor used in this study offers a crude version of the finger physiology (*24*, *25*), the mechanism of spectral selection it helped unravel depends on a very limited set of ingredients and should therefore be relevant to human digital touch. Namely, it requires that the surface of the tactile sensor displays a regularly ridged topography whose spatial period and amplitude are much smaller than the receptive field diameter and the mechanoreceptor's depth. In these conditions, such ridges have little influence on the skin deformations induced by a coarse texture (of spatial scale larger than the interridge distance λ). However, by shaping the interfacial contact stress field, such epidermal ridges give rise to an amplification of the subsurface stress modulations induced by a texture of characteristic wavelength equal to λ. In the time domain, this spatial period corresponds to a frequency $f_0 = v/\lambda$ where v is the finger/substrate relative velocity. In natural exploratory conditions, v is observed to be on the order of 10 to 15 cm/s (*1*). With a typical interridge distance $\lambda \approx 500$ µm, this yields a frequency $f_0 \approx 200$ to 300 Hz on the order of the best frequency of the Pacinian fibers that mediate the coding of fine textures. Fingerprints thus allow for a conditioning of the texture-induced mechanical signal that facilitates its processing by specific mechanoreceptors. It should be noted that this process is strongly dependent on the orientation of the ridges with respect to the scanning direction (fig. S7). In humans, fingerprints are organized in elliptical twirls so that each region of the fingertip (and thus each PC) can be ascribed with an optimal scanning orientation. Further studies are needed to elucidate how this may reflect on the exploratory procedures (such as fingertip trajectory and contacting zone) used by humans during texture evaluation tasks.

Remarkably, the response function of the fingerprinted system displayed in Fig. 3 is analogous to a Gabor filter because it provides both spatial and spectral resolution. Such filters are classically used in image analysis and have been identified in visual systems at the neural level (*26*). They are known to provide orientation discrimination, contrast enhancement, and motion detection. One may therefore expect, beyond the spectral filtering process discussed here, other interesting functional consequences of fingerprints, presumably relevant to the design of realistic haptic interfaces for humanoid robots (*27*, *28*).

References and Notes

1. L. A. Jones, S. J. Lederman, *Human Hand Function* (Oxford Univ. Press, 2006).
2. I. Darian-Smith, in *Handbook of Physiology: The Nervous System: Sensory Processes* (American Physiological Society, Bethesda, MD, 1984), vol. 3, chap. 17.
3. K. O. Johnson, J. R. Phillips, *J. Neurophysiol.* **46**, 1177 (1981).
4. D. Katz, *The World of Touch*, I. E. Krueger, Transl. and Ed. (Hillsdale, NJ, Erlbaum, 1989; original work published 1925).
5. M. Hollins, S. J. Bensmaïa, S. Washburn, *Somatosens. Mot. Res.* **18**, 253 (2001).
6. M. Hollins, S. J. Bensmaia, *Can. J. Exp. Psychol.* **61**, 184 (2007).
7. S. J. Lederman, M. M. Taylor, *Percept. Psychophys.* **12**, 401 (1972).
8. M. A. Srinivasan, J. M. Whitehouse, R. H. Lamotte, *J. Neurophysiol.* **63**, 1323 (1990).
9. J. C. Makous, R. M. Friedman, C. J. Vierck, *J. Neurosci.* **15**, 2808 (1995).
10. S. J. Bensmaia, M. Hollins, *Somatosens. Mot. Res.* **20**, 33 (2003).
11. S. J. Bensmaia, M. Hollins, *Percept. Psychophys.* **67**, 842 (2005).
12. R. S. Johansson, *J. Physiol.* **281**, 101 (1978).
13. M. Hollins, S. R. Risner, *Percept. Psychophys.* **62**, 695 (2000).
14. M. Cartmill, *Am. J. Phys. Anthropol.* **50**, 497 (1979).
15. N. Cauna, *Anat. Rec.* **119**, 449 (1954).
16. R. S. Fearing, J. M. Hollerbach, *Int. J. Robot. Res.* **4**, 40 (1985).
17. Materials and methods are available as supporting material on *Science* Online.
18. J. Scheibert, A. Prevost, J. Frelat, P. Rey, G. Debrégeas, *Europhys. Lett.* **83**, 34003 (2008).
19. A comparable spectral amplification is observed with finely abraded glass substrates (see fig. S5).
20. R. D. Howe, M. R. Cutkosky, *IEEE Trans. Robot. Autom.* **9**, 140 (1993).
21. K. L. Johnson, *Contact Mechanics* (Cambridge Univ. Press, Cambridge, 1985).
22. N. Wiener, *Nonlinear Problems in Random Theory* (MIT Press, Cambridge, MA, 1958).
23. F. Rieke, D. Warland, R. de Ruyter van Steveninck, W. Bialek, *Spikes: Exploring The Neural Code* (MIT Press, Cambridge, MA, 1999).
24. K. Dandekar, B. I. Raju, M. A. Srinivasan, *J. Biomed. Eng.* **125**, 682 (2003).
25. Q. Wang, V. Hayward, *J. Biomech.* **40**, 851 (2007).
26. J. P. Jones, L. A. Palmer, *J. Neurophysiol.* **58**, 1233 (1987).
27. R. Crowder, *Science* **312**, 1478 (2006).
28. V. Maheshwari, R. F. Saraf, *Science* **312**, 1501 (2006).
29. This project was supported primarily by CNRS basic funding and in part by the EU-NEST (New and Emerging Science and Technology) program, MONAT (Measurement of Naturalness) project (contract 21, number 29000). We are grateful to D. Chatenay and L. Bourdieu for fruitful discussions and careful reading of the manuscript.

Supporting Online Material

www.sciencemag.org/cgi/content/full/1166467/DC1
Materials and Methods
Figs. S1 to S7
References

26 September 2008; accepted 16 January 2009
Published online 29 January 2009;
10.1126/science.1166467
Include this information when citing this paper.

Texture-Induced Modulations of Friction Force: The Fingerprint Effect

E. Wandersman, R. Candelier, G. Debrégeas, and A. Prevost*
Laboratoire Jean Perrin, Ecole Normale Supérieure, UPMC Université Paris 6,
CNRS FRE 3231, 24 rue Lhomond, 75005 Paris, France

(Received 13 July 2011; published 11 October 2011)

Modulations of the friction force in dry solid friction are usually attributed to macroscopic stick-slip instabilities. Here we show that a distinct, quasistatic mechanism can also lead to nearly periodic force oscillations during sliding contact between an elastomer patterned with parallel grooves, and abraded glass slides. The dominant oscillation frequency is set by the ratio between the sliding velocity and the grooves period. A model is derived which quantitatively captures the dependence of the force modulations amplitude with the normal load, the grooves period, and the slides roughness characteristics. The model's main ingredient is the nonlinearity of the friction law. Since such nonlinearity is ubiquitous for soft solids, this ''fingerprint effect'' should be relevant to a large class of frictional configurations and have important consequences in human digital touch.

DOI: 10.1103/PhysRevLett.107.164301 PACS numbers: 46.55.+d, 68.35.Ct, 81.40.Pq

Surface texture engineering by nano- or micropatterning techniques has proven to be an efficient tool to tune frictional or adhesive properties at solid-solid [1–3] or solid-liquid interfaces [4]. Many of the existing designs are directly inspired by natural surfaces. Superhydrophobic surfaces, for example, reproduce the microscopic pattern observed on lotus flower leaves [5]. Surfaces with a shark skinlike texture provide significant drag reduction in turbulent flows [6]. Geckos feet fibrillar structure provides them with remarkable adhesion capabilities, and has allowed the design of functional adhesives [7].

In comparison, the effect of micropatterning in solid-solid friction has so far attracted much less attention. In a recent paper however, we suggested that epidermal ridges—the regular pattern characteristics of humans and primates glabrous skin surface—strongly modify the skin internal stress elicited upon actively rubbing the fingertip over a finely abraded surface, thus enhancing tactile sensitivity [8]. More precisely, such patterns were shown to produce a nearly periodic modulation of the texture-induced subcutaneous stress field at a frequency set by the ratio between the scanning velocity and the pattern period. This finding led to the integration of fingerprintlike structures in several robotic hand designs [9,10]. Interestingly, this effect not only shows up in local stress measurements but is also observed in the global friction force signal measured while scanning a human finger on a rough surface [11]. Since the friction force signal conveys a large part of the tactile information for texture discrimination, as recently evidenced in psychophysical assays [12], it is crucial from both biological and robotic points of views to understand the physical origin of such texture-induced friction force modulations and to identify the parameters which control their spectral characteristics.

To address this question, we investigate in this Letter the friction dynamics between a patterned elastomer block and a finely abraded glass surface in a sphere-on-plane geometry (Fig. 1). The elastomer blocks (thickness ≈ 18 mm) were obtained by molding liquid polydimethylsiloxane–cross-linker mixture (PDMS, Sylgard 184, Dow Corning) in concave spherical lenses of radius of curvature $R = 128.8$ mm. Prior to molding, the surface of the lenses was patterned with a periodic square grating of depth 40 μm and spatial period $\lambda = 125$, 218, or 760 μm (width $\lambda/2$) using soft photolithography techniques [8]. The elastomer Young's modulus was measured to be $E = 2.2 \pm 0.1$ MPa. The abraded planes consisted in microscope glass slides sandblasted or abraded using a silicon carbide powder-water mixture. The surface topography was measured with an optical profilometer (M3D, Fogale Nanotech) from which the root mean-squared height $h_{\rm rms}$ and surface profile autocorrelation spectrum $C(q)$ were computed [13]. Two substrates were considered, referred to as ''rough-'' ($h_{\rm rms} \approx 2.3$ μm) and ''rough+'' ($h_{\rm rms} \approx 5$ μm), respectively. For both, $C(q)$ displays a self-affine behavior as usually observed for real surfaces [14] of the form $C(q) = C_0[1 + (q/q_c)^2]^{-\alpha}$ with $(C_0, q_c, \alpha) = (1.310^{-22}$ m^4, 610^4 m^{-1}, 1.29) and (1.310^{-20} m^4, 8.510^3 m^{-1}, 1.32) for substrate rough- and rough+, respectively. Substrates were rubbed against the elastomer surface along the x direction at constant velocity v (range 0.01–0.5 mm s^{-1}) with a motorized translation stage (LTA-HL, Newport), under constant normal force F_N (range 0.02–2 N). F_N and tangential force F_S were measured with a 1 mN accuracy at 1 kHz by monitoring the deflections of two orthogonal cantilevers (Fig. 1, normal and tangential stiffness respectively 733 ± 3 Nm^{-1} and 9743 ± 47 Nm^{-1}) using capacitive position sensors (MCC-20 and MCC-10, Fogale Nanotech). The apparent contact zone, imaged in a light-transmitted geometry (Fig. 1) had a diameter ranging from 1 to 6 mm (a few λ to about 50λ), much larger than the substrate roughness characteristic scale.

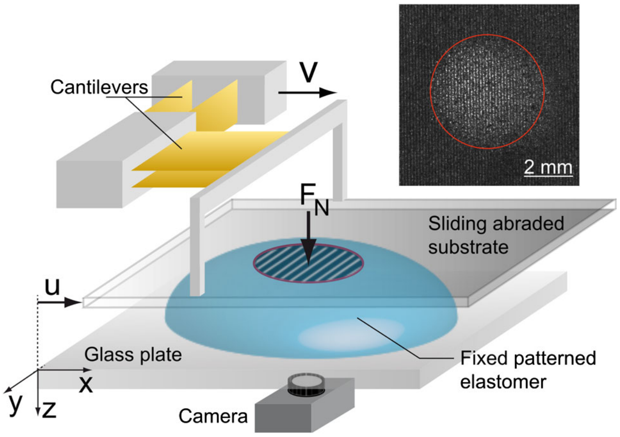

FIG. 1 (color online). Sketch of the setup. Inset: image of a typical contact at $F_N = 0.5$ N with $\lambda = 125$ μm. The red circle defines the apparent contact perimeter.

Typical F_S signals in steady sliding are shown on Figs. 2(a)–2(d) as a function of the scanned distance $u = v.t$ with $v = 0.1$ mm s^{-1} perpendicular to the direction of the ridges and $F_N = 0.5$ N. Minute but clearly measurable nearly periodic oscillations are observed, with no equivalent in the normal force signals. Their amplitude weakly depends on λ and increases with F_N. They are significantly more pronounced with the rough+ than with the rough- substrate [Figs. 2(b) and 2(d)]. The effect entirely vanishes when the direction of the ridges is aligned with the direction of motion. In the range of velocities explored, these modulations are independent of v. All experiments presented further are thus done at $v = 0.1$ mm s^{-1} and u is taken as the time-varying variable.

The power spectrum $S_{[\delta F_S]}(q)$ of $\delta F_S(u) = F_S(u) - \bar{F}_S$ (the bar stands for time averaging) was computed by averaging over a 20 mm travel distance. All spectra exhibit well-defined peaks at $q_\lambda = 2\pi/\lambda$ and at corresponding harmonics [Fig. 2(e)]. $S_{[\delta F_S]}$ at $q = q_\lambda$ increases with F_N as AF_N^ν (Fig. 3) where values of A and ν are collected in Table I. As mentioned above, A depends weakly on λ and is significantly higher for the rough+ than for the rough- substrate. The exponent ν is close to 1 for all experimental configurations.

In parallel to the force measurements, rapid imaging of the contact zone was performed using a fast camera (Fastcam APX-RS, Photron, Japan) operating at 60 Hz. At all loads, contact occurs only at the summits of the ridges, thus yielding a large contrast between the top and bottom of the pattern and allowing for a precise tracking of the edges of the ridges with ≈ 10 μm accuracy. No stick-slip motion of the ridges was observed. Thus, the measured force oscillations cannot be accounted for by periodic stick-slip events whose frequency is set by the period of the pattern as reported in [2]. This is further supported by the observation that the fluctuations are quasistatic (v independent).

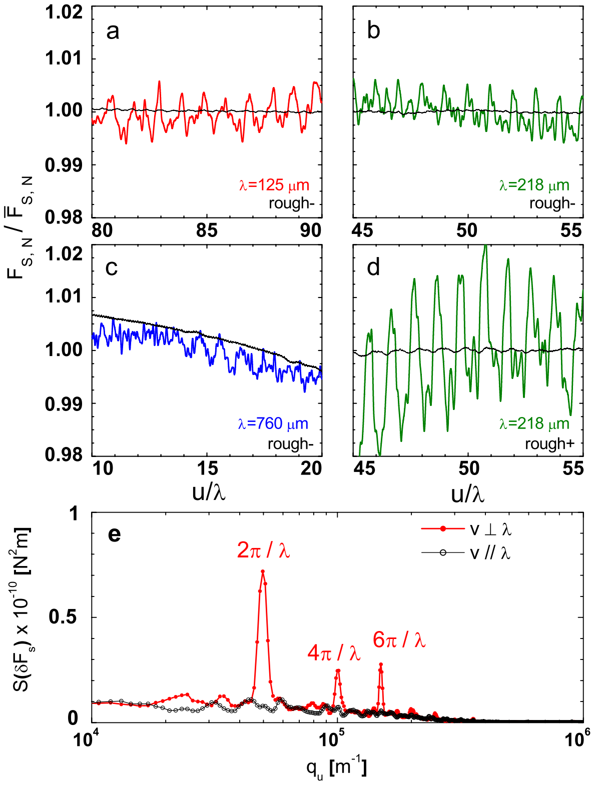

FIG. 2 (color online). (a)–(d) Blow up of $F_S/\bar{F}_S$ fluctuations ($F_N/\bar{F}_N$ in thin black lines) versus u/λ at $F_N = 0.5$ N for different λ and both substrates in steady sliding. (e) Averaged power spectra of F_S fluctuations ($\lambda = 125$ μm, $F_N = 0.5$ N, "rough-" substrate), both with v perpendicular (●) and parallel (○) to the ridges.

In the rest of this Letter, we aim at understanding the physical origin of the observed friction force modulation and the dependence of its amplitude with the normal load, pattern period, and substrate roughness characteristics. We first consider a perfectly smooth elastomer surface (no patterning) rubbed against an abraded glass slide. We denote $p(x, y, u)$ and $\tau(x, y, u)$ the normal and tangential stress field at a given position u of the substrate, such that $F_N(u) = \int p(x, y, u)dxdy$ and $F_S(u) = \int \tau(x, y, u)dxdy$. Under a local Amontons-Coulomb friction law assumption, i.e., $\tau(x, y, u) = \mu_0 p(x, y, u)$ with μ_0 a uniform (material dependent) friction coefficient, the friction force reads $F_S(u) = \mu_0 F_N$ and is thus expected to be time independent. We therefore hypothesize a weakly nonlinear relationship between $p(x, y, u)$ and $\tau(x, y, u)$ which is equivalent to postulating a pressure dependence of the local friction coefficient, i.e., $\mu = \tau/p = \mu(p)$. The friction force now reads

$$F_S(u) = \int \mu(p)p(x, y, u)dxdy. \quad (1)$$

The spatial variations of $p(x, y, u)$ can be decomposed into a time-averaged component $\bar{p}(x, y)$ set by the macroscale

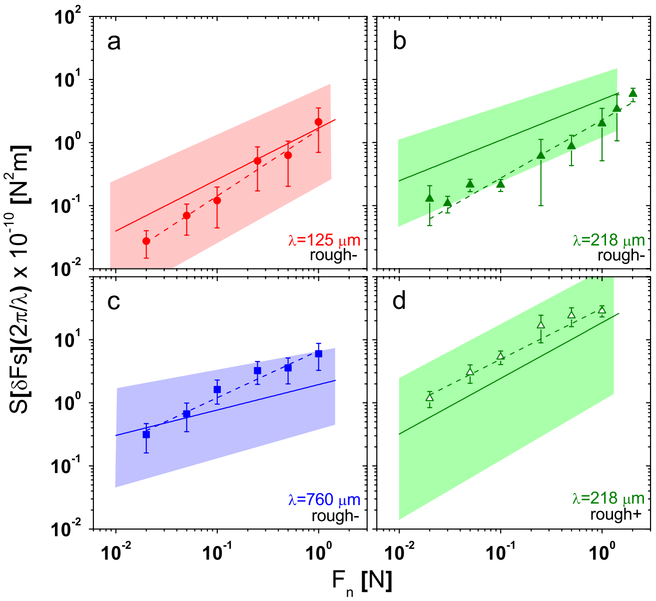

FIG. 3 (color online). (a)–(d) $S_{[\delta F_S]}(q_\lambda)$ versus F_N. Dashed lines are best experimental fits, solid lines are model predictions. Shaded areas bound the values of A by tuning the parameters of the model within their experimental errors.

plane-on-sphere contact geometry and a time-fluctuating component $\delta p(x, y, u)$ associated with the microscopic roughness of the glass slide. For simplicity, we further assume that the elastomer is in intimate contact with the glass surface. This assumption is expected to fail at the microasperities scale but should be valid at intermediate scale such as the interridge distance λ. In this limit, the texture-induced pressure modulations are set by the topography of the glass substrate and are independent of the local mean pressure imposed by the Hertzian geometry $\bar{p}(x, y)$. The pressure modulation field $\delta p(x, y, u)$ is thus a sole function of the position of the substrate with respect to the contact zone $(u - x, y)$, so that the pressure field reads

$$p(x, y, u) = K(u)[\bar{p}(x, y) + \delta p(u - x, y)]. \qquad (2)$$

TABLE I. Experimental and model parameters with $A \times 10^{-10}$ given in SI units.

Configuration	A^{exp}	ν^{exp}	A^{model}	ν^{model}
$\lambda = 125$ μm, rough−	1.6 ± 0.9	1.1 ± 0.3	1.7	0.87
$\lambda = 218$ μm, rough−	2.3 ± 0.5	0.9 ± 0.1	4.8	0.64
$\lambda = 218$ μm, rough+	32 ± 4	0.8 ± 0.15	19	0.88
$\lambda = 760$ μm, rough−	7 ± 2	0.8 ± 0.2	2.0	0.4

The normalization factor $K(u)$ ensures that F_N remains constant during sliding. This condition imposes

$$K(u) = \left(1 + \frac{1}{F_N}\int \delta p(u - x, y)dxdy\right)^{-1}$$
$$\approx 1 - \frac{1}{F_N}\int \delta p(u - x, y)dxdy. \qquad (3)$$

The latter expansion is valid when the contact diameter is much larger than the texture scale. Indeed, in this limit, the integral of the roughness-induced pressure field becomes vanishingly small with respect to the confining force F_N. Rewriting Eq. (1), one obtains

$$\delta F_s(u) = F_s(u) - \bar{F}_s$$
$$= \int [\mu(\bar{p}) - \langle\mu\rangle]\delta p(u - x, y)dxdy,$$

where $\langle\mu\rangle$ is defined as the ratio $\bar{F}_S/F_N$.

The friction force fluctuations thus appear as the convolution product of a function characterizing the friction coefficient spatial heterogeneities and the texture-induced pressure modulations field. The presence of regular ridges at the surface of the elastomer imposes that the stress between ridges vanishes. This can be accounted for, in first approximation, by introducing a λ-periodic Heavyside function $H(x) = \theta[\sin(2\pi x/\lambda)]$ under the integral, which directly results in a spectral selection of the associated spatial mode.

In Fourier space [13], the fluctuating component of the friction force thus reads

$$S_{[\delta F_S]}(q_u) = (2\pi)^4 \int dq_v |\mathcal{F}(H(x)[\mu(x, y) - \langle\mu\rangle])|^2 S_{[\delta p]}.$$

Wave vector q_u (q_v) refers to the parallel (perpendicular) direction to the sliding direction.

Under the assumption of intimate contact, $S_{[\delta p]}$ can be simply expressed as a function of the roughness spectrum $C(q)$ [13] as $S_{[\delta p]}(q) = (E^*/2)^2 q^2 C(q)$, where q is the norm of (q_u, q_v) and E^* the reduced Young's modulus. Lacking any established constitutive law for our system, the friction coefficient spatial field, on the other hand, is estimated empirically from global force measurements. For all experimental configurations, a power-law dependence is observed between both force components $\bar{F}_S = B.F_N^\gamma$ with $\gamma = 0.87 \pm 0.04$ (Fig. 4). We postulate a power-law relationship between the local shear stress and the local pressure $\tau(x, y) = \beta \bar{p}^m(x, y)$ [15]. Assuming that $\bar{p}(x, y)$ follows a Hertz profile, $\bar{F}_S$ can be derived by analytically integrating $\tau(x, y)$ over the contact area, yielding $\gamma = (m + 2)/3$ and an exact relationship between β, B, and γ. Figure 4 shows a comparison between $\bar{F}_S$ versus F_N obtained experimentally and through integration of τ over the contact area. Note that the choice of a power law is simply dictated by the fact that it constitutes the simplest functional form consistent with the global force measurements in the explored range.

Both predicted and measured amplitudes of $S_{[\delta F_S]}(q_\lambda)$ with F_N are presented on Fig. 3, for all experimental

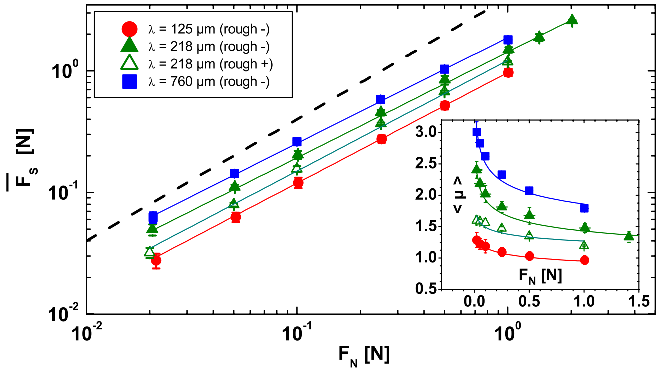

FIG. 4 (color online). Time-averaged friction force $\bar{F}_s$ versus F_N. Different symbols correspond to different configurations. Solid lines are power-law fits with exponent γ. Combined fits yield $\gamma = 0.87 \pm 0.04$. The dashed line has a slope of 1. Inset: Average dynamic friction coefficient $\bar{F}_S/F_N$ versus F_N. Solid lines are power-law fits with exponent $\gamma - 1$.

configurations, using the set of parameters (β, m, C_0, q_c, α) obtained as described earlier. Using the mean values of these parameters, the predicted amplitude of F_S modulations is in reasonable agreement with the data, without any adjustable parameter (solid lines on Fig. 3). The model captures, in particular, the analytic increase of $S_{[\delta F_s]}(q_\lambda)$ with F_N, with an exponent ν comparable to its experimental counterpart (see Table I and Fig. 3). For all λ we determined the boundaries on $S_{[\delta F_S]}(q_\lambda)$ based on the experimental uncertainties of the parameters (shaded areas on Fig. 3). The large uncertainty on A and ν (~ 0.1) in the model is mostly due to the experimental inaccuracy in evaluating the parameter m. Exploring the model predictions beyond the range of the experimental parameters reveals that ν increases linearly with m and decreases linearly with λ in the investigated range (not shown). The predicted amplitude A is trivially proportional to C_0, slightly decreases with λ, and falls rapidly to zero when m approaches unity, i.e., when Amontons-Coulomb friction's law is assumed locally.

This study shows that any nonlinearity in the friction law leads to the development of texture-induced friction force fluctuations. Since purely linear friction laws are scarcely observed, the present mechanism should be relevant to most practical situations. More generally, whenever the local and global friction coefficients are not the same [16] force fluctuations should occur. However, these are expected to be in practice hardly detectable when the fixed substrate (here the PDMS block) is smooth and the contact zone diameter is much larger than the typical roughness scale. In contrast, the presence of a regular pattern at the surface of the block operates a spectral filtering of the texture-induced pressure modulation which induces a mode selection of the force fluctuations at a particular frequency. The amplitude of these force fluctuations can then become an order of magnitude larger than in the smooth case as shown by the present study. This mechanism was here examined for the simplest possible pattern, i.e., regular parallel stripes, but richer force signal spectra should be similarly obtained with more complex patterns.

In essence, the macroscopic friction force signal carries information about the spectral content of the microscopic substrate topography at frequencies defined by the elastomer micropattern. A practical consequence is that F_S fluctuations amplitudes could be used to discriminate surfaces having small differences in their roughness at scales much smaller than the contact extension. Hence, under the same conditions, force fluctuations are roughly 10 times larger for the substrate having a $h_{\rm rms} \approx 5\ \mu$m than for the one with $h_{\rm rms} \approx 2.3\ \mu$m. This mechanism could also facilitate the detection of motion. The transition between static and sliding contact should manifest as the sudden appearance of large single mode oscillations of the friction force. One may finally foresee the possibility to evaluate the scanning velocity, based on the sole friction force signal, by continuously extracting the peak frequency of these oscillations. We believe that this "spectrotribometry" approach may be relevant to human digital touch and prehension, owing to the presence of fingerprints, and that it could be easily implemented in tactile robotic sensing devices.

The authors deeply thank F. Petrellis for illuminating mathematical surgery, F. Zalamea for his valuable help, A. Chateauminois and C. Frétigny for fruitful discussions, and acknowledge financial support from ANR-DYNALO NT09-499845.

---

*alexis.prevost@lps.ens.fr

[1] C. J. Rand and A. J. Crosby, J. Appl. Phys. **106**, 064913 (2009).
[2] R. Bennewitz *et al.*, J. Phys. Condens. Matter **20**, 015004 (2008).
[3] F. Wu-Bavouzet, J. Cayer-Barrioz, A. Le Bot, F. Brochard-Wyart, and A. Buguin, Phys. Rev. E **82**, 031806 (2010).
[4] P. Joseph *et al.*, Phys. Rev. Lett. **97**, 156104 (2006).
[5] B. Bhushan, Y. C. Jung, and K. Koch, Phil. Trans. R. Soc. A **367**, 1631 (2009).
[6] B. Dean and B. Bhushan, Phil. Trans. R. Soc. A **368**, 4775 (2010).
[7] L. F. Boesel, C. Greiner, E. Artz, and A. del Campo, Adv. Mater. **22**, 2125 (2010).
[8] J. Scheibert, S. Leurent, A. Prevost, and G. Debrégeas, Science **323**, 1503 (2009).
[9] Y. Zhang, J. Micromech. Microeng. **20**, 085012 (2010).
[10] D. D. Damian, H. Martinez, K. Dermitzakis, A. Hernandez-Arieta, and R. Pfeifer, in *Proceedings of the International Conference on Intelligent Robots and Systems* (IEEE, New York, 2010), p. 904.

[11] A. Prevost, J. Scheibert, and G. Debrégeas, Comm. Int. Biol. **2**, 422 (2009).

[12] M. Wiertlewski, J. Lozada, and V. Hayward, IEEE. Trans. Robot. **27**, 461 (2011).

[13] B. N. J. Persson, J. Phys. Condens. Matter **20**, 312001 (2008).

[14] B. N. J. Persson, J. Chem. Phys. **115**, 3840 (2001).

[15] C. H. Scholz, *The Mechanics of Earthquakes and Faulting* (Cambridge University Press, Cambridge, U.K., 2010).

[16] O. Ben-David and J. Fineberg, Phys. Rev. Lett. **106**, 254301 (2011).

Sensors **2011**, *11*, 7934-7953; doi:10.3390/s110807934

OPEN ACCESS

sensors

ISSN 1424-8220

www.mdpi.com/journal/sensors

Article

The Role of Exploratory Conditions in Bio-Inspired Tactile Sensing of Single Topogical Features

Raphaël Candelier, Alexis Prevost and Georges Debrégeas *

Laboratoire Jean Perrin, Ecole Normale Superieure, UPMC, CNRS FRE 3231, Paris 75005, France;
E-Mails: raphael.candelier@ens.fr (R.C.); alexis.prevost@lps.ens.fr (A.P.)

* Author to whom correspondence should be addressed; E-Mail: georges.debregeas@lps.ens.fr;
Tel: +33-1-4432-3590; Fax: +33-1-4432-3433.

Received: 1 July 2011; in revised form: 30 July 2011 / Accepted: 1 August 2011 /
Published: 11 August 2011

Abstract: We investigate the mechanism of tactile transduction during active exploration of finely textured surfaces using a tactile sensor mimicking the human fingertip. We focus in particular on the role of exploratory conditions in shaping the subcutaneous mechanical signals. The sensor has been designed by integrating a linear array of MEMS micro-force sensors in an elastomer layer. We measure the response of the sensors to the passage of elementary topographical features at constant velocity and normal load, such as a small hole on a flat substrate. Each sensor's response is found to strongly depend on its relative location with respect to the substrate/skin contact zone, a result which can be quantitatively understood within the scope of a linear model of tactile transduction. The modification of the response induced by varying other parameters, such as the thickness of the elastic layer and the confining load, are also correctly captured by this model. We further demonstrate that the knowledge of these characteristic responses allows one to dynamically evaluate the position of a small hole within the contact zone, based on the micro-force sensors signals, with a spatial resolution an order of magnitude better than the intrinsic resolution of individual sensors. Consequences of these observations on robotic tactile sensing are briefly discussed.

Keywords: MEMS tactile sensor array; biomimetic sensor; mechanoreceptors; receptive field; friction; topological feature localization; hyperacuity; human tactile perception

---

1. Introduction

The human hand is an extraordinary tool which cannot be matched by any existing robotic device. It allows us both to manipulate objects with extreme precision and to extract a wealth of information such as their shape, weight, temperature and surface texture [1,2]. These capabilities owe for a large part to the cutaneous tactile sensitivity of hands that provide information regarding the forces acting on the skin. Tactile perception is mediated by specialized nerve endings (mechanoreceptors) located in the first layers of the derma. The tactile information, contained in the sequence of spikes traveling up the afferent fibers, is processed by the central nervous system to assess various physical characteristics of the probed objects such as its curvature, overall shape, temperature. Tactile perception informs about the regions of contact, the relative skin/object motion within this contact, and the direction and intensity of the interfacial forces. This information is essential to texture discrimination, grasping tasks and precise manipulation of objects. When the sense of touch is artificially canceled, even if the other sensing modalities (such as vision) are maintained, the hand becomes clumsy [3].

The performance of the human hand has driven a large effort towards the design of skin-like sensors to incorporate tactile capabilities in humanoid robots. General designs are based on a biomimetic approach which consists in mimicking the human tactile organ by reproducing one or several of its characteristics. These range from the mechanical properties and topography of natural skin to the sensitivity, frequency bandwidths, localization and density of the various mechanoreceptors. Different types of designs have been implemented up to now and a review can be found in [4]. One can find large-area thin film devices which measure one single component of the stress field (mostly the pressure) with a relatively high sensitivity but a low spatial resolution except for some very recent designs [5-8]. Such "e-skins" (electronic skins) have the advantage of being rather flexible so they can be wrapped around robotic arms for instance. One can also find systems in which one or several discrete measuring units are used as mechanoreceptors equivalent and are distributed within an elastic material. Such units range from strain gauges to piezoelectric-electric components such as PVDF films and piezo-resistive elements [9-13]. More recently, Micro-Electro-Mechanical Systems (MEMS) micro-force sensors have been increasingly used as they allow simultaneous measurements of both pressure and shear components with an enhanced sensitivity and a highly linear and hysteresis-free output [14-18]. Still, the design of large-area, highly flexible, mechanically robust and cost-effective MEMS device remains challenging.

Beyond these technological issues, efforts are still needed to establish signal processing and tactile encoding schemes that would enable one to extract the relevant information from the measured force signals. Following Dahiya *et al.* classification [4], one can distinguish two types of tasks assigned to robotic tactile sensing, referred to as "perception for action" and "action for perception". The first case refers to situations where tactile sensing aims at providing information on the interaction between the sensor and the object, such as the existence of slippage or rolling motion, the location of the contacting area, the direction and amplitude of the contacting forces, in order to safely manipulate the object. The signal processing should therefore produce an output which does not depend crucially on the physical properties of the object. In the second situation, tactile sensing aims at assessing object properties by active exploration. In human sensing, it has long been recognized that individuals usually adopt stereotyped patterns of interaction between the hand and the object, known as "exploratory procedure", whose characteristics depend on the type of information sought for [19-21]. Within a given exploratory procedure however, the mechanical conditions experienced by the various mechanoreceptors are expected to greatly vary. A fundamental question thus arise to how the sensing system manage, in spite of this inevitable variability of the exploratory conditions, to produce an output that only depends on the intrinsic properties of the touched object.

In both situations, the raw response of the sensors depends on many parameters, some of which being directly related to the physical properties of the object whereas others being contextual (*i.e.*, dependent on the way the object is touched). The challenge is to consistently extract some of these parameters without a complete knowledge of the others. As an illustration of this problem, let's imagine a robotic device whose task is to lift an object with the minimal squeezing force. If one knows the friction coefficient of the skin/object interface and its weight, then it is easy to set the minimal force. If such properties are unknown, the applied force will have to be dynamically adjusted based on the detection of interfacial slip.

Here we focus on the reverse problem, *i.e.*, how to precisely extract physical characteristics of the probed surface based on the sole output of embedded micro-force sensors. For that purpose, we study, experimentally and theoretically, how the responses of subcutaneous force sensors scanned quasi-statically (low velocity) across a micro-textured surface, depend on the exploratory conditions. The paper is organized as follows. In part 2, we describe a novel bio-inspired tactile sensor designed by integrating a linear array of 10 MEMS micro-force sensors in a millimeter thick elastomer layer. The calibration of the individual sensors by point-like indentation of the skin surface as well as the experimental set-up are detailed. In part 3, the response of the sensors to perfectly smooth surfaces in both static and frictional conditions is studied. A linear model of mechanical transduction is introduced to interpret the observed stress profiles. In part 4, the sensors' responses to the passage of elementary topographical features on a flat substrate is measured. We examine how these responses vary with (i) the sensors' location within the substrate/skin contact zone, (ii) the skin thickness and (iii) the normal applied force. The role of these exploratory conditions is discussed within the framework of the linear model presented before. Based on these results, in part 5, a signal processing scheme is proposed which returns the location of elementary surface defects within the contact zone. We show how the use of multiple sensors increases the spatial resolution of the tactile device well beyond the intrinsic resolution of individual sensors (hyperacuity). In part 6, the impact of this study on robotic tactile sensing and future works are discussed.

2. Bio-Inspired Fingertip Design and Calibration

The bio-inspired tactile sensor used in this study consists of a 10 mm long linear array of 10 individual MEMS micro-force sensors embedded in a spherical elastomer cap mimicking the derma-epiderma (Figure 1). The sensitive part of each micro-force sensor consists of a vertical silicon cylinder (of diameter 100 μm and height 400 μm) attached to a circular silicon membrane (radius 350 μm, thickness 10 μm) suspended on its perimeter (Figure 1, Right). The membrane bears 4 pairs of piezoresistive gauges that give access to its internal stress state, from which one can extract the force acting on the cylinder. Once covered with an elastic layer, it allows for the measurement of the three components of the subcutaneous stress in a region of lateral extension of order 200 μm. Successive sensors are 1 mm apart and aligned along the x-axis, which is the scanning direction in dynamic sensing experiments.

Sensors are numbered from left (①) to right (⑩) and a consistent color code is used in all figures, from blue to red.

The soft layer covering the sensors consists of an elastomer spherical cap with a large radius of curvature. This geometry yield an extended circular contact zone when put in contact with a flat surface. Two layer geometries were tested: a thick layer (maximum thickness $h = 3.04$ mm, radius of curvature $R = 129.7$ mm) and a thin layer ($h = 1.78$ mm, $R = 311.2$ mm). Both were obtained by molding the liquid cross-linker/polymer melt prior to its cross-linking in a concave spherical lens whose surface has been finely abraded with a Silicon Carbide powder (The average size of abrasive grains is about 37 μm. The resulting surface has a microscopic *rms* roughness of about 1.28 μm whose main effect is to dramatically reduce the adhesive properties of the elastomer layer. Note that the current layer surface is not textured with fingerprint-like ridges whose effect has been discussed elsewhere [22-25]). The elastomer used here is a cross-linked PolyDiMethylSiloxane (PDMS) (The PDMS elastomer is prepared using a Sylgard 184-Dow Corning kit: dimethylvinylated and trimethylated silica are mixed with a curing agent (tetramethyltetravinylcyclotetrasiloxane) in a $10:1$ mass ratio. Air bubbles are removed by a 5 min centrifugation at 3,000 rpm followed by exposure to a partial vacuum for a few hours. The liquid PDMS is then poured into the spherical mold, and cured at 70 °C for 48 h in an oven.) whose Young's elastic modulus was measured to be approximately $E = 3$ MPa and whose Poisson ratio was taken to be $\nu = 0.5$ as usually reported for this particular material.

Substrates to be scanned by the sensor, as well as the indentors used during the calibration procedure, are mounted on a three-axis motorized micro-positioning stage (micro-actuators, Newport, Inc.). A double-cantilever system combined with capacitive position sensors (MCC-30 and MCC-5, Fogale Nanotech) allows one to measure the total normal and tangential loads, respectively F_z and F_x, exerted on the tactile device (Figure 1, Left). In a typical experiment, the soft sensor is scanned at constant velocity c under a prescribed F_z, across smooth or patterned Plexiglas substrates.

Figure 1. Scheme of the tactile sensing device and blow-up image of one individual micro-force sensor. (**Left**) Sketch of the experimental setup. The sensing device is made of a linear array of 10 MEMS micro-force sensors mounted on a rigid base (lower gray block), covered with a PDMS spherical cap. Flat substrates or indentor (in the form of a small rod, not shown) can be displaced and applied onto the surface of the sensing device. (**Right**) Picture of one MEMS micro-force sensor as seen from above.

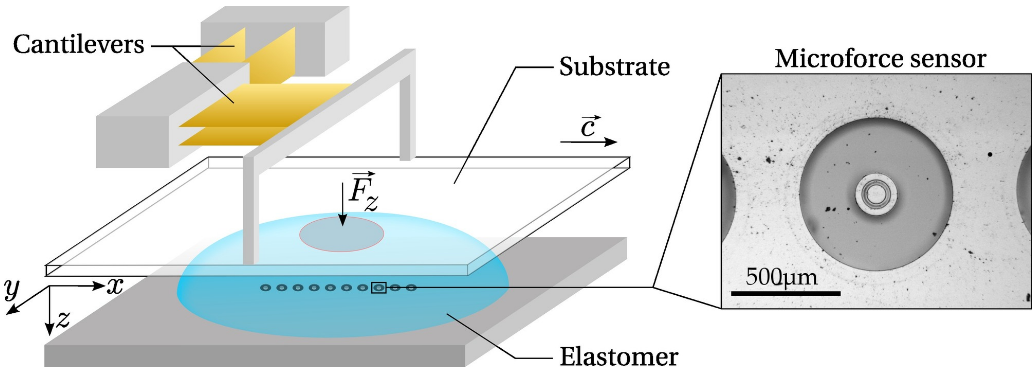

Figure 2. Characterization of the intrinsic receptive fields. (**Top**) Sketch showing the local indentation procedure. A 500 μm in diameter cylinder is indented at the surface of the elastomer cap at varying positions (x, y). (**Middle**) Normal (left) and tangential (right) stress fields, respectively σ_z and σ_x, measured by the micro-force sensors ①, ⑤ and ⑩ as a function of the indentor's position (x, y) under a unit normal force $F_z = 1$ N. (**Bottom**) Normal (left) and tangential (right) stress measured by each of the 10 micro-force sensors (from blue to red) as a function of the indentor's position x for $y = 0$ under a unit normal force and for a layer thickness $h = 3.04$ mm. The experimental stress measured by sensor ⑤ (white circles) is compared to the prediction of a Finite Element calculation (black solid curve).

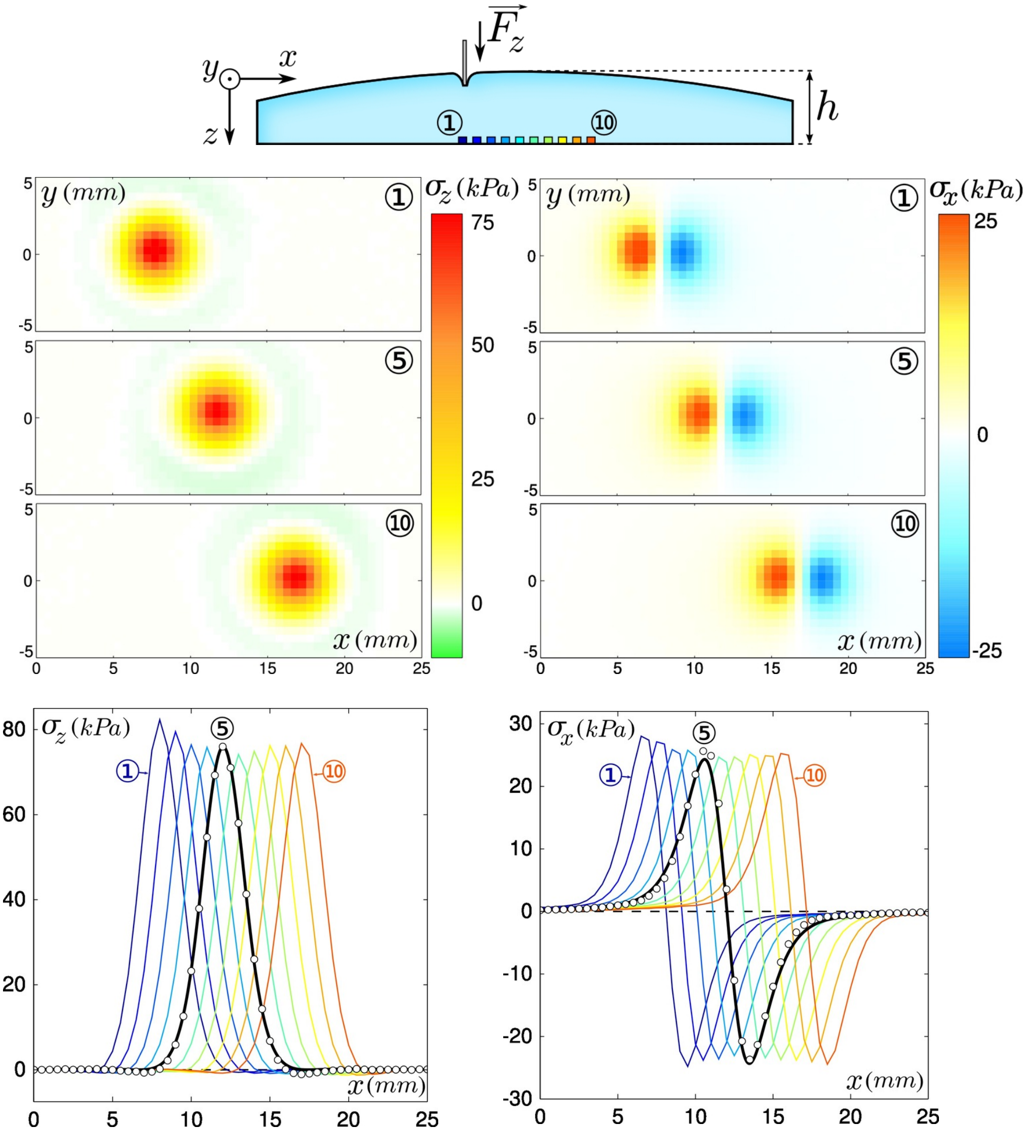

The tactile device is calibrated by applying a localized normal force at different locations on the soft layer's surface, as depicted in the top sketch of Figure 2. A thin cylinder indentor (500 μm in diameter) is iteratively loaded normally to the elastomer surface up to a prescribed load $F_z = 0.4$ N at every node of a 500 μm rectangular mesh covering the entire sensitive surface of the tactile device. Regardless of the indentor's location, the micro-force sensors response varies linearly with the applied load. By analogy to the concept of receptive fields defined in neurophysiological experiments [26], we define the Intrinsic Receptive Field (IRF) of the sensor (In contrast with the exploratory receptive fields introduced in Section 4, which depend on the exploratory conditions.) as its spatial response to a localized indentation. Typical IRF's are shown in the middle panel of Figure 2 for both the normal and tangential stress in response to a unit load ($F_z = 1$ N) as a function of the (x, y) position of the indentor. These point-load response profiles are similar from one sensor to the next, and are centered on the sensor's location. They are compared with the result of a Finite Elements simulation using CAST3M (CAST3M is an open source Finite Element simulation software developed at CEA, France. For additional information, see the link http://www-cast3m.cea.fr/cast3m/index.jsp. in $2D$ plane stress axisymmetric conditions. The stress field at the bottom of an elastic layer of finite thickness h rigidly attached to a solid plane is calculated as its surface is normally indented by a 500 μm flat cylindrical indentor. In the limit where the indentor diameter is much smaller than the layer thickness, the calculated stress field is similar to that obtained for a punctual indentor (the so-called Green function) and is a function of h only. As shown in the bottom panels of Figure 2, the measured and calculated response profiles can be correctly adjusted for both stress components. This adjustment provides a Volt-to-Pascal calibration for each micro-force sensor, as well as an estimated value of the thickness of the layer on top of each sensor. The latter is consistent with the geometry of the elastic cap since the layer thickness is found to vary continuously along the line of sensors with a maximal thickness of the layer located close to sensor ⑥. Such thickness variation can be clearly seen on Figure 2 through an inverse variation of the maxima of σ_z (corresponding to the point where the indentor lays right above the sensor).

3. Average Stress and Linear Model of Tactile Transduction

3.1. Stress Profiles Measurements

We first investigate the response of the sensing device to a smooth and flat Plexiglas substrate in both static and frictional conditions. The substrate is pressed over the device with a constant normal force $F_z = 0.8$ N, forming a circular contact area of diameter 4–5 mm (see sketch on top of Figure 3). The interfacial contact stress field is centro-symmetric with respect to the center of the contact zone, the latter being roughly above sensor ⑥. In the lower plane where sensors are located, the normal and tangential stress fields σ_z and σ_x (middle panels of Figure 3), are respectively symmetric and antisymmetric with respect to the center of the contact zone. A slight asymmetry in the x-direction is however observed. This effect can be accounted for by the development of a minute tangential force during normal loading due to the double cantilever system. In comparison, the tangential stress field σ_y (not shown) is perfectly antisymmetric with respect to the x axis.

The substrate is then moved quasi-statically at constant velocity ($c = 500$ μ m/s) in the positive x direction (This velocity was chosen to avoid sensors breakage and skin wear. In natural physiological conditions, scanning velocities are typically in the cm/s range. However, at such velocities and for such a rigid system, the characteristic intrinsic frequencies are orders of magnitude larger than those elicited at the interface and in addition the friction coefficient for these types of materials exhibits a weak velocity dependence. One thus expects very little dynamical effects.). The average response of the micro-force sensors measured during steady sliding is shown on Figure 3, Bottom. The stress signals along the

y axis (*i.e.*, perpendicular to the direction of motion) contain very little additional physical information as compared to σ_x and σ_z, and will thus be discarded from the subsequent analysis. The steady state profiles significantly differ from their static counterparts due to the development of a tangential interfacial stress field in the contact zone.

Figure 3. Static and dynamical mean stress as measured by the sensors and compared to the model's predictions for a flat substrate. (**Top**) Sketch: a flat substrate is rubbed against the surface of the sensing device with a normal force $F_z = 0.8$ N ($h = 3.04$ mm). Vertical dashed lines represent the boundaries of the contact zone and scale with the actual sensors' locations. (**Middle**) Averaged stress versus sensors location x in the static regime ($c = 0$) for the 10 sensors (colored circles) compared to the model's prediction (black curve) for the normal component σ_z (left) and similarly for the tangential component σ_x along the direction of motion (right). Position $x = 0$ is the center of the contact. Error bars show the measured standard deviation and colors correspond to the locations depicted on the upper sketch. (**Bottom**) Same as above but in the steady sliding regime (c = 500 μ m/s).

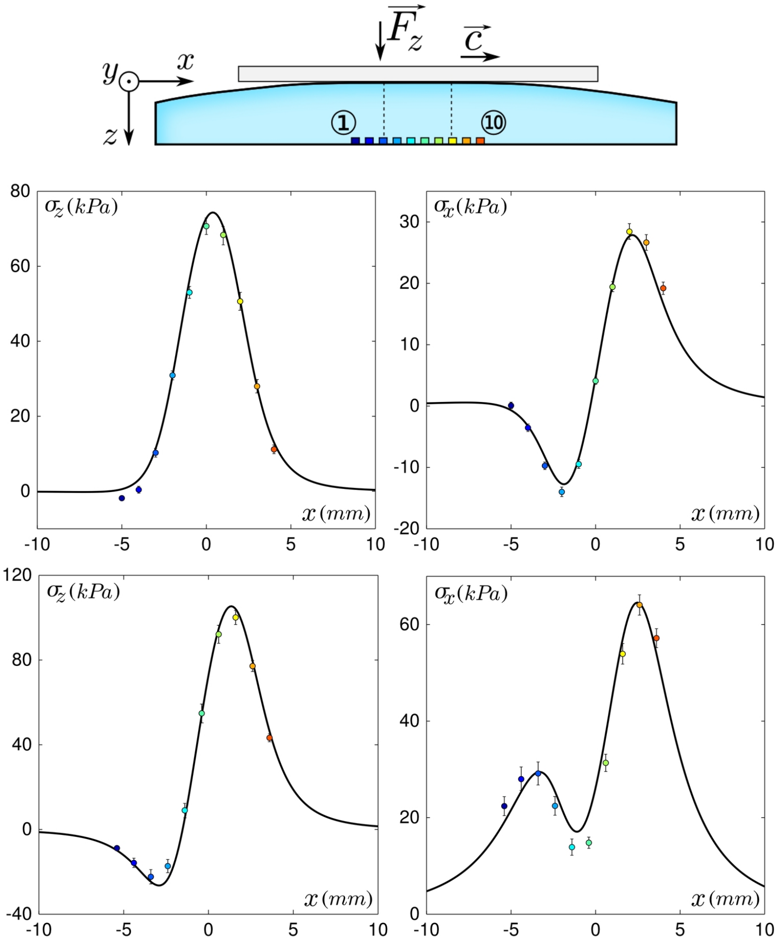

3.2. *Linear Model of Tactile Transduction*

In order to interpret the subcutaneous stress profiles presented above, one first needs to calculate the stress field that develops between the elastic layer and the substrate during steady-state sliding.

Unfortunately, there is no analytical solution to this mechanical problem in our confined geometry (although a solution has recently been proposed in a 2D equivalent configuration [27]). To circumvent this difficulty, we make the assumption that the normal stress field is unmodified by the application of a tangential force as would be the case in a semi-infinite configuration. Under this weakly restrictive hypotheses, an approximate semi-analytical solution can be derived whose three main ingredients are:

- *(i) Interfacial pressure field*: The interfacial pressure field at a sphere-on-plane contact is given by Hertz' classical calculation [28]. This result is valid in the limit of infinite semi-elastic media, *i.e.*, when the thickness of both objects is much larger than the contact radius. In our case, the latter is comparable with the elastic layer thickness. We therefore use a semi-analytical modified Hertz profile as recently proposed by Frétigny and Chateauminois [29]. As shown in Figure 4, Left, this corrected profile shows a 11% reduction in contact radius, associated with a 12% increase in maximum pressure.

- *(ii) Interfacial shear stress field*: In steady sliding regime, we postulate that at each point within the contact zone the Amontons–Coulomb Law of friction is satisfied, *i.e.*, that the local tangential stress and pressure are proportional, $p_x = \mu_d . p_z$, where the dynamic friction coefficient $\mu_d \simeq 3$ is evaluated as the time-averaged ratio of the total tangential to normal forces F_x/F_z.

- *(iii) Stress propagation in the elastic media*: Under linear elasticity and quasi-static hypothesis, the application of a force on the surface of an elastic material creates a bulk stress which is entirely set by the Green tensor **g**. The stress at point $(x,\ y,\ z)$ in response to a force $\vec{f}$ applied at the origin $(x = 0,\ y = 0,\ z = 0)$ on the surface of the material is therefore given by $\mathbf{g}(x, y, z).\vec{f}$. For a semi-infinite elastic medium the analytical solution of the Green tensor is known [28] but, again, this result has to be corrected to take into account the finite thickness of the elastic layer and its attachment to a rigid base. We have carried out a finite element simulation to obtain the stress profile generated by localized normal indentation (see Section 2). This calculation indicates that a reasonable approximation of the corrected Green tensor can be obtained with a simple rescaling of the semi-infinite solution by a numerical factor k while the spatial coordinates are rescaled by $k^{-1/2}$ to ensure force conservation. Figure 4, Center shows the normal component g_{zz} of the Green tensor for a semi-infinite ($h = \infty$, analytical) and a finite elastic layer ($h = 3.04$ mm, Finite Elements calculation). The scaling of the semi-infinite solution with a factor $k = 1.48$ is also displayed for comparison. The same factor also yields a correct approximation for the tangential component of the Green tensor g_{zx} (see Figure 4, Right). We make the assumption that corrections to the other components of the Green tensor can be obtained with the same scaling.

These ingredients being established, the stress profiles along the sensors' line can be obtained by convoluting the interfacial stress field with the Green tensor, so that it now reads

$$\begin{aligned}\sigma_\alpha(x_i) = & \iint p_x(x, y).g_{x\alpha}(x - x_i, y - y_i, h)dxdy \\ + & \iint p_z(x, y).g_{zx}(x - x_i, y - y_i, h)dxdy\end{aligned}$$

where (x_i, y_i) is the position of the sensor, and $\alpha \in \{x, y, z\}$. The resulting profiles are compared to the experimental data in Figure 3. A very good agreement between the data points and the model for a value of 3.0 MPa for Young's modulus and a Poisson ratio of 0.5, which are compatible with the material's elastic properties, substantiates the various hypotheses and simplifications (Note that in order to account for the observed minute tangential force in the static condition, a finite tangential stress field proportional to the normal stress field has been postulated).

Figure 4. Effect of the finite thickness of the elastic layer. (**Left**) Sphere-on-plane contact pressure profile calculated for a semi-infinite elastic medium (Hertz' calculation, dashed black line) and an elastic layer of thickness h (blue line) such that $h/a = 1.3$ where a is the contact radius. This ratio corresponds to the experimental conditions. (**Center-Right**) Normal component g_{zz} (center) and tangential component g_{xz} (right) of the Green tensor in $(x,\ y = 0,\ z = h)$: the profile for the semi-infinite layer (dashed line) can be rescaled (blue line) to approximate the profile obtained by Finite Elements simulation for a layer of thickness $h = 3.04$ mm (dotted line).

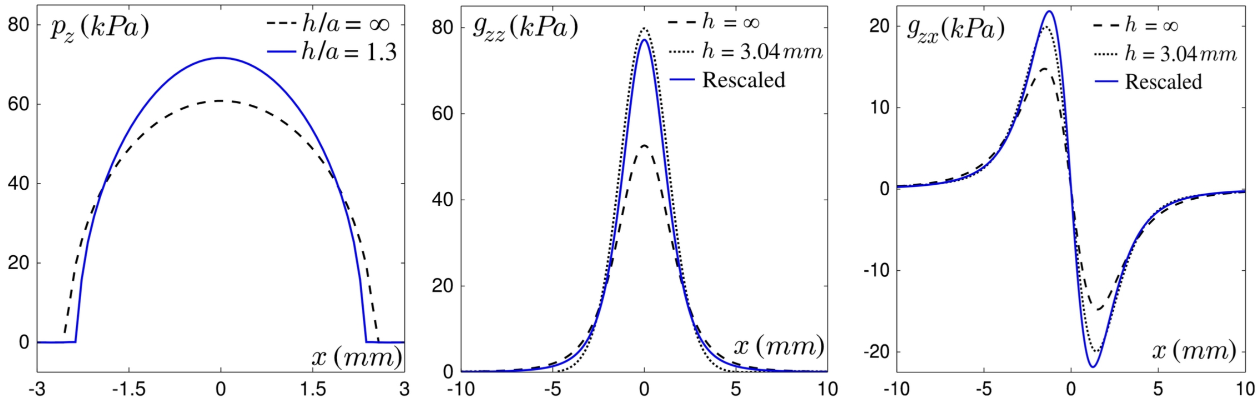

4. Response to Fine Topographical Features Scanned Across the Tactile Sensor: The Exploratory Receptive Field

4.1. Exploratory Receptive Fields

We now turn to the response of the tactile sensor to the passage of an elementary topographical defect on the substrate. The tactile sensor is scanned at constant velocity and confining force F_z across a flat surface bearing a line of discrete holes 500 μm in diameter and 1 mm in depth (The choice of using holes rather than bumps was dictated to both facilitate the fabrication of the substrates and the modelling. Upward bumps and downward holes impose different boundary conditions within the feature surface, namely a deformation for the former and a constant (zero) stress for the latter; The geometry is different from [30], since our aim here is to create a topological feature whose size is much smaller than that of the contact). Such an aspect ratio in the hole dimensions prevents the elastomer from contacting the bottom of the holes. Furthermore, the distance between neighboring holes was chosen to be larger than the contact zone diameter so that each hole produces an independent realization of the same mechanical stimulation. By scanning along adjacent parallel trajectories, one can explore the complete $2D$ response function associated with this elementary defect, for one given set of exploratory conditions.

Figure 5. Generation of the Exploratory Receptive Fields (ERF). (**Left**) Sketches of the scanning protocol for lines of isolated defects (top: top view, bottom: side view). Dashed circle and lines represent the boundaries of the contact zone, which scale with the actual sensors' locations. The substrate moves at constant velocity c. The relative position of the nearest defect to a given sensor is denoted $(u(t), v(t))$. **Right-Top** Normal stress responses to 3 successive defects for sensor ⑥ ($h = 3.04$ mm, $F_z = 0.8$ N, $c = 500\ \mu$ m/s). The raw signals, converted in stress unit, are shown for only 8 scanning lines and are shifted vertically from one to the next for clarity. **Right-Bottom** ERF of the normal stress ς_z for sensor ⑥, reconstructed from the average of 14 responses to defects. Color code units are kPa.

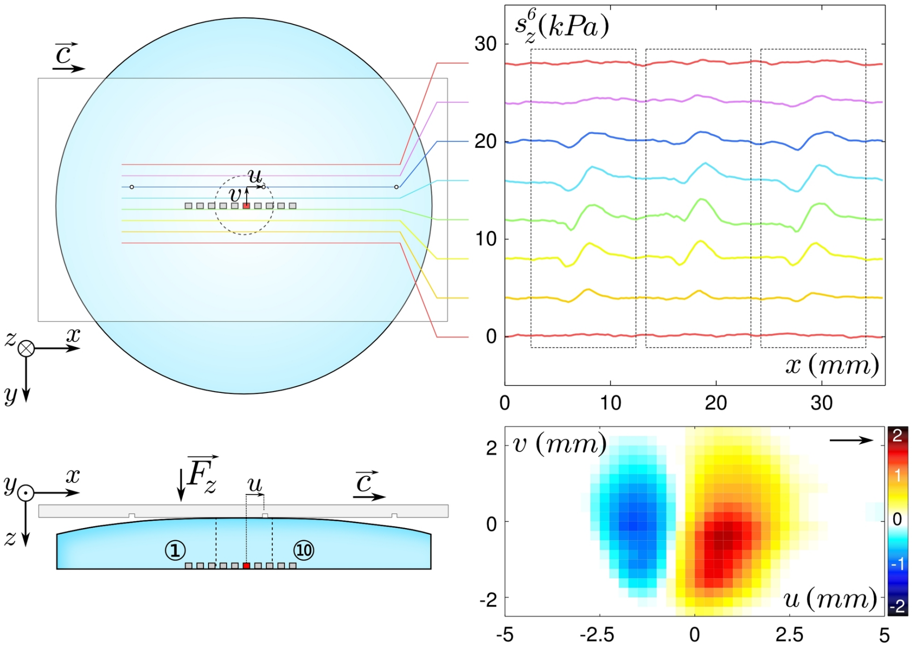

A sketch of the experiment and the corresponding signals measured by a micro-force sensor are shown in Figure 5. Since the hole surface area is small compared to the contact zone area, its passage shows up as a small deviation from the base line (which correspond to the smooth substrate situation). These deviations remain however large with respect to the electro-mechanical noise of the sensor. We define the normal and shear responses ς_z^i and ς_x^i for each micro-force sensor i as the deviation of the normal and shear stress due to the presence of a defect located at position (u,v) at the interface

$$\begin{aligned}\varsigma_z^i(u,v) &= s_z^i(u,v) - \sigma_z^i \\ \varsigma_x^i(u,v) &= s_x^i(u,v) - \sigma_x^i\end{aligned}$$

where $s_z^i(u,v)$ and $s_x^i(u,v)$ are the stress signals and σ_z^i and σ_x^i are the time-averaged stress already characterized in the previous section. Both ς_z and ς_x can be seen as an "exploratory receptive field" (ERF), which are the dynamic counterparts of the IRF displayed in Figure 2, Bottom. A typical two-dimensional ERF for the normal stress for one given micro-force sensor, constructed from an average over 14 realizations, is shown in the bottom-right panel of Figure 5.

The spatial characteristics of the ERF can be quantitatively interpreted within the scope of the linear model of tactile transduction presented in the previous section. To a first approximation, one assumes that the presence of a small hole on the flat substrate locally cancels the normal and shear stress without modifying the Hertz-like stress field in the rest of the contact zone. Under such an assumption, the defect-induced stress variations measured by the micro-force sensors can be calculated analytically. As long as the defect's surface remains small with respect to the contact zone area, the stress variations for a sensor i located at (x_i, $y_i = 0$) writes:

$$\begin{aligned} \varsigma_x^i(u,v) &= -[p_x(u,v)g_{xx}(u-x_i, v-y_i, h) + p_z(u,v)g_{zx}(u-x_i, v-y_i, h)]A_d \\ \varsigma_z^i(u,v) &= -[p_x(u,v)g_{xz}(u-x_i, v-y_i, h) + p_z(u,v)g_{zz}(u-x_i, v-y_i, h)]A_d \end{aligned} \qquad (1)$$

where A_d is the surface area of the defect. This calculation can be performed for any exploratory conditions and geometrical characteristics of the layer, which allows for a direct comparison with the measured ERF's.

4.2. *The Role of Exploratory Conditions*

As outlined in the introduction, the characteristics of tactile transduction depend not only on the intrinsic properties of the tactile sensor, but also on the mechanical conditions of the frictional interaction between the substrate and the sensing device. These conditions are controlled by several quantities: some of them are contextual (namely the global applied force and the skin/substrate contact location), some are intrinsic to the sensor (the skin radius of curvature and elastic moduli), and one is characteristic of the skin/substrate interfacial interaction (the friction coefficient). In this section, we systematically vary those different parameters and analyze how they affect the measured and calculated ERF's.

The first parameter we focus on is the position of the contact zone relative to the micro-force sensors location. Figure 6(a,c) shows the two-dimensional ERF's for all 10 sensors for both stress components under a confining force $F_z = 0.8$ N. It appears that the passage of the small topographical feature produces a signature whose shape strongly depends on the precise location of the sensor. It is remarkable for instance that the normal ERF $\varsigma_z(u,v)$ evolves from a positive spot for the most left-handed probing positions to a negative spot for the most right-handed ones. Note that the outmost sensors do respond to the defect's passage although they lay outside of the contact zone.

The corresponding calculated profiles, displayed in Figure 6(b,d), correctly capture the spatial distribution experimentally observed for the ten sensors, as well as their amplitudes. There are however some discrepancies, in particular for the right-hand side sensors (from ⑥ to ⑩) whose amplitudes are systematically higher than expected both for the normal and shear stress. This may come from a coupling between tangential and normal stresses, ignored in our model: the friction-induced shear stress field produces a torque on the elastic layer which is balanced by a desymmetrization of the interfacial pressure profile (see [27] for a discussion of this effect in a cylinder/plane geometry).

This simple model captures the essential features of the position-dependence of the sensors' response. It allows one in turn to interpret the origin of the observed variability in the ERF's. Equation (1) shows that the signal measured by the sensor depends on the product of its intrinsic response function **g** by the time-averaged interfacial stress field (p_z, p_x). In the sphere/plane geometry used in the experiments, the latter is given by Hertz calculation (Figure 4) which rapidly varies over the contact zone. As a result, the average stress field *seen* by a given sensor, and thus its ERF, is extremely sensitive to its exact location below the contact zone.

Figure 6. Measured and predicted ERF. Each row corresponds to one sensor, from ① to ⑩ starting from the top. Each column corresponds to the measured **(a)** and predicted **(b)** normal stress ς_z, and measured **(c)** and predicted **(d)** shear stress ς_x. Standard deviations are typically $0.6\,kPa$ for ς_z and $0.4\,kPa$ for ς_x. The arrow indicates the defect's displacement. The color code is the same for all plots. $h = 3.04\,mm$ and $F_z = 0.8$ N.

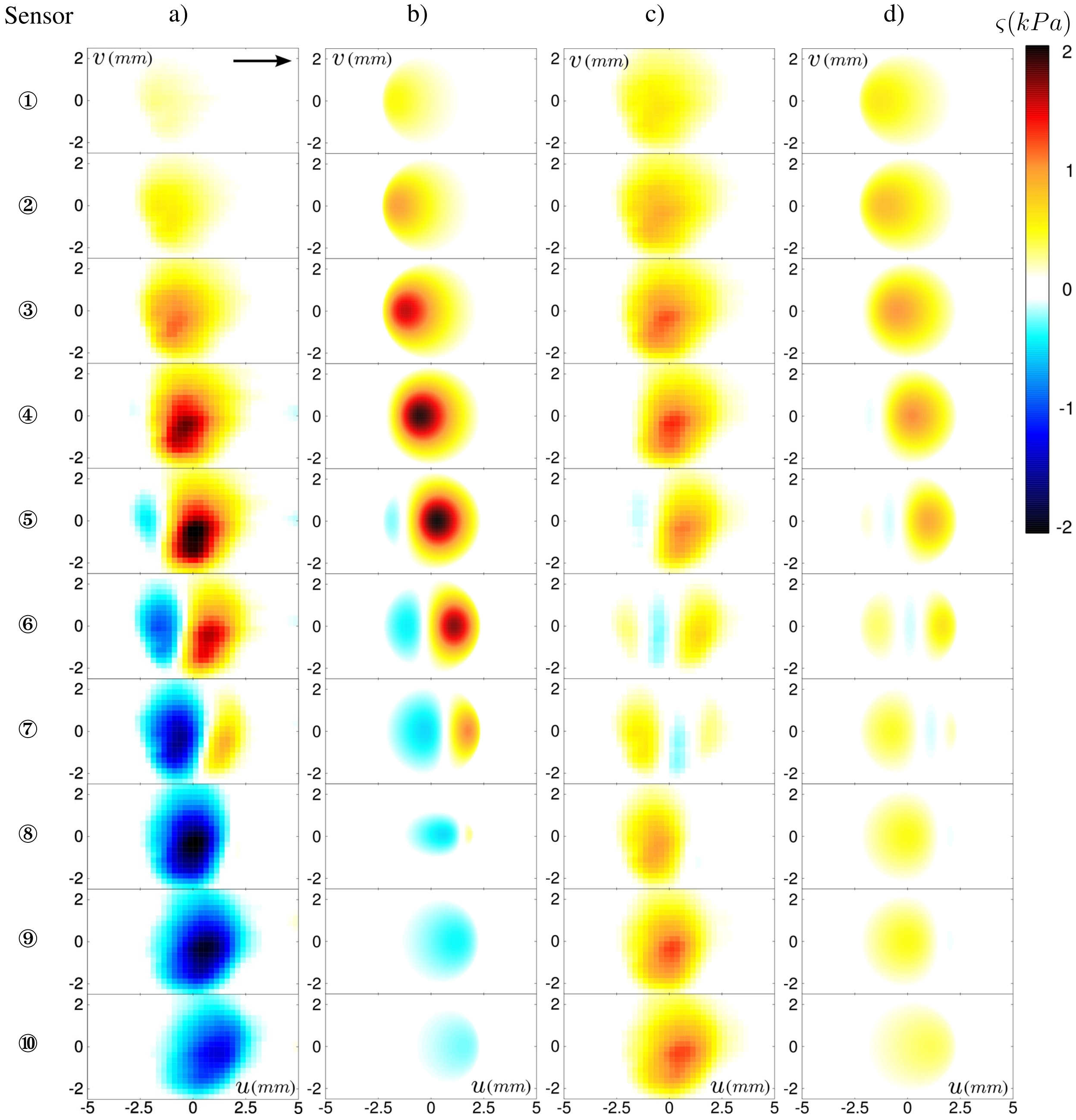

The use of two tactile devices with different layer thicknesses allows us to analyze the role of this geometrical parameter: in Figure 7, Left the recorded normal stress variations as the defect is scanned along the sensor mid-line are shown for one micro-force sensor located below the center of the contact zone, for both layers. With the thinner one, the response amplitudes are higher although the global shape of the responses is maintained. Increasing the normal applied force F_z from 0.2 to 0.8 N (see Figure 7, Right) similarly increases the stress amplitude, but also widens the profiles as the contact radius a is increased. Notice however that this parameter weakly modifies the global shape of the responses over our experimental range.

Figure 7. Role of two exploratory parameters: experimental data (points) at the ERF median line ($v = 0$) are compared to the model prediction (solid curves) for a sensor at the center of the contact. (**Left**) Average normal stress variations σ_z for two layer thicknesses: $h = 1.78$ mm (blue circles) and $h = 3.04$ mm (red squares). The arrow indicates the defect's displacement. $F_z = 0.8$ N. (**Right**) Average normal stress variations σ_z for four normal forces from 0.2 to 0.8 N ($h = 1.78$ mm).

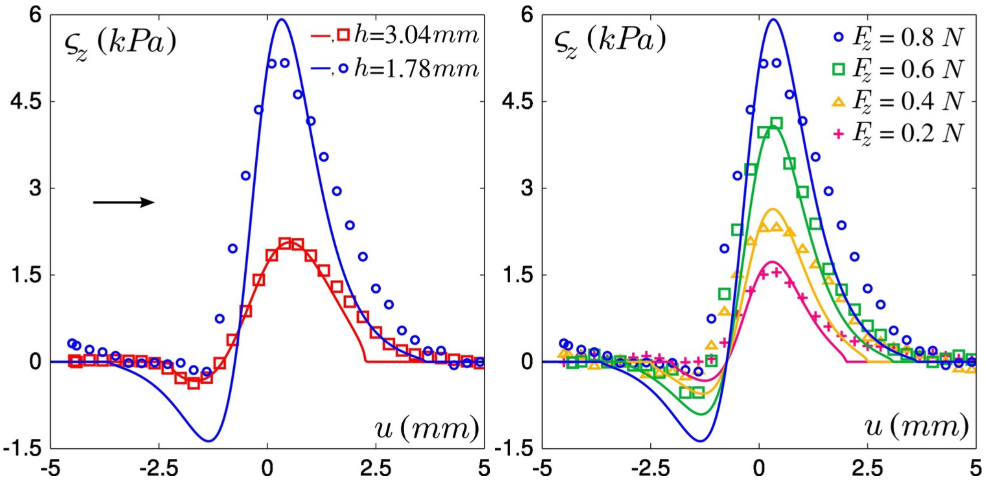

As can be seen on Figure 7, the dependence on the layer thickness and on the normal applied force are correctly captured by our model. It should be noticed however that the quality of the fit deteriorates when the thinner layer is used, e.g., in Figure 7, Left the positive peak is broadened and the amplitude of the negative peak is smaller than predicted. This may be accounted for by the narrower intrinsic receptive fields (IRF) of the thin-layer sensor, which results in a greater sensibility to short-scale details of the surface stress fields. Discrepancies between observed and calculated profiles may thus result from the crude approximation made when estimating the local modification of the interfacial stress field induced by the hole.

Altogether, these observations validate our model of tactile transduction. The latter can further be used to overcome some experimental limitations of our tactile device: the accessible range of normal load can be extended beyond the breakage limit of the micro-force sensors, and the dynamical friction coefficient can be varied. In Figure 8(a,b), the predicted ERF for both stress components are shown for a normal force $0.33\,N < F_z < 7.15\,N$, a friction coefficient $\mu_d = 3$ and a layer thickness of $h = 3.04$ mm. The ERF's are calculated for a sensor located at the center of the contact. This series of graphs corresponds to increasing values of the contact radius a from 0.75 h to 1.8 h. It appears that the increase of the applied force up to large values essentially maintains the shape of the response profile, except for a scaling factor given by the ratio a/h. It should be noted however that the modification of the ERF is more pronounced for sensors located at the edge of the contact (not shown). For those sensors, the main effect of increasing the contact area is to move the relative position of the sensor with respect to the contact zone. Figure 8(c,d) show how varying the dynamical friction coefficient μ_d in the 0–6 range modify the ERF of a centrally located sensor. In contrast to the normal applied force, an increase of the friction coefficient strongly affects the shape of the sensors' response.

Figure 8. Evolution of the predicted ERF for a sensor at the center of the contact zone ($x = 0$, $y = 0$) in response to a single defect in (u, v) scanned at constant speed from left to right ($h = 3.04$ mm, $c = 500$ μ m/s). Two parameters are explored: **(a–b)** the applied normal force F_z and **(c–d)** the dynamic friction coefficient μ_d. Columns (a) and (c) show the normal stress profiles σ_z, columns (b) and (d) show the shear stress profiles in the direction of motion σ_x.

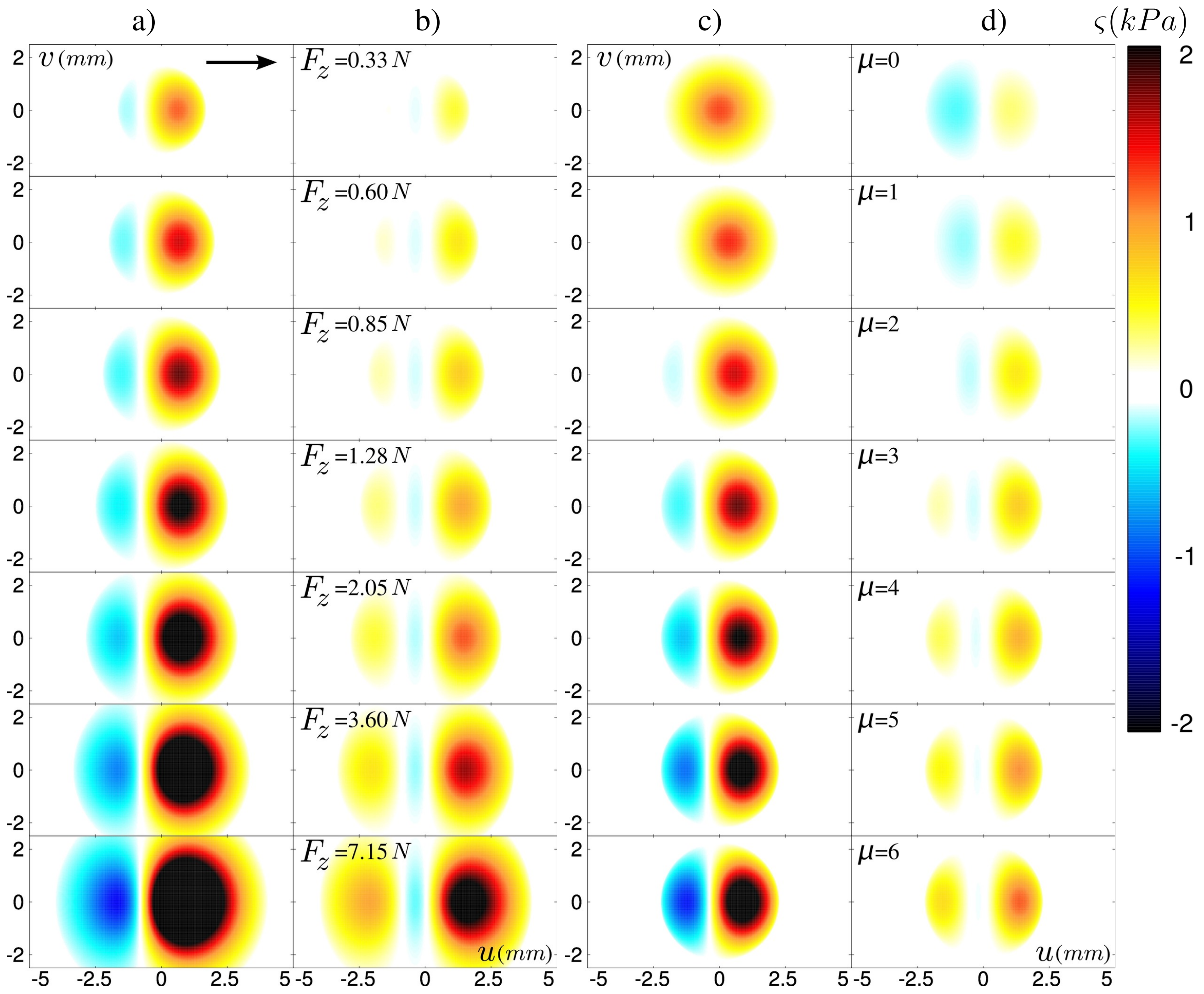

4.3. Discussion

In our device, the sensor base is much more rigid than its soft covering layer. This mechanical contrast complicates the calculation of both the IRF and the contact stress field. As a result, no exact scaling can be exhibited between the ERF and the various exploratory or mechanical parameters. It is therefore interesting to examine the dependence of the predicted ERF in the limit where the base and layer would have similar mechanical properties. In this case, one can show that the ERF can be written as:

$$\varsigma_z^i(\tilde{u},\tilde{v}) \approx -\tilde{A}_d\tilde{F}^{1/3}\sqrt{1-(\tilde{u}^2+\tilde{v}^2)/\tilde{F}^{2/3}}\,[\tilde{g}_{zz}(\tilde{u}-\tilde{x}_i,\tilde{v}-\tilde{y}_i,1)+\mu\tilde{g}_{xz}(\tilde{u}-\tilde{x}_i,\tilde{v}-\tilde{y}_i,1)]$$

where all lengths are expressed in unit of h, $\tilde{F}=\frac{F_z(1-\nu^2)}{ER^2}$ is the reduced confining force (E: Young's modulus, ν: Poisson ratio, R: radius of curvature), and $\tilde{g}_{zz},\tilde{g}_{xz}$ are normalized Green functions.

This expression shows that, in this ideal situation, the ERF only depends on 3 independent parameters characterizing the exploratory conditions: $\tilde{F}$, μ and $(\tilde{x}_i,\tilde{y}_i)$. Notice that the amplitude of the ERF increases non-linearly with the normal load and that this parameter also controls the width of the ERF. In practice, these three parameters can be extracted from the average stress profiles, like those presented in Figure 3.

The present model has been developed to account for finite-thickness elastic layers on top of a rigid plane as generally found for most robotic tactile sensors. In human skin, however, the receptors are embedded in soft tissues which can be reasonably described by a semi-infinite elastic medium. As shown in Figure 4, the finite-size effect of the elastic layer changes only marginally both the amplitude and lateral extension of the Hertz profiles and Green functions, suggesting that the results presented here should be of relevance also for e-skin devices and biological systems.

Moreover, such an approach opens possibilities of anticipating the ERF for a given set of exploratory parameters using either the model described above or machine learning techniques. Detection of fine textural features, such as individual topological defects, thus becomes conceivable by direct comparison with the measured signals.

5. Predicting the Defect's Position

The Exploratory Receptive Fields (ERF) exhibited in the previous sections are characteristic responses of the sensors, for one given set of exploratory conditions, to the passage of an elementary surface defect. Under linear hypothesis, these fields entirely characterize the transduction of textural information from the substrate to the sensors array in this particular context of exploration. In addition of being useful building blocks for the understanding of more complex tactile inputs, the complete characterization of the ERFs for isolated defects is relevant for several practical situations, like Braille reading for instance. One may then ask how much information can be retrieved by inverting the problem, *i.e.*, how precisely the position of the defect within the contact can be determined based on the sole signals delivered by the micro-force sensors.

For simplicity, we focus on the prediction of the position u in the x-direction (which is both the axis of the linear array and the scanning direction) of defects scanned right above the sensors line. Our inversion procedure is based on the prior knowledge of the ERF: the averaged sensors' response to the passage of 14 holes yields characteristic subcutaneous stress variation profiles $\bar{\varsigma}^i(u)$ for any position u of the hole.

From this, we can now estimate the position of the hole for a given realization by evaluating the value of u that minimizes the following quantity

$$\xi(u) = \sum_{i \in \mathcal{S}} \left(\varsigma^i - \bar{\varsigma}^i(u)\right)^2$$

where ς^i is the instantaneous measured stress variation field and the sum is performed over a subset of sensors $\mathcal{S}$. We are interested in both the maximum resolution thus attainable and on its dependence with the number of sensors and force components used in this estimation. First, the minimization is computed using the normal component σ_z only. The difference between the predicted and the actual position of the defect, noted δu_z, is shown in Figure 9, Left for 500 independent realizations, using 1, 2 and 5 sensors respectively . For each realization, regardless of the actual defect position within the contact, the subset of sensors used for the estimation is chosen randomly among all 10 available sensors. As expected, the prediction accuracy rapidly increases as the number of sensors used in the estimation, and thus the available information, increases. A similar analysis was conducted using only the x component of the micro-force sensors and using both x and z components. The results are summarized in Figure 9, Right which displays the evolution of the standard deviation of δu_z, denoted s_z^u, as a function of the number of sensors used.

Figure 9. Detection of the defect's position along the direction of motion. (**Left**) Distance between the actual and predicted positions of the defect δu_z for 500 random positions of the defect in the contact zone. The predicted positions are derived by comparing the measured normal stress signals to the average stress profiles for 1, 2 and 5 sensors chosen at random for each realization. The dashed horizontal lines on all three plots are boundaries of the contact zone. (**Right**) Prediction accuracy s^u as a function of the number of sensors used when only the shear stress signal is used (s_x^u, green circles), then when only the normal stress is used (s_z^u, blue squares) and finally when both signals are used (s_{xz}^u, black triangles). In all three cases, the prediction accuracy converges asymptotically to 150 μm.

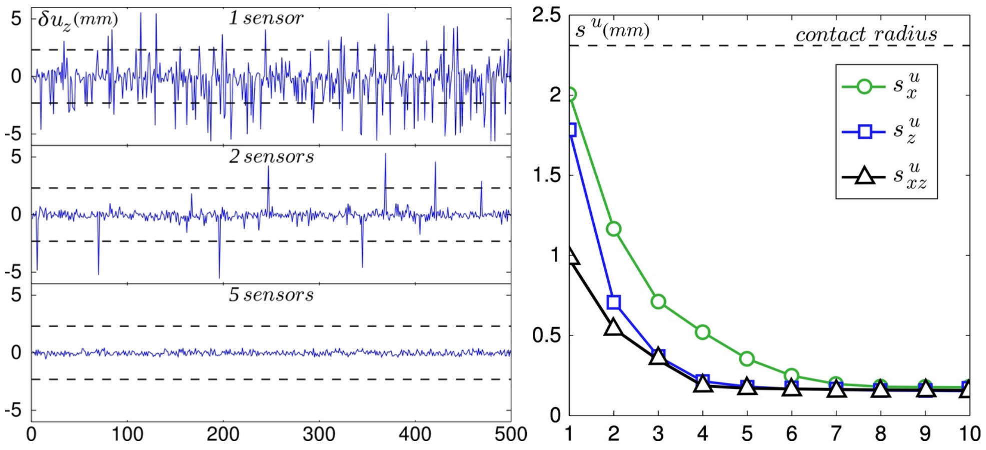

This graph calls for several comments. First, the spatial resolution obtained with a single sensor is of order 1–2 mm, which corresponds to the width of the IRF, *i.e.*, the intrinsic spatial resolution of individual sensors directly related to the thickness of the overlying elastomer layer. Second, the resolution length rapidly decays as the number of sensors (or equivalently the number of components) used in the inversion procedure is increased and asymptotically reaches a minimum of order 150 μm when the total number of components reaches 5. Note that this value is an order of magnitude smaller than the intrinsic resolution length of each sensor, a situation classically referred to as *hyperacuity*. Finally, the normal component appears to be more efficient than the shear component in this inversion procedure as indicated by the fact that the resolution obtained using the normal component alone is systematically better than the one obtained using the shear component.

6. Conclusions

The work presented in this paper aimed at clarifying how the response of a tactile sensor scanned across a textured surface depends on the characteristics of the exploration procedure. In a typical bio-inspired tactile device, the responses of the embedded sensors to a localized indentation on the surface are similar from one to the next. These so-called IRFs are entirely controlled by the elastic layer's thickness. However, the sensors' response to the passage of a textural feature appears to strongly depend on their exact location within the skin/surface contact zone. This effect was evidenced by measuring the Exploratory Receptive Field of each sensor defined as its spatial response to the passage of a unique small feature (a circular hole) on the surface. A linear model of tactile transduction allowed us to correctly predict the form of these ERF based on the knowledge of the sensors' IRF as well as on a few contextual parameters, namely the location of the sensor with respect to the contact zone, the applied normal load and the dynamic friction coefficient. This model allowed us to discuss the effect of each of these parameters in shaping the ERF.

This result has important consequences for robotic tactile sensing. In order to consistently retrieve textural information from the stress signals measured with an embedded sensor, one needs to know how to relate the topographical properties of the scanned surface with the measured signals. The present work indicates that this operation cannot be implemented based on the sole knowledge of the intrinsic properties of the sensor. In a structured environment, *i.e.*, when the exploratory conditions are perfectly controlled and stable, one may obtain these responses empirically by measuring the sensors' response to isolated defects. This approach, used in Section 5, allowed us to retrieve the instantaneous position of a small defect with a much higher resolution than the intrinsic resolution of the individual micro-force sensors. In a non-controlled environment however, a different approach is needed. In this context, the linear model detailed in this paper could be useful since it allows one to predict the form of the ERF based on a few contextual parameters. The latter could be obtained dynamically by analyzing the low frequency force signals whose spatial dependence are characteristics of the averaged surface stress field (see Figure 3).

The dependence of the sensors' response to exploratory conditions obviously complicates the inversion task. However, one may argue that it could ultimately be beneficial to the efficiency of the tactile system. For a given set of exploratory conditions, each sensor is associated with a specific spatial response and is thus sensitive to a particular type of textural features. By actively varying the exploratory procedures, one may actually tune these response functions in order to extract more detailed information on the surface. This strategy may actually exist in human tactile sensing where the exploratory procedures are known to be function of the type of information one seeks to obtain and on the physical characteristics of the probed object [19–21].

This study was limited to the response to small isolated defects. It has relevance for comparisons with neurophysiological measurements for which the ERF have been measured via reverse correlation techniques [31-33]. In more complex situations, typically when several defects lay within the contact zone, elastic interactions between the defects should be taken into account. This work should therefore be considered as a first step towards an analytical understanding of interfacial transduction of texture information.

Acknowledgements

The authors would like to thank A. Chateauminois for the computation of the modified Hertz stress field, J. Scheibert and J. Frelat for their help on the finite element simulation and P. Rey for design and fabrication of the MEMS linear arrays. This work was supported by ANR TRANSTACT.

References

1. Hollins, M. Somesthetic senses. *Annu. Rev. Psychol.* **2010**, *61*, 243-271.
2. Johansson, R.; Flanagan, J. Coding and use of tactile signals from the fingertips in object manipulation tasks. *Nat. Rev. Neurosci.* **2009**, *10*, 345-59.
3. Westling, G.; Johannson, R.S. Factors influencing the force control during precision grip. *Exp. Brain Res.* **1984**, *53*, 277-284.
4. Dahiya, R.S.; Metta, G.; Valle, M.; Sandini, G. Tactile sensing—From humans to humanoids. *IEEE Trans. Rob.* **2010**, *26*, 1-20.
5. Maheshwari, V.; Saraf, R.F. High-resolution thin-film device to sense texture by touch. *Science* **2006**, *312*, 1501-1504.
6. Someya, T.; Sekitani, T.; Iba, S.; Kato, Y.; Kawaguchi, H.; Sakurai, T. A large-area, flexible pressure sensor matrix with organic field-effect transistors for artificial skin applications. *Proc. Natl. Acad. Sci. USA* **2004**, *101*, 9966-9970.
7. Mannsfeld, S.C.B.; Tee, B.C.K.; Stoltenberg, R.M.; Chen, C.V.H.H.; Barman, S.; Muir, B.V.O.; Sokolov, A.N.; Reese, C.; Bao, Z. Highly sensitive flexible pressure sensors with microstructured rubber dielectric layers. *Nat. Mater.* **2010**, *9*, 859-864.
8. Takei, K.; Takahashi, T.; Ho, J.C.; Ko, H.; Gillies, A.G.; Leu, P.W.; Fearing, R.S.; Javey, A. Nanowire active-matrix circuitry for low-voltage macroscale artificial skin. *Nat. Mater.* **2010**, *9*, 821-826.
9. Cutkosky, R.; Howe, M. Dynamic tactile sensing: perception of fine surface features with stress rate sensing. *IEEE Trans. Rob. Autom.* **1993**, *9*, 140-151.
10. Tanaka, M.; Leveque, J.; Tagami, H.; Kikuchi, K.; Chonan, S. The "haptic finger"—A new device for monitoring skin condition. *Skin Res. Technol.* **2003**, *9*, 131-136.

11. Mukaibo, Y.; Shirado, H.; Konyo, M.; Maeno, T. Development of a Texture Sensor Emulating the Tissue Structure and Perceptual Mechanism of Human Fingers. In *Proceedings of the 2005 IEEE International Conference on Robotics and Automation*, Barcelona, Spain, 18–22 April 2005; pp. 2565-2570.
12. Hosoda, K.; Tada, Y.; Asada, M. Anthropomorphic robotic soft fingertip with randomly distributed receptors. *Robot. Auton. Syst.* **2006**, *54*, 104-109.
13. Wettels, N.; Santos, V.; Johansson, R.; Loeb, G. Biomimetic tactile sensor array. *Adv. Rob.* **2008**, *22*, 829-849.
14. Beccai, L.; Roccella, S.; Arena, A.; Valvo, F.; Valdastri, P.; Menciassi, A.; Carrozza, M.C.; Dario, P. Design and fabrication of a hybrid silicon three-axial force sensor for biomechanical applications. *Sens. Actuat. A* **2005**, *120*, 370-382.
15. Edin, B.; Beccai, L.; Ascari, L.; Roccella, S.; Cabibihan, J.; Carrozza, M. Bio-Inspired Approach for the Design and Characterization of a Tactile Sensory System for a Cybernetic Prosthetic Hand. In *Proceedings of the 2006 IEEE International Conference on Robotics and Automation, ICRA 2006*, Orlando, FL, USA, 15–19 May 2006; pp. 1354-1358.
16. Beccai, L.; Roccella, S.; Ascari, L.; Valdastri, P.; Sieber, A.; Carrozza, M.; Dario, P. Development and experimental analysis of a soft compliant tactile microsensor for anthropomorphic artificial hand. *IEEE/ASME Trans. Mechatron.* **2008**, *13*, 158-168.
17. Vásárhelyi, G.; Adam, M.; Vazsonyi, E.; Vizvary, Z.; Kis, A.; Barsony, I.; Ducso, C. Characterization of an integrable single-crystalline 3-D tactile sensor. *IEEE Sens. J.* **2006**, *6*, 928-934.
18. Oddo, C.M.; Beccai, L.; Felder, M.; Giovacchini, F.; Carrozza, M.C. Artificial roughness encoding with a bio-inspired mems-based tactile sensor array. *Sensors* **2009**, *9*, 3161-3183.
19. Klatzky, R.; Lederman, S. Hand movements: A window into haptic object recognition. *Cognit. Psychol.* **1987**, *19*, 342-368.
20. Klatzky, R.; Lederman, S.; Pellegrino, J.; Doherty, S.; McClosky, B. Procedures for haptic object exploration *vs.* manipulation. In *Vision and Action: The Control of Grasping*; Goodale, M., Ed.; Ablex: New York, NY, USA, 1990; pp. 110-127.
21. Lederman, S.; Klatzky, R. Action for perception: Manual exploratory movements for haptically processing objects and their features. In *Hand and Brain: The Neurophysiology and Psychology of Hand Movements*; Academic Press: London, UK, 1996; pp. 431-446.
22. Yamada, D.; Maeno, T.; Yamada, Y. Artificial finger skin having ridges and distributed tactile sensors used for grasp force control. *J. Rob. Mechatronics* **2002**, *14*, 140-146.
23. Scheibert, J.; Leurent, S.; Prevost, A.; Debregeas, G. The role of fingerprints in the coding of tactile information probed with a biomimetic sensor. *Science* **2009**, *323*, 1503-1506.
24. Oddo, C.M.; Beccai, L.; Wessberg, J.; Wasling, H.B.; Mattioli, F.; Carrozza, M.C. Roughness encoding in human and biomimetic artificial touch: Spatiotemporal frequency modulation and structural anisotropy of fingerprints. *Sensors* **2011**, *11*, 5596-5615.
25. Wandersman, E.; Candelier, R.; Debregeas, G.; Prevost, A. Texture-induced modulations of friction force: The fingerprint effect. *Soft Condens. Matter* **2011**, arXiv:1107.2578v1.

26. Johansson, R. Tactile sensibility in human hand-receptive-field characteristics of mechanoreceptive units in glabrous skin area. *J. Physiol.* **1978**, *281*, 101-123.
27. Scheibert, J.; Prevost, A.; Debrégeas, G.; Katzav, E.; Adda-Bedia, M. Stress field at a sliding frictional contact: Experiments and calculations. *J. Mech. Phys. Solids* **2009**, *57*, 1921-1933.
28. Johnson, K.L. *Contact Mechanics*; Cambridge University Press: Cambridge, UK, 1985.
29. Fretigny, C.; Chateauminois, A. Solution for the elastic field in a layered medium under axisymmetric contact loading. *J. Phys. D* **2007**, *40*, 5418-5426.
30. Levesque, V.; Hayward, V. Experimental evidence of lateral skin strain during tactile exploration. In *Proceedings of Eurohaptics*, Dublin, Ireland, July 2003; pp. 261-275.
31. DiCarlo, J.J.; Johnson, K.O.; Hsiao, S.S. Structure of receptive fields in area 3b of primary somatosensory cortex in the alert monkey. *J. Neurosci.* **1998**, *18*, 2626-2645.
32. DiCarlo, J.J.; Johnson, K.O. Velocity invariance of receptive field structure in somatosensory cortical area 3b of the alert monkey. *J. Neurosci.* **1999**, *19*, 401-419.
33. DiCarlo, J.J.; Johnson, K.O. Spatial and temporal structure of receptive fields in primate somatosensory area 3b: Effects of stimulus scanning direction and orientation. *J. Neurosci.* **2000**, *20*, 495-510.

THEME 3 : MECANIQUE DU CONTACT ET PHYSIQUE DU FROTTEMENT

Résumé: Nous avons étudié la mécanique de contacts étendus élastomère rugueux/verre lisse en développant deux types de mesures pour mesurer les champs de contraintes/déplacements à l'interface. La première est basée sur l'utilisation du capteur MEMS précédemment décrit, tandis que l'autre se fonde sur l'imagerie de contact par corrélation d'images. Nous avons utilisé ces deux méthodes pour étudier la transition vers le glissement dans un contact sphère-plan. Cette transition s'accompagne d'un anneau de micro-glissements sur la périphérie du contact en accord qualitatif avec un modèle classique de mécanique du contact dérivé par Cattaneo et Mindlin. Des écarts à ce modèle subsistent cependant, que l'on peut relier aux propriétés de complaisance de la couche rugueuse. Récemment, nous avons étudié le frottement de surfaces micro-texturées constituées d'un grand nombre de micro-aspérités sphériques distribuées aléatoirement spatialement et en hauteur. En configuration de contact plan-plan, nous avons mis en évidence l'existence de fronts de glissement quasi-statiques qui se propagent normalement aux lignes d'isopression. En configuration sphère-plan, nous avons caractérisé la dépendance d'aire réelle de contact et des champs de pressions locales avec la charge normale appliquée. Nous avons comparé nos mesures avec deux modèles de mécanique du contact multi-aspérités. Nous avons ainsi validé pour la première fois expérimentalement ces deux modèles.

Le frottement entre deux surfaces solides met en jeu des échelles spatiales qui vont de la taille moléculaire à celle du contact macroscopique formé. Les contraintes macroscopiques sont contrôlées par la géométrie des objets en contact d'une part, tandis que les processus dissipatifs sont généralement confinés dans les premières couches moléculaires en contact d'autre part. La plupart des surfaces naturelles sont cependant rugueuses à des échelles intermédiaires que l'on ne peut pas ignorer, de l'ordre du micromètre. L'interface entre deux de ces surfaces est alors constituée d'un grand nombre de microcontacts isolés qui supportent l'ensemble de la charge appliquée. Cette couche d'épaisseur micrométrique possède des caractéristiques mécaniques qui sont déterminées par les propriétés statistiques des aspérités, comme la distribution des hauteurs de leurs sommets. Bien que d'épaisseur très faible, la réponse mécanique de cette couche sous sollicitation normale ou tangentielle, est déterminante pour l'établissement des contraintes mécaniques entre deux solides rugueux en contact statique ou frottant. Une description complète des mécanismes de frottement ne peut donc s'affranchir des effets à cette échelle mésoscopique.

Je me suis intéressé à la réponse mécanique de telles interfaces dans des régimes transitoires (mise en glissement) et des régimes de frottement stationnaires. Nous avons utilisé des surfaces planes d'élastomère rugueux au contact de verre lisse dans différentes géométries de contact (sphère-plan, cylindre-plan, et plan-plan). Le type d'élastomère sur lequel nous nous sommes concentrés étant relativement mou (module d'Young de quelques MPa), il est possible de mesurer les contraintes/déformations élastiques induites par le contact, à la fois à l'interface de frottement mais également en volume. Pour mesurer les contraintes/déformations sous le contact, nous avons mis à profit le capteur MEMS décrit dans la partie précédente et utilisé pour l'étude de la perception tactile digitale humaine. Nous avons également développé des méthodes d'imagerie de contact non-invasive, basée sur la corrélation d'images. Ces méthodes ont permis de mesurer avec une résolution spatiale bien inférieure à la taille du contact, les champs des déplacements à l'interface du contact, et d'en déduire ceux des contraintes par inversion.

Plus récemment, nous avons utilisé les avancées en termes de micro-usinage pour fabriquer des surfaces rugueuses modèles dont les caractéristiques topographiques sont proches de celles utilisées dans le cadre du modèle séminal de contact multi-aspérités de

Greenwood et Williamson[5]. Nous avons montré qu'avec de telles surfaces, il était possible, non seulement de mesurer optiquement les champs de déplacements à l'interface de contact, mais aussi la distribution des aires des microcontacts que l'on peut directement relier à la pression locale dans le contact. Ce type de surfaces a permis une comparaison directe à quelques modèles de contact multi-aspérités existants, largement utilisés sans que leur validité n'ait été directement testée expérimentalement. La raison tient notamment à la difficulté de mesurer l'aire de contact réelle pour des surfaces présentant une rugosité multi-échelles.

A. Mesures des contraintes sous le contact

Nous avons développé un dispositif de mesure MEMS, analogue à celui utilisé pour étudier les mécanismes de transduction mécanique de l'information tactile (Thème 2), en substituant au film d'élastomère sphérique un film plan rugueux. Sa rugosité de surface *rms*, d'environ 1.8 µm, a été obtenue par moulage contre une surface de Plexiglas rodée. Un unique capteur MEMS de première génération a été placé au centre du film (50x50 mm²) et à une profondeur de 2 mm sous la surface du film rugueux **(Fig. 10a)**.

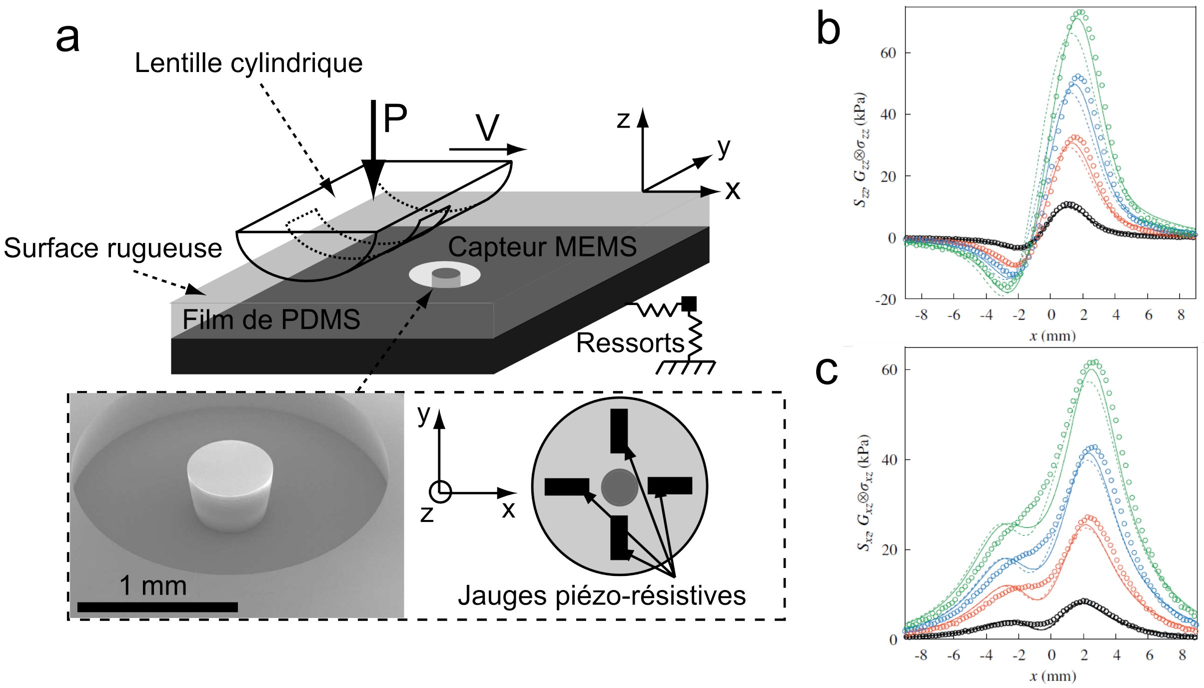

Figure 10 – (a) *Schéma de principe du dispositif expérimental, montré ici pour le cas d'un contact cylindre-plan en glissement stationnaire. Le cylindre a un rayon de courbure de 129 mm. Les substrats de verre frottés sont des lamelles de microscope collées à ce cylindre (traits pointillés). La photo est un détail de la partie sensible du capteur MEMS. Les déformations de la membrane sont enregistrées à l'aide de jauges piezo-résistives.* **(b)** *Contraintes normales à V=1mm/s, le long de y=0 pour P=0.34 N (noir), 1.03 N (rouge), 1.72 N (bleu), 2.75 N (vert), mesurées (cercles), calculées avec le modèle exact (lignes continues), calculées avec le modèle Goodman (lignes pointillées).* **(c)** *Contraintes tangentielles.*

Nous avons d'abord considéré le contact statique (sans aucun déplacement relatif) entre une *sphère* de verre lisse et ce dispositif, pour différentes charges normales *P* **[1]**. Pour le contact sphère-plan obtenu, nous avons mesuré les profils spatiaux des contraintes

---

[5] J. Greenwood and J. Williamson, *Proc. Royal Society of London. Series A* **295**, 300-319 (1966).

normales en indentant le film d'élastomère en différentes positions et en enregistrant la réponse du capteur MEMS. Nous avons ainsi mis en évidence que les profils mesurés présentaient des écarts significatifs à ceux calculés numériquement, par éléments finis et en supposant une loi de frottement de type Amontons-Coulomb. Cette loi stipule qu'un glissement irréversible doit se produire dès lors que le rapport entre la contrainte tangentielle et normale excède un coefficient de frottement supposé uniforme. Ces déviations se sont avérées être d'autant plus importantes que la charge normale imposée était faible. Nous avons également montré qu'elles disparaissaient complétement quand l'interface de contact était lubrifiée. Ces observations ont pu être interprétées comme la conséquence directe de la complaisance finie de la couche rugueuse **[1]**.

Nous avons ensuite considéré le cas d'un contact *cylindre*-plan en régime stationnaire de frottement **(Fig. 10a)**, obtenu en déplaçant à vitesse constante V un cylindre contre le dispositif MEMS **[2]**. Nous avons ainsi mesuré le champ des contraintes normales **(Fig. 10b)** et tangentielles **(Fig. 10c)** pour différentes charges normales P. En choisissant cette géométrie de contact, nous avons pu comparer quantitativement nos mesures aux prédictions d'un modèle que nous développé en collaboration avec E. Katzav et M. Adda-Bedia (LPS-ENS). Ce modèle quasi-statique, bidimensionnel et semi-analytique est exact, et permet d'obtenir les champs de contraintes (à l'interface et en volume) en régime de glissement stationnaire, pour un contact entre un cylindre et un film élastique d'épaisseur finie reposant sur une paroi rigide. Il fait l'hypothèse d'une loi de frottement locale de type Amontons-Coulomb (*i.e.* les contraintes tangentielle et normale à l'interface sont proportionnelles, avec un coefficient de frottement indépendant de la pression locale). Enfin, il s'affranchit de l'hypothèse classique de Goodman qui consiste à supposer que le champ des contraintes normales est inchangé en situation de glissement stationnaire.

Nous avons ainsi mis en évidence des écarts entre les profils de contraintes (normale et tangentielle) mesurés et ceux calculés, inférieurs à 14% sur toute la gamme de charge normale étudiée **(Figs. 10b-10c)**. Nous avons de plus comparé les profils mesurés et ceux calculés avec le modèle exact aux résultats d'un deuxième modèle qui fait l'hypothèse de Goodman. Cette comparaison montre que le modèle exact reproduit mieux les données d'autant mieux que la charge normale P est élevée. Aucun des deux modèles ne reproduit cependant complétement les profils mesurés, ce qui nous a amené à revoir la validité de deux hypothèses utilisées pour les calculs, à savoir *(i)* celle d'une interface lisse, et *(ii)* celle d'un coefficient de frottement indépendant de la pression locale. Ceci nous a conduit à proposer une fois de plus que ces observations traduisaient un effet de complaisance de la couche rugueuse d'épaisseur micrométrique **[2]**.

B. Mesures des contraintes à l'interface – Imagerie de contact

Les méthodes que nous avons développées avec le capteur MEMS ont permis d'obtenir une mesure directe des contraintes locales à des échelles spatiales inférieures à la taille du contact. Elles sont cependant strictement limitées à des mesures sous le contact, là où se trouve implanté le capteur MEMS (dans notre cas, environ 2 mm sous l'interface), et ne permettent d'avoir une information sur la nature des contraintes à l'interface qu'au prix de complexes procédures de déconvolution du signal mesuré. Il faut en effet tenir compte non-seulement de la fonction d'appareil intrinsèque des capteurs de force, mais aussi d'effets de taille finie (épaisseur finie du film d'élastomère) qui rendent difficile la comparaison directe avec les modèles mécaniques usuels qui considèrent le plus souvent un milieu déformable semi-infini au contact d'un indenteur.

Nous avons donc développé des techniques d'imagerie du contact, qui permettent de s'affranchir de ces difficultés tout en offrant une mesure spatialement résolue des champs de déplacements à l'interface entre une surface rugueuse à des échelles microscopiques et une surface rigide de verre. En combinant ces mesures avec des méthodes d'inversion des champs de déplacements, il devient possible d'extraire les champs de contraintes à l'interface.

Contrairement aux méthodes de marquage traditionnellement utilisées pour des élastomères lisses (notamment développées par A. Chateauminois et C. Frétigny au Laboratoire SIMM-ESPCI et dont une brève description est donnée plus bas en Section D), la méthode que nous avons développée est exclusivement adaptée à des interfaces multi-contacts et permet une mesure non-invasive puisque les micro-aspérités sont des marqueurs naturellement présents à la surface. Le PDMS Sylgard 184 étant un élastomère transparent, il est possible d'éclairer l'interface de contact en transmission. On obtient alors des images de l'interface comme celle de la **Fig. 11a-b** dont il est possible d'extraire par corrélation d'images **(Figs. 11c-11d)**, les champs de déplacements à la fois dans le contact et hors du contact. Avec le grandissement utilisé pour visualiser des contacts circulaires de diamètre maximal plusieurs millimètres, nous avons pu mesurer les champs de déplacements 2D (u_x, u_y) avec une résolution spatiale d'environ 140 µm (déterminée par la taille de la boite de corrélation) et une résolution sur les déplacements d'environ 230 nm.

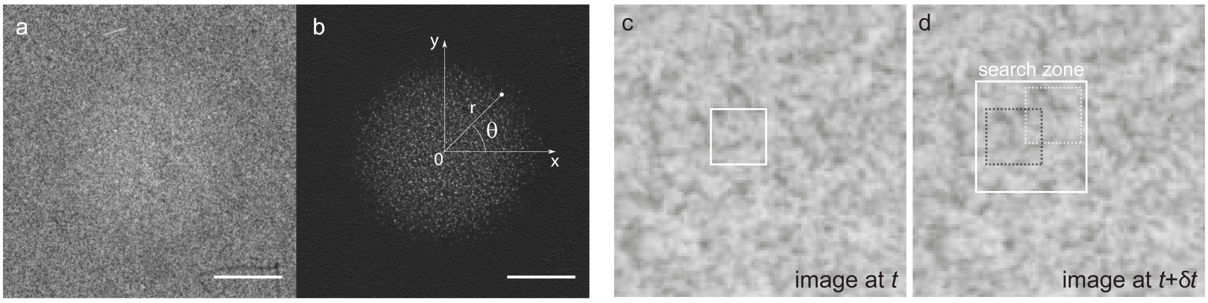

Figure 11 – (a) *Image de l'interface entre une sphère et un plan rugueux de PDMS, éclairée en transmission* $(P = 1\ N)$. **(b)** *Différence entre l'image (a) et une image hors-contact. La barre blanche correspond à 1 mm de long.* **(c)-(d)** *Principe de la corrélation d'images pour mesurer les champs de déplacements. On cherche dans l'image (d), la boite carrée qui corrélée avec celle dans l'image (c) maximise la fonction de corrélation. La localisation du maximum de la fonction de corrélation 2D donne le déplacement* (u_x, u_y).

Nous avons utilisé cette méthode pour étudier la mise en glissement d'un solide sur une piste. Dans la description classique d'Amontons-Coulomb, quand deux solides sont mis en contact sous charge normale P et soumis à une force de cisaillement Q, aucun mouvement relatif ne se produit tant que $Q < \mu_S P$, où μ_S est le coefficient de frottement statique. Cependant, pour la plupart des situations réelles, la transition statique-dynamique est loin d'obéir à ce scénario très simple et ceci d'autant plus que la plupart des interfaces de solides usuels en contact est de type multi-contacts. Dès que $Q > 0$, un glissement partiel se produit à cause des contraintes hétérogènes qui existent au sein du contact et qui résultent de la géométrie des solides en contact ainsi que des conditions de chargement de l'interface de frottement. Au cours des dix dernières années, un nombre croissant de travaux expérimentaux[6], notamment ceux du groupe de J. Fineberg (Hebrew University of Jerusalem, Israël), et théoriques[7] a été consacré au sujet. J. Fineberg et son équipe ont étudié les modifications d'aire réelle de contact d'une interface multi-contacts formée entre deux blocs de Plexiglas rodés à des échelles microscopiques et soumise à un chargement adiabatique latéral. L'aire réelle est déduite de la quantité d'intensité lumineuse transmise à travers l'interface qui est éclairée avec une nappe laser évanescente. Quant à ses variations temporelles, elles sont enregistrées avec une caméra rapide. J. Fineberg et ses coauteurs ont ainsi mis en évidence que la transition statique-dynamique s'accompagnait de modifications discrètes de l'aire réelle de contact bien avant le seuil macroscopique de glissement et que ces modifications résultaient de la propagation de fronts de rupture dynamiques subsoniques à supersoniques. En utilisant des jauges de contraintes placées au-dessus de l'interface de frottement, ces auteurs ont également mis en évidence une corrélation possible entre l'extension des modifications d'aire de contact et le paysage des contraintes proches de l'interface.

Dans l'article donné en référence **[3]**, nous avons cherché à caractériser cette transition de frottement statique-dynamique, pour le cas d'une sphère de verre lisse chargée linéairement de façon adiabatique contre un plan rugueux microscopique de PDMS, en utilisant la méthode de corrélation d'images décrite plus haut. Pour différentes conditions (vitesse de charge, charge normale appliquée, différentes rugosités *rms* de l'élastomère), nous avons mesuré les déplacements longitudinaux u_x (dans la direction de la charge tangentielle), et transverses u_y. Pour un milieu élastique incompressible et semi-infini, les déplacements verticaux et latéraux sont découplés et le déplacement (u_x, u_y) peut alors s'écrire comme la convolution du tenseur de Green (réponse en termes de déplacements à une force localisée en surface) et du champ des contraintes à l'interface. Nous avons utilisé une procédure itérative numérique de Van-Cittert initialement développée par A. Chateauminois et C. Frétigny (SIMM-ESPCI), pour extraire les champs de contraintes, à la fois pendant la phase de charge initiale et en régime de frottement stationnaire.

---

[6] S.M. Rubinstein, J. Fineberg, *Nature (London)* **430**, 1005 (2004) ; S.M. Rubinstein, G. Cohen, J. Fineberg, *Phys. Rev. Lett.* **98**, 226103 (2007) ; O. Ben-David, S. M. Rubinstein, J. Fineberg, *Nature (London)* **463**, 76 (2010) ; O. Ben-David, J. Fineberg, *Phys. Rev. Lett.* **106**, 254301 (2011).

[7] O.M. Braun, I. Barel, M. Urbakh, *Phys. Rev. Lett.* **103**, 194301 (2009) ; J. Scheibert, D.K. Dysthe, *Europhys. Lett.* **92**, 54001 (2010) ; J. Trømborg, J. Scheibert, D. S. Amundsen, K. Thogersen, A. Malthe-Sorenssen, *Phys. Rev. Lett.* **107**, 074301 (2011) ; E. Bouchbinder, E.A. Brener, I. Barel, M. Urbakh, *Phys. Rev. Lett.* **107**, 235501 (2011) ; D.S. Amundsen, J. Scheibert, K. Thøgersen, J. Trømborg, A. Malthe-Sørenssen, *Tribol. Lett.* **45**, 357 (2012) ; Y. Bar-Sinai, R. Spatschek, E.A. Brener, E. Bouchbinder, *Phys. Rev. E* **88**, 060403(R) (2013).

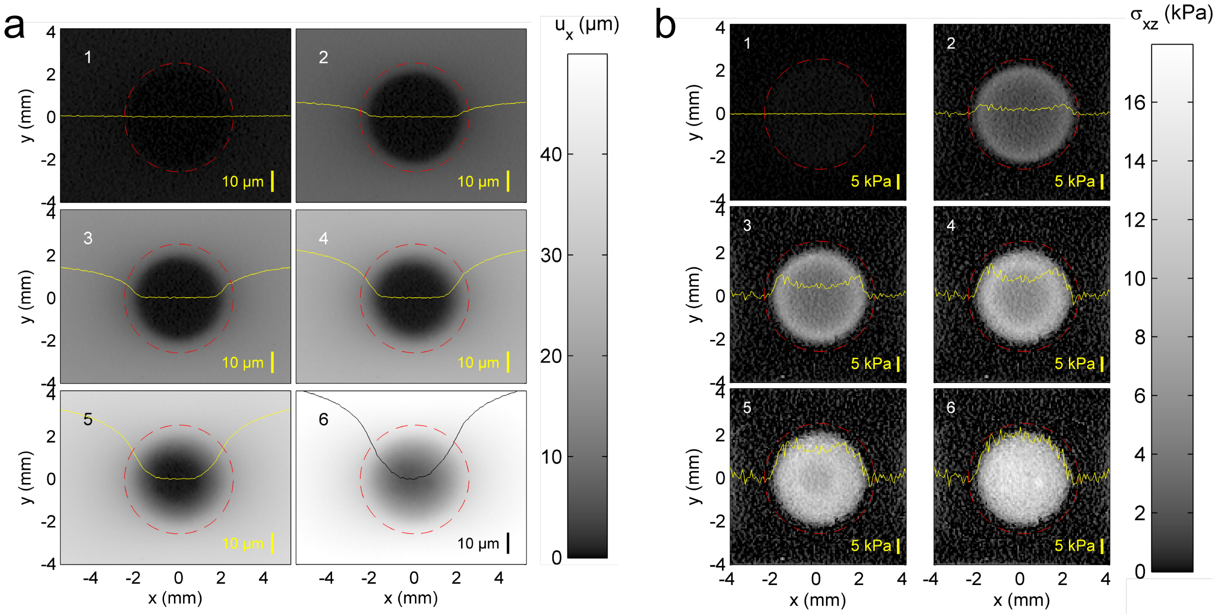

Figure 12 – (a) *Champs de déplacements u_x dans la direction du mouvement pour 6 valeurs croissantes de la force tangentielle (vignettes 1 à 6 ; vignette 1, $Q = 0\ N$, et vignette 6, $Q \sim 0.5\ N$ au seuil de glissement) sous une charge normale constante $P = 0.5\ N$ et à vitesse de charge $V = 5\ \mu m/s$. Les cercles en pointillés rouges délimitent la zone de contact apparente. Une coupe $u_x(x, y = 0)$ est représentée en jaune sur les vignettes 1 à 5, et en noir sur la vignette 6.* **(b)** *Champs de contraintes σ_{xz} correspondants obtenus par inversion des champs u_x et u_y par la méthode de Green. Les profils en jaune sont des coupes le long de $y = 0$.*

Nous avons ainsi mis en évidence l'existence d'une région annulaire de micro-glissement qui envahit progressivement le contact quand la charge tangentielle appliquée augmente, en accord quasi-quantitatif avec le modèle classique de Cattaneo et de Mindlin[8] (CM), aussi bien sur les champs de déplacement **(Fig. 12a)** que sur les champs de contraintes **(Fig. 12b)**. Pour calculer les champs de contraintes/déplacements, CM fait l'hypothèse que *(i)* les deux surfaces en regard sont lisses, *(ii)* le champ de pression interfacial est inchangé lors de la mise en charge et est de type Hertz, et *(iii)* la loi de frottement d'Amontons-Coulomb est valable localement, *i.e.* que le glissement ne se produit que quand la contrainte de cisaillement σ_{xz} est égale à $\mu\sigma_{zz}$ où μ est le coefficient de frottement macroscopique. CM prédit ainsi que le rayon de la zone circulaire centrale collée c évolue, sous charge normale P, avec la charge tangentielle appliquée Q selon la loi suivante

$$\frac{c}{a_H} = \left(1 - \frac{Q}{\mu P}\right)^{1/3} \quad (3)$$

où a_H est le rayon du contact de Hertz. Pour nos expériences, nous avons établi que cette relation restait vraie au premier ordre.

Une comparaison fine entre les mesures et le modèle de CM a cependant révélé des écarts significatifs, qui se traduisent par l'existence d'un déplacement u_x non-nul au centre du contact dès que la charge appliquée $Q > 0$, en contradiction avec l'hypothèse d'une loi d'Amontons-Coulomb locale. L'explication la plus probable tient au fait que les déplacements mesurés avec la méthode de corrélation d'images sont moyennés sur l'épaisseur de la couche

---

[8] C. Cattaneo, *Rend. Accad. Naz. Lincei* **27**, 214 (1938) ; R.D. Mindlin, *Trans. ASME, Ser. E, J. Appl. Mech.* **16**, 259 (1949) ; Voir aussi le livre de K.L. Johnson, Contact Mechanics (Cambridge University Press, 2003), pages 216-220.

rugueuse et intègrent donc à la fois le glissement du sommet des micro-aspérités et leur déformation élastique latérale. Cette constatation nous a permis d'extraire une loi de frottement locale reliant contraintes tangentielles et normales qui diffère de la loi rigide-plastique supposée dans le modèle de CM **(Fig. 13)**.

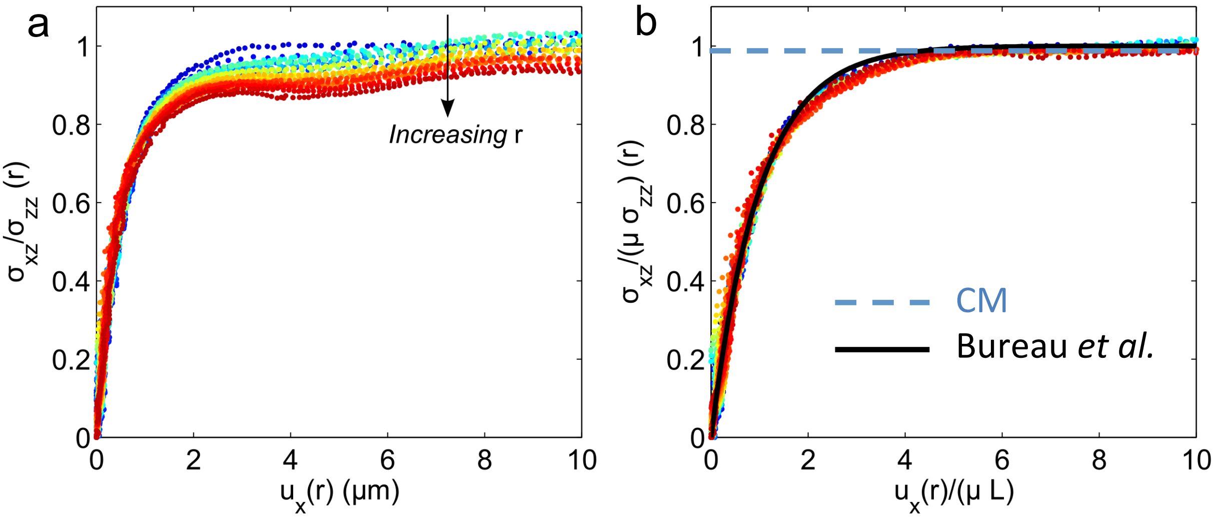

Figure 13 – (a) *Loi de frottement locale* σ_{xz}/σ_{zz} *versus* u_x *pour différentes positions dans le contact circulaire en partant du centre* $(r = 0)$ *et pour* r *croissant vers la périphérie du contact. Les champs* u_x*, et* σ_{xz} *sont moyennés angulairement à partir des champs 2D de la Fig. 12. Le champ* $\sigma_{zz}(r)$*, non-mesuré, est donné par le modèle de Hertz.* **(b)** *Une fois « rescalées », les données suivent une loi maîtresse avec une dépendance exponentielle faisant intervenir un coefficient de frottement local* μ *et une longueur* $L \sim 0.8$ *µm directement reliée à la rugosité de la surface de l'élastomère utilisé, en très bon accord avec les prédictions du modèle de Bureau et al. Ceci démontre l'existence d'une loi de frottement locale de type élasto-plastique et non pas rigide-plastique comme utilisée dans le modèle CM (ligne pointillée bleue).*

Cette loi constitutive locale est en effet de type élasto-plastique et fait intervenir une échelle de longueur caractéristique liée à la rugosité de la couche, en accord avec les prédictions d'un modèle développé par Bureau *et al.*[9], pour analyser la réponse macroscopique en cisaillement d'une interface plane multi-contact, chargée uniformément.

L'interface rugueuse y est modélisée par le contact entre deux surfaces planes, dont l'une est lisse et indéformable, et dont l'autre présente une topographie rugueuse décrite par le modèle de Greenwood-Williamson (GW). Ce modèle classique de mécanique du contact multi-aspérités considère que les micro-aspérités sont élastiquement indépendantes les unes des autres, ont toutes le même rayon de courbure au sommet, et obéissent à un contact Hertzien. De plus, les hauteurs z de leurs sommets sont distribuées aléatoirement selon une loi $\psi(z)$. Le modèle de GW permet de décrire statistiquement la réponse macroscopique de l'interface sous charge normale, et de prédire, pour une indentation donnée, le nombre total de microcontacts, l'aire réelle de contact et la charge normale totale portée par les micro-aspérités. Pour décrire la réponse macroscopique sous charge tangentielle, Bureau *et al.* ont étendu le modèle de GW en faisant l'hypothèse que chacune des micro-aspérités obéissait localement au modèle de CM. Ils prédisent ainsi une relation qui donne l'évolution du rapport entre les charges tangentielle Q et normale P (intégrées sur tout le contact), avec le déplacement relatif des deux solides en contact. C'est précisément cette relation que nous

---

[9] L. Bureau, C. Caroli, T. Baumberger, *Proc. R. Soc. London, Ser. A* **459**, 2787 (2003).

avons étendue et validée à des échelles spatiales mésoscopiques **[3]**, en considérant le rapport des contraintes locales de cisaillement et de pression **(Fig. 13b)**.

C. Surfaces micro-texturées

J'ai récemment étendu mes travaux sur le frottement solide multi-contacts en développant des interfaces multi-contacts contrôlées à des échelles mésoscopiques et permettant une mesure simultanée des forces normales et tangentielles qui s'exercent sur chacune des aspérités en contact. Ce travail a impliqué un chercheur postdoctoral (V. Romero (ANR DYNALO) ainsi qu'E. Wandersman (Maître de Conférences, Université Paris 6).

Nous avons tiré parti des avancées récentes en micro-usinage pour réaliser par moulage des surfaces d'élastomère de PDMS constituées de quelques milliers d'aspérités sphériques de rayon de courbure constant déterminé par le rayon de la fraise boule utilisée, et dont les distributions spatiales et de hauteurs peuvent être contrôlées à souhait. Nous avons ainsi réalisé différents types de surfaces allant du motif régulier[10] au motif aléatoire[11] (**Fig. 14a** pour un exemple de motif aléatoire).

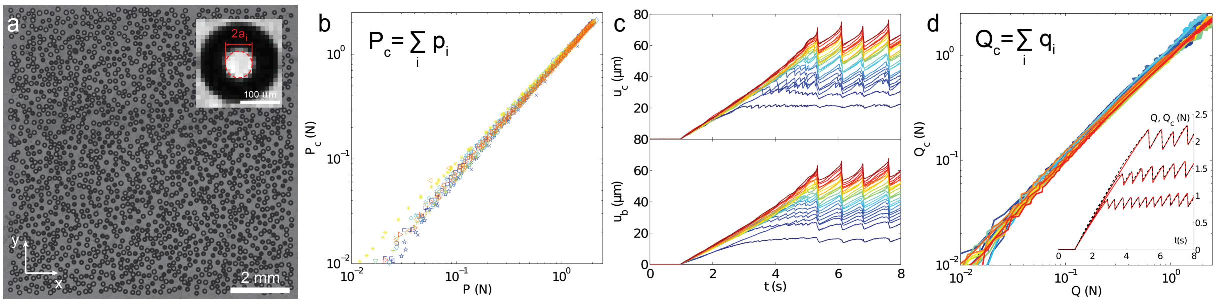

Figure 14 – (a) *Image en transmission d'un contact entre un plan lisse de verre et un substrat aléatoire (rayon de courbure des aspérités 100 µm, densité surfacique 0.4) sous charge normale* $P = 2\ N$*. Pour chaque aspérité #i en contact, on observe un disque blanc (insert) dont le diamètre* $2a_i$ *donne directement accès à la force normale* p_i *exercée sur son sommet, en supposant un modèle de Hertz.* **(b)** *Force normale totale calculée* P_c*, obtenue en sommant les* p_i *sur toutes les aspérités, versus P. Chaque couleur correspond à un type de réseau différent.* **(c)** *Déplacement des centres de 23 microcontacts choisis arbitrairement (haut) et de la « back-layer » (bas). Les forces normales* p_i *augmentent du bleu au rouge.* **(d)** *Force tangentielle calculée* Q_c *obtenue en sommant les forces tangentielles locales* q_i *obtenues en supposant un modèle de raideur de contact. Chaque couleur correspond à un réseau différent. Insert :* $Q_c(t)$ *(line brisée noire) et* $Q(t)$ *(line continue rouge) pour* $P = 0.5, 1, 2\ N$ *(vitesse d'entraînement 80 µm/s).*

Depuis quelques années, un certain nombre de travaux ont été consacrés aux propriétés adhésives et frictionnelles de surfaces texturées, notamment dans le but de mieux comprendre « l'effet Gecko », ou encore de mettre au point des surfaces aux caractéristiques

---

[10] Il s'agit d'un réseau hexagonal d'aspérités dont les hauteurs sont soit constantes, soit aléatoirement choisies au sein d'une distribution uniforme.

[11] Les centres des aspérités sont distribuées spatialement aléatoirement avec une distribution uniforme et de façon à ce qu'aucune aspérité ne recouvre ses voisines. Pour les expériences réalisées, les hauteurs d'aspérités ont été choisies soit constantes, soit tirées aléatoirement au sein d'une distribution uniforme.

frictionnelles contrôlées. Pour fabriquer de telles surfaces, on a le plus souvent recours à la photolithographie qui ne permet de réaliser qu'un nombre restreint de topographies, comme par exemple des assemblées de piliers cylindriques. S'il est possible de suivre les déformations latérales de ces piliers (sous charge normale modérée au dessous de laquelle les piliers ne flambent pas), et d'en déduire la force latérale qui s'exerce sur chaque pilier sous cisaillement, il est en revanche beaucoup plus difficile d'extraire la force normale qui s'exerce sur chacun d'entre eux.

Un des avantages à utiliser des aspérités sphériques est qu'il devient possible de mesurer cette force normale. En effet, au contact d'une surface de verre lisse, chaque micro-aspérité forme un contact circulaire, que l'on peut imager en lumière transmise. Et sa taille est directement reliée à la force normale appliquée.

Avec les surfaces que nous avons développées, nous avons montré que, moyennant calibration et en supposant un microcontact de Hertz, il était possible d'obtenir une mesure des forces normales sur chaque aspérité **(Fig. 14a)**. Nous avons vérifié *a posteriori* que l'hypothèse d'un contact de Hertz était justifiée en comparant la somme de ces forces locales normales à la charge normale totale mesurée indépendamment **(Fig. 14b)**. Nous avons également montré qu'il était possible, en suivant optiquement le centre des micro zones de contact **(Fig. 14c)**, d'extraire les forces latérales de contact s'exerçant sur les aspérités, quand l'interface rugueuse est soumise à un déplacement macroscopique. Comme pour les forces normales, nous avons également vérifié que la somme des forces locales de cisaillement était égale à la force de cisaillement totale mesurée indépendamment **(Fig. 14d)**.

Nous avons donc mis au point des surfaces d'élastomère qui sont intéressantes à deux titres. D'une part, étant composées d'aspérités sphériques, ce surfaces permettent une mesure simultanée des forces normales et tangentielles locales qui s'appliquent sur chaque aspérité. D'autre part, elles constituent une première réalisation expérimentale contrôlée des surfaces traditionnellement utilisées dans les modèles de contact multi-aspérités (modèle de Greenwood-Williamson, Greenwood-Tripp[12], etc.) En ce sens, elles offrent la possibilité de tester finement ces modèles de mécanique du contact.

Autour de cet unique système, nous avons étudié successivement deux problématiques. La première est celle de la transition statique-dynamique dans un multi-contact plan-plan dans la continuité des travaux expérimentaux du groupe de J. Fineberg et des études théoriques et numériques associées **[4]**. La seconde est plus centrée sur l'effet des interactions élastiques entre aspérités en géométrie sphère-plan **[5]**.

- *Transition statique-dynamique dans un multi-contact plan-plan* **[4]**

Pour ce travail récent **[4]**, nous nous sommes limités à la topographie la plus simple, celle d'un réseau hexagonal d'aspérités de même hauteur et de rayon de courbure constant égal à 100 μm. Pour toutes les vitesses d'entraînement testées et accessibles expérimentalement, on observe d'abord une phase de charge transitoire suivie d'un régime de stick-slip. Durant la phase transitoire, nous avons observé l'existence de fronts précurseurs de glissement analogues à ceux observés par F. Fineberg et ses collaborateurs. Ces fronts lents démarrent des bords des contacts, parcourent une distance l inférieure à la taille du contact et s'arrêtent. Quelques instants plus tard dans la charge, un nouveau front se propage, démarrant toujours des bords et s'arrêtant au bout d'une distance l plus grande. Le processus se répète

---

[12] J.A. Greenwood, J.H. Tripp, *Trans. ASME, Ser. E, J. Appl. Mech.* **34**, 153 (1967).

jusqu'à ce qu'un front envahisse tout le contact. En régime de stick-slip, les fronts de glissement sont de nature différente et se propagent continûment des bords du contact jusqu'au centre[13]. Nous n'avons pas encore étudié en détail la phase transitoire initiale et avons préféré nous concentrer d'abord sur les propriétés des fronts de glissement en régime de stick-slip **[4]**.

Ces fronts, que l'on peut visualiser aisément sur la distribution spatiale des vitesses instantanées (obtenues en dérivant temporellement les déplacements des microcontacts), séparent une région centrale collée d'une région périphérique qui a glissé **(Figs. 15a-c)**. Nos mesures mettent également en évidence la présence de fronts secondaires si l'interface a eu le temps de recoller après le passage du premier front **(Figs. 15b-15c)**. Avec des mesures en caméra rapide, nous avons caractérisé la dynamique de propagation de ces fronts et avons montré qu'ils étaient quasi-statiques jusqu'à des temps relativement proches de l'instant de slip macroscopique. Très proche du seuil macroscopique de glissement, nos mesures semblent cependant indiquer que ces fronts deviennent dynamiques, possiblement en accord avec des prédictions théoriques très récentes[14]. Comme il est possible avec notre système de mesurer le champ des forces normales locales, nous avons également constaté qu'en moyenne, ces fronts se propageaient normalement aux lignes d'iso-pression.

Pour mieux comprendre la dépendance de la zone collée c en fonction du temps, nous avons développé un modèle quasi-statique simple unidimensionnel qui tient compte du paysage de pression locale, permet de reproduire qualitativement les données expérimentales et donne un critère simple pour les conditions d'apparition des fronts secondaires. Le système est modélisé par une ligne d'aspérités élastiquement indépendantes et également espacées le long d'un axe. Chaque aspérité chargée tangentiellement se met à glisser quand son déplacement atteint un déplacement maximal dont la valeur est définie par un critère d'Amontons-Coulomb. Dans ce cadre, la position du front et donc la taille de la zone collée c est entièrement déterminée par la position de la dernière aspérité qui a glissé. En l'absence de gradient de pression, toutes les aspérités glissent donc au même moment et aucun front n'existe. En revanche, en présence d'un gradient de pression, un front se propage normalement aux lignes d'isopression. Pour une distribution de pression parabolique comme dans l'expérience, la position du front peut être déterminée analytiquement. Nous avons ainsi montré que, proche du seuil de glissement t_S

$$c \propto (t_s - t)^{1/2} \quad (4)$$

en accord qualitatif avec nos mesures.

---

[13] A noter une différence notable entre nos expériences et celles du groupe de J. Fineberg. Dans nos expériences, les fronts se propagent transversalement à la direction de cisaillement. Chez Fineberg *et al.*, les fronts se propagent systématiquement le long de la direction de cisaillement.

[14] Y. Bar-Sinai, R. Spatschek, E.A. Brener, E. Bouchbinder, *Phys. Rev. E* **88**, 060403(R) (2013).

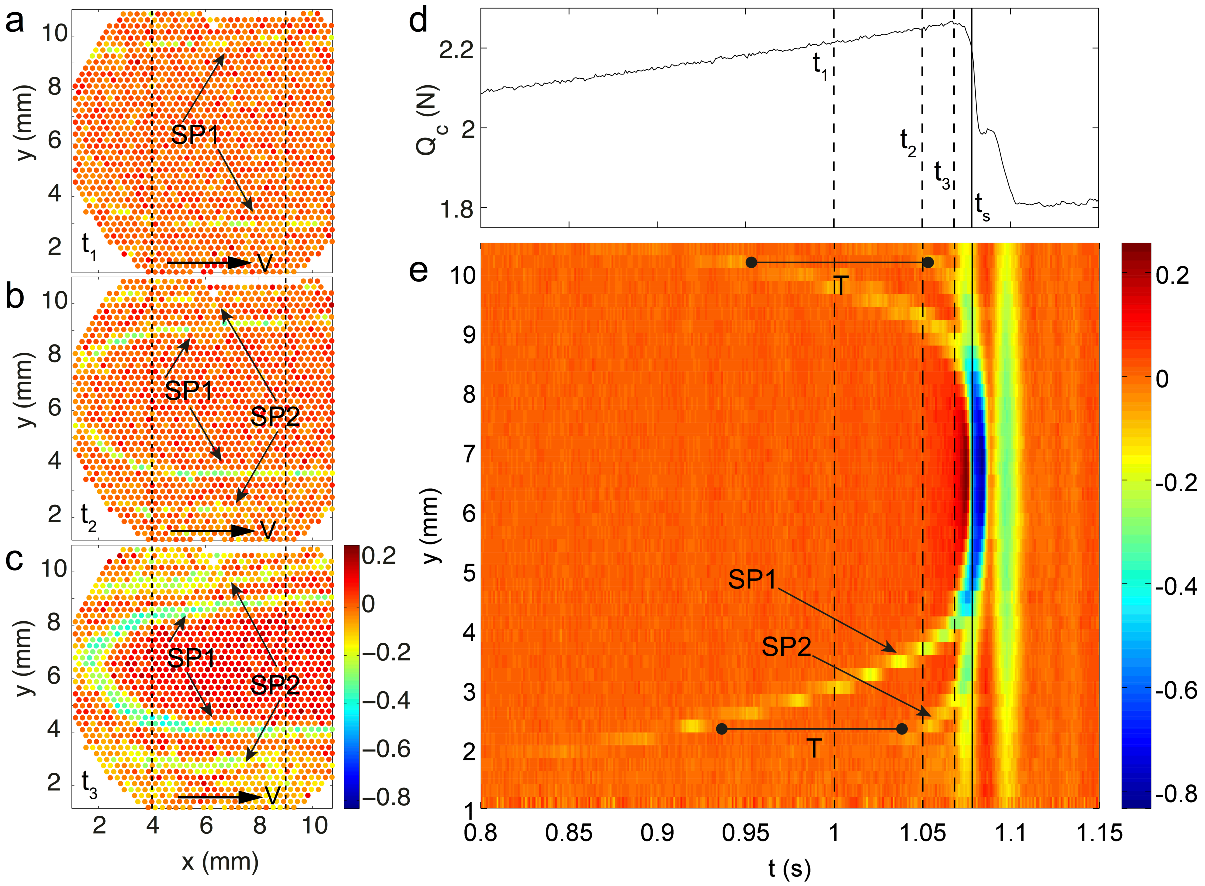

Figure 15 – (a-b-c) *Champs des vitesses instantanées des aspérités obtenus aux temps* t_1, t_2, t_3 *du panel* **(d)** *qui représente la dépendance temporelle de la force tangentielle calculée* $Q_c(t)$. *On observe la propagation d'un premier front noté SP1, suivi d'un second front noté SP2* $(P = 2.36\ N, V = 50\ \mu m/s)$. **(e)** *Diagramme spatio-temporel du champ de vitesse le long de y moyenné pour* $4\ mm < x < 9\ mm$. *Les vitesses sont données en* mm/s *et T correspond au retard initial entre SP1 et SP2.*

L'idée que la direction de propagation des fronts de glissement puisse être dictée par les gradients de pression à l'interface de frottement n'a jamais clairement été évoquée dans les travaux de l'équipe de J. Fineberg. A ce titre, notre système pourrait permettre de sonder plus en détail ces différents aspects.

- *Interactions élastiques entre aspérités dans un contact sphère-plan* **[5]**

Dans un deuxième temps, nous avons utilisé les surfaces à micro-aspérités sphériques en géométrie sphère-plan **[5]**. Nous avons utilisé pour cela deux types de surfaces, de densité surfacique d'aspérités, respectivement 0.1 et 0.4, et consistant en des assemblées de calottes sphériques $(R = 100\ \mu m)$ dont les hauteurs sont distribuées uniformément entre $30\ \mu m$ et $60\ \mu m$. Nous avons caractérisé la dépendance de l'aire de contact réelle fonction de la charge normale appliquée, ainsi que la distribution spatiale des microcontacts.

L'aire de contact réelle obtenue en sommant les contributions individuelles des microcontacts varie quasi-linéairement avec la charge normale (loi de puissance d'exposant 0.94 ± 0.01) en accord avec les modèles théoriques et les développements asymptotiques aux très faibles charges normales, qui prédisent une relation linéaire. Nous avons cependant montré que les écarts à la linéarité sont d'autant plus importants que le rayon de courbure de l'indenteur sphérique diminue. Cela traduit simplement le fait que l'augmentation de l'aire réelle de contact lors d'un incrément de charge normale est essentiellement due à une augmentation du nombre des microcontacts en périphérie du contact et non d'un accroissement de l'aire des microcontacts existants ou de nouveaux microcontacts au sein du contact **(Figs. 16a-c)**.

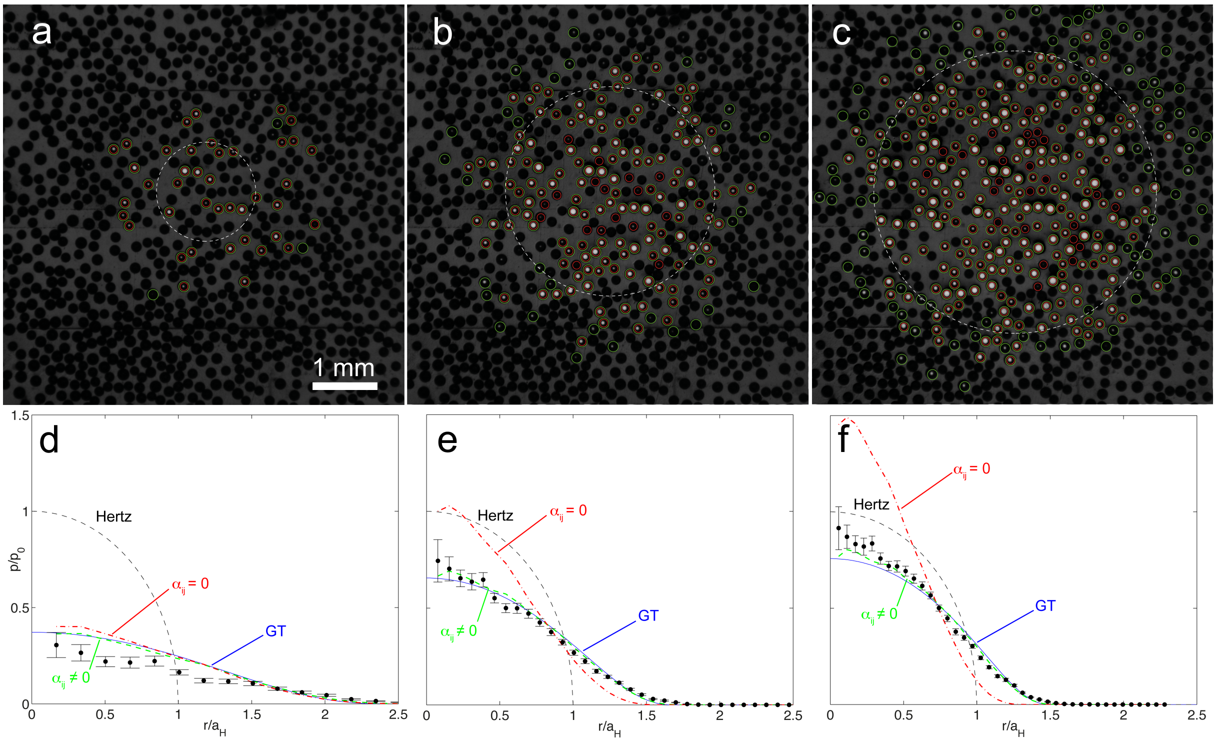

Figure 16 – (a-b-c) *Images des microcontacts (disques blancs) entre une sphère (rayon de courbure 128.8 mm) et une surface de PDMS à micro-aspérités (densité surfacique 0.4),* **(a)** $P = 0.02\ N$, **(b)** $P = 0.2\ N$, **(c)** $P = 0.5\ N$. *Sur chaque image, les cercles verts (resp. rouges) correspondent aux positions des microcontacts prédits par le modèle de Ciaravella et al., avec interaction (resp. sans interaction) entre aspérités. Le couplage entre aspérités est entièrement contenu dans une matrice d'interaction* $[\alpha_{ij}]$ *qui peut être mise à 0 si on souhaite le supprimer. Pour chaque P, le contact de Hertz (cercle blanc en ligne discontinue) de rayon* a_H *est superposé aux images.* **(d-e-f)** *Profils de pression moyennés angulairement fonction de la distance* r/a_H *au centre du contact. Les points de mesure sont en noir et le modèle GT en ligne continue bleue. Les lignes discontinues rouges (resp. vertes) correspondent aux prédictions du modèle de Ciaravella et al., avec interaction (resp. sans interaction).*

De telles prédictions sont déjà contenues dans le modèle classique de mécanique du contact de Greenwood et Tripp (GT). Ce modèle est l'extension directe au cas d'un contact sphère-plan du modèle de contact multi-aspérités de Greenwood et Williamson (GW) en contact plan-plan, et dont nous avons donné plus haut les principaux ingrédients et hypothèses (section B). Contrairement au modèle de GW qui peut être résolu analytiquement, l'introduction d'une courbure dans le problème ne permet plus de le faire pour le modèle GT, et passe nécessairement par une résolution numérique. Nous avons utilisé pour cela une distribution uniforme des hauteurs des sommets identique à celle utilisée dans nos expériences. Nous avons ainsi pu extraire les profils de pression et valider pour la première fois expérimentalement le modèle de GT **(Figs. 16d-f)**.

Nous avons également comparé nos mesures à un modèle de mécanique du contact beaucoup plus récent de Ciaravella *et al.*[15], qui consiste en une version modifiée des modèles de GW et GT. Contrairement à ceux-ci, ce modèle intègre au premier ordre les corrections induites par le couplage élastique entre aspérités. L'ensemble des aspérités reposant sur une même couche élastique, cela consiste à tenir compte du fait que le déplacement normal de chaque aspérité en contact dépend de la distribution spatiale des pressions exercées sur les aspérités voisines. Contrairement aux modèles *statistiques* de GW et GT, le modèle de Ciaravella *et al.* permet de calculer les déplacements induits pour chaque aspérité, offrant ainsi la possibilité de comparer directement les distributions spatiales expérimentales et théoriques. Nos mesures apparaissent en très bon accord avec les prédictions de ce modèle **(Figs. 16a-c)**. En revanche, les profils de pression déduits de ce modèle sont quasiment identiques à ceux de GT **(Figs. 16d-f)** suggérant que les effets de couplage élastique entre aspérités restent des effets du second ordre. En analysant plus finement les distributions de densité et d'aire moyenne de microcontacts fonction de la pression locale, nous avons mis en évidence des écarts entre le modèle de GT et le modèle de Ciaravella *et al.* Ceux-ci se traduisent notamment par le fait qu'il existe une pression seuil p^* de l'ordre de 10 à 10^3 Pa, qui sépare deux régimes distincts. Au-dessus de p^*, l'évolution de la densité de microcontacts (et de l'aire moyenne des microcontacts) suit une loi de puissance d'exposant compatible avec les prédictions du modèle de GT. En-dessous de p^*, l'évolution suit toujours une loi de puissance mais l'exposant est différent. Ces résultats suggèrent que le couplage élastique entre aspérités ne se manifeste que pour les aspérités les plus faiblement chargées, *i.e.* celles situées à l'extrême périphérie du contact. Partout ailleurs dans le contact, ce couplage est négligeable.

Au-delà de ces aspects, ces mesures constituent la première validation expérimentale de deux modèles de mécanique du contact largement utilisés et jamais testés, à notre connaissance directement, sur des interfaces modèles.

D. Aspects miroirs - Surfaces rigides rugueuses contre substrat de PDMS lisse

Au cours des dix dernières années, je me suis concentré sur les régimes de frottement transitoire et stationnaire en considérant essentiellement des interfaces rugueuses où la rugosité est toujours du côté de la surface la plus molle, *i.e.* sur l'élastomère.

Parallèlement à mes travaux, A. Chateauminois et C. Frétigny (Laboratoire SIMM – ESPCI) développaient des approches similaires d'imagerie du contact résolues spatialement, mais appliquées au cas miroir. La rugosité est cette fois-ci du côté de l'indenteur rigide qui est placé en regard d'une surface d'élastomère lisse. Au cours de la thèse de D. T. Nguyen, ils ont développé des méthodes de mesure des champs de déplacements ultra-résolues spatialement, qui combinées à des méthodes d'inversion permettaient de déduire les champs de contraintes interfaciales. Nous nous sommes naturellement rapprochés jusqu'à concrétiser cette collaboration en obtenant un financement commun ANR (projet DYNALO).

Nous avons développé en commun deux aspects, le premier concernant la mesure de la loi frottement à des échelles mésoscopiques en régime stationnaire, d'un contact sphère de verre rodée frottant contre un élastomère de PDMS lisse ; le deuxième concernant la mise au point d'un système de micro-aspérités sphériques rigides en contact normal et en frottement stationnaire contre un PDMS lisse.

---

[15] M. Ciavarella, V. Delfine, G. Demelio, *JMPS* **54**, 2569-2591 (2006) ; M. Ciavarella, J. Greenwood, M. Paggi, *Wear* **265**, 729–734 (2008).

- *Loi de frottement à une interface PDMS lisse-verre rugueux en régime stationnaire* **[6]**

Dans leurs expériences, A. Chateauminois et C. Frétigny ont choisi d'utiliser une géométrie de contact sphère-plan qui permet de localiser le contact. L'indenteur est généralement une sphère de silice de petit rayon de courbure qui peut être lisse ou rendue rugueuse, soit à des échelles de longueurs micrométriques (sablage, attaque acide ou une combinaison des deux), soit à des échelles de longueurs nanométriques (dépôt de nanoparticules colloïdales de silice sur la surface de la lentille).

Au cours de sa thèse, D. T. Nguyen a cherché à caractériser la loi de frottement local en régime de frottement stationnaire, à l'interface entre un élastomère de PDMS lisse et différents types de lentilles de silice rendues rugueuses.

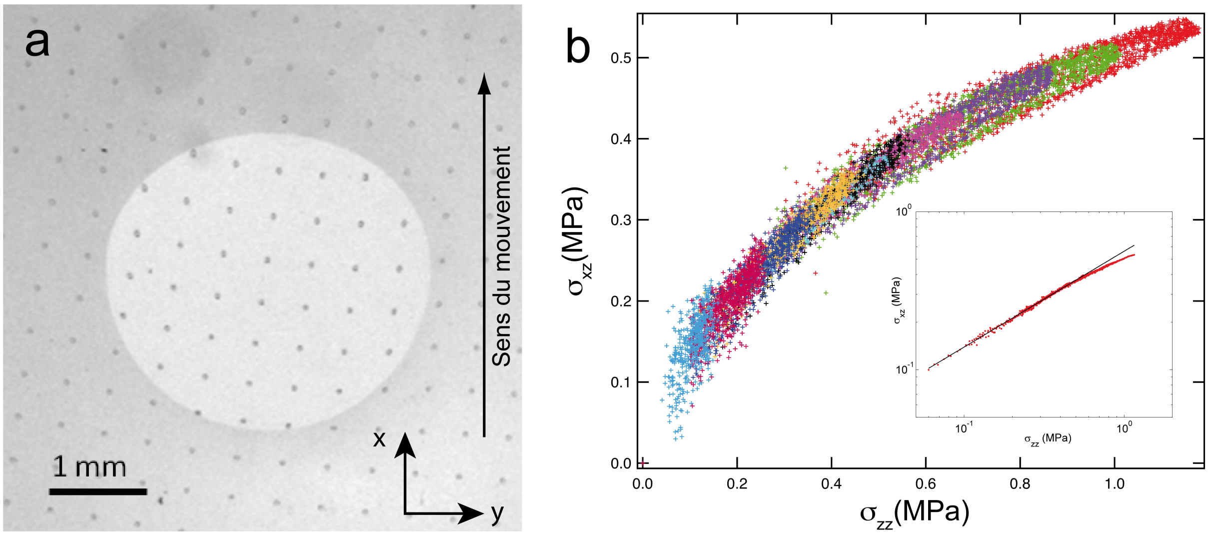

Figure 17 – (a) *Technique de marquage d'une surface lisse de PDMS développée par Nguyen et al. Un réseau de trous de taille et profondeur micrométriques est incrusté sur la surface de l'élastomère lisse. Au contact d'un indenteur sphérique lisse, le réseau apparaît comme une grille de disques noirs. Contre une lentille rugueuse, la diffusion de la lumière transmise empêche toute identification du réseau. En revanche, une fois l'élastomère mis en mouvement, le motif devient visible.* **(b)** *Loi de frottement locale* σ_{xz} *versus* σ_{zz} *pour l'ensemble des expériences réalisées conjointement au SIMM et LJP (les différentes couleurs correspondent à différentes expériences à différentes charges normales). Insert : Tracé en échelle log-log des données moyennées sur une fenêtre glissante (points rouges). La ligne noire est un ajustement par une loi de puissance d'exposant* ~ 0.606 *(pour* $\sigma_{zz} < 0.5\ MPa$*). Nos mesures empiriques de la référence* **[4]** *du Thème 2, donnaient un exposant de* 0.61.

Pour mesurer les déplacements latéraux de la surface lisse de l'élastomère, Nguyen *et al.* ont marqué celle-ci avec un réseau de trous de dimensions micrométriques (techniques de photolithographie douce et moulage), qui apparaissent comme des disques noirs quand l'interface est imagée en transmission **(Fig. 17a)**. Contre une lentille rodée, la rugosité ne permet plus de voir le réseau. En revanche, en frottement stationnaire, et moyennant un temps d'exposition suffisant, le réseau de disques redevient visible, ce qui permet toujours une mesure des déplacements latéraux à la surface de l'élastomère. Les déplacements verticaux dans la zone de contact sont quant à eux déduits d'une mesure d'indentation de la lentille dans le bloc d'élastomère.

Dans ces expériences, c'est l'élastomère marqué qui bouge par rapport au plan image de la caméra, et il est donc possible en inclinant le réseau pour différentes expériences, d'augmenter artificiellement la résolution spatiale. En accumulant ainsi quelques centaines d'images, D. T. Nguyen a pu obtenir un champ des déplacements avec une résolution spatiale ($\sim 10\,\mu m$) bien meilleure que le pas du réseau ($\sim 400\,\mu m$), pour une résolution sur les déplacements inférieure au micromètre.

En utilisant des techniques d'inversion des champs des déplacements en éléments finis (pour tenir compte des grandes déformations en bord de contact), il est possible d'extraire le champ des contraintes interfaciales $\sigma_{xz}(x, y)$ et normales $\sigma_{zz}(x, y)$.

Notre contribution à ce travail a été essentiellement expérimentale. Le dispositif de mesure développé par A. Chateauminois permet de ne travailler que dans des gammes de charge normale comprise entre 1 et 17 N [16]. Le montage que j'ai développé permet en revanche d'imposer des forces normales beaucoup plus faibles comprises entre 0.02 et 2 N.

Etablir une loi de frottement locale en régime stationnaire de frottement supposait de mesurer les contraintes interfaciales et normales jusqu'à des valeurs proches de 0, ce que notre montage permettait de faire. Nous avons donc combiné mesures obtenues sur leur montage et le notre pour obtenir une loi de frottement reliant σ_{xz} et σ_{zz} pour des pressions σ_{zz} dans toute la gamme [~ 0 – 1.2] MPa. Pour une lentille rendue rugueuse par sablage, qui présente une rugosité *rms* 1-2 µm, et une topographie auto-affine avec une distribution gaussienne des hauteurs des sommets, nous avons ainsi mesuré que la contrainte de cisaillement varie avec la pression locale selon une loi de puissance d'exposant ~ 0.61 **(Fig. 17b)**. Ce comportement sous-linéaire persiste pour des surfaces de verre présentant une distribution des hauteurs des sommets non-gaussienne (verre rodé puis attaqué chimiquement au HCl) avec un exposant mesuré d'environ 0.63. Il est intéressant de noter qu'une dépendance similaire avec un exposant ~ 0.61 a été trouvée dans nos expériences de mesure des fluctuations de la force de frottement macroscopique (*cf.* Thème 2 : Physique de la perception tactile, référence **[4]**), en utilisant une approche empirique **(Fig. 17b, insert)**.

Ces résultats, présentés et discutés dans la référence **[6],** constituent une première mesure de la loi de frottement locale à une interface multi-contacts. Clairement, celle-ci ne suit pas la loi classique d'Amontons-Coulomb pour laquelle σ_{xz} serait proportionnel à σ_{zz}. Qualitativement, on peut supposer qu'elle résulte de la combinaison de deux effets, une saturation progressive de l'aire réelle de contact et/ou une interaction élastique entre aspérités. Il n'existe cependant pas de modèle de mécanique de contact qui prédise une telle loi et il est difficile à ce stade de relier la valeur de l'exposant aux caractéristiques topographiques.

La mesure sur différentes topographies suggère cependant une certaine généralité à ce résultat dont il conviendrait de tenir compte pour la dérivation de la plupart des modèles de mécanique d'interfaces multi-contacts qui supposent le plus souvent une loi de frottement locale de type Amontons-Coulomb.

- *Surfaces de verre micro-texturées – Mesures d'aire de contact réelle et frottement stationnaire* **[5]**

Très récemment, j'ai développé en collaboration avec A. Chateauminois et C. Frétigny un procédé alternatif pour fabriquer des surfaces à aspérités sphériques rigides. Ce procédé nous a été suggéré par M. Chaudhury (Université Leligh, Pennsylvania, USA) et consiste à

---

[16] A. Chateauminois, C. Frétigny, *Eur. Phys. J. E* **27**, 221 (2008).

mouler un élastomère contre une surface solide recouverte de microgouttelettes liquides condensées. On obtient ainsi un moule en PDMS, image en négatif du motif de gouttelettes. On s'en sert ensuite pour répliquer l'équivalent rigide sur un support en silice en utilisant une technique d'impression sol-gel. Ce procédé a été mis à profit par S. Yashima et A. Chateauminois pour déposer des micro-aspérités sur la surface d'une lentille de silice et obtenir ainsi une rugosité contrôlée.

Bien que de telles surfaces ne permettent pas un aussi bon contrôle des distributions des aspérités que le permet le micro-usinage, elles demeurent néanmoins intéressantes, d'une part car les aspérités obtenues sont parfaitement lisses, d'autre part parce que leurs rayons de courbure sont distribués **(Fig. 18)**. Après caractérisation *a posteriori* (profilométrie optique), nous avons ainsi obtenu des surfaces dont la distribution des hauteurs des sommets est gaussienne. Ce type de surfaces a été utilisé pour des expériences de contact normal avec un bloc épais d'élastomère et les résultats de mesure d'aire de contact confrontés à ceux obtenus avec les surfaces à aspérités molles.

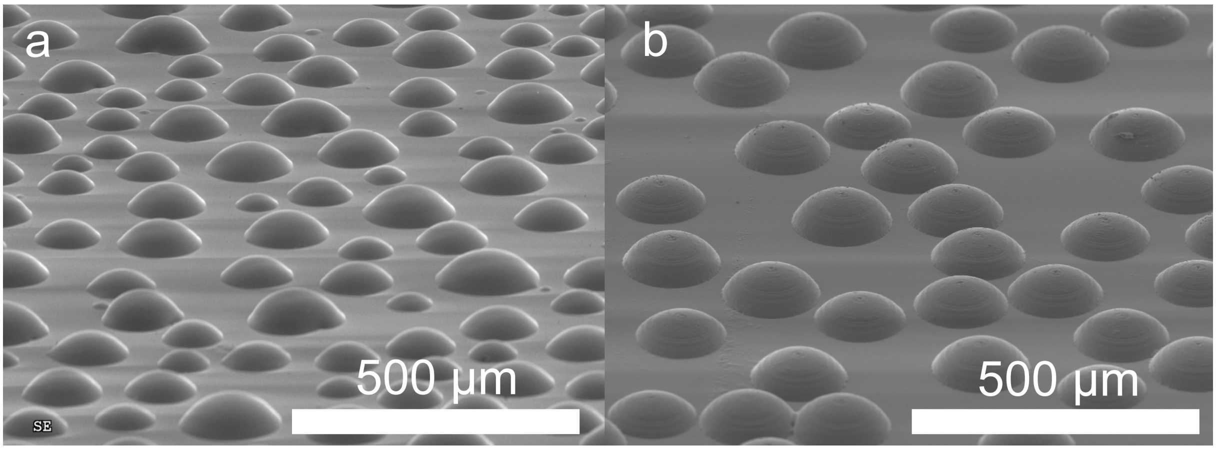

Figure 18 – (a) *Image SEM d'une surface sol-gel à aspérités sphériques rigides obtenue par la technique d'évaporation de gouttelettes.* **(b)** *Image SEM d'une surface de PDMS obtenue par micro-usinage. Les aspérités ont une rugosité rms de l'ordre de* 0.5 *µm, que n'ont pas les aspérités obtenues par évaporation.*

On retrouve que l'aire réelle de contact suit une loi de puissance d'exposant plus faible qu'avec les surfaces à aspérités molles, en accord avec l'effet de courbure déjà discuté au paragraphe C. Une comparaison détaillée entre les surfaces à aspérités molles et rigides est donnée dans le *preprint* **[5]**, récemment soumis à *Soft Matter*. Nous y discutons également de mesures de forces de frottement en régime stationnaire pour différentes charges normales. Il ressort de cette étude que les contraintes tangentielles mesurées sur un contact macroscopique entre une lentille lisse et un bloc de PDMS lisse ne peuvent pas être simplement transposées à l'échelle des micro-aspérités. Nos mesures montrent en effet que la contrainte tangentielle moyenne mesurée sur les microcontacts est systématiquement plus grande que celle mesurée sur un contact macroscopique.

Références :

[1]. "Experimental evidence of non-Amontons behaviour at a multi-contact interface", J. Scheibert, A. Prevost, J. Frelat, P. Rey, G. Debrégeas, *Euro. Phys. Lett.* **83**, 34003 (2008).

[2]. "Stress Field at a Sliding Frictional Contact: Experiments and Calculations", J. Scheibert, A. Prevost, G. Debrégeas, E. Katzav, M. Adda-Bedia, *J. Mech. Phys. Solids*, **57**, 1921-1933 (2009).

[3]. "Probing the micromechanics of a multi-contact interface at the onset of frictional sliding", A. Prevost, J. Scheibert, G. Debrégeas, *Euro. Phys. J. E* **36**, 13017 (2013).

[4]. "Probing Locally the Onset of Slippage at a Model Multicontact Interface", V. Romero, E. Wandersman, G. Debrégeas, A. Prevost, *Phys. Rev. Lett.* **112**, 094301 (2014).

[5]. "Normal contact and friction of rubber with model randomly rough surfaces", S. Yashima, V. Romero, E. Wandersman, C. Frétigny, M. Chaudhury, A. Chateauminois, A. Prevost, soumis à *Soft Matter* (Octobre 2014).

[6]. "Non Amontons-Coulomb local friction law of randomly rough contact interfaces with rubber", D. T. Nguyen, E. Wandersman, A. Prevost, Y. Le Chenadec, C. Frétigny, A. Chateauminois, *Euro. Phys. Lett.* **104**, 64001 (2013).

Journal of the Mechanics and Physics of Solids 57 (2009) 1921–1933

Contents lists available at ScienceDirect

Journal of the Mechanics and Physics of Solids

journal homepage: www.elsevier.com/locate/jmps

Stress field at a sliding frictional contact: Experiments and calculations

J. Scheibert *,[1], A. Prevost, G. Debrégeas, E. Katzav [2], M. Adda-Bedia

Laboratoire de Physique Statistique de l'ENS, UMR 8550, CNRS/ENS/Université Paris 6/Université Paris 7, 24 rue Lhomond, 75231 Paris, France

ARTICLE INFO

Article history:
Received 6 October 2008
Received in revised form
9 May 2009
Accepted 31 August 2009

PACS:
46.55.+d
81.40.Pq
85.85.j

Keywords:
Contact mechanics
Layered rubber material
Friction
MEMS
Integral transforms

ABSTRACT

A MEMS-based sensing device is used to measure the normal and tangential stress fields at the base of a rough elastomer film in contact with a smooth glass cylinder in steady sliding. This geometry allows for a direct comparison between the stress profiles measured along the sliding direction and the predictions of an original *exact* bidimensional model of friction. The latter assumes Amontons' friction law, which implies that in steady sliding the interfacial tangential stress is equal to the normal stress times a pressure-independent dynamic friction coefficient μ_d, but makes no further assumption on the normal stress field. Discrepancy between the measured and calculated profiles is less than 14% over the range of loads explored. Comparison with a test model, based on the classical assumption that the normal stress field is unchanged upon tangential loading, shows that the exact model better reproduces the experimental profiles at high loads. However, significant deviations remain that are not accounted for by either calculations. In that regard, the relevance of two other assumptions made in the calculations, namely (i) the smoothness of the interface and (ii) the pressure-independence of μ_d is briefly discussed.

1. Introduction

The sliding contact between non-conforming elastic bodies is a classical problem in contact mechanics (Cattaneo, 1938; Mindlin, 1949; Johnson, 1985; Hills and Nowell, 1994). Knowledge of the surface and subsurface stress fields in such systems is central to solid friction, seismology, biomechanics or mechanical engineering. Typical applications include hard disk drives (e.g. Talke, 1995), tribological coatings (e.g. Holmberg et al., 1998), train wheels on rails (e.g. Guagliano and Pau, 2007), human joints (e.g. Barbour et al., 1997) and tactile perception (e.g. Howe and Cutkosky, 1993; Scheibert et al., 2009).

Theoretically, calculations of the contact stress field in the quasi-static steady sliding regime have been performed for both homogeneous (Poritsky, 1950; Bufler, 1959; Hamilton and Goodman, 1966; Hamilton, 1983) and layered elastic half-spaces (King and O'Sullivan, 1987; Nowell and Hills, 1988; Shi and Ramalingam, 2001), for cylindrical (Poritsky, 1950; Bufler, 1959; Hamilton and Goodman, 1966; King and O'Sullivan, 1987; Nowell and Hills, 1988), circular (Hamilton and Goodman, 1966; Hamilton, 1983) or elliptical (Shi and Ramalingam, 2001) contacts. These calculations assume a locally valid Amontons' friction law, stating that everywhere within the sliding contact region, the interfacial tangential stress $q = \mu_d p$ with p being the interfacial normal stress and μ_d the dynamic friction coefficient. Up to now, no quantitative comparison between such calculations and experimental stress fields has been performed. The present work first aims at

---

* Corresponding author.
E-mail addresses: julien.scheibert@fys.uio.no, julien.scheibert@lps.ens.fr (J. Scheibert).

[1] Now in Physics of Geophysical Processes, University of Oslo, Oslo, Norway.

[2] Now in Department of Mathematics, King's College, London, UK.

0022-5096/$ - see front matter © 2009 Elsevier Ltd. All rights reserved.
doi:10.1016/j.jmps.2009.08.008

filling this lack, by taking advantage of a recently proposed experimental method (Scheibert, 2008; Scheibert et al., 2008b, 2009), which allows for direct measurements of the stress field at the rigid base of a frictional elastomer film.

For such a layered system, no exact stress calculation in a steady sliding contact has neither been provided up to now. All previous works indeed rely on the classical Goodman's assumption which states that the normal displacements at the interface due to tangential stress are negligible (Goodman, 1962). This implies in particular that the interfacial pressure field is unaltered when a macroscopic tangential load is applied. For a contact between elastic half-spaces, such a normal/tangential decoupling occurs only if (i) both materials are identical, (ii) both are incompressible or (iii) one of the both is perfectly rigid while the other is incompressible (Bufler, 1959; Dundurs and Bogy, 1969). For layered systems, Goodman's assumption is never strictly true. However, it is expected to be increasingly valid (i) the higher the Poisson's ratio (Kuznetsov, 1978), (ii) the lower the ratio of the contact size a over the film thickness h or (iii) the lower the friction coefficient. Rigorously, one has to keep in mind that Goodman's assumption does not have any physical ground since it does not impose the continuity of the normal displacements between the two solids in contact. The present work presents an exact stress analysis which, for a single linear elastic incompressible layer (film) under plane strain conditions, goes beyond the classical description by relaxing Goodman's assumption.

In Section 2, we describe the experimental setup along with the calibration of the apparatus. In Section 3, we present both the normal and tangential stress profile measurements at the base of the elastomer film obtained with a cylinder-on-plane contact in steady sliding. In Section 4, we present the exact model for the quasi-static steady sliding of a rigid circular frictional indentor against the film. In Section 5, the results of this exact calculation are compared to that of a semi-analytical test model implemented with Goodman's assumption. The measurements are directly compared to both models and discussed.

2. Setup and calibration

Local contact stress measurements are performed with a micro-electro mechanical system (MEMS) force sensor embedded at the rigid base of an elastomer film (Fig. 1). The MEMS' sensitive part (Fig. 1, inset) consists of a rigid cylindrical post (diameter 550 µm, length 475 µm) attached to a suspended circular silicon membrane (radius 1 mm, thickness 100 µm, 330 µm below the MEMS top surface). When a force is applied to the post, the resulting (small) deformations of the membrane are measured via four couples of piezo-resistive gauges embedded in it and forming a Wheatstone bridge (see inset of Fig. 1). The MEMS thus allows to measure simultaneously the applied stress along three orthogonal directions, averaged over the MEMS's millimetric extension, in a way that will be determined through calibration.

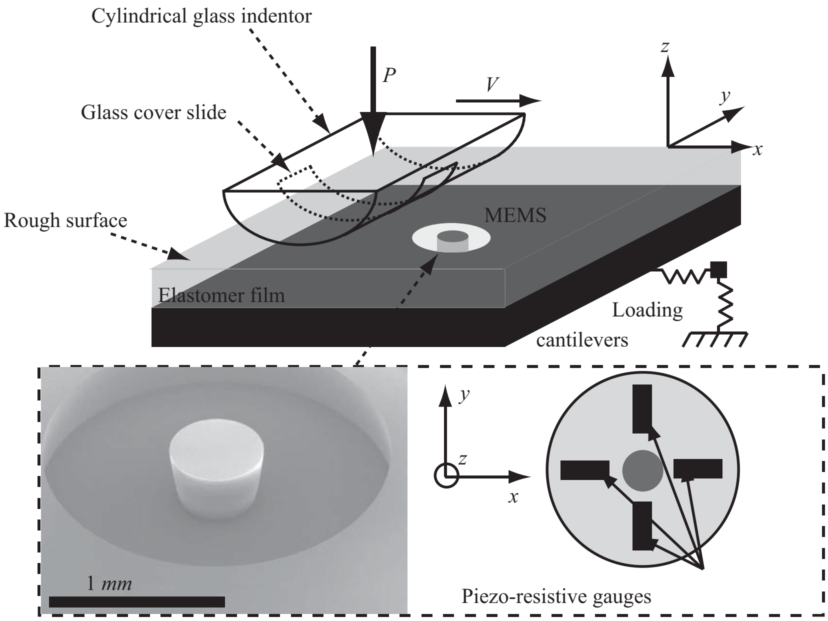

Fig. 1. Sketch of the experimental setup. A cylindrical glass lens (radius of curvature 129.2 mm) to which is glued a glass cover slide is driven along the x direction against a rough, nominally flat PDMS elastomer film (uniform thickness $h = 2$ mm, lateral dimensions 50×50 mm) at a constant prescribed normal load P and a constant velocity V using a linear DC servo-motor (LTA-HS, Newport). The local normal and tangential stress at the rigid base of the film, respectively σ_{zz} and σ_{xz}, are measured by a MEMS force sensor, whose sensitive part is shown in the lower inset (left hand), along with a sketch (right hand) showing the piezo-resistive gauges implementation within the silicon membrane. P and the tangential load Q applied on the film are measured through the extension of two orthogonal loading cantilevers (normal stiffness $641 \pm 5\,\mathrm{N\,m^{-1}}$, tangential stiffness $51\,100 \pm 700\,\mathrm{N\,m^{-1}}$) by capacitive position sensors (respectively, MCC30 and MCC5, FOGALE nanotech).

In the present experiments, the MEMS sensor is located at the rigid base of a rough, nominally flat elastomer film of uniform thickness $h = 2\,\mathrm{mm}$ ($\sim$4 times larger than the post's diameter) and lateral dimensions $50 \times 50\,\mathrm{mm}$. The elastomer is a cross-linked Poly(DiMethylSiloxane) (PDMS, Sylgard 184, Dow Corning) of Young's modulus $E = 2.2 \pm 0.1\,\mathrm{MPa}$ and Poisson's ratio $\nu = 0.5$ (Mark, 1999). The ratio of its loss over storage moduli, measured in a parallel plate rheometer, remains lower than $\sim$0.1 for frequencies smaller than 1 kHz (Scheibert, 2008). In this range the PDMS elastomer can thus be considered as purely elastic. The film is obtained by pouring the cross-linker/PDMS liquid mix directly on the sensitive part of the MEMS (cylindrical post and membrane) so that the resulting elastic film is in intimate contact with the MEMS sensitive part. The parallelepipedic mold used in this process is topped with a Poly(MethylMethAcrylate) plate roughened by abrasion with an aqueous solution of silicon carbide powder (mean diameter of the grains 37 μm). After curing at room temperature for at least 48 h and demolding, the resulting *rms* surface roughness is measured with an interferential optical profilometer (M3D, FOGALE Nanotech) to be $1.82 \pm 0.10\,\mu\mathrm{m}$. This roughness is sufficient to avoid any measurable pull-off force against smooth glass indentors, as discussed in Fuller and Tabor (1975). When the film is put in contact against an indentor, the normal and tangential loads applied, P and Q respectively, are measured through the extension of two orthogonal loading cantilevers (normal stiffness $641 \pm 5\,\mathrm{N\,m^{-1}}$, tangential stiffness $51\,100 \pm 700\,\mathrm{N\,m^{-1}}$) by capacitive position sensors (respectively, MCC30 and MCC5, FOGALE nanotech).

The stress sensing device (MEMS with its PDMS film) has been calibrated in an earlier work (Scheibert et al., 2008b), for the normal stress only. The method is recalled here and extended to the tangential stress. The surface of the film is indented with a rigid cylindrical rod of diameter 500 μm, under a normal load P. With this flat punch indentor, all sensor outputs are found to be linear with P. By successively varying the position of this rod along the x direction, and assuming homogeneity of the surface properties of the film, the radial profiles of the normal and tangential output voltages, respectively $U_{zz}(x)$ and $U_{xz}(x)$, are constructed point by point. These profiles are then compared to the results of finite element calculations (software Castem 2007) for the stress σ_{zz} and σ_{xz} at the base of a smooth axi-symmetrical elastic film (with the same elastic moduli and thickness as in the experiment) perfectly adhering to its rigid base and submitted to a prescribed normal displacement over a central circular area of diameter 500 μm. For frictionless conditions, these numerical results could have been obtained semi-analytically by using the model developed in Fretigny and Chateauminois (2007) but finite element calculations have been preferred because they allowed for variable boundary conditions. As expected for contact regions of dimensions smaller than the film thickness, the stress calculated at the base of the film are found to be insensitive to the frictional boundary conditions.

The vertical dimensions of the MEMS being smaller than the thickness of the elastomer film, one can ignore the stress field modifications induced by the MEMS 3D structure and consider that the base of the film is a plane. We can then relate the measured output voltage U to the stress field at the base of the film σ by writing down that

$$U_{\alpha z}(x,y) = A_{\alpha z} G_{\alpha z} \otimes \sigma_{\alpha z}(x,y) \tag{1}$$

where $\alpha = x$ or z. A_{zz} and A_{xz} are conversion constants (units of mV/Pa), G_{zz} and G_{xz} are normalized apparatus functions and $\otimes$ is a convolution product. Note that we use the sign convention that σ_{zz} is positive for compressive loading. Eq. (1) implicitly assumes decoupling between the MEMS outputs. This has been checked to be true for the bare sensor by submitting it to either a uniform pressure or a pure tangential load applied directly on the silicon cylindrical post. When the MEMS is embedded in the elastomer film, this remains true for the normal output, as checked by applying a uniform pressure at the surface of the film. The analogous check for the tangential output is not possible because any tangential stress applied on the film surface results in tangential stress as well as normal stress gradients at its base, which cannot be measured separately since they induce the same deformation mode of the MEMS silicon membrane. One can still use Eq. (1) in the limit of contact configurations involving small pressure gradients. This is the case when one uses indentors with large radius of curvature such as the cylinders considered in the rest of this study. In this limit, the tangential output is likely to be insensitive to normal stress since the silicon sensor is much stiffer than the elastomer.

In Fourier space, Eq. (1) becomes

$$A_{\alpha z} G_{\alpha z}(x,y) = \mathcal{F}^{-1}\left(\frac{\mathcal{F}\{U_{\alpha z}\}(f_x,f_y)}{\mathcal{F}\{\sigma_{\alpha z}\}(f_x,f_y)}\right)(x,y) \tag{2}$$

where $\mathcal{F}$ is the bidimensional spatial Fourier transform, $\mathcal{F}^{-1}$ its inverse, and f_x, f_y are the spatial frequencies in the x, y directions, respectively. The $U_{zz}(x,y)$, $U_{xz}(x,y)$, $\sigma_{zz}(x,y)$ and $\sigma_{xz}(x,y)$ fields are built from the corresponding profiles along the x-axis, assuming axi-symmetry, and then transformed using a fast Fourier transform (FFT) algorithm. The rapid decay of $\mathcal{F}\{\sigma_{zz}\}$ and $\mathcal{F}\{\sigma_{xz}\}$ with increasing spatial frequency yields a divergence of the ratio in Eq. (2). To circumvent this difficulty, a white noise of amplitude 10 times weaker than the weakest relevant spectral component is added to both terms of the ratio before applying the FFT. The result is found to be insensitive to the particular amplitude of this white noise. A_{zz} and A_{xz} are determined so that the integrals of G_{zz} and G_{xz} are equal to 1. The integrals of both U_{xz} and σ_{xz} being zero, G_{xz} is determined up to an additive constant, which was taken such that G_{xz} vanishes far from the MEMS location.

Both G_{zz} and G_{xz} exhibit a bell shape with a typical width of the order of 600 μm, comparable to the lateral dimension of the sensitive part of the MEMS (Fig. 2). For subsequent calculations, G_{zz} is approximated by a gaussian of standard deviation 561 μm (Fig. 2(a)). The shape of G_{xz} is more complex and is therefore approximated by a gaussian of standard deviation 688 μm decorated by a rectangular foot of lateral extent 2.7 mm and amplitude 4.1% of the maximum amplitude of G_{xz}

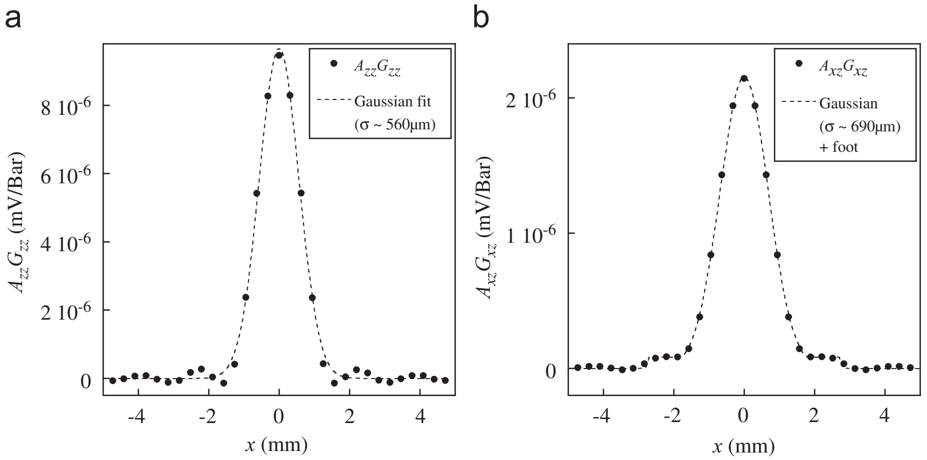

Fig. 2. Apparatus functions $A_{zz}G_{zz}$ and $A_{xz}G_{xz}$ of the MEMS sensor for (a) the normal stress and (b) the tangential stress, respectively. Black dots are the results of the calibration method. Dashed lines are the approximated apparatus functions used for subsequent calculations.

(Fig. 2(b)). We checked that a simple gaussian approximation of G_{xz} was not sufficient to reproduce the measured U_{xz} profile when convoluted with σ_{xz}.

To validate this calibration procedure, the stress profiles $S_{zz}(x) = U_{zz}(x)/A_{zz}$ and $S_{xz}(x) = U_{xz}(x)/A_{xz}$ in the x direction for cylinder-on-plane contacts under a pure normal load are measured point by point in the same way as for the rod indentation. Note that the sign convention for S_{zz} is the same as for σ_{zz}. The indentor is a glass cover slide (thickness 150 μm, y dimension $L = 8$ mm) glued with a very thin film of cyanoacrylate onto the cylindrical part of a plano-convex cylindrical glass lens of radius of curvature 129.2 mm (Fig. 1). The contact length in the y direction is therefore 8 mm, a dimension which is large enough to create locally, at its center, a y invariant stress state, but small enough to make the contact insensitive to flatness imperfections at the scale of the elastomeric film lateral size. Both the glass and the PDMS surfaces are passivated using a vapor-phase silanization procedure which reduces and homogenizes the surface energy (Chaudhury and Whitesides, 1991). Each contact is formed using the following loading sequence. The indentor is pressed against the PDMS film up to the prescribed load P within 2% relative error. Due to the associated tangential displacement of the extremity of the normal cantilever, a significant tangential load Q is induced. From this position, the contact is renewed by manual separation which results in a much smaller but finite Q. To correct for this residual load, the indentor is displaced a few micrometers tangentially down to $Q = 0$. Finite element calculations using the same geometrical and loading conditions are performed with both zero and infinite static friction coefficients μ_s in order to provide limiting boundary conditions. The calculated stress profiles $\sigma_{zz}(x)$ and $\sigma_{xz}(x)$ at the base of the elastic film are then convoluted by the apparatus functions G_{zz} and G_{xz} to allow for comparison with the corresponding experimental measurements. The value $A_{zz} = 19.00$ mV/bar obtained by deconvolution allows for the pressure profile measurements to lie between the $\mu_s = 0$ and ∞ limiting calculated profiles, in the whole load range further used in this work (Fig. 3(a)). An equally good agreement is obtained for the tangential stress profiles with $A_{xz} = 7.95$ mV/bar, a value 7% higher than the one determined by deconvolution[3] (Fig. 3(b)). We checked that $G_{yz} = G_{xz}$ and $A_{yz} = A_{xz}$. These apparatus functions are assumed to remain valid for contacts in the steady sliding regime.[4]

3. Steady sliding measurements

The steady sliding experiments are carried out as follows. Prior to sliding, contacts are prepared under normal load only, ranging from 0.34 to 2.75 N, using the loading sequence described in Section 2. The cylindrical indentor is then translated tangentially over 20 mm along the positive x direction at constant velocity V between 0.2 and 2 mm s^{-1}. Reproducibility is such that $Q(t)$ differs from less than 1% between two successive experiments (same P and V). The signals display a short transient followed by a steady sliding regime for which both $Q(t)$ and $P(t)$ exhibit uncorrelated fluctuations of relative amplitude smaller than 4%. This observation indicates that the surface properties can be considered as homogeneous

---

[3] This difference is very likely due to the above mentioned fact that the MEMS' tangential output is sensitive to pressure gradients over the size of the sensor. These gradients are estimated to represent less than 6% of the tangential output for the rod indentation situation used to determine A_{xz}. For the large cylinder-on-plane contacts under normal loading that are considered in this calibration, the normal stress gradients vanish with increasing normal load. They represent at most 4% of the tangential output over the whole range of P used here.

[4] In steady sliding, the normal stress gradients represent a decreasing proportion of the tangential output with increasing normal load, less than 16% for $P = 0.34$ N, less than 9% for $P = 0.69$ N, down to less than 4% beyond $P = 2.40$ N.

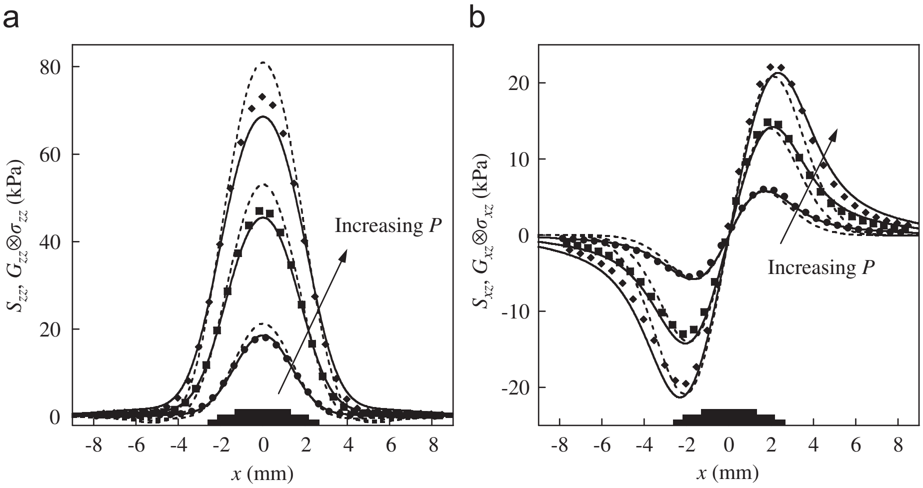

Fig. 3. Validation of the calibration procedure. Measured stress profiles under normal loading by the rigid cylinder ($P = 0.69$ N (●), 1.72 N (■) and 2.75 N (◆) (a) normal stress $S_{zz}(x)$ and (b) tangential stress $S_{xz}(x)$. Comparison is made with $G_{zz} \otimes \sigma_{zz}(x)$ and $G_{xz} \otimes \sigma_{xz}(x)$ for $\mu_s = 0$ (solid lines) and $\mu_s = \infty$ (dashed lines). The black rectangular patches on the x-axis represent the contact widths (3.00, 4.50 and 5.34 mm for $P = 0.69$, 1.72 and 2.75 N, respectively) obtained from the finite element calculations for $\mu_s = 0$.

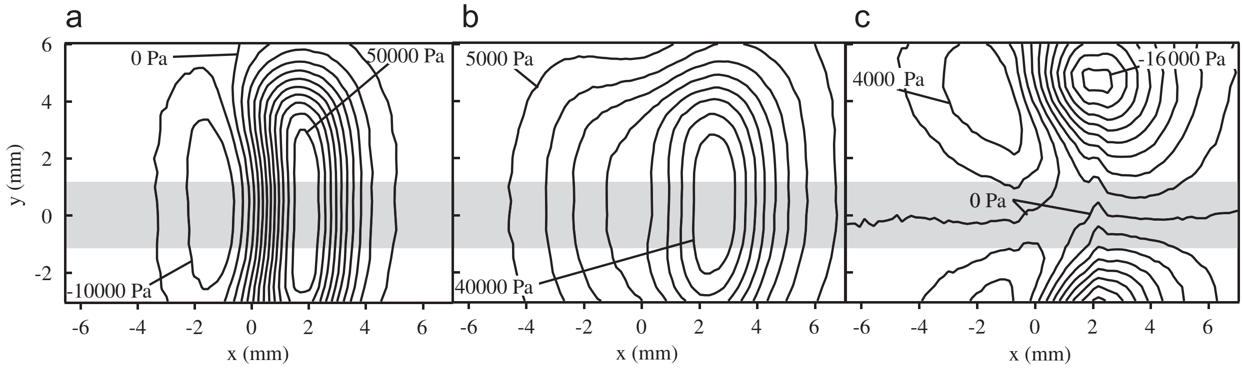

Fig. 4. Measured stress field for a cylinder-on-plane contact in steady sliding regime at $V = 0.4\,\mathrm{mm\,s^{-1}}$ and $P = 1.72$ N. (a) Normal stress S_{zz}. (b) Tangential stress along the direction of movement S_{xz}. (c) Tangential stress orthogonal to the direction of movement S_{yz}. Lines are iso-stress curves obtained by interpolation of 19 x-profiles made of 10 000 data points each. The shaded zone defines the region in which quasi two-dimensional conditions are met. The measured field is not centered on the contact due to limitations in the movement of the translation stage.

throughout the explored area. It allows us to derive the stress profiles along the sliding direction directly from the MEMS signals through the relation $S_{\alpha z}(x) = U_{\alpha z}(Vt)/A_{\alpha z}$ (with $\alpha = x$, y and z).

Fig. 4 shows the measured steady sliding stress field for all three components S_{zz}, S_{xz} and S_{yz} at $P = 1.72$ N and $V = 0.4\,\mathrm{mm\,s^{-1}}$. They have been constructed from the interpolation of 19 profiles along x at different locations with respect to the MEMS, with 0.5 mm steps along the y-axis. Each profile is made of 10 000 data points, one every 2 μm. The line $x = 0$ corresponds to the center of the cylinder-on-plane stress profile measured under normal load, while the axis $y = 0$ corresponds to the symmetry line of the steady-state stress field. These fields are to a good approximation y invariant over a width of a few millimeters (shaded region in Fig. 4) comparable to the extension of the MEMS field of integration. This observation allows us to consider that the x profiles at $y = 0$ provide an experimental realization of a two-dimensional (i.e. y invariant) cylinder-on-plane friction experiment. In the following we will focus on these profiles and compare them with calculated stress profiles under plane strain conditions. For a given P, the profiles obtained with a sliding velocity V in the range $0.2 < V < 2.0\,\mathrm{mm\,s^{-1}}$ are almost undistinguishable. Thus, in the following, only the profiles obtained with $V = 1.0\,\mathrm{mm\,s^{-1}}$ are shown.

Fig. 5 shows the measured stress profiles $S_{zz}(x)$ and $S_{xz}(x)$ for four different normal loads. For both components, the profiles exhibit a similar shape with a maximum at the leading edge of the moving indentor whose amplitude increases with P. The tangential component is positive throughout the contact, whereas the normal component exhibits a negative minimum at the trailing edge.

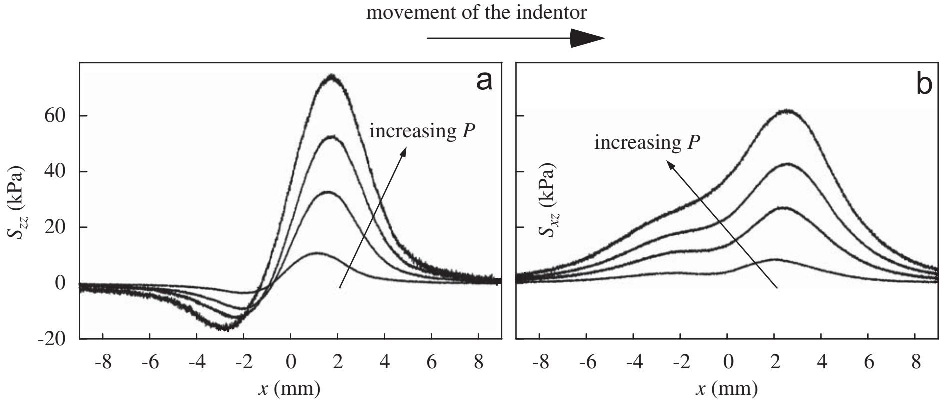

Fig. 5. Measured stress profiles at $y = 0$ for a cylinder-on-plane contact in steady sliding regime at $V = 1\,\mathrm{mm\,s^{-1}}$ for $P = 0.34$, 1.03, 1.72 and 2.75 N. (a) Normal stress S_{zz}. (b) Tangential stress S_{xz} along the direction of movement.

4. Exact model

To allow for a direct quantitative comparison with the previous experimental stress profiles we have developed the following bidimensional exact model (Fig. 6). A linear incompressible elastic film, of thickness h and Young's modulus E, is loaded under plane strain conditions by a rigid circular body of radius R moving at a constant velocity V. We postulate quasi-static motion, i.e. the characteristic time h/c for sound waves of velocity c to travel across the film is assumed to be smaller than the characteristic time a/V associated with the indentor motion, so that the elastic film is at equilibrium at all times. The problem is made dimensionless by expressing the coordinates (x, z), displacements $u_i(x, z)$ and stress $\sigma_{ij}(x, z)$ in units of h, $h^2/2R$ and $Eh/6R$, respectively.

The constitutive equations for the elastic film can be written as

$$\sigma_{ij} = -\Sigma\delta_{ij} + \frac{\partial u_i}{\partial x_j} + \frac{\partial u_j}{\partial x_i} \tag{3}$$

where Σ is the pressure. The equilibrium equations in the film and the condition of incompressibility are

$$\nabla\Sigma = \Delta\vec{u} \tag{4}$$

$$\nabla \cdot \vec{u} = 0 \tag{5}$$

We specify the following boundary conditions:

$$u_x(x, 0) = u_z(x, 0) = 0 \tag{6}$$

$$\sigma_{xz}(x, 1) + \mu_d\sigma_{zz}(x, 1) = 0 \tag{7}$$

$$\sigma_{zz}(x, 1) = 0 \quad \text{for } |x| > a \tag{8}$$

$$u_z(x, 1) = -u(x) \quad \text{for } |x| < a \tag{9}$$

where $z = 0$ and 1 correspond to the locations of the base and the surface of the elastic film, respectively. Eq. (6) accounts for the perfect adhesion of the film to its rigid base, Eq. (7) corresponds to Amontons' law of friction with a dynamic friction coefficient μ_d, Eq. (8) insures that the surface of the film is traction-free outside the contact zone and Eq. (9) defines the normal displacement induced by the indentor over the contact zone of width $2a$. For a circular rigid indentor the normal displacement has a parabolic profile given by

$$u(x) = \frac{1}{\alpha} - (x - x_0)^2 \tag{10}$$

where x_0 represents the asymmetry of the steady sliding contact and $\alpha = h^2/2R\delta$ with δ being the normal displacement of the indentor. Both x_0 and α are selected by the system for a given width of the contact zone area a and friction coefficient μ_d.

As suggested by the strip geometry and the boundary conditions, the resolution involves the use of Fourier sine and cosine transforms (Adda-Bedia and Ben Amar, 2001). Any spatial distribution function $D(x, y)$ of the problem (displacement, strain or stress) may be decomposed into

$$D(x, y) = \int_0^\infty D^{(c)}(k, y)\cos kx\, dk + \int_0^\infty D^{(s)}(k, y)\sin kx\, dk \tag{11}$$

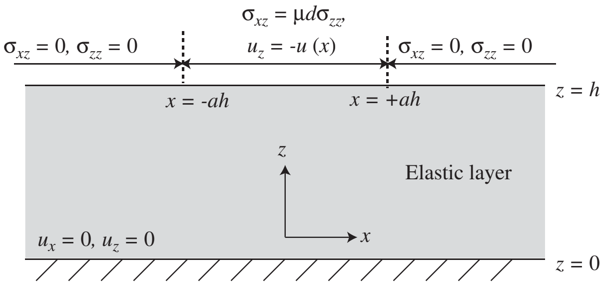

Fig. 6. Sketch of the system considered in the exact model. An elastic film is perfectly adhering on its rigid base ($z = 0$). At its surface ($z = h$) it is stress free outside of the contact region ($|x| < ah$), with a being a result of the calculation. Within the contact region, the normal displacements u_z are prescribed and in steady sliding $\sigma_{xz} = \mu_d \sigma_{zz}$ is assumed everywhere at the interface, μ_d being the dynamic friction coefficient.

Substituting this representation into the bulk equations (3)–(5) and the boundary conditions (6)–(9) and exploiting the parity properties of the sine and cosine functions, lead to the following equations:

$$\int_0^\infty \sigma_{zz}^{(c)}(k,1)\cos kx\,dk = 0, \quad |x| > a \tag{12}$$

$$\int_0^\infty \sigma_{zz}^{(s)}(k,1)\sin kx\,dk = 0, \quad |x| > a \tag{13}$$

and

$$\int_0^\infty [F_0(k)\sigma_{zz}^{(c)}(k,1) + \mu_d F_1(k)\sigma_{zz}^{(s)}(k,1)]\frac{\cos kx}{2k}\,dk = -\frac{1}{2}[u(x)+u(-x)], \quad |x| < a \tag{14}$$

$$\int_0^\infty [-\mu_d F_1(k)\sigma_{zz}^{(c)}(k,1) + F_0(k)\sigma_{zz}^{(s)}(k,1)]\frac{\sin kx}{2k}\,dk = -\frac{1}{2}[u(x)-u(-x)], \quad |x| < a \tag{15}$$

where

$$F_0(k) = \frac{\sinh(2k) - 2k}{\cosh(2k) + 1 + 2k^2} \tag{16}$$

$$F_1(k) = \frac{2k^2}{\cosh(2k) + 1 + 2k^2} \tag{17}$$

The conditions (12), (13) are identically satisfied by

$$\sigma_{zz}^{(c)}(k,1) = \int_0^a \phi(t) J_0(kt)\,dt \tag{18}$$

$$\sigma_{zz}^{(s)}(k,1) = \int_0^a t\psi(t) J_1(kt)\,dt \tag{19}$$

irrespective of $\phi(t)$ and $\psi(t)$, with $J_0(x)$ and $J_1(x)$ being the Bessel functions of the first kind. The functions $\phi(t)$ and $\psi(t)$ now become the unknowns in the problem.

In two-dimensional contact problems, the indentation depth is undeterminate, which requires differentiating the boundary conditions (14)–(15) with respect to x before replacement into the representation (18)–(19). One then classically gets a set of coupled integral equations (see e.g. Spence, 1975; Gladwell, 1980), that are here of Abel type which fix the functions $\phi(t)$ and $\psi(t)$. Inverting this set of equations using the Abel transform yields

$$\phi(x) + \int_0^a M_{00}(x,t)\phi(t)\,dt + \mu_d \int_0^a M_{10}(x,t)\psi(t)\,dt = -4x \tag{20}$$

$$\psi(x) + \mu_d \int_0^a M_{01}(x,t)\phi(t)\,dt - \int_0^a M_{11}(x,t)\psi(t)\,dt = 0 \tag{21}$$

where $M_{ij}(x,t) = (-1)^j x^{1-j} t^i \int_0^\infty k(F_{|i-j|}(k) - \delta_{ij}) J_i(kt) J_j(kx)\,dk$. Eqs. (20) and (21) are independent of the parameters x_0 and α which allows to solve them once the constant μ_d and a are fixed. This simplifies the numerical scheme. Then, x_0 and α are fixed *a posteriori* by using Eq. (14) and the derivative of Eq. (15) with respect to x at, say $x = 0$. This leads to the following equations:

$$4x_0 = \mu_d \int_0^a \phi(t) \int_0^\infty F_1(k) J_0(kt)\, dk\, dt - \int_0^a t\psi(t) \int_0^\infty F_0(k) J_1(kt)\, dk\, dt \tag{22}$$

$$\frac{1}{\alpha} = x_0^2 - \int_0^a \phi(t) \int_0^\infty \frac{F_0(k)}{2k} J_0(kt)\, dk\, dt - \mu_d \int_0^a t\psi(t) \int_0^\infty \frac{F_1(k)}{2k} J_1(kt)\, dk\, dt \tag{23}$$

The displacement and stress fields can be easily expressed as functions of $\phi(x)$, $\psi(x)$, x_0 and α and thus can also be calculated numerically. The lineic normal load P_L applied to the film surface can then be calculated using the following expression:

$$P_L = -\int_{-a}^a \sigma_{zz}(x,1)\, dx = -\pi \int_0^a \phi(t)\, dt \tag{24}$$

Using the constitutive equations and providing simple algebraic transformations the normal stress $\sigma_{zz}(x,0)$ and the tangential stress $\sigma_{xz}(x,0)$ at the rigid base are given by

$$\sigma_{zz}(x,0) = \int_0^a [Z_1(x,t) + \mu_d Z_3(x,t)]\phi(t)\, dt - \int_0^a [\mu_d Z_2(x,t) - Z_4(x,t)] t\psi(t)\, dt \tag{25}$$

$$\sigma_{xz}(x,0) = -\int_0^a [\mu_d Z_5(x,t) + Z_3(x,t)]\phi(t)\, dt + \int_0^a [Z_2(x,t) - \mu_d Z_6(x,t)] t\psi(t)\, dt \tag{26}$$

where the kernels $Z_i(x,t)$ are explicitly

$$Z_1(x,t) = \int_0^\infty A(k)\cos(kx) J_0(kt)\, dk \tag{27}$$

$$Z_2(x,t) = \int_0^\infty B(k)\cos(kx) J_1(kt)\, dk \tag{28}$$

$$Z_3(x,t) = \int_0^\infty B(k)\sin(kx) J_0(kt)\, dk \tag{29}$$

$$Z_4(x,t) = \int_0^\infty A(k)\sin(kx) J_1(kt)\, dk \tag{30}$$

$$Z_5(x,t) = \int_0^\infty C(k)\cos(kx) J_0(kt)\, dk \tag{31}$$

$$Z_6(x,t) = \int_0^\infty C(k)\sin(kx) J_1(kt)\, dk \tag{32}$$

with $A(k)$, $B(k)$ and $C(k)$ being

$$A(k) = \frac{2(\cosh(k) + k\sinh(k))}{\cosh(2k) + 1 + 2k^2} \tag{33}$$

$$B(k) = \frac{2k\cosh(k)}{\cosh(2k) + 1 + 2k^2} \tag{34}$$

$$C(k) = \frac{2(\cosh(k) - k\sinh(k))}{\cosh(2k) + 1 + 2k^2} \tag{35}$$

In practice, the input parameters of the model are chosen to be μ_d and P_L, and the resulting normal and tangential stress profiles at the base of the film are derived.

5. Discussion

We recall here that the calculation presented in the previous section is the first one relaxing Goodman's assumption for the frictional steady sliding of a layered material. In order to assess the impact of this increment on the mechanical description of such contacts, we directly compare, for various combinations of the input parameters μ_d and P_L, the stress profiles obtained from both our exact calculation and an additional calculation derived along the same lines as the exact one but with Goodman's assumption. The latter test model, referred to as Goodman's model is detailed in Appendix A.

Fig. 7 shows the normal stress profiles $\sigma_{zz}^s = \sigma_{zz}(x,1)$ at the surface of the film. For each normal stress profile, the corresponding tangential stress is obtained by multiplying the former by the friction coefficient μ_d, i.e. $\sigma_{xz}^s = \mu_d \sigma_{zz}^s$ following Amontons' law—see Eq. (7). As expected, for $\mu_d = 0$, the exact calculation matches Goodman's result and yields

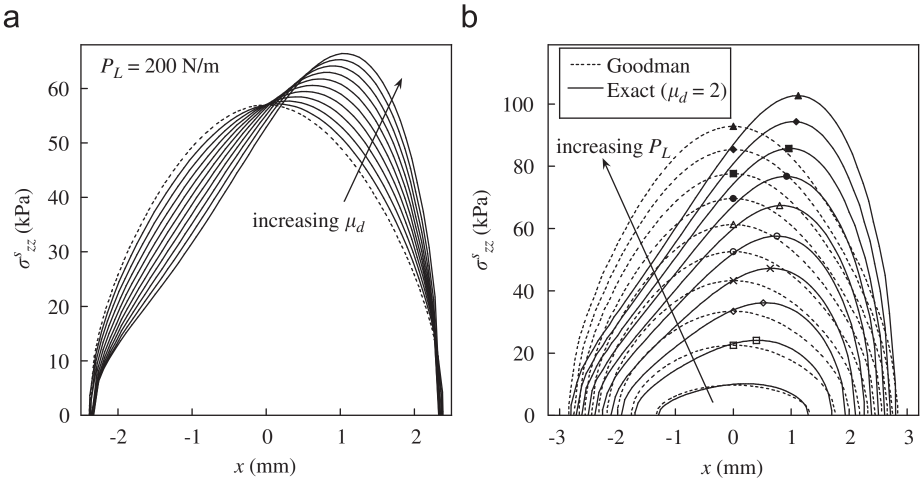

Fig. 7. Normal stress profiles $\sigma^s_{zz} = \sigma_{zz}(x, 1)$ at the surface of the film, calculated with the exact model (solid lines) or with Goodman's model (dashed lines). (a) μ_d increases from 0.3 to 3.0 with steps of 0.3 for the same lineic normal load $P_L = 200\,\mathrm{N\,m^{-1}}$. For all cases, the contact radius is 2.36 ± 0.03 mm. (b) P_L increases from 20 to 380 Pa m^{-1} with steps of 40 Pa m^{-1} for the same friction coefficient $\mu_d = 2.0$. For the exact model, contact widths are 2.60, 3.40, 3.88, 4.24, 4.52, 4.80, 5.02, 5.24, 5.44 and 5.62 mm, respectively. For Goodman's model, contact widths are 2.68, 3.52, 4.00, 4.36, 4.66, 4.90, 5.12, 5.32, 5.52 and 5.68 mm, respectively. For all these graphs, the following parameters were used: $E = 2.2$ MPa, $R = 130$ mm, $h = 2$ mm.

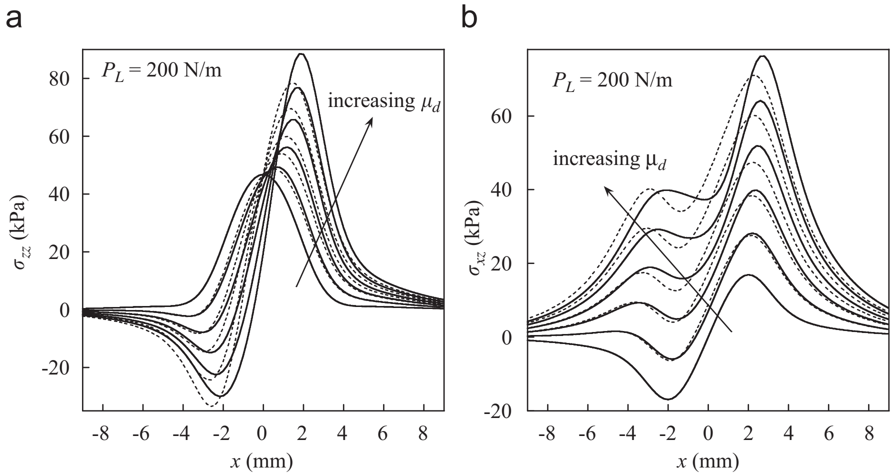

Fig. 8. (a) Normal stress profiles $\sigma_{zz}(x, 0)$ and (b) tangential stress profiles along the direction of movement $\sigma_{xz}(x, 0)$ calculated at the base of the elastic film with the exact model (solid lines) or with Goodman's model (dashed lines). μ_d increases from 0 to 3.0 with steps of 0.6 for the same lineic normal load $P_L = 200\,\mathrm{N\,m^{-1}}$. The contacts widths are equal to that given in the legend of Fig. 7(a). The following parameters were used: $E = 2.2$ MPa, $R = 130$ mm, $h = 2$ mm.

symmetric fields with an integral (area below the curve) equal to P_L. For increasing μ_d at constant P_L, the profiles maintain their integral while becoming increasingly asymmetric, with a growing maximum shifting towards the leading edge of the moving indentor. A similar behavior for the envelope is observed for an increasing P_L at constant μ_d. Interestingly, Goodman's model deviates significantly from the exact one, even in the favorable situation considered here where the material is incompressible and the film is relatively thick.

Fig. 8 shows both the normal and tangential stress profiles, $\sigma_{zz}(x, 0)$ and $\sigma_{xz}(x, 0)$, at the base of the film, where the stress σ is actually measured. σ is related to σ^s at the free surface of the film through a convolution with the Green function for an elastic membrane of thickness h. Since the latter has a typical width $\simeq h$, σ cannot exhibit spatial modulations over length scales smaller than $h = 2$ mm. The spatial resolution of the MEMS ($\simeq 1$ mm) is therefore sufficient to probe the stress field σ at the base of the elastic film. For $\mu_d = 0$, the normal stress profile is symmetric with an integral equal to P_L, whereas the tangential stress profile is antisymmetric with a vanishing integral. For a given lineic load P_L, an increasing μ_d qualitatively results in growing additional contributions to the profiles, anti-symmetric for the normal stress and symmetric for the tangential stress. The integral of the normal stress profile remains equal to P_L while the integral of the tangential stress profile becomes $\mu_d P_L$. Similar features are observed in Fig. 9, which shows $\sigma_{zz}(x, 0)$ and $\sigma_{xz}(x, 0)$ for an increasing lineic load

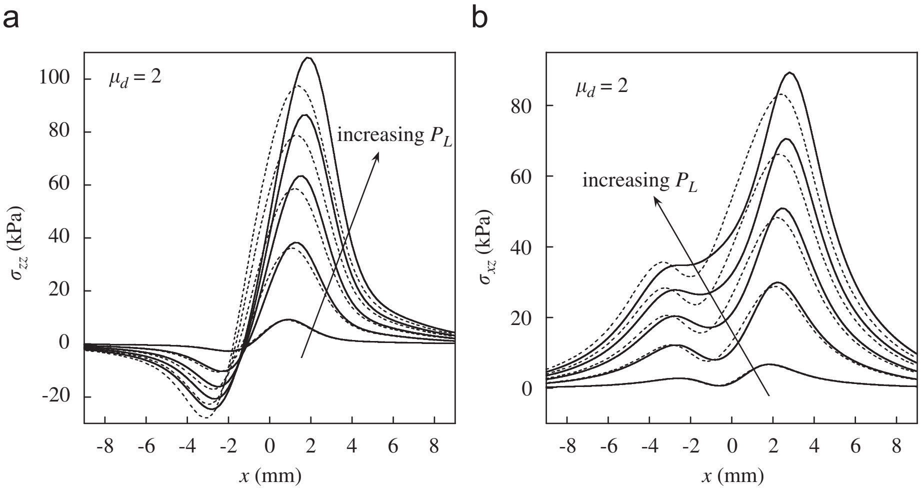

Fig. 9. (a) Normal stress profiles $\sigma_{zz}(x,0)$ and (b) tangential stress profiles along the direction of movement $\sigma_{xz}(x,0)$ calculated at the base of the elastic film with the exact model (solid lines) or with Goodman's model (dashed lines). P_L increases from 20 to 380 Pa m^{-1} with steps of 80 Pa m^{-1} for the same friction coefficient $\mu_d = 2.0$. The contact widths are equal to that given in the legend of Fig. 7(b). The following parameters were used: $E = 2.2$ MPa, $R = 130$ mm, $h = 2$ mm.

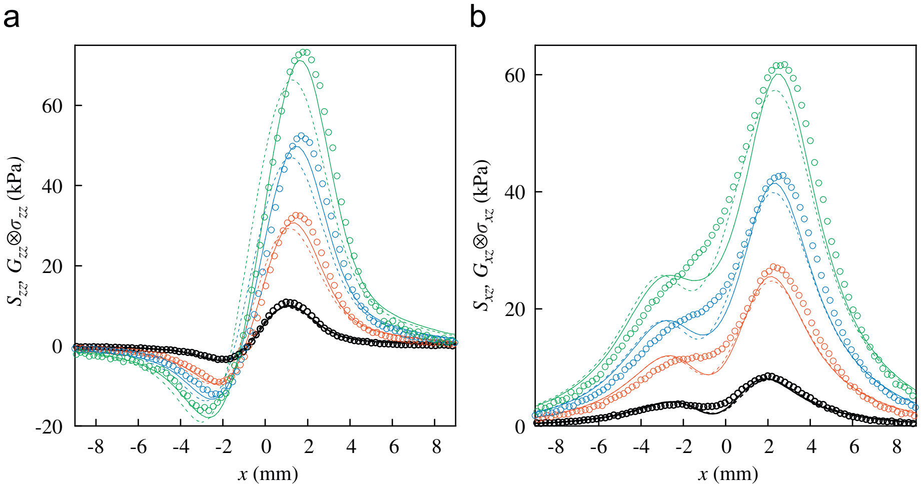

Fig. 10. (Color online) Measured stress profiles (◦, for clarity only one percent of the data points is shown) at $y = 0$ (a) S_{zz} and (b) S_{xz} in steady sliding regime for increasing normal loads ($P = 0.34$ N in black, 1.03 N in red, 1.72 N in blue and 2.75 N in green) and $V = 1$ mm s^{-1}. Comparison is made with (a) $G_{zz} \otimes \sigma_{zz}$ and (b) $G_{xz} \otimes \sigma_{xz}$ where σ_{zz} and σ_{xz} are computed from the exact model (solid lines) or from Goodman's model (dashed lines).

P_L and a given friction coefficient μ_d. Goodman's model yields qualitatively similar results but with growing errors for increasing P_L or μ_d. In particular, Goodman's model underestimates the amplitude of the maxima of both stress components at positive x and overestimates the amplitude of both the negative part of the normal stress and the dip in the tangential profiles at negative x.

The measured stress profiles $S_{zz}(x)$ and $S_{xz}(x)$ along $y = 0$ can be now quantitatively compared to the stress profiles $\sigma_{zz}(x)$ and $\sigma_{xz}(x)$ calculated at the base of the elastic film and convoluted with the apparatus functions G_{zz} and G_{xz} determined in Section 2. In the limit of a bidimensional geometry, the input parameters used in the calculation—namely the applied lineic load P_L and the dynamic friction coefficient μ_d—should ideally be deduced from the macroscopic measurements of P (the normal load) and Q (the tangential load) by using P/L and Q/P, respectively, with L being the contact length. This approach yields inconsistent stress profiles for two reasons. First, with our finite sized punch experimental system, the contribution of edge effects to the total normal load P is not negligible. For a given x, the interfacial pressure has a minimum around $y = 0$, so that P/L over-estimates the effective lineic load at the location of the measured profile. Second, the measured macroscopic friction coefficient Q/P turns out to be a decreasing function of P (and thus of the local pressure), assuming values from 1.5 ± 0.1 at $P = 0.34$ N down to 1.36 ± 0.04 at $P = 2.75$ N, which are typical for PDMS on glass steady sliding contacts (see e.g. Galliano et al., 2003; Wu-Bavouzet et al., 2007). These averaged values under-estimate the effective friction coefficient at the location of the measured profile since the pressure has a minimum around $y = 0$. To circumvent this difficulty, we extracted P_L and μ_d from the measured stress profiles as $P_L = \int_{-\infty}^{\infty} S_{zz}\,dx$ and $\mu_d = \int_{-\infty}^{\infty} S_{xz}\,dx / \int_{-\infty}^{\infty} S_{zz}\,dx$. With such definitions, P_L is found to increase from 20 to 220 N m^{-1} and μ_d to decrease from 2.6 to 2.0 when P varies from 0.34 to 2.75 N.

Fig. 10 shows the measured profiles together with the predicted stress profiles convoluted with the apparatus functions, for both our exact model and Goodman's model. The two calculations predict profiles in reasonable agreement with the experimental ones. In particular, they account for both the negative part of $S_{zz}(x)$ and the dip of $S_{xz}(x)$ at negative x. In order to quantify the deviations between the experimental and calculated profiles, we compute the quantity $\chi = \sqrt{\sum_i (E_i - C_i)^2 / \sum_i E_i^2}$, where E_i are the experimental data points and C_i are the calculated ones. For the tangential stress, both models yield similar values of $\chi = 11 \pm 1\%$, with no clear load dependance. For the normal stress profiles, the exact model yields an almost constant $\chi = 11 \pm 3\%$ over the range of normal loads P explored. For Goodman's model, χ increases with the load, between 12% and 28 %, indicating a decreasingly good fit to the experimental data with increasing P. The exact model is therefore the one that follows most closely the evolution of the experimental profiles with increasing normal load (Fig. 10), which is consistent with the fact that Goodman's assumption is expected to fail as the ratio of contact size a to film thickness h becomes large.

Although the exact model accounts for the data better, non-negligible robust deviations are observed for which we do not have any definitive explanation. Two central assumptions used in both models are, however, amenable to refinement and may explain the observed deviations. First, the interface is assumed to be molecularly smooth, whereas the surface of the elastomer exhibits a micrometric roughness. The resulting multicontact interface is thus expected to exhibit finite compressive and shear compliances. This feature has been shown to modify, with respect to smooth contacts, both the stress (Greenwood and Tripp, 1967; Scheibert et al., 2008b; Chateauminois and Fretigny, 2008) and displacement (Scheibert et al., 2008a) fields. These effects are expected to induce vanishing corrections at increasingly high loads. The second questionable assumption is the existence of a single pressure-independent friction coefficient. This is clearly at odds with the observed decrease of Q/P as a function of P. Such a behavior is usually attributed to the finite adhesion energy of the interface (e.g. Carbone and Mangialardi, 2004), and is sensitive to the geometrical properties of the film roughness.

6. Conclusion

This work provides the first spatially resolved direct measurement of the stress field at a sliding contact. The choice of a cylinder-on-plane geometry has allowed us to quantitatively compare the profiles measured at the center line of the contact with bidimensional calculations. An exact model was developed to predict the stress field at the sliding contact assuming linear elasticity and a locally valid Amontons' friction law, but without the classical Goodman's assumption on the normal displacements. This model correctly captures the measured stress profiles with typical deviations of less than 14%. In the range of loads explored experimentally, this calculation does not differ drastically from the classical calculation involving Goodman's assumption. However, the present model is expected to provide significant improvements over Goodman's model as the thickness of the film is further reduced or as the load is further increased. In these cases, Goodman's assumption becomes increasingly inaccurate.

Robust deviations between the experiments and the model have been briefly discussed along two lines, namely the finite compliance of the multicontact interface and the pressure-dependence of the friction coefficient. However, the cylinder-on-plane experiment described here, which was specifically designed to allow for a comparison with bidimensional models, is not best suited to study such fine effects. As discussed, the resulting edge effects do not allow one to use well-controlled or measured macroscopic quantities, e.g. P and Q, as input parameters in the models. This could be done for instance with a sphere-on-plane geometry, but it would require for comparison a more complex three-dimensional stress analysis. Work in this direction is in progress.

Appendix A. Goodman's model

The calculation scheme involves first solving the exact model described in Section 4, but with $\mu_d = 0$, to obtain the corresponding interfacial (symmetric) pressure field $p_0(x)$. The second step is to solve the same constitutive equations for the following new boundary conditions:

$$u_x(x,0) = u_z(x,0) = 0 \tag{A.1}$$

$$\sigma_{xz}(x,1) + \mu_d \sigma_{zz}(x,1) = 0 \tag{A.2}$$

$$\sigma_{zz}(x,1) = 0 \quad \text{for } |x| > a \tag{A.3}$$

$$\sigma_{zz}(x,1) = -p_0(x) \quad \text{for } |x| < a \tag{A.4}$$

where $z = 0$ and 1 correspond to the locations of the base and the surface of the elastic film, respectively, and $p_0(x)$ is the pressure field that results from the first step. Eq. (A.1) accounts for the perfect adhesion of the film to its rigid base, Eq. (12) corresponds to Amontons' law of friction with a dynamic friction coefficient μ_d and Eq. (A.3) insures that the surface of the film is traction-free outside the contact zone of width $2a$. Eq. (A.4) corresponds to Goodman's assumption which implies that the interfacial normal stress field is not affected by frictional stress, and so $p_0(x)$ from the previous step is used.

The Fourier transform of Eqs. (A.3) and (A.4) yields

$$\int_0^\infty \sigma_{zz}^{(c)}(k)\cos kx\,dk = 0 \quad \text{for } |x| > a \tag{A.5}$$

$$\int_0^\infty \sigma_{zz}^{(c)}(k)\cos kx\,dk = -p_0(x) \quad \text{for } |x| < a \tag{A.6}$$

Eq. (A.5) is identically satisfied by

$$\sigma_{zz}^{(c)}(k) = \int_0^a F(t)J_0(kt)\,dt \tag{A.7}$$

where $J_0(x)$ is the Bessel function of the first kind. By replacing (A.7) into Eq. (A.6) we get the following integral equations that determine the function $F(t)$:

$$\int_x^a \frac{F(t)}{\sqrt{t^2-x^2}}\,dt = -p_0(x) \equiv \int_x^a \frac{\phi(t)}{\sqrt{t^2-x^2}}\,dt, \quad |x| < a \tag{A.8}$$

where ϕ is the function defined in Eq. (18) (see Section 4) obtained for the particular case where $\mu_d = 0$. The solution for $F(x)$ is readily given by $F(x) = \phi(x)$.

The normal stress $\sigma_{zz}(x,0)$ and the tangential stress $\sigma_{xz}(x,0)$ at the rigid base are then given by

$$\sigma_{zz}(x,0) = \int_0^a [Z_1(x,t) + \mu_d Z_3(x,t)]\phi(t)\,dt \tag{A.9}$$

$$\sigma_{xz}(x,0) = -\int_0^a [\mu_d Z_5(x,t) + Z_3(x,t)]\phi(t)\,dt \tag{A.10}$$

where the kernels $Z_i(x,t)$ and $A(k)$, $B(k)$ and $C(k)$ are given by Eqs. (27)–(35).

References

Adda-Bedia, M., Ben Amar, M., 2001. Fracture spacing in layered materials. Physical Review Letters 86 (25), 5703–5706.

Barbour, P.S.M., Barton, D.C., Fisher, J., 1997. The influence of stress conditions on the wear of UHMWPE for total joint replacements. Journal of Materials Science-Materials in Medicine 8 (10), 603–611.

Bufler, H., May 1959. Zur theorie der rollenden reibung. Archive of Applied Mechanics (Ingenieur Archiv) 27 (3), 137–152.

Carbone, G., Mangialardi, L., 2004. Adhesion and friction of an elastic half-space in contact with a slightly wavy rigid surface. Journal of the Mechanics and Physics of Solids 52 (6), 1267–1287.

Cattaneo, C., 1938. Sul contatto di due corpi elastici: Distribution locale dei sforzi. Rendiconti dell'Accademia nazionale dei Lincei 27, 214.

Chateauminois, A., Fretigny, C., 2008. Local friction at a sliding interface between an elastomer and a rigid spherical probe. European Physical Journal E 27, 221–227.

Chaudhury, M.K., Whitesides, G.M., 1991. Direct measurement of interfacial interactions between semispherical lenses and flat sheets of poly(dimethylsiloxane) and their chemical. Langmuir 7, 1013–1025.

Dundurs, J., Bogy, D.B., 1969. Edge-bonded dissimilar orthogonal elastic wedges under normal and shear loading. Journal of Applied Mechanics 36 (3), 650.

Fretigny, C., Chateauminois, A., 2007. Solution for the elastic field in a layered medium under axisymmetric contact loading. Journal of Physics D: Applied Physics 40 (18), 5418–5426.

Fuller, K.N.G., Tabor, D., 1975. The effect of surface roughness on the adhesion of elastic solids. Proceedings of the Royal Society of London. Series A, Mathematical and Physical Sciences 345 (1642), 327–342.

Galliano, A., Bistac, S., Schultz, J., 2003. Adhesion and friction of PDMS networks: molecular weight effects. Journal of Colloid and Interface Science 265 (2), 372–379.

Gladwell, G.M., 1980. Contact Problems in the Classical Theory of Elasticity. Springer, Berlin.

Goodman, L.E., 1962. Contact stress analysis of normally loaded rough spheres. Transactions of ASME, Series E, Journal of Applied Mechanics 29 (3), 515–522.

Greenwood, J.A., Tripp, J.H., 1967. The elastic contact of rough spheres. Transactions of ASME, Series E, Journal of Applied Mechanics 34, 153.

Guagliano, M., Pau, M., 2007. Analysis of internal cracks in railway wheels under experimentally determined pressure distributions. Tribology International 40 (7), 1147–1160.

Hamilton, G.M., 1983. Explicit equations for the stresses beneath a sliding spherical contact. Proceedings of the Institution of Mechanical Engineers C: Journal of Mechanical Engineering Science 197 (1983), 53–59.

Hamilton, G.M., Goodman, L.E., 1966. The stress field created by a circular sliding contact. Journal of Applied Mechanics 33 (2), 371.

Hills, D., Nowell, D., 1994. Mechanics of Fretting Fatigue. Kluwer Academic Publishers, Dordrecht.

Holmberg, K., Matthews, A., Ronkainen, H., 1998. Coatings tribology-contact mechanisms and surface design. Tribology International 31 (1–3), 107–120.

Howe, R., Cutkosky, M., 1993. Dynamic tactile sensing: perception of fine surface features with stress rate sensing. IEEE Transactions on Robotics and Automation 9, 140–151.

Johnson, K.L., 1985. Contact Mechanics. Cambridge University Press, Cambridge.

King, R.B., O'Sullivan, T.C., 1987. Sliding contact stresses in a two-dimensional layered elastic half-space. International Journal of Solids and Structures 23 (5), 581–597.

Kuznetsov, Y.A., 1978. The superposition principle in the solution of contact friction stress problems. Wear 50 (1), 183–189.

Mark, J.E. (Ed.), 1999. Polymer Data Handbook. Oxford University Press, Oxford.

Mindlin, R.D., 1949. Compliance of elastic bodies in contact. Transactions of ASME, Series E, Journal of Applied Mechanics 16, 259.

Nowell, D., Hills, D.A., 1988. Contact problems incorporating elastic layers. International Journal of Solids and Structures 24 (1), 105–115.

Poritsky, H., 1950. Stresses and deflections of cylindrical bodies in contact with application to contact of gears and of locomotive wheels. Journal of Applied Mechanics—Transactions of the ASME 17 (2), 191–201.

Scheibert, J., 2008. Mécanique du contact aux échelles mésoscopiques. Edilivre, Collection Universitaire.

Scheibert, J., Debrégeas, G., Prevost, A., 2008a. Micro-slip field at a rough contact driven towards macroscopic sliding. Arxiv:0809.3188v1.

Scheibert, J., Leurent, S., Prevost, A., Debrégeas, G., 2009. The role of fingerprints in the coding of tactile information probed with a biomimetic sensor. Science 323, 1503–1506.

Scheibert, J., Prevost, A., Frelat, J., Rey, P., Debrégeas, G., 2008b. Experimental evidence of non-Amontons behaviour at a multicontact interface. EPL 83 (3), 34003.

Shi, Z., Ramalingam, S., 2001. Stresses in coated solids due to normal and shear tractions on an elliptical region. Surface and Coatings Technology 138 (2–3), 192–204.

Spence, D.A., 1975. The hertz contact problem with finite friction. Journal of Elasticity 5 (3), 297–319.

Talke, F.E., 1995. On tribological problems in magnetic disk recording technology. Wear 190 (2), 232–238.

Wu-Bavouzet, F., Clain-Burckbuchler, J., Buguin, A., De Gennes, P.G., Brochard-Wyart, F., 2007. Stick-slip: wet versus dry. The Journal of Adhesion 83 (8), 761–784.

Eur. Phys. J. E (2013) **36**: 17
DOI 10.1140/epje/i2013-13017-0

THE EUROPEAN PHYSICAL JOURNAL E

Regular Article

Probing the micromechanics of a multi-contact interface at the onset of frictional sliding

A. Prevost[1,a], J. Scheibert[2], and G. Debrégeas[1]

[1] CNRS/UPMC Univ Paris 06, FRE 3231, Laboratoire Jean Perrin LJP, F-75005, Paris, France
[2] Laboratoire de Tribologie et Dynamique des Systèmes, CNRS, Ecole Centrale de Lyon, Ecully, France

Received 31 May 2012 and Received in final form 24 October 2012

Abstract. Digital Image Correlation is used to study the micromechanics of a multi-contact interface formed between a rough elastomer and a smooth glass surface. The in-plane elastomer deformation is monitored during the incipient sliding regime, *i.e.* the transition between static and sliding contact. As the shear load is increased, an annular slip region, in coexistence with a central stick region, is found to progressively invade the contact. From the interfacial displacement field, the tangential stress field can be further computed using a numerical inversion procedure. These local mechanical measurements are found to be correctly captured by Cattaneo and Mindlin (CM)'s model. However, close comparison reveals significant discrepancies in both the displacement and stress fields that reflect the oversimplifying hypothesis underlying CM's scenario. In particular, our optical measurements allow us to exhibit an elasto-plastic-like friction constitutive equation that differs from the rigid-plastic behavior assumed in CM's model. This local constitutive law, which involves a roughness-related length scale, is consistent with the model of Bureau *et al.* (Proc. R. Soc. London, Ser. A **459**, 2787 (2003)) derived for homogeneously loaded macroscopic multi-contact interfaces, thus extending its validity to mesoscopic scales.

1 Introduction

The transition from static to sliding friction is a crucial process in various fields, ranging from contact mechanics [1], earthquakes dynamics [2] to human/humanoid object grasping [3]. In the classical Amontons-Coulomb's framework, when two solids are brought in contact under a normal load P and subjected to a shear force Q, no relative motion occurs until Q exceeds some threshold value $Q_s = \mu_s P$, where μ_s is called the static-friction coefficient. However, in most real situations, the transition from static to dynamic friction does not follow this ideal simple scenario. As soon as $Q > 0$, partial slippage generally sets in owing to the large stress heterogeneity within the contact zone, which depends on the geometry of the objects in contact as well as on the loading conditions. Understanding this incipient sliding regime thus requires to gain access to the interfacial micromechanics within the contact zone.

In the past ten years, several experimental groups developed new optical methods to obtain spatially resolved mechanical measurements [4–8], which triggered intense subsequent theoretical and numerical investigations [9–15]. Fineberg and collaborators studied the onset of sliding of a multi-contact interface, in a plane-plane contact configuration, submitted to an adiabatic tangential loading [6,7]. Using fast imaging of the interface illuminated with an evanescent laser sheet, they were able to measure local changes in the real area of contact. This simple optical measurement allowed them to reveal that, prior to macroscopic sliding, a series of dynamical rupture fronts travelled along the interface. In their experiments however, the contact was one-dimensional. Chateauminois and collaborators have considered more realistic, fully two-dimensional, contacts [16,17]. By patterning a smooth elastomer's surface with a regular grid of micro-markers, they were able to monitor, using Particle Image Velocimetry techniques, the entire 2D displacement field at the interface. They applied this procedure to a smooth sphere loaded against a *smooth* flat elastomer block in a *torsional* configuration [17]. The authors showed that the transition from static to kinetic friction involves an annular micro-slip front propagating from the outer edge of the circular contact towards the center. Using an inversion procedure, they computed the interfacial shear stress field from the measured displacements field. We emphasize that in their experiment, macroscopic adhesion was important due to the smoothness of the surfaces in contact. In most practical situations however, interfaces are rough at microscopic length scales, giving rise to a multi-contact frictional interface at which macroscopic adhesive effects are strongly reduced.

In this paper, we expand on this latter two-dimensional approach. We report on micromechanical measurements

---

[a] e-mail: `alexis.prevost@upmc.fr`

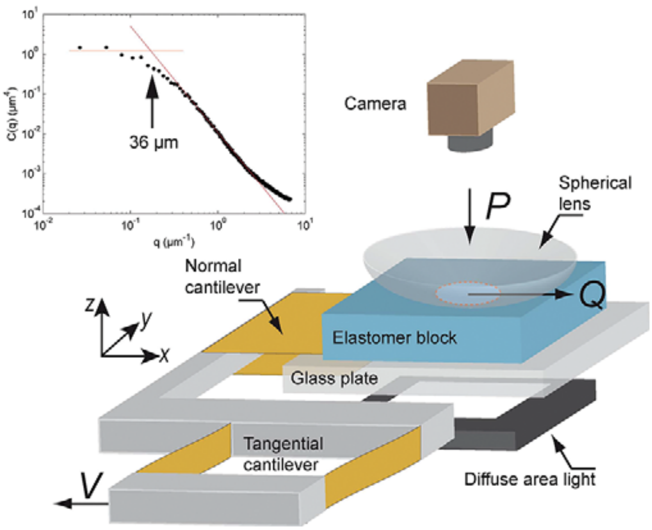

Fig. 1. (Color online) Sketch of the experimental setup. The normal cantilever used to measure P has a stiffness $k_N = 689 \pm 5\,\mathrm{N\,m^{-1}}$, while the tangential cantilever used to measure Q has a stiffness $k_T = 9579 \pm 25\,\mathrm{N\,m^{-1}}$. Inset: log-log plot of the height power spectrum $C(q)$ with q the norm of the wave vector, as defined in [18], for the PDMS block used in these experiments. The thin red horizontal line is a guide for the eye, while the oblique one is a power law fit of exponent ~ -2.67.

at the onset of sliding between a smooth sphere and a flat elastomer block whose surface is microscopically rough. There are several important differences with respect to [17]. First, the interface is of the multi-contact type. Second, the loading is linear instead of torsional. Third, the displacement field measurement is truly non-invasive as we take advantage of the optically diffusive nature of the multi-contact interface to extract the displacement fields at all times using Digital Image Correlation (DIC), from which the interfacial stress fields can be further computed.

In sect. 2, we present the experimental setup and sample preparation and show how the displacement field is extracted from successive images of the interface. Macroscopic force measurements and resulting displacement fields are then presented in sect. 3. Section 4 details the procedure used to compute the interfacial stress fields from the measured displacement fields. In sect. 5, these results are compared to the predictions of Cattaneo and Mindlin (CM)'s classical contact mechanics model. In sect. 6, we interpret the observed deviations as the effect of the rough layer, which introduces a micrometric length scale in the problem. Eventually, in sect. 7, general conclusions and perspectives are drawn.

2 Experiment, materials and methods

2.1 Experimental setup

Figure 1 shows a sketch of the experimental setup. It consists of a planoconvex glass lens (optical grade, Thorlabs LA1301, BK7, radius of curvature $R = 128.8\,\mathrm{mm}$) glued onto a lens holder and rigidly attached to an optical table. The lens surface is in frictional contact against a thick elastomer block maintained by van der Waals adhesion to a supporting glass plate. The latter is connected *via* a set of two orthogonal cantilevers to a translation stage that can be driven at constant velocity V using a DC actuator (LTA-HL, Newport Inc.). Two capacitive position sensors (respectively, MCC-20 and MCC-10, Fogale Nanotech), each facing the mobile part of one cantilever, allow one to measure both P and Q, respectively the normal and tangential (shear) force, with a 1 mN resolution in the range [0–2 N]. Both force signals are digitized and recorded at a sampling rate of 1 kHz using a NI-PCI6251 DAQ board. Imaging of the contact is done by illuminating the interface through the transparent elastomer block with a white LED diffusive array and a long-working distance Navitar objective. Images of the interface are recorded with a CCD camera (Redlake ES2020M, 1600×1200 pixels^2, 8 bits, 24 frames/s at maximum). Synchronization between the camera and the DAQ acquisition device is ensured by having the DAQ board trigger the camera.

2.2 Sample preparation and characterization

The elastomer block ($50 \times 50\,\mathrm{mm}$, thickness 15 mm) is made of crosslinked PolyDiMethylSiloxane (PDMS Sylgard 184, Dow Corning). It is obtained by mixing in a 10:1 stoichiometric ratio a PDMS melt and a cross-linker agent in a rectangular mold. The mixture is cured for 48 hours in an oven at 70 °C. The free surface of the elastomer block is rendered rough by mechanically abrading the lid's upper surface with a silicon carbide powder solution of typical grain size 17 μm. After careful demoulding, the surface roughness of the PDMS sample is characterized with an optical profilometer (M3D, Fogale Nanotech). Its height power spectrum [18] is found to decay as a power law from a maximum value of $\sim 30\,\mu$m down to the micrometer scale (fig. 1, inset). The characteristic thickness h of the rough interface, defined as the standard deviation of the height distribution, is measured to be $0.595 \pm 0.013\,\mu$m.

Such PDMS elastomers have been reported to have a bulk elastic Young's modulus E in the range [2–4 MPa] [16,19–21] (depending on the preparation protocol) and a Poisson's ratio ν close to 0.5 [22]. For the sample used in these experiments, a JKR test is performed between its smooth back side and the bare glass lens, yielding a Young's modulus $E = 3.43 \pm 0.05\,\mathrm{MPa}$. For the friction experiments, the glass lens surface is passivated in a PerfluoroDecylTricloroSilane saturated vapor phase in order to reduce the macroscopic PDMS/glass adhesion and to minimize heterogeneities in the interfacial properties. Prior to each experiment, both glass and PDMS surfaces are cleaned with ethanol and dried with filtered air.

2.3 Contact imaging and displacement fields measurements

2.3.1 Contact imaging

Figure 2a shows a typical image of the elastomer/glass interface under normal load. This image is obtained in

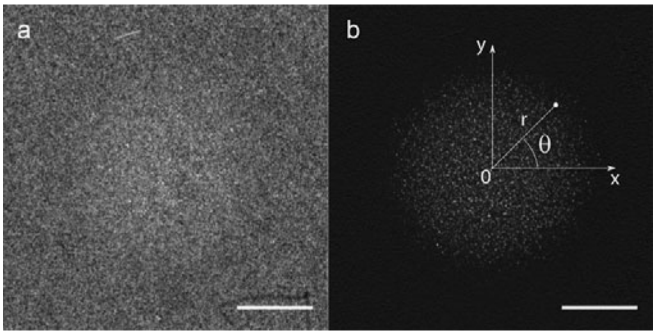

Fig. 2. (a) Image of the interface at $P = 0.1$ N. (b) Difference between image (a) and a reference image without contact. For both images, the white bar is 1 mm long. In (b) are shown the x and y axis along with the r, θ coordinates system.

transmission geometry by illuminating the sample with a diffuse white light. The interface appears spatially heterogeneous as a result of the diffusive nature of the rough layer. In the contact region, additional bright spots are present corresponding to the micro-junctions that favorably transmit light at the glass-PDMS interface. At the chosen magnification, images have a field of view of about 11.2×8.4 mm (with a pixel size of $\sim 7.04\,\mu$m). The contact region is difficult to visualize from the raw image (fig. 2a) but can be clearly identified in fig. 2b by subtracting a reference background image recorded prior to the contact[1]. This operation allows one to reveal hundreds of contact-induced micro-junctions contained within a circular (apparent) contact region (fig. 2b for $P = 0.1$ N). These characteristic features of the frictional joint remain true for the explored range of normal load P used in these experiments.

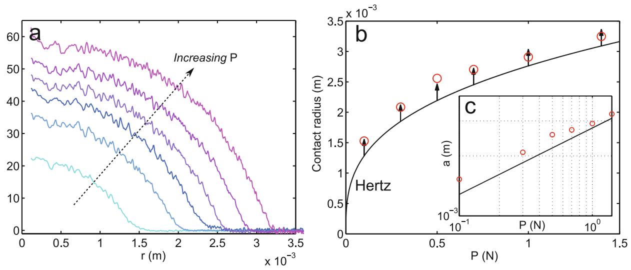

Fig. 3. (Color online) (a) Angularly averaged intensity profiles $I(r)$ for increasing loads P. The lowest P curve is in cyan, while the highest one is in pink. This color code is kept within this paper to describe any normal dependence of the variables involved. (b) Apparent contact radius *versus* P. The red circles correspond to the measured apparent contact radius a. The thin black line is Hertz contact radius a_H with $E = 3.43$ MPa. Black vertical arrows have the same length, equal to $\sqrt{Rh}$. (c) Inset: same as (b) on a log-log scale. The solid black line corresponding to Hertz prediction has a slope of 1/3.

Taking advantage of the axial symmetry of the contact, the apparent contact radius is computed in the following way. Centers of the apparent contact $r = 0$ are first determined using a standard center of symmetry search algorithm. For each load P, the image intensity $I(x, y)$ is then averaged azimuthally over the angle θ (fig. 3a)[2]. The apparent radius of contact a is then estimated as the minimum radius such that $I(r) = 0$. Figure 3b shows the resulting contact radius a and its load dependence along with Hertz[3] contact radius a_H derived for $E = 3.43$ MPa. As clearly seen, the estimated radius a is systematically larger than a_H. This deviation can be accounted for by taking into account the multi-contact nature of the interface. As established by Greenwood and Tripp [23,24], the surface roughness extends the apparent contact region by a quantity of the order of $\sqrt{Rh} \sim 280\,\mu$m with respect to the smooth configuration. As shown in fig. 3b, such a correction to Hertz's contact radii does allow one to recover the measured apparent contact radii a.

2.3.2 Displacement field measurements

Interfacial displacement fields were computed from snapshots acquired at 8 frames/s ($\Delta t = 0.125$ s), and 4 frames/s for the highest P ($\Delta t = 0.25$ s), using a Digital Image Correlation technique (DIC) (see *e.g.* [25] and references therein). This method consists in finding, for a given sub-image centered at position (x, y) in a reference frame, the displacement (u_x, u_y) that provides the maximum intensity correlation with a subsequent (deformed) image (figs. 4a and b). A 2D correlation function (fig. 4c) was computed using a direct calculation. Sub-pixel resolution was achieved by fitting the correlation function with a 2D Gaussian surface using the pixel of maximum correlation and its 8 nearest neighbors. The error on the displacements was evaluated using a series of images of the surface of the elastomer block, not in contact and uniformly displaced at constant velocity along the x-direction. DIC was performed between an image at $t = 0$ and images at increasing times t, allowing one to extract the displacements u_x between ~ 0.14 pixels and ~ 14 pixels. The error was then taken as the standard deviation of the $u_x - Vt$ displacements distribution. This error was found to decrease with the box size λ, in the range [10–100] pixels (fig. 4d). The optimal λ was chosen based on the best compromise between spatial resolution and displacement measurement accuracy. For the current experiments, the smallest apparent contact radius is ~ 217 pixels long. In order to extract at least 10 independent displacement measurements along the contact, the displacement fields were computed

---

[1] Careful image difference was done to take into account a possible rigid-body displacement of the PDMS block between the unloaded (reference) and loaded situations.

[2] In order to keep the statistical errors constant, the number of pixels within each annulus is kept constant, equal to 3000. Thus, the width of the annuli decreases with their radius r.

[3] Hertz contact is the contact between two non-conforming elastic half-planes having smooth surfaces and well-defined radii of curvature. For instance, the Hertz contact radius a_H in the case of a rigid sphere pressed against an elastic plane is $a_H = (\frac{3PR(1-\nu^2)}{4E})^{1/3}$, with P the normal load, R the sphere radius, and E and ν the Young's modulus and Poisson's ratio of the elastic plane.

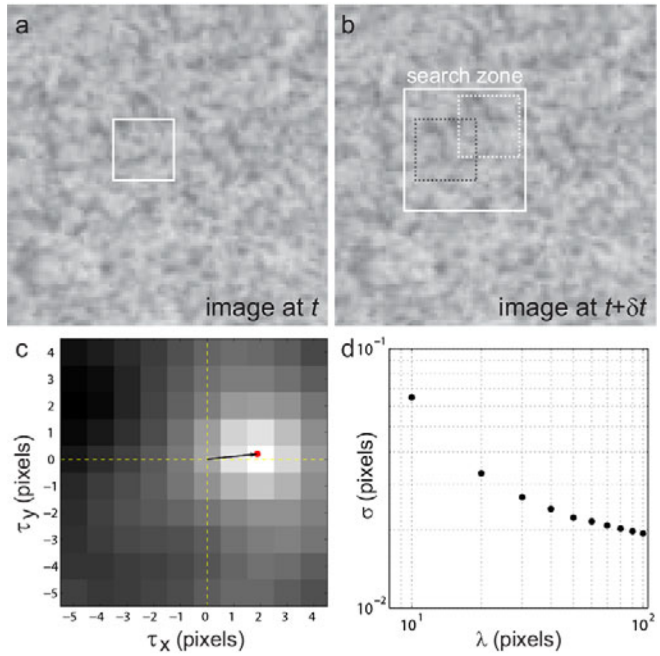

Fig. 4. (Color online) Principles of the DIC measurement. (a) Image at time t. (b) Image at time $t + \delta t$. (c) 2D correlation function $C(\tau_x, \tau_y)$ obtained by correlating the white-line-delimited box in (a) (size $\lambda = 20$ pixels) with boxes in (b) (dashed lines), displaced by (τ_x, τ_y) within the search zone. The red dot indicates the sub-pixel location of the maximum of the correlation function. The black arrow shows the resulting displacement vector. (d) Log-log plot of the standard deviation σ of the displacements distribution *versus* the box size λ.

with $\lambda = 20$ pixels, on a 10 pixels wide square grid, yielding a resolution on the displacement of $\sim$ 0.033 pixels ($\sim$ 232 nm), with a spatial resolution of $\sim 140\,\mu$m.

3 Force and displacement fields

We performed a series of 6 experiments in which the elastomer block was driven at a prescribed velocity[4] $V = 5\,\mu$m/s, under constant normal force P in the range [0.1–1.4 N]. For all runs, P was found to vary by less than 1% over the duration of the experiment and the apparent contact zone remains circular. The velocity V was chosen low enough for visco-elastic interfacial dissipation to be negligible [26]. Since the normal loading of the contact produces a significant shear force due to the small coupling between normal and lateral motion of each cantilever, the contact was manually renewed prior to each experiment, until the initial shear force Q was less than 1% of P. During this separation procedure, no measurable pull-off force was observed, indicating that adhesion forces are negligible [27,28] at the contact length scale.

Figure 5 shows the measured evolution of the tangential Q *versus* $\delta = Vt$ for the 6 values of the normal load $P = \{0.1, 0.3, 0.5, 0.7, 1.0, 1.4\}$ N. Each curve exhibits two distinct phases: an initial quasi-linear loading associated with the incipient sliding regime, followed by a plateau associated with a macroscopic steady sliding regime. The transition between these two regimes involves a monotonous decrease of the slope. In particular, we do not observe any static-friction peak in the loading curve, which hampers a direct determination of the force threshold Q_s at which macroscopic sliding sets on from the sole global force measurements. Q_s was thus determined using the measured displacement fields at the center of the contact as detailed further down.

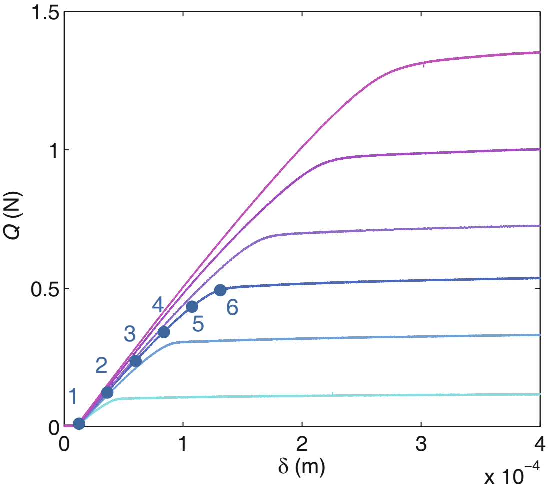

Fig. 5. (Color online) Shear force Q *versus* $\delta = Vt$ for loads $P = 0.1, 0.3, 0.5, 0.7, 1.0, 1.4$ N (bottom to top). The color code is the same as in fig. 3a. Numbered disks from 1 to 6 correspond to the 6 instants at which the displacement and stress fields are displayed, respectively, in figs. 6 and 10.

Displacement fields u_x and u_y at time t were determined by correlating images at time t with a reference image at $t = 0$ prior to any tangential loading using the algorithm described earlier. Since the lens holder is not infinitely rigid, any applied shear force is expected to induce minute rigid-body displacement of the lens that needs to be subtracted from the measured displacement u_x. To quantify this compliance effect, we independently measured the displacement of the lens holder while tangentially loading the elastomer block under controlled shear force using the same correlation technique. The solid lens displacement was found to vary linearly with Q, yielding a shear stiffness $\approx 0.68\,\mu\mathrm{m\,N}^{-1}$. Actual interfacial displacements along the x-direction were then corrected for this finite compliance effect.

Figure 6 shows the typical u_x and u_y displacement fields at $P = 0.5$ N for all 6 positions in fig. 5. As soon as Q increases, the displacement in the outer region of the apparent contact increases. In contrast, the measured displacement remains essentially null within a central circular region. As Q increases, the radius c of this stick region decreases and eventually vanishes, marking the onset of the macroscopic sliding phase. Figure 7 shows the time evolution of the displacement $u_x(r)$, averaged over the azimuthal angle θ, for different radii $r = \{0, 0.5a, 0.75a, a\}$

---

[4] In practice, the actual velocity was slightly smaller than the prescribed velocity, decreasing monotonically from 4.9 μm/s at $P = 0.1$ N to 4.76 μm/s at $P = 1.4$ N.

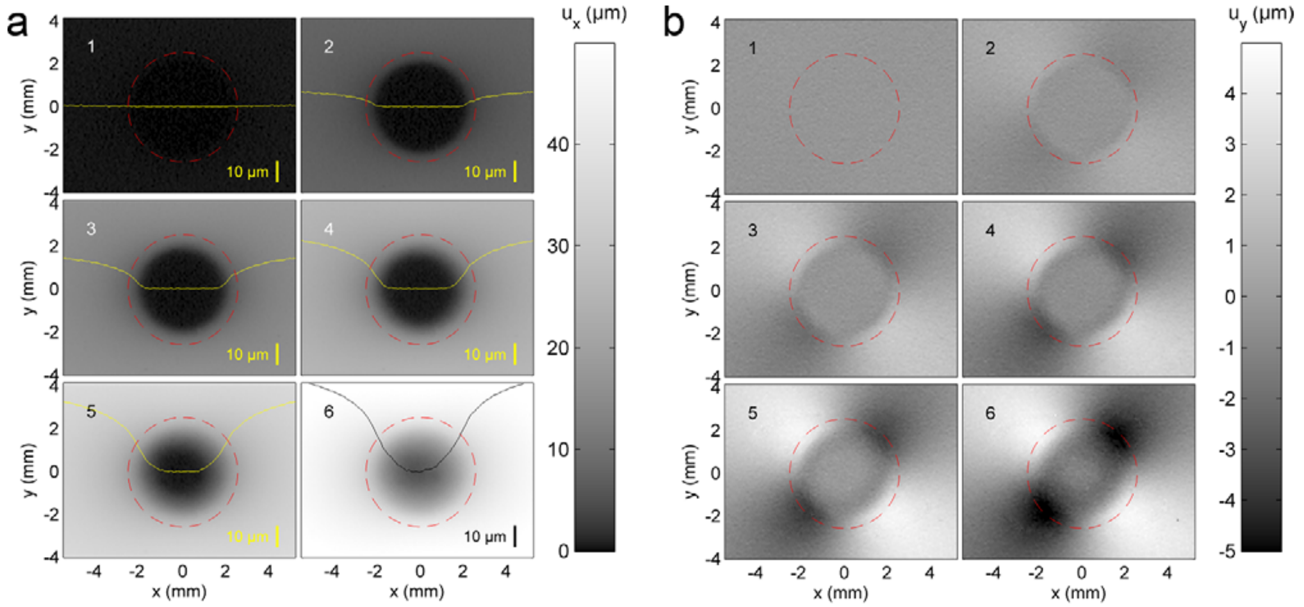

Fig. 6. (Color online) Snapshots of the 2D displacement fields u_x and u_y at $P = 0.5\,\mathrm{N}$ for the loading experiment of fig. 5 taken at instants labeled 1 to 6. On all displacement fields, the red dashed circle delimits the initial apparent contact area of radius a as determined in sect. 2.3.1, without any shear applied. Checks were done that upon shearing, a does not change. The yellow curves (respectively black curve) on snapshots indexed 1 to 5 (respectively 6) are cuts of the u_x 2D displacements fields at $y = 0$ and are meant as visual guides. (a) u_x displacement fields. (b) u_y displacement fields.

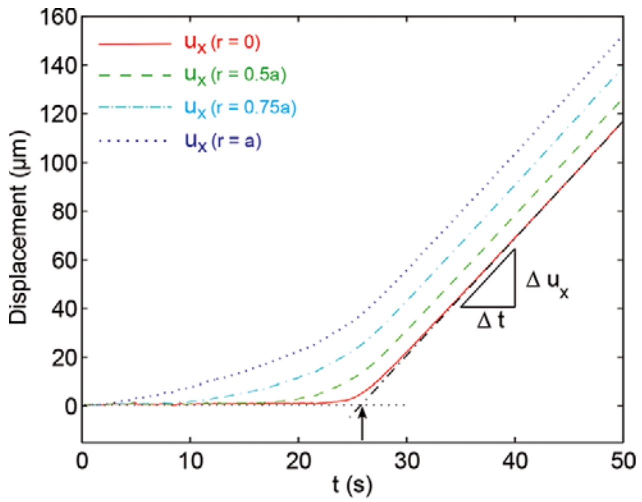

Fig. 7. (Color online) Angularly averaged radial displacement $u_x(r)$, with $r = 0$ being the center of the contact, for values of $r = 0, 0.5a, 0.75a, a$ at a normal load $P = 0.5\,\mathrm{N}$. The ratio $\frac{\Delta u_x}{\Delta t}$ is $\sim 4.81\,\mu\mathrm{m/s}$. The horizontal black dotted line is the $y = 0$ axis. The dashed dotted line is a linear fit of $u_x(r = 0)$ at long times. The intersection of both lines, shown with the vertical black arrow, was arbitrarily chosen as the definition for the onset time of macroscopic sliding.

at a normal load $P = 0.5\,\mathrm{N}$. In the fully developed sliding regime, the displacement u_x varies linearly and uniformly with time t (while u_y remains stationary), indicating that the PDMS sample is sliding as a whole at the driving velocity. In the incipient sliding regime, the time evolution of the displacement u_x strongly depends on r. As previously mentioned, the transition to sliding initiates in the outmost part of the contact zone and is completed when the center region (corresponding to the $r = 0$ curve) starts sliding. In order to properly extract the onset time t_s of macroscopic slippage, the central displacement time signal $u_x(r = 0)(t)$ is used. The time t_s is evaluated as the intersection between the linear fit of $u_x(r = 0)(t)$ at long times and the time axis. This time of macroscopic slippage allows us to unambiguously identify a threshold force Q_s and an associated macroscopic friction coefficient $\mu_s = Q_s/P$. The dynamical friction coefficient is further defined as $\mu_d = Q(t \geq t_s)/P$. Figure 8, which shows both friction coefficients *versus* P, indicates that μ_s and μ_d both display a slow decay with P, as it is usually found for elastomers [20,29].

4 Tangential stress fields

Tangential stress fields at the contacting interface were derived using a Green's tensor inversion procedure as described in [16]. For a semi-infinite elastic medium, the Green's tensor characterizes the displacements at the interface induced by a point force applied at the free surface [30]. In the limit of a semi-infinite and incompressible elastic body, two assumptions which are well suited to our experiments, the lateral and vertical displacements are decoupled, allowing one to express the lateral displacements as a function of the lateral shear stresses only [20]. For a point loading (Q_x, Q_y), the surface displacements u_x and

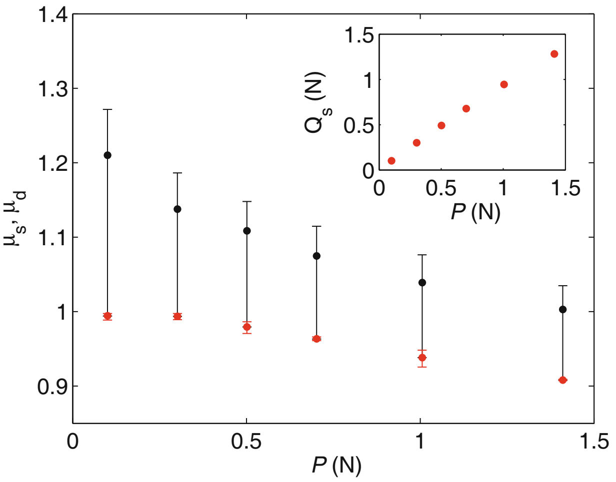

Fig. 8. (Color online) Friction coefficients μ_s (lower red disks) and μ_d (upper black disks) *versus* P. μ_s is defined as the ratio Q_s/P, where Q_s (shown in the inset) has been determined as described earlier and schematically shown in fig. 7. μ_d is taken as the mean of Q/P for all $Q \geq Q_s$. Minimum and maximum values of μ_d over this range are shown with the black vertical segments surrounding each point.

u_y are thus given, respectively, by

$$u_x = G_{xx}Q_x + G_{xy}Q_y,$$
$$u_y = G_{yx}Q_x + G_{yy}Q_y, \qquad (1)$$

with the components of the Green's tensor $\underline{G}$ given by

$$G_{xx} = \frac{3}{4\pi E}\left(\frac{1}{r} + \frac{x^2}{r^3}\right),$$
$$G_{xy} = G_{yx} = \frac{3}{4\pi E}\left(\frac{xy}{r^3}\right),$$
$$G_{yy} = \frac{3}{4\pi E}\left(\frac{1}{r} + \frac{y^2}{r^3}\right). \qquad (2)$$

For an extended contact, u_x and u_y are obtained by convolving $\underline{G}$ with the shear stress at the interface $\underline{\sigma}$ and can be formally written as

$$u_i = G_{ij} * \sigma_{jz}, \qquad (3)$$

where subscripts i, j stand for x or y. The stress fields σ_{xz} and σ_{yz} can then be obtained by deconvolution. This was done as in [16] using a classic iterative Van-Cittert algorithm. The stress at step $n+1$ is obtained by adding to the one at time n a corrective term[5] proportional to the difference between the experimental displacement and the convolved one obtained using eq. (3). Convergence was considered to be attained when the rms difference between the calculated and the measured displacements was less than the displacement resolution, *i.e.* 0.033 pixels.

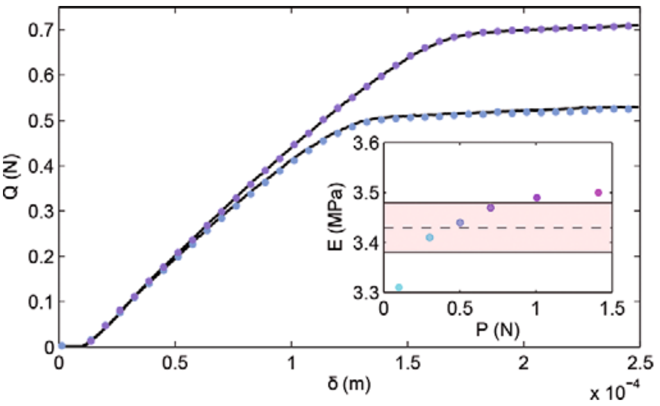

Fig. 9. (Color online) Comparison between Q *versus* δ curves as measured in the experiment (black solid lines) and obtained by summing up the shear stress within the contact zone (dots), at $P = 0.5$ N (lower curve) and $P = 0.7$ N (upper curve). For clarity, 1 experimental point out of 10 is shown. Inset: optimum E values *versus* P. The shaded area represents the value $E = 3.43 \pm 0.05$ MPa obtained with the JKR test (see sect. 2.2).

The inversion procedure provides shear stress fields in units of Young's modulus E (see eqs. (2) and (3)). The value of E can then be directly fitted from the comparison between the shear force signal $Q(t)$, obtained through spatial integration of the calculated shear stress over the contact, and the actual measured force signal. As shown in fig. 9 for $P = 0.5$ N and $P = 0.7$ N, the match between both signals is very satisfactory, which validates the inversion method. The extracted Young's modulus shows a weak though systematic dependence with the load (see inset) which is presumably due to the effect of finite thickness of the PDMS block as discussed in [31]. However, except for the two extreme load values, it remains within the error bars of E as independently measured with the JKR test. Note that in the determination of the stress fields, we have used the fitted values for E rather than the JKR value.

Figure 10 displays the shear stress fields σ_{xz} computed at successive moments (indicated by the 6 labeled dots in fig. 5) during the incipient sliding phase. As expected, in all 6 configurations, the shear stress vanishes outside the apparent contact zone whose border is indicated by a red dashed circle. Within the contact, σ_{xz} is radially symmetric with respect to the center of the contact. Once macroscopic sliding has initiated (position 6), σ_{xz} is maximum at the center of the contact and decreases continuously towards the edge of the contact. During the transient loading, however, the shear stress exhibits a local minimum at the center of the contact.

5 Comparison with models predictions

These precise local mechanical measurements are directly amenable to comparison with existing theoretical models of incipient sliding. The first model, for a non-adhesive elastic sphere-on-plane contact, was derived independently by Cattaneo and Mindlin (CM) [32,33]. Since

---

[5] In practice, an initial guess at step $n = 0$ is taken as proportional to the experimental displacements. Such an iterative deconvolution procedure can very rapidly lead to numerical divergence if not slowed down. Empirically, only 5% of the difference in displacements is thus added to the stress at step n, enabling convergence in typically hundreds of iterations.

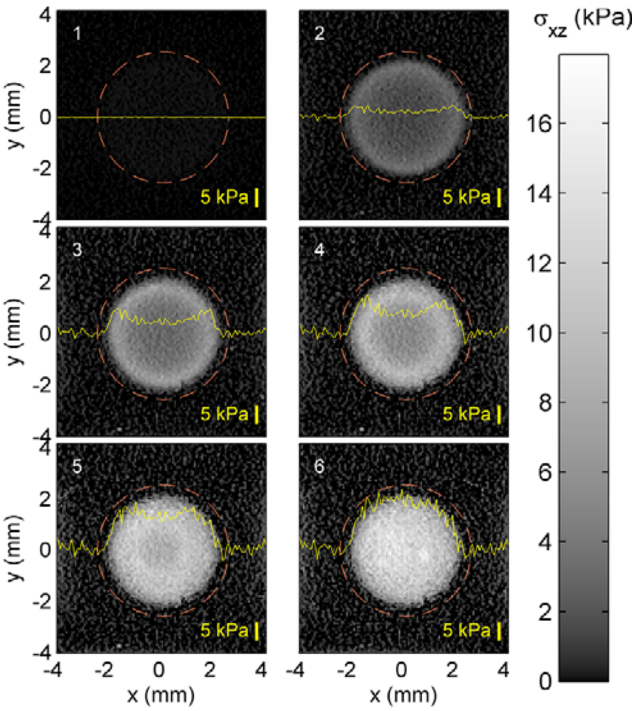

Fig. 10. (Color online) Snapshots of the 2D stress fields $\sigma_{xz}(x,y)$ at $P = 0.5\,\mathrm{N}$ for the loading experiment of fig. 5 taken at instants labeled 1 to 6. The yellow curves are cuts along $y = 0$ and are intended to ease the visualization of a lower stress region around the center. On all stress fields, the red dashed circle delimits the initial apparent contact area a as determined in sect. 2.3.1.

then, this classic model has been refined and extended in various ways (see *e.g.* [1,34,35] and references therein), for instance by introducing macroscopic adhesion [36,37] or elasto-plasticity of the materials [38]. Since i) adhesive forces were found to be negligible in our experiments (no measurable pull-off force upon retraction of the contact) and ii) PDMS was used well within its linear elastic limit[6], our measurements were compared to CM's model.

CM's calculations assume that 1) both surfaces are *smooth*, 2) the pressure distribution σ_{zz} within the contact is unchanged upon shearing and given by Hertz contact theory, and 3) Amontons-Coulomb's law of friction is valid locally at any position within the contact, *i.e.* slip occurs wherever the shear stress σ_{xz} reaches $\mu\sigma_{zz}$, μ being the macroscopic friction coefficient[7]. CM's model predicts the coexistence of an inner adhesive circular region of radius c, which decreases with Q according to

$$c = a_H \left(1 - \frac{Q}{\mu P}\right)^{1/3}, \qquad (4)$$

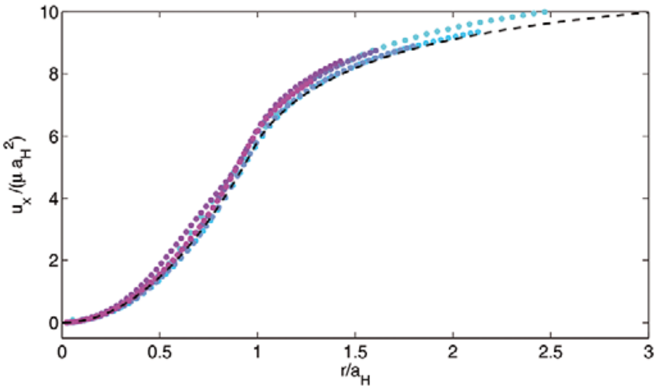

Fig. 11. (Color online) $u_x/(\mu {a_H}^2)$ in m^{-1}, in steady sliding *versus* r/a_H at all P (the color code is the same as in figs. 3 and 5). The dashed black line represents Johnson's prediction with $E = 3.43\,\mathrm{MPa}$. The value of μ is obtained by averaging over all images in steady sliding, *i.e.* for all $t \geq t_s$.

surrounded by an outer slip annulus, which is in full qualitative agreement with our experimental results. Using a superposition principle, CM's calculations provide complete analytic expressions for σ_{xz}, σ_{yz}, u_x and u_y within the contact, in both stick and slip regions [1,34]. Further derivations by Johnson [1] also give u_x and u_y outside the contact, thus providing the entire displacement field at the interface. Note that CM's model has previously been supported by global force and displacement measurements as well as by wear trace inspection [40,41]. However, no comparison had yet been performed on the displacement and stress distributions at mesoscopic scales.

Figures 11 and 12 show a direct comparison (*i.e.* without any adjustable parameter) between the measured and predicted displacement fields, in steady sliding and during the loading phase, respectively (see appendix A for the predicted u_x field expressions). In steady sliding (fig. 11), all $u_x(r)$ curves at all loads have been rescaled by $\mu {a_H}^2$, with $\mu = \langle \mu_d \rangle = \langle Q(t \geq t_s) \rangle / P$, where $\langle\,\rangle$ stands for time averaging, and a_H is the Hertz contact radius computed using the value of Young's modulus E deduced from the JKR test, *i.e.* $E = 3.43\,\mathrm{MPa}$. The agreement with CM is found to be good at all normal loads P. During the transient loading (fig. 12), a similar overall agreement is achieved, for both u_x averaged over the azimuthal angle θ (fig. 12a) and for its angular dependence (fig. 12b). However, a closer look at fig. 12a reveals that significant deviations occur as Q increases, becoming more pronounced as Q reaches Q_s. To quantify these deviations, fig. 12c displays, for the example of $P = 0.3\,\mathrm{N}$, the difference $\Delta u_x(r)$ between the measured displacements and CM's predictions at 4 different positions, 3 within the contact ($r = \{0, 0.5a_H, a_H\}$) and 1 outside of it at $r = 1.5a_H$, as a function of Q. As clearly shown, $\Delta u_x(r)$ increases with Q reaching a maximal value of a few μm when $Q \sim Q_s$ at all points r, with $Q_s = 0.3\,\mathrm{N}$. Such deviations will be extensively discussed further down.

Similarly, the tangential stress fields $\sigma_{xz}(x,y)$ were angularly averaged to obtain $\sigma_{xz}(r)$ at all shear loads Q

---

[6] Strains obtained by deriving the displacement fields do not exceed 3%. This is well within the linearly elastic regime of the material [39].

[7] CM's model postulates the existence of a single, stress-independent friction coefficient, *i.e.* static- and dynamic-friction coefficients are equal, and thus predicts no static overshoot in the Q curve.

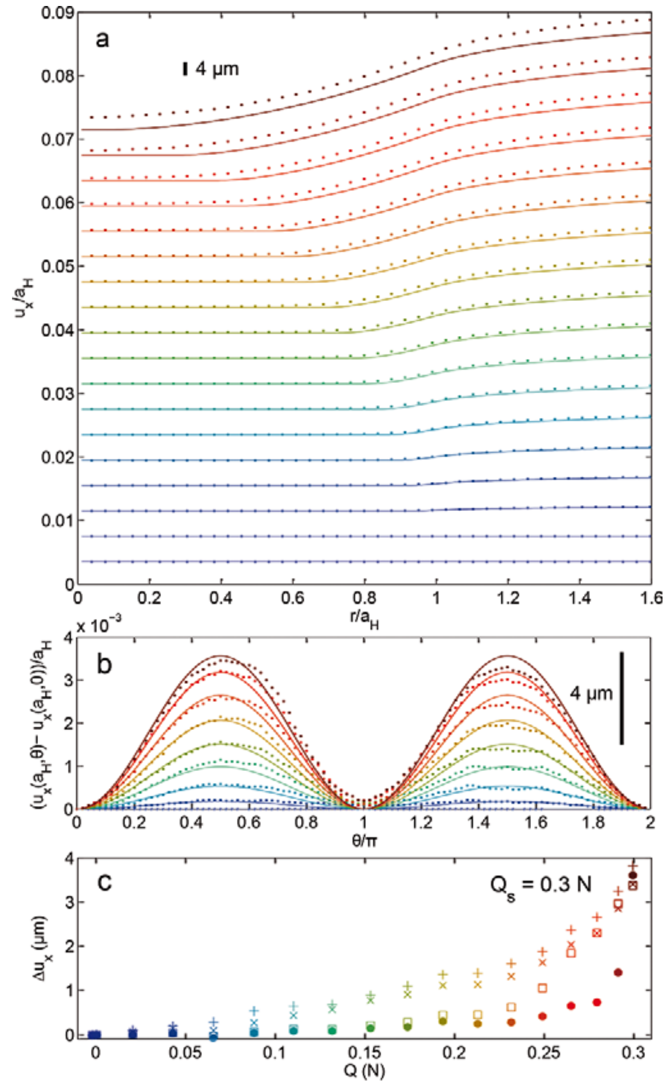

Fig. 12. (Color online) (a) $u_x(r)/a_H$ *versus* r/a_H in the loading phase for $P = 0.3\,\mathrm{N}$ ($a_H \approx 1.85\,\mathrm{mm}$), shown for 1 out of 8 images, *i.e.* every 1 second. Points are the measured displacements. Solid lines represent CM's predictions with $E = 3.43\,\mathrm{MPa}$. All curves have been arbitrarily shifted vertically to ease visualization. (b) $(u_x(a,\theta)-u_x(a,0))/a_H$ *versus* θ/π shown for 1 out of 16 images, *i.e.* every 2 seconds, with the same color code and marker convention as in (a). (c) Deviation Δu_x between $u_x(r)$ measured and CM's predictions *versus* Q for $r \sim 0$ (●), $r = 0.5a_H$ (□), $r = a_H$ (×), and $r = 1.5a_H$ (+). The color code is the same as in (a) and (b). The threshold force Q_s is 0.3 N as indicated in the figure.

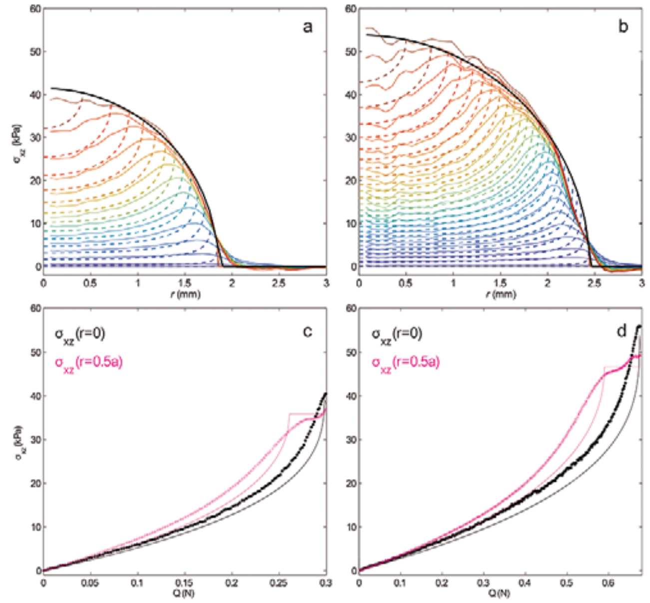

Fig. 13. (Color online) Angularly averaged stress fields $\sigma_{xz}(r)$ at $P = 0.3\,\mathrm{N}$ (a) and $P = 0.7\,\mathrm{N}$ (b). On both plots, the black solid lines represent $\mu_s\sigma_{zz}(r)$ where $\sigma_{zz}(r)$ is here the Hertz pressure profile taking for E the optimum values obtained from the inversion procedure and given in the inset of fig. 9. Small-Q curves are shown in blue, while high-Q curves are in red. Profiles are shown every 1.25 second. Solid lines are the measured stresses, while dashed lines correspond to CM's predictions. (c), (d) $\sigma_{xz}(r = 0)$ and $\sigma_{xz}(r = 0.5a)$ *versus* Q for the data shown in (a) and (b), respectively. Symbols correspond to the measured stresses, while solid lines are CM's predictions.

(fig. 13). When $Q = Q_s$, if one assumes that Amontons-Coulomb's friction law remains valid at a local length scale, one expects the shear and normal stresses to be related with $\sigma_{xz} = \mu_s\sigma_{zz}$. Taking Hertz's pressure profile[8] for σ_{zz}, we have computed $\mu_s\sigma_{zz}$. Figures 13a and b clearly show a rather good agreement between Hertz (black solid line) and our experimental measurements, except for a small tail at the edge of the contact. The latter presumably results from the multi-contact characteristics of the interface, and is to be related to the tail in the intensity profiles as discussed earlier in sect. 2.3.1. When $Q < Q_s$, the stress profiles have qualitatively the same radial dependence as predicted by CM's model and indicated with the dashed lines (figs. 13a and b) (see appendix A for the predicted $\sigma_{xz}(r)$ field expressions). Quantitative analysis however reveals that deviations are clearly present as shown for $\sigma_{xz}(r = \{0, 0.5a\})$ in figs. 13c and d. Yet, these stress profiles provide a mean to extract the diameter of the stick region c. In CM's model, σ_{xz} is maximum at $r = c$. Assuming that it is still true in our case, it is thus possible to give an estimate of c and compare it to CM's predictions given by eq. (4) (fig. 14). Clearly, the agreement for such a macroscopic quantity is good, even though the amplitudes of σ_{xz} are not exactly captured by CM's stress predictions.

6 Local constitutive law of friction

At this point, we have shown that our measurements agree with CM's model, not only qualitatively with the existence of an inner stick region surrounded by a growing annulus

---

[8] In Hertz's contact theory, $\sigma_{zz}(r) = \sigma_0\sqrt{1 - r^2/a_H{}^2}$ with $\sigma_0 = (\frac{6PE^{*2}}{\pi^3 R^2})^{\frac{1}{3}}$ and $E^* = \frac{E}{1-\nu^2}$ is the reduced modulus.

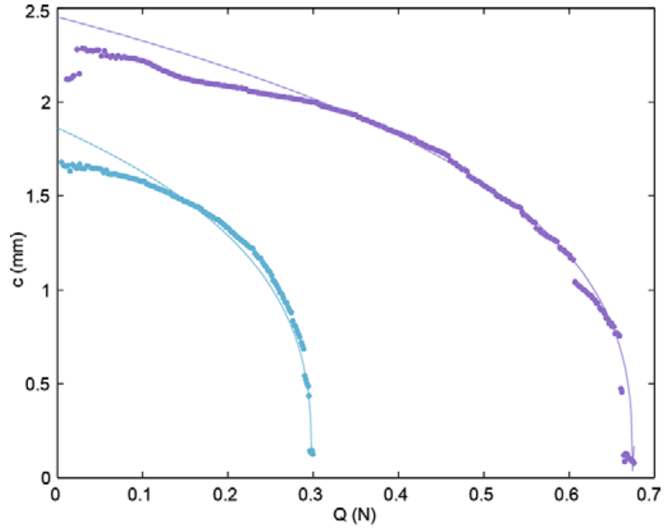

Fig. 14. (Color online) Tangential load dependence of c (●) compared to CM's model predictions (thin solid lines, eq. (4)) for two normal loads, respectively $P = 0.3\,\mathrm{N}$ and $P = 0.7\,\mathrm{N}$. The color code is the same as used in figs. 3 and 5. Sub-pixel determination of c was obtained by fitting σ_{xz} around its maximum value with a second-order polynomial.

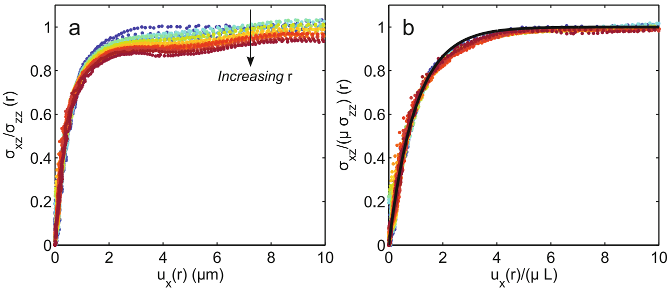

Fig. 15. (Color online) (a) $\frac{\sigma_{xz}}{\sigma_{zz}}$ *versus* u_x for $P = 0.7\,\mathrm{N}$ and at different r taken every $70\,\mu\mathrm{m}$ between 0 and $a_H - \sqrt{Rh}$. Small-r valued curves are shown in dark blue, while largest-r valued curves are in dark red. (b) $\frac{\sigma_{xz}}{\mu\sigma_{zz}}$ *versus* $u_x/(\mu L)$ for the same load at different r. The solid black curve is $1 - e^{-\alpha}$ with α a dimensionless increasing number and corresponds to the predictions of eq. (5).

of slip, but also quantitatively since both displacement and stress distributions are found to follow reasonably well the predicted shape and amplitude. However, close comparison reveals discrepancies, the most striking being that the displacement in the vicinity of the center of the contact is not strictly null during the transient phase, but slowly increases with Q as evidenced in fig. 12c. This observation is at odds with the rigid-plastic-like constitutive law assumed in CM's model, which implies that the displacement u_x at the center of the contact should remain null as long as $\sigma_{xz} \leq \mu_s\sigma_{zz}$. A possible explanation can be found when considering the principle of the DIC measurement itself, which is based on correlation boxes containing pixels corresponding to both micro-contacts and out-of-contact regions. Contrary to experiments with smooth marked PDMS such as in [16,17], the measured displacements are thus averaged over the thickness h of the rough layer and combine two intricate contributions: true slip at the micro-contacts and elastic shear deformation of the rough layer.

In order to characterize the local shear behavior of the interface, we examine the relationship between the tangential stress σ_{xz} and displacement u_x measured at various positions r within the contact. Assuming that the pressure profile σ_{zz} is given by Hertz's contact theory, we compute the ratio $\frac{\sigma_{xz}(r)}{\sigma_{zz}(r)}$ as a function of the displacement at positions r, $u_x(r)$. Figure 15a shows, on the example of $P = 0.7\,\mathrm{N}$, the typical measured behavior obtained for all normal loads P. Two distinct regimes can be identified. At small u_x, σ_{xz}/σ_{zz} increases quasi-linearly with u_x. At large u_x, however, σ_{xz}/σ_{zz} asymptotically reaches a constant value. This observation can be understood as a direct consequence of the shear response of the multi-contact interface. This problem has been theoretically analyzed by Bureau and coworkers in the context of a plane-on-plane frictional contact configuration [42]. The surface topography is described using Greenwood-Williamson's model [43] by an assembly of spherical asperities of equal radius, and whose heights are randomly distributed with an exponential distribution. In addition, the response of each asperity upon tangential loading is described by CM's model. The macroscopic normal and shear forces P and Q are distributed uniformly over the multi-contact interface. The model predicts the evolution of the ratio Q/P as a function of the relative displacement δ of the centers of mass of both solids in contact, in the form

$$\frac{Q}{P} = \mu\left(1 - e^{-\frac{\delta}{\mu L}}\right), \tag{5}$$

where μ is a microscopic friction coefficient and where $L = \frac{2-\nu}{2(1-\nu)}h$ is an elastic length whose value is controlled by the rms roughness of the interface h, and which depends on the material properties only through the Poisson's ratio ν. This prediction allowed the authors to interpret global friction force *versus* displacement measurements at the interface between two Plexiglas surfaces submitted to minute shear oscillations.

In our sphere-on-plane configuration, the interfacial stress field is not uniform. However, one may expect that at intermediate length scales, smaller than the macroscopic contact size but larger than the inter-asperity distance, the local ratio between both components σ_{xz} and σ_{zz} also obeys eq. (5). The validity of this result is demonstrated in fig. 15, in which the local stress ratio is plotted as a function of the measured displacement, for various radii r and for $P = 0.7\,\mathrm{N}$ (fig. 15a). The different curves exhibit very similar behaviors, with however a slight pressure dependence visible at large displacements. Each individual curve was fitted using eq. (5) with μ and L as two independent fitting parameters, yielding a master curve shown in fig. 15b. Considering all 6 experiments at different normal loads P, the fitting parameters are found to have very little dependence on σ_{zz} with $\mu = 0.93 \pm 0.08$

and $L = 0.80 \pm 0.23\,\mu$m. The local friction coefficient μ is found consistent with the macroscopic static-friction coefficient μ_s (see fig. 8). The value of the elastic length is to be compared with $L = 0.89\,\mu$m predicted within Bureau *et al.*'s model when considering the Poisson's ratio $\nu = 0.5$ of PDMS and the rms roughness $h = 0.595\,\mu$m of our surface (see sect. 2.2).

This quantitative agreement suggests that Bureau *et al.*'s macroscopic model for the shear response of multi-contact interfaces can be extended to mesoscopic scales. It also shows that the observed deviations from CM's model are fully compatible with an elasto-plastic-like behavior of the rough interface, not taken into account in Amontons-Coulomb friction law. In this respect, the type of measurements performed here can be used to estimate the shear stiffness k of a multicontact interface, a quantity which has recently received significant attention (see *e.g.* [44–47]). By extending Bureau *et al.*'s model locally, one can define k as the initial slope of the curves in fig. 15, *i.e.* $k = (\frac{\partial \sigma_{xz}}{\partial u_x})_{u_x=0} = \frac{\sigma_{zz}}{L}$. Taking 25 kPa as a typical pressure value in our experiments, one finds $k \sim 30\,\text{kPa}/\mu\text{m}$ to be the corresponding typical shear stiffness.

A few additional experiments were performed for a different roughness ($h \sim 1.3\,\mu$m) and different driving velocities up to $20\,\mu$m/s in order to test the robustness of these measurements. In the transient regime ($Q \leq Q_s$), the results appear to be consistent with the observations reported in this work (figs. 11–14 and fig. 15), provided the data is rescaled with respect to the velocity and maximum shear force. In contrast, the long-time behavior ($Q > Q_s$) appears to depend on both the driving velocity and the elastomer's curing protocol [48]. The characteristics of these long transients remain unexplained to date and are beyond the scope of the present work.

7 Conclusion

Building on Chateauminois *et al.*'s earlier work [16,17], we have developed a novel imaging technique to probe locally the spatial distribution of tangential displacement and associated shear stress averaged over the micrometric thickness of a heterogeneous *multi-contact* interface. The method, based on Digital Image Correlation, uses both micro-contacts and micro-asperities as displacement tracers, yielding a sub-micrometer resolution in the measured displacement with a typical $140\,\mu$m spatial resolution. We emphasize that this technique is only suited for rough elastic surfaces against smooth rigid bodies.

This method was used to study the transition from static friction to macroscopic sliding of a smooth glass sphere tangentially loaded against a microscopically rough elastomer plane. This model geometry allowed us to directly compare the measured micro-mechanical fields to a classical model by Cattaneo and Mindlin. We showed that their model does capture reasonably well both the shape and amplitude of the measured displacement and stress fields. However, close comparison reveals that significant deviations occur, which have been shown to involve a characteristic length scale of the order of the micrometric surface roughness. In this respect, we characterized the elastic shear response of our multi-contact interface prior to slippage, which is ignored in CM's model. The latter was shown to be well captured by the model of Bureau *et al.*'s developed in [42].

This surprisingly good agreement suggests that a description of the roughness in terms of a collection of identical spherical asperities provides a reasonably good approximation of the PDMS surface topography. This may reflect the existence of a dominant length scale ($l_c \sim 30\,\mu$m) introduced by the abrading method, which is set by the size of the abrading grains. The surface is essentially smooth at length scales larger than l_c, consistent with the observation that the micro-contacts appear homogenously distributed within the contact zone when imaged at length scales greater than l_c. This length scale also shows up in the height power spectrum as a cut-off l_c^{-1} (fig. 1, inset) beyond which this function rapidly decays.

Consequences of multi-scale surface roughness, ignored in Bureau *et al.*'s model, still need to be examined. Within the context of contact asperity models, like that of Bureau *et al.* or [49], the shape of loading curves like the ones shown in fig. 15 is controlled by the distribution of micro-contact areas. A first step towards a more faithful description of the surface topography is to introduce distributions of radii of curvature for the asperities. For normal contacts, such refinements (see *e.g.* [50] and [51]) were found to change only marginally the micro-contact area distribution, so we expect Bureau *et al.*'s results to be rather robust. Alternative and more recent models based on a spectral description of the roughness [18,52] may allow to revisit this topic. However, to our best knowledge, predictions about the tangential behaviour of such multi-scale contacts are not yet available in the literature, and are thus well beyond the scope of the present study.

Overall, the present study suggests the need to replace the rigid-plastic-like Amontons-Coulomb friction law with an elasto-plastic constitutive friction law in CM-like derivations of the displacement/stress fields, and more generally in any micromechanical analysis of contact mechanics problems (as done in *e.g.* [53]). The effective modulus of the elastic part of this constitutive law is i) proportional to the local applied pressure and ii) inversely proportional to the thickness of the rough interfacial layer. The type of measurements developed and validated in this work opens the way for more focused studies in any other contact geometry or loading configurations, for which no explicit model might be available. The time resolution of the measurements being entirely controlled by the frame rate of the imaging system, we anticipate that the very same method could also be used in the fast transient regimes involved in frictional instabilities.

The authors are indebted to Antoine Chateauminois of Laboratory PPMD of ESPCI-Paris (France) for his valuable help on the inversion procedure and to both Antoine Chateauminois and Christian Frétigny of PPMD, ESPCI-Paris (France) for fruitful discussions. This work was partly supported by ANR-DYNALO contract NT09-499845.

Appendix A.

This appendix summarizes Cattaneo-Mindlin (CM) as well as Johnson's results [1,34] for both u_x and σ_{xz}, respectively, the tangential displacement and stress fields in the direction of loading, for a sphere of radius R pressed under a load P against an elastic half-space of Poisson ratio ν and reduced Young's modulus $E^* = E/(1-\nu^2)$.

For a perfectly adhering contact of radius α submitted to a shear stress field given by

$$\sigma_{xz}^{\alpha}(r) = \mu\sigma_0(1 - r^2/\alpha^2)^{1/2},$$

the displacement field $u_{x,\alpha}(r,\theta) = u_{x,\alpha}$ is given by

$$\begin{aligned} r \le \alpha, \quad u_{x,\alpha}^{\mathrm{in}}(r,\theta) &= A\frac{\pi}{4}\big[4(2-\nu)\alpha^2 - (4-3\nu)r^2\cos^2\theta \\ &\quad -(4-\nu)r^2\sin^2\theta)\big], \\ r > \alpha, \quad u_{x,\alpha}^{\mathrm{out}}(r,\theta) &= A\big[(2-\nu)\big\{(2\alpha^2 - r^2)\sin^{-1}(\alpha/r) \\ &\quad +\alpha r(1-(\alpha/r)^2)^{1/2}\big\} + \frac{\nu}{2}\cos 2\theta \\ &\quad \times\big\{r^2\sin^{-1}(\alpha/r) + (2\alpha^2 - r^2) \\ &\quad \times(1-(\alpha/r)^2)^{1/2}(\alpha/r)\big\}\big], \end{aligned}$$

where $A = \frac{\mu\sigma_0}{8G\alpha}$, with $G = \frac{E}{2(1+\nu)}$ the shear modulus, μ the friction coefficient and $\sigma_0 = (\frac{6PE^{*2}}{\pi^3R^2})^{\frac{1}{3}}$ using Hertz contact model. The associated angularly averaged displacements thus read

$$\begin{aligned} r \le \alpha, \quad u_{x,\alpha}^{\mathrm{in}}(r) &= A\frac{\pi}{2}(2-\nu)(2\alpha^2 - r^2), \\ r > \alpha, \quad u_{x,\alpha}^{\mathrm{out}}(r) &= A(2-\nu)\big\{(2\alpha^2 - r^2)\sin^{-1}(\alpha/r) \\ &\quad +\alpha r(1-(\alpha/r)^2)^{1/2}\big\}. \end{aligned}$$

Using a superposition principle, CM predict that for a sphere on plane contact with partial slip, with a radius of contact a_H and a radius of the stick zone c

$$\begin{aligned} r \le c, \quad u_x(r,\theta) &= u_{x,a_H}^{\mathrm{in}} - \frac{c}{a_H}u_{x,c}^{\mathrm{in}}, \\ c < r < a_H, \quad u_x(r,\theta) &= u_{x,a_H}^{\mathrm{in}} - \frac{c}{a_H}u_{x,c}^{\mathrm{out}}, \\ r \ge a_H, \quad u_x(r,\theta) &= u_{x,a_H}^{\mathrm{out}} - \frac{c}{a_H}u_{x,c}^{\mathrm{out}}. \end{aligned}$$

Note that these expressions correspond to displacement fields relative to points distant from the contact. In the present experiment, the displacements are measured relative to the rigid sphere. One thus has to subtract $u_x(r=0,\theta)$ from the previous expressions in order to compare with the measurements.

In steady sliding, there is no stick zone ($c = 0$) and using the previous expressions, it is straightforward to show that, for $\nu = 1/2$, the angularly averaged displacement fields satisfy the following relations given by

$$\begin{aligned} r \le a_H, \quad \frac{u_x(r)}{\mu a_H^2} &= \frac{3}{4R}(2-(r/a_H)^2), \\ r > a_H, \quad \frac{u_x(r)}{\mu a_H^2} &= \frac{3}{2\pi R}\big\{(2-(r/a_H)^2)\sin^{-1}(a_H/r) \\ &\quad +(r/a_H)(1-(a_H/r)^2)^{1/2}\big\}. \end{aligned}$$

Finally, the corresponding stress fields σ_{xz} have no angular dependence and are given by

$$\begin{aligned} 0 \le r \le c, \quad \sigma_{xz}(r) &= \frac{3\mu P}{2\pi a_H^3}((a_H^2 - r^2)^{1/2} - (c^2 - r^2)^{1/2}), \\ c < r \le a_H, \quad \sigma_{xz}(r) &= \frac{3\mu P}{2\pi a_H^3}((a_H^2 - r^2)^{1/2}), \\ r > a_H, \quad \sigma_{xz}(r) &= 0. \end{aligned}$$

References

1. K.L. Johnson, *Contact Mechanics* (Cambridge University Press, 2003).
2. C.H. Scholz, *The Mechanics of Earthquakes and Faulting* (Cambridge University Press, 2010).
3. R.S. Johansson, J.R. Flanagan, Nat. Rev. Neurosci. **10**, 345 (2009).
4. T. Baumberger, C. Caroli, O. Ronsin, Phys. Rev. Lett. **88**, 075509 (2002).
5. K.W. Xia, A.J. Rosakis, H. Kanamori, Science **303**, 1859 (2004).
6. S.M. Rubinstein, G. Cohen, J. Fineberg, J. Phys. D **42**, 214016 (2009).
7. O. Ben-David, G. Cohen, J. Fineberg, Science **330**, 211 (2010).
8. S. Maegawa, A. Suzuki, K. Nakano, Tribol. Lett. **38**, 313 (2010).
9. O.M. Braun, I. Barel, M. Urbakh, Phys. Rev. Lett. **103**, 194301 (2009).
10. J. Scheibert, D.K. Dysthe, EPL **92**, 54001 (2010).
11. M. Di Bartolomeo, A. Meziane, F. Massi, L. Baillet, A. Fregolent, Tribol. Int. **43**, 1620 (2010).
12. J. Trømborg, J. Scheibert, D.S. Amundsen, K. Thøgersen, A. Malthe-Sørenssen, Phys. Rev. Lett. **107**, 074301 (2011).
13. E. Bouchbinder, E. Brener, I. Barel, M. Urbakh, Phys. Rev. Lett. **107**, 235501 (2011).
14. D.S. Amundsen, J. Scheibert, K. Thøgersen, J. Trømborg, A. Malthe-Sørenssen, Tribol. Lett. **45**, 357 (2012).
15. D.S. Kammer, V.A. Yastrebov, P. Spijker, J.-F. Molinari, Tribol. Lett. **48**, 27 (2012).
16. A. Chateauminois, C. Frétigny, Eur. Phys. J. E **27**, 221 (2008).
17. A. Chateauminois, C. Frétigny, L. Olanier, Phys. Rev. E **81**, 026106 (2010).
18. B.N.J. Persson, J. Chem. Phys. **115**, 3840 (2001).
19. J. Scheibert, A. Prevost, J. Frelat, P. Rey, G. Debrégeas, EPL **83**, 34003 (2008).
20. J. Scheibert, A. Prevost, G. Debrégeas, E. Katzav, M. Adda-Bedia, J. Mech. Phys. Solids **57**, 1921 (2009).
21. B. Lorenz, B.N.J. Persson, J. Phys.: Condens. Matter **21**, 015003 (2009).

22. Mark J.E. (Editor), *Polymer Data Handbook* (Oxford University Press, 1999).
23. J.A. Greenwood, J.H. Tripp, Trans. ASME, Ser. E, J. Appl. Mech. **34**, 153 (1967).
24. J. Scheibert, *Mécanique du Contact aux Échelles Mésoscopiques* (Edilivre, Collection Universitaire, 2008).
25. F. Hild, S. Roux, Strain **42**, 69 (2006).
26. O. Ronsin, K.L. Coeyrehourcq, Proc. R. Soc. London, Ser. A **457**, 1277 (2001).
27. K.R. Shull, Matter Sci. Eng. R. **36**, 1 (2002).
28. K.N.G. Fuller, D. Tabor, Proc. R. Soc. London, Ser. A **345**, 327 (1975).
29. E. Wandersman, R. Candelier, G. Debrégeas, A. Prevost, Phys. Rev. Lett. **107**, 164301 (2011).
30. L. Landau, E. Lifshitz, *Theory of Elasticity* (Butterworth Heinemann, 1986).
31. E.K. Dimitriadis, F. Horkay, J. Maresca, B. Kachar, R.S. Chadwick, Biophys. J. **82**, 2798 (2002).
32. C. Cattaneo, Rend. Accad. Naz. Lincei, **27**, 214 (1938).
33. R.D. Mindlin, Trans. ASME, Ser. E, J. Appl. Mech. **16**, 259 (1949).
34. D. Hills, D. Nowell, *Mechanics of Fretting Fatigue* (Kluwer Academic Publishers, 1994).
35. M. Ciavarella, Int. J. Solids Struct. **35**, 2349 (1998).
36. A. Savkoor, *Dry adhesive contact of elastomers*, Mechanical engineering dissertation, Technical University of Delft (1987).
37. A. Savkoor, G. Briggs, Proc. R. Soc. London, Ser. A **356**, 103 (1977).
38. I. Etsion, J. Tribol., Trans. ASME **132**, 020801 (2010).
39. D.T. Nguyen, P. Paolino, M.C. Audry, A. Chateauminois, C. Frétigny, Y. Le Chenadec, M. Portigliatti, E. Barthel, J. Adhes. **87**, 235 (2011).
40. K.L. Johnson, Proc. R. Soc. London, Ser. A **230**, 531 (1955).
41. K.L. Johnson, J. Mech. Eng. Sci. **3**, 362 (1961).
42. L. Bureau, C. Caroli, T. Baumberger, Proc. R. Soc. London, Ser. A **459**, 2787 (2003).
43. J.A. Greenwood, J.B.P. Williamson, Proc. R. Soc. London, Ser. A **295**, 300 (1966).
44. M. Gonzalez-Valadez, A. Baltazar, R.S. Dwyer-Joyce, Wear **268**, 373 (2010).
45. S. Akarapu, T. Sharp, M.O. Robbins, Phys. Rev. Lett. **106**, 204301 (2011).
46. C. Campaná, B.N.J. Persson, M.H. Müser, J. Phys.: Condens. Matter **23**, 085001 (2011).
47. M.E. Kartal, D.M. Mulvihill, D. Nowell, D.A. Hills, Tribol. Int. **44**, 1188 (2011).
48. A. Kurian, S. Prasad, A. Dhinojwala, Macromolecules **43**, 2438 (2010).
49. G.N. Boitnott, R.L. Biegel, C.H. Scholz, N. Yoshioka, W. Wang, J. Geophys. Res. **97**, 8965 (1992).
50. G. Carbone, F. Bottiglione, J. Mech. Phys. Solids **56**, 2555 (2008).
51. S.R. Brown, C.H. Scholz, J. Geophys. Res., Solid Earth Planets **90**, 5531 (1985).
52. M.H. Müser, Phys. Rev. Lett. **100**, 055504 (2008).
53. A. Brzoza, V. Pauk, Arch. Appl. Mech. **78**, 531 (2008).

Probing Locally the Onset of Slippage at a Model Multicontact Interface

V. Romero, E. Wandersman, G. Debrégeas, and A. Prevost[*]
Sorbonne Universités, UPMC Univ Paris 06, UMR 8237, Laboratoire Jean Perrin, F-75005 Paris, France
CNRS, UMR 8237, Laboratoire Jean Perrin, F-75005 Paris, France

(Received 7 November 2013; published 4 March 2014)

We report on the multicontact frictional dynamics of model elastomer surfaces rubbed against bare glass slides. The surfaces consist of layers patterned with thousands of spherical caps distributed both spatially and in height, regularly or randomly. Use of spherical asperities yields circular microcontacts whose radii are a direct measure of the contact pressure distribution. Optical tracking of individual contacts provides the in-plane deformations of the tangentially loaded interface, yielding the shear force distribution. We then investigate the stick-slip frictional dynamics of a regular hexagonal array. For all stick phases, slip precursors are evidenced and found to propagate quasistatically, normally to the isopressure contours. A simple quasistatic model relying on the existence of interfacial stress gradients is derived and predicts qualitatively the position of slip precursors.

DOI: 10.1103/PhysRevLett.112.094301 PACS numbers: 46.55.+d, 68.35.Ct, 81.40.Pq

In recent years, our understanding of the transition from static to dynamic friction has been markedly changed with the development of new imaging techniques to probe spatially the interfacial dynamics at the onset of sliding [1–4]. The transition from the stick to the slip phases was found to involve the propagation of dynamical rupture fronts, far from the Amontons-Coulomb classic picture. Using true contact area imaging with evanescent illumination of a one-dimensional Plexiglas-Plexiglas plane contact, Rubinstein *et al.* [1] measured slow fronts with velocities orders of magnitude lower than the Rayleigh wave velocity v_R, along with sub-Rayleigh and fast intersonic fronts. Up to the macroscopic slippage, these fronts progressively invade the contact over a length $l(t)$ from the trailing edge [2]. Interestingly, using strain gauges sensors distributed directly above the interfacial plane, the same group reported strong correlations between $l(t)$ and the ratio of tangential to normal local stresses [5]. However, in all these experiments, the contact was treated as a one-dimensional interface. For a two-dimensional contact, simultaneous measurements of both pressure and tangential interfacial fields is still lacking and out of reach using Ben-David and Fineberg's approach. It also remains unclear what physical mechanism sets the dynamics of $l(t)$ and slip fronts direction of propagation, despite numerous theoretical as well as numerical works [6–10].

In this Letter, we take advantage of recent developments in micromilling techniques to design model elastomer multicontact surfaces. These consist of thousands of spherical caps distributed on top of a rectangular block, all made from the same elastomer. We show that spherical caps provide a unique way to measure optically local normal and shear forces once in contact with bare glass slides. We apply this novel technique to analyze the stick-slip frictional dynamics of an hexagonal array of spherical caps of equal height and radius of curvature. Local analysis first reveals that pressure gradients are inherently present for this plane-plane contact, and second that each stick-slip event is mediated by slip precursors. These are found to be quasistatic and to propagate normally to the isopressure lines. We compare our findings with a simplified pressure gradient based model where individual asperities are taken as elastically independent.

Microstructured surfaces are obtained by pouring and curing (see Ref. [11] for details) a PolyDimethylSiloxane (PDMS Sylgard 184, Dow Corning) in a Plexiglas mold fabricated with a desktop CNC Mini-Mill machine (Minitech Machinary Corp., USA). The molds consist of 10×10 mm^2 square cavities, 2.5 mm deep. Their bottom surface is covered with spherical holes whose constant radius of curvature $R = 100$ μm is set by the ball miller used. Holes are positioned spatially with 1 μm resolution either over a regular lattice or at random and their maximum depths are either equal or taken at random from a uniform distribution in the range 40–60 μm. Resulting PDMS surfaces are decorated with spherical caps which match the designed pattern. For the present work, different types of patterns were fabricated–two hexagonal lattices with a base surface coverage $\Phi = 0.4$, one with constant height asperities (LC) and one with random height asperities (LR), and two random distributions with random height asperities (RR), with $\Phi = 0.2$ and 0.4. Samples are maintained by adhesion against a solid glass plate, cleaned with isopropanol then dried, and put in contact with a clean bare glass slide under constant normal load P. The glass slide is mounted on a double cantilever system (see Supplemental Material [12] and [11]) which allows us to measure both P and the applied shear force Q with mN resolution in the range [0–2.5] N. All experiments are performed at room temperature. The glass slide can be driven at constant velocity v in the range [4–1000] μm/s along the x direction. The interface is imaged in transmission with an LED array through the glass slide, with a megapixel CMOS sensor based camera (Photon Focus, 130 Hz) or a fast camera (Photron Fastcam APX-RS, 1000 Hz). As shown on Fig. 1(a), light is transmitted at every single microcontact and refracted by the spherical caps elsewhere, resulting in a myriad of white circular spots, whose radii a_i can be extracted using image analysis [Fig. 1(a), inset]. Assuming Hertz's model to describe the glass-spherical cap contact, the local applied load p_i is given by

$$p_i = \frac{4Ea_i^3}{3(1-\nu^2)R}, \qquad (1)$$

where E is the elastomer Young's modulus and $\nu = 0.5$ [11] its Poisson's ratio. This allows computing the total normal load $P_c = \sum_i p_i$. For all experiments, a linear relationship is systematically found between P_c and P over 2 orders of magnitude in P, irrespective of the type of disorder and pressure distributions [Fig. 1(b)]. Hertz assumption is thus clearly validated in normal contact conditions. However, the slope of P_c versus P depends slightly on the optical threshold used to detect a_i. To recover a unit slope, we thus calibrated the optical threshold with a reference sample whose Young's modulus $E = 4.1 \pm 0.1$ MPa has been measured independently with a JKR test [13]. We then kept the resulting threshold for other samples and tuned E within experimental errors to recover a unit slope. Upon shearing the interface, obtained by driving the translation stage at constant v in the range [20–120] μm/s, the microcontacts size changes marginally from circular to slightly elliptic, still allowing p_i to be extracted within Hertz assumption.

Contrary to the usual pillar geometry of asperities [14–16], spherical asperities do not bend nor buckle. It is thus possible to locate unambiguously with sub-pixel accuracy (1/24 pixels, ~400 nm) positions of the microcontacts centers and follow, using a custom made algorithm written in MATLAB (MathWorks), their displacements with respect to their initial position, u_c [Fig. 1(c), upper panel]. The same methods allow us to extract the displacement of the back layer by monitoring positions of the base of spherical asperities, u_b [Fig. 1(c), lower panel]. Defining $\delta = u_c - u_b$ as the displacement of the cap top with respect to the back layer, we measured $\delta \approx \alpha v t$ with $\alpha \approx 0.032$ for the LC pattern. Neglecting any microslip at the edges of the microcontacts [11], the local shear force q_i is proportional to a_i [13], according to

$$q_i = \frac{8Ea_i}{3(2-\nu)}\delta. \qquad (2)$$

The total shear force Q_c is obtained writing that $Q_c = \sum_i q_i$. For all patterns, Eq. (2) provides a good approximation for the local shear force as shown on Fig. 1(d). A one-to-one linear relationship between Q_c and Q over 2 orders of magnitude is found. The inset of Fig. 1(d) illustrates this agreement with $Q(t)$ and $Q_c(t)$.

We now turn onto analyzing in details the frictional dynamics of the LC pattern, the simplest available texture, sheared along x. Q is found to increase up to a static threshold, beyond which a stick-slip instability always sets for all P and v within [20 μm/s–120 μm/s] [Fig. 1(d), inset]. In the stick-slip regime, the spatial distribution of local normal forces is found to be nonuniform with a characteristic saddle-like shape [Fig. 2(a)] and is time invariant. Such nonuniformity presumably results from combined effects of a curvature of the PDMS sample at long wavelengths, contact loading configuration and history [5] and Poisson expansion [14]. Analysis of the displacement curves $u_c(t)$ reveals that during initial and subsequent stick phases, slip precursors nucleate and eventually invade the whole contact. In the stick-slip regime, they can be best evidenced when looking at two-dimensional velocity field

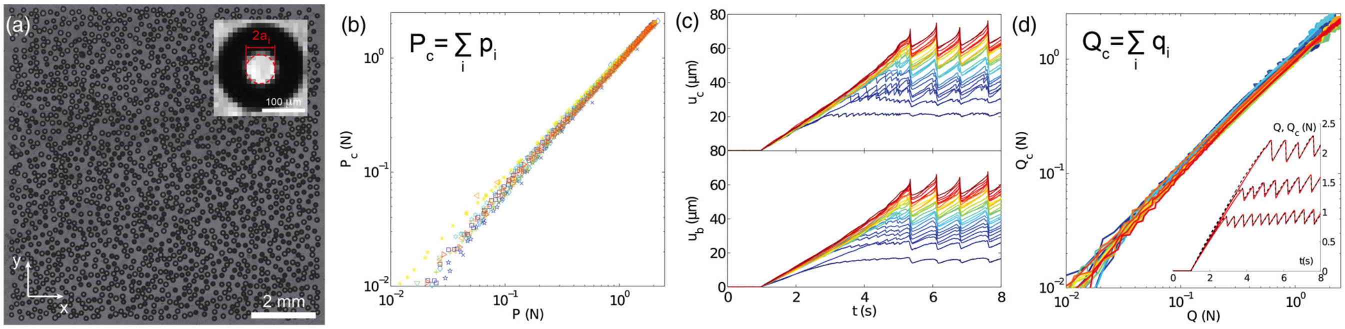

FIG. 1 (color online). (a) Contact image of a RR sample ($\Phi = 0.4$, $P = 2$ N). Inset: single asperity in contact (contact diameter $2a_i$). (b) P_c versus P for all patterns (different colored symbols) loaded normally. (c) Microcontact (back layer) displacements $u_c(t)$ [$u_b(t)$] for 23 microcontacts chosen at random in the LC sample ($v = 80$ μm/s, $P = 2$ N). p_i increases from bottom to top (blue to red). (d) Q_c versus Q for all patterns (different colored lines) in shear experiments. Inset: $Q(t)$ (solid lines) and $Q_c(t)$ (dashed lines) for the LC pattern with $P = 0.5$, 1, 2 N (bottom to top) and $v = 80$ μm/s.

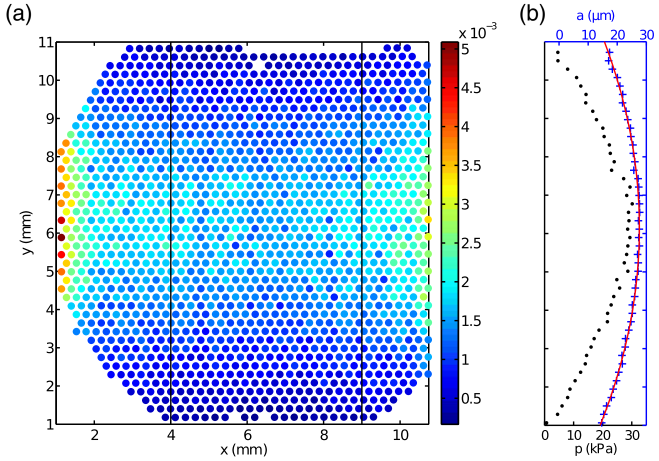

FIG. 2 (color online). (a) Spatial distribution of normal local forces (in N) for the LC pattern in the stick-slip regime ($P = 2.36$ N, $v = 50$ μm/s). (b) Pressure (filled circle) and radii (plus sign) distributions averaged along x in the region bounded by the two vertical lines in (a). The line is a fit $a(y) = a_0 + a_1 y + a_2 y^2$ with $\{a_0, a_1, a_2\} = \{8.37\ \mu\text{m}, 6.27\ 10^{-3}, -0.51\ \text{m}^{-1}\}$.

snapshots du_c/dt [Figs. 3(a)–3(c)] at three instants shown on Fig. 3(d) (see Supplemental Material [12]). In the stick phase ($t \leq t_s$, where t_s is the time of slip, different for each event), they appear as spatially localized structures with large negative velocities, indicative of a collective backsnapping of the microcontacts [Figs. 3(a)–3(c)]. A secondary slip pulse also forms several asperities behind the first one [Figs. 3(b)–3(c)]. These two consecutive slip pulses are systematically observed for all stick-slip events, and always nucleate on the contact edges. When focusing on the central band $4 \leq x \leq 9$ mm, front lines are essentially oriented along x normally to the isopressure lines (see Figs. 3(a)–3(c) [17]). Within this band, the velocity field along the y direction is averaged over x to help visualizing how the front propagates spatially over time.

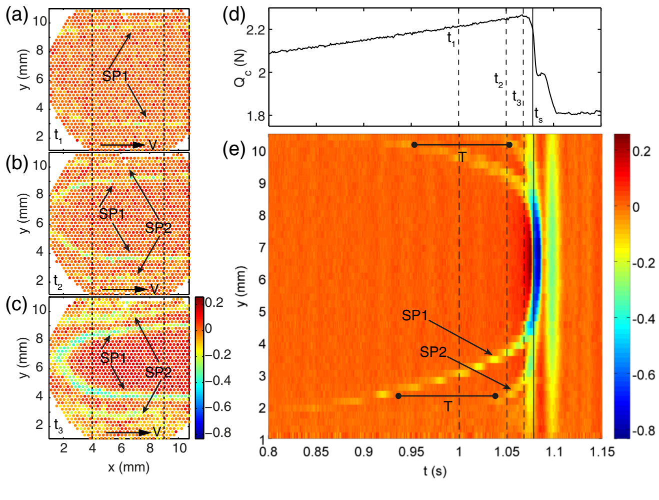

FIG. 3 (color online). (a)–(c) Velocity field snapshots, obtained at 1000 Hz, at times t_1 (a), t_2 (b), and t_3 (c). SP1 (SP2) stands for 1st (2nd) slip pulse. The black arrow shows the direction of sliding. Vertical lines delimit the region defined in Fig. 2(a). ($P = 2.36$ N, $v = 50$ μm/s) (d) $Q_c(t)$ for the stick-slip event of (a)–(c). Dashed lines are drawn at times t_1, t_2, and t_3. (e) Spatiotemporal plot of the velocity field along y averaged for $4 \leq x \leq 9$ mm. Velocities are given in mm/s. T is the delay between SP1 and SP2.

On the resulting spatiotemporal plot [Fig. 3(e)], both first and second slip pulses are visible, each of them consisting of two branches, almost symmetric with respect to the $y \approx 6$ mm axis. The first slip pulse appears to propagate initially with a constant velocity before continuously accelerating as t approaches t_s, reaching a maximum velocity of about 0.5 m/s, 2 orders of magnitude lower than v_R (≈ 30 m/s for PDMS). The observed scenario remains qualitatively similar for the first loading stick phase, but slip precursors are more heterogeneously distributed, preventing a direct quantitative analysis. This difference is likely related to slight pressure distribution rearrangements during the first loading phase. For the present work, we have thus chosen to focus on the stick-slip regime only.

For each stick-slip event, front positions were obtained by detecting individual times of slip for each asperity in contact, using their displacement $u_c(t)$, allowing us to obtain them with a better accuracy. Mean front positions versus mean times of slip were deduced by averaging both individual slip times of all asperities at the same y position (within the central x band) and mean front positions on all stick-slip events. Similarly to the velocity spatiotemporal representation, such curves are almost axisymmetric around $y \approx 6$ mm, allowing us to extract the distance c to this axis of symmetry, which is a direct measure of the remaining stick zone extension. This procedure was applied for 6 experiments at $P = 2.36$ N with increasing driving velocities v. Figure 4 shows the resulting c versus $(t_s - t)$ for the first slip pulse [Fig. 4(a)] and the same data with the time axis multiplied by v [Fig. 4(b)]. All curves at different v are found to overlap on the same master curve, suggesting that propagation of slip precursors results from a quasistatic

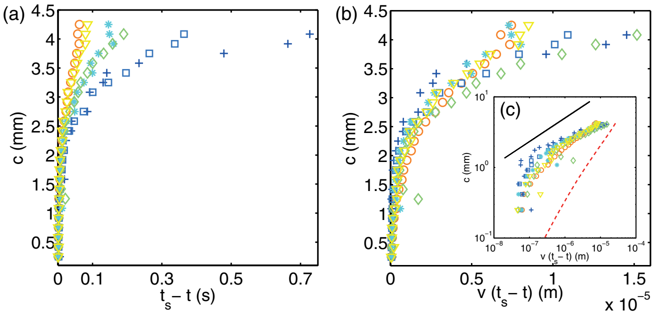

FIG. 4 (color online). (a) c versus $(t_s - t)$ for the first slip pulse and $v = 20$(plus sign), 30(square), 50(diamond), 80(asterisk), 100(triangle), 120(circle) μm/s. (b) c versus $v(t_s - t)$. (c) Log-log plot of (b). The solid line is a power law of exponent 1/3. The dashed line is the model prediction.

mechanism. Note that these curves do not include any data at $t > t_s$ in the slip phase. For $t > t_s$, a fast front which can be seen as the second vertical yellow line on Fig. 3(e), propagates from the center to the edges with a velocity larger than 2–3 m/s. This front whose nature is possibly inertial is not further studied here.

On the experimental side, our measure of $c(t)$ is analogous to that of $L - l(t)$ of [2,5], with L being the size of the system. Our work provides two additional features of these slip fonts: (i) their quasistatic nature; (ii) the way the two-dimensional pressure landscape controls their propagation, as discussed below. On the theoretical [9,18,19] and numerical [7,8] sides, recent investigations have predicted similar quasistatic behaviors for the slip front position $l(t)$, and its relation to the stress landscape [7], L and local friction laws [8,9,18,19]. In particular, [9,18,19] assume rate and state interfacial friction laws, and predict the existence of a critical length l_c beyond which the system becomes unstable. For $l < l_c$, slip fronts are found to be quasistatic [18,19], but the precise analytical form of $l(t)$ is not well established. For $l > l_c$, a dynamic front invades the interface with a velocity $\sim v_R$, leading to macroscopic slippage. The slight change of slope of $c(t)$ observed at $t \sim t_s$ [Fig. 4(c)] could be a signature of such a transition, as in [2]. However, front velocities at $t \sim t_s$ (Fig. 4) appear to be 2 orders of magnitude smaller than v_R, ruling out inertia as the driving mechanism.

To understand the form and quasistatic nature of $c(t)$, let us model our system with asperities distributed along y (the direction normal to the isopressure lines) on a one-dimensional regular lattice, and let us neglect the elastic interaction between them (i.e., absence of any back layer). In the Amontons-Coulomb description, slip of an asperity i occurs once $q_i = \mu_s p_i$, where μ_s is a static friction coefficient. Combining Eqs. (1) and (2) yields the maximum displacement δ_s^i, beyond which slip occurs, as

$$\delta_s^i = \mu_s a_i^2 / R. \tag{3}$$

An asperity i initially at position y_0^i will slip when its position reaches $y_s^i = y_0^i + \delta_s^i \approx y_0^i$, since $\delta_s^i \ll y_0^i$. With Eq. (3), the front position and time of slip, respectively $y_w = y_s^i$ and $t_s^i = \delta_s^i/(\alpha v)$, are thus predicted for a given pressure profile. In an ideal plane-plane contact with a uniform pressure, all asperities should slip simultaneously and no slip pulse should be observed. In our experiments, however, pressure gradients are clearly present along y [Fig. 2(a)]. Taking a continuous limit, the contact radius a_i can be well fitted by a parabola $a(y) = a_0 + a_1 y + a_2 y^2$ [Fig. 2(b)]. This expression, with Eq. (3), provides the position of the front with respect to its position at threshold, $c(\delta) = y_w(\delta_s) - y_w(\delta)$, where $\delta_s = (\mu_s/R)(a_0 - (a_1^2/4a_2))^2$ is the threshold displacement at $t = t_s$. It reads

$$c(\delta) = -\frac{1}{2a_2}(a_1^2 - 4a_2(a_0 - (R\delta/\mu_s)^{1/2}))^{1/2}. \tag{4}$$

This quasistatic model can be extended to any pressure distribution and provides a description of the first loading phase, where all microspheres start from their initial unloaded position. Once a sphere slips, it relaxes back from δ_s^i by $\delta_r^i = (\Delta\mu/\mu_s)\delta_s^i$ before the beginning of a next loading phase, where $\Delta\mu = \mu_s - \mu_d$ with μ_d a dynamical friction coefficient. The model can be extended to the stick-slip events by replacing μ_s by $\Delta\mu$ in Eq. (4). Note that close to the threshold ($\delta - \delta_s \ll \delta_s$), $c(\delta)$ behaves asymptotically as $c(\delta) = K(\delta_s - \delta)^{1/2}$ with $K = (2R/(\Delta\mu(a_1^2 - 4a_0a_2)))^{1/2}$. One thus expects $c(\delta)$ to follow a power law of exponent 1/2. Predictions of Eq. (4) are plotted on Fig. 4(c), with $\{a_0, a_1, a_2\}$ given by the parabolic fit [see caption of Fig. 2(b)] and $\Delta\mu = 0.157$, obtained by averaging values of $\Delta\mu$ for all experiments. The predicted curve qualitatively succeeds in reproducing the measured trend and right order of magnitude of $c(\delta)$, but fails quantitatively. Careful examination of the data suggests that c follows indeed a power law, but with an exponent closer to 1/3 than 1/2 [Fig. 4(c)]. Our model lacks ingredients which could explain the discrepancies. First, it is limited to a one-dimensional description, whereas the slip propagation is clearly two dimensional. Second, it does not take into account the elastic coupling between asperities. Including both effects is expected to improve comparison, but is beyond the scope of this Letter.

Despite its limitations, this model provides a simple mechanism to generate slip pulses, relying on interfacial stress gradients. Interestingly, it also predicts the existence of second slip pulses whose propagation is delayed by T, as evidenced on Fig. 3(e). T results from the sum of (i) the individual relaxation time τ of a sphere sliding back from δ_s^i by δ_r^i, and (ii) the time to reach δ_s^i again, yielding $T = \tau + \delta_r^i/(\alpha v)$. Such relationship is actually verified experimentally (not shown), asserting furthermore the quasistatic character of the measured slip pulses. Taking $\tau = 7.6 \pm 0.5$ ms, the averaged relaxation time over all trajectories, one gets $\delta_r^i \approx 0.35\ \mu$m, comparable to the measured averaged value of 1 μm. In addition, the second slip pulse can only be identified if $T(i = 0) < t_s$. This gives a limiting driving velocity v_l above which no second slip pulse can be observed, $v_l = \frac{1}{\tau}(\delta_r - \delta_r^{i=0}) = \frac{\Delta\mu}{\alpha R \tau}((4a_2a_0 - a_1^2/4a_2)^2 - a_0^2)$. Using the experimental values, one gets $v_l \approx 4.4$ mm/s, much larger than the maximum tested driving velocity. This agrees with a systematic observation of a second slip pulse at all velocities.

This work has been limited to the stick-slip regime, where slip fronts could be characterized and compared to a noninteracting model. A similar phenomenology is observed for the first stick event, and will be explored in a future work. Our results demonstrate how combining surface micropatterning and interface imaging allows accessing the mechanics at the level of single asperities. This has been applied to a hexagonal array of equal height microasperities, revealing that slip precursors propagate quasistatically orthogonally to the isopressure lines. It will be extended to more elaborate patterns in a future work.

We acknowledge funding from ANR (DYNALO NT09-499845) and CONICYT, and we thank A. Chateauminois, C. Frétigny, and R. Candelier for fruitful discussions.

---

*alexis.prevost@upmc.fr

[1] S. M. Rubinstein and G. Fineberg, Nature (London) **430**, 1005 (2004).

[2] S. M. Rubinstein, G. Cohen, and J. Fineberg, Phys. Rev. Lett. **98**, 226103 (2007).

[3] O. Ben-David, S. M. Rubinstein, and J. Fineberg, Nature (London) **463**, 76 (2010).

[4] M. C. Audry, C. Fretigny, A. Chateauminois, J. Teissere, and E. Barthel, Eur. Phys. J. E **35**:83 (2012).

[5] O. Ben-David and J. Fineberg, Phys. Rev. Lett. **106**, 254301 (2011).

[6] O. M. Braun, I. Barel, and M. Urbakh, Phys. Rev. Lett. **103**, 194301 (2009).

[7] J. Scheibert and D. K. Dysthe, Europhys. Lett. **92**, 54001 (2010).

[8] J. Trømborg, J. Scheibert, D. S. Amundsen, K. Thogersen, and A. Malthe-Sorenssen, Phys. Rev. Lett. **107**, 074301 (2011).

[9] E. Bouchbinder, E. A. Brener, I. Barel, and M. Urbakh, Phys. Rev. Lett. **107**, 235501 (2011).

[10] D. S. Amundsen, J. Scheibert, K. Thøgersen, J. Trømborg, and A. Malthe-Sørenssen, Tribol. Lett. **45**, 357 (2012).

[11] A. Prevost, J. Scheibert, and G. Debrégeas, Eur. Phys. J. E **36**, 17 (2013).

[12] See Supplemental Material at http://link.aps.org/supplemental/10.1103/PhysRevLett.112.094301 for a sketch of the experimental setup and a movie of the two-dimensional velocity field during the stick-slip event of Fig. 3.

[13] K. L. Johnson, *Contact Mechanics* (Cambridge University Press, New York, 2003).

[14] K. Brörmann, I. Barel, M. Urbakh, and R. Bennewitz, Tribol. Lett. **50**, 3 (2013).

[15] B. Murarash, Y. Itovich, and M. Varenberg, Soft Matter **7**, 5553 (2011).

[16] E. Degrandi-Contraires, C. Poulard, F. Restagno, and L. Léger, Faraday Discuss. **156**, 255 (2012).

[17] This observation was reproduced with samples with the same hexagonal pattern but a different pressure distribution.

[18] M. Otsuki and H. Matsukawa, Sci. Rep. **3**, 1586 (2013).

[19] Y. Bar-Sinai, R. Spatschek, E. A. Brener, and E. Bouchbinder, Phys. Rev. E **88**, 060403(R) (2013).

Normal contact and friction of rubber with model randomly rough surfaces

S. Yashima,[a,d,‡] **V. Romero,**[b,c,‡] **E. Wandersman,**[b,c] **C. Frétigny,**[a] **M.K. Chaudhury,**[e] **A. Chateauminois**[a] **and A. M. Prevost**[b,c,*] ***24st October 2014, Accepted Xth XX 2014***

***First published on the web Xth XX 2014* DOI: 10.1039/b000000x**

We report on normal contact and friction measurements of model multicontact interfaces formed between smooth surfaces and substrates textured with a statistical distribution of spherical micro-asperities. Contacts are either formed between a rigid textured lens and a smooth rubber, or a flat textured rubber and a smooth rigid lens. Measurements of the real area of contact A versus normal load P are performed by imaging the light transmitted at the microcontacts. For both interfaces, $A(P)$ is found to be sub-linear with a power law behavior. Comparison to two multi-asperity contact models, which extend Greenwood-Williamson (J. Greenwood, J. Williamson, *Proc. Royal Soc. London Ser. A* **295**, 300 (1966)) model by taking into account the elastic interaction between asperities at different length scales, is performed, and allows their validation for the first time. We find that long range elastic interactions arising from the curvature of the nominal surfaces are the main source of the non-linearity of $A(P)$. At a shorter range, and except for very low pressures, the pressure dependence of both density and area of micro-contacts remains well described by Greenwood-Williamson's model, which neglects any interaction between asperities. In addition, in steady sliding, friction measurements reveal that the mean shear stress at the scale of the asperities is systematically larger than that found for a macroscopic contact between a smooth lens and a rubber. This suggests that frictional stresses measured at macroscopic length scales may not be simply transposed to microscopic multicontact interfaces.

Introduction

Surface roughness has long been recognized as a key issue in understanding solid friction between macroscopic bodies. As pointed out by the pioneering work of Bowden and Tabor[1], friction between rough surfaces involves shearing of myriads of micro-asperity contacts of characteristic length scales distributed over orders of magnitude. The statistical averaging of the contributions of individual micro-asperity contacts to friction remains an open issue which largely relies on the contact mechanics description of multicontact interfaces. In early multi-asperities contact models such as the seminal Greenwood-Williamson's model (GW)[2], randomly rough surfaces are often assimilated to a height distribution of non interacting spherical asperities which obey locally Hertzian contact behavior. Along these guidelines, some early models also attempted to describe the fractal nature of surface roughness by considering hierarchical distributions of asperities[3]. More refined exact elastic contact mechanics theories were also developped by Westergard[4], Johnson[5] and Manners[6,7], amongst others, in order to solve the problem of elastic contacts between one dimensional periodic wavy surfaces. Most of the subsequent generalisations of elastic contact theories to randomly rough surfaces are more or less based on a spectral description of surface topography[8–11]. Within the framework of linear (visco)elasticity or elasto-plastic behavior, these theories allow estimation of the pressure dependence of the distribution of microcontacts size and pressure at various length scales. From an experimental perspective, elucidation and validation of these models using microscopic randomly rough surfaces such as abraded or bead blasted surfaces is compromised by the difficulties in the measurement of the actual distribution of microcontact areas at the micrometer scale. Although early attempts were made by Dieterich and Kilgore[12] with roughened surfaces of transparent materials using contact imaging techniques, direct comparison of the experimental data with contact mechanics models lacks clarity.

In this study, we take advantage of recent advances in sol-gel and micro-milling techniques to engineer two types of model randomly rough and transparent surfaces with topographical characteristics compatible with GW's model of rough surfaces[2]. They both consist of statistical distributions of spherical asperities whose sizes (~ 20 μm up to 200 μm) allow for an optical measurement of the spatial distributions of the microcontacts areas. In their spirit, these experiments are

---

[a] *Soft Matter Science and Engineering Laboratory (SIMM), CNRS / UPMC Univ Paris 6, UMR 7615, ESPCI, F-75005 Paris, France*
[b] *CNRS, UMR 8237, Laboratoire Jean Perrin (LJP), F-75005, Paris, France. E-mail: alexis.prevost@upmc.fr*
[c] *Sorbonne Universités, UPMC Univ Paris 06, UMR 8237, Laboratoire Jean Perrin, F-75005, Paris, France*
[d] *Laboratory of Soft and Wet Matter, Hokkaido Univ, Sapporo, Japan*
[e] *Department of Chemical Engineering, Lehigh University, Bethlehem PA 18015, USA*
‡ *These authors contributed equally to this work.*

along the line of Archard's previous investigations[3], which used model perspex surfaces consisting of millimeter sized spherical asperities of equal height. However, in Archard's investigations, a small number of asperities were used. Furthermore, technical limitations in the estimation of variation of heights of asperities did not allow for a statistical analysis of the load dependence of the distributions of microcontact areas. Here, using a sphere-on-plane contact geometry with different statistical distributions of micro-asperities, we probe the elastic interactions between asperities (see *e.g.*[13–16]) by directly comparing the measured distributions of the real area of contact to the predictions of two different multi-asperity contact models. We show how the use of textured surfaces allows an accurate validation of these models that permits an investigation of the statistical distribution of contact pressure, number of microcontacts and microcontact radii distributions. In the last part of the paper, we present the results of a preliminary study that illustrates how such model systems can be used to investigate the relationship between frictional properties and real contact areas.

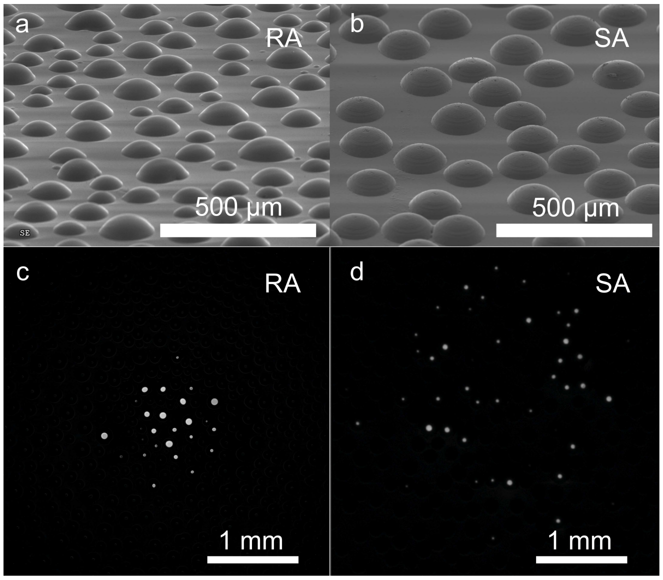

Fig. 1 (a) SEM image topography of a RA$^+$ sol-gel replica ($\phi = 0.41$). (b) Same with an SA PDMS replica of a micro-milled mold ($\phi = 0.4$). (c) microcontacts spatial distribution with RA$^+$ ($P = 22$ mN). (d) Same with the SA of (b) and a lens of radius of curvature 128.8 mm ($P = 20$ mN). (c-d) are image differences with a reference non-contact image. Note the size difference in the apparent contact related to the difference in curvature of both indenters.

Materials and Techniques

Two types of randomly rough surfaces covered with spherical caps were designed using two different techniques as described below. The first surface (RA for Rigid Asperities) consists of glass lenses (BK7, Melles-Griot, radius of curvature 13 mm) covered with a distribution of micrometer sized rigid asperities with varying heights and radii of curvature. The second surface (SA for Soft Asperities) is made of a nominally flat silicone slab decorated with a random spatial distribution of soft spherical micro-asperities with equal radius of curvature and varying heights.

RA lenses

RA's topography was obtained by replicating condensed liquid droplets on a hydrophobic surface. Water evaporating from a bath heated at 70°C was first allowed to condense on a HexaMethylDiSilazane (HMDS) treated hydrophobic glass slide kept at room temperature, resulting in a surface with myriads of droplets. This surface was then covered with a degassed mixture of a PolyDiMethylSiloxane cross-linkable liquid silicone (PDMS, Sylgard 184, Dow Corning) cured at 70°C for 2 hours. One is left, upon demolding, with a PDMS surface with concave depressions, which are negative images of the condensed water droplets. These PDMS samples then serve as molds to replicate rigid equivalents on the glass lenses using a sol-gel imprinting process fully described elsewhere[17]. An example of the resulting pattern with smooth spherical caps of various sizes is shown in Fig. 1a. By changing the time of exposure t_{exp} of the HMDS treated glass to water vapor, different surfaces with different asperity sizes and densities are obtained as a result of droplet coalescence during the water condensation process. Two patterns with small (*resp.* large) asperities were made with $t_{exp} = 15$ s (*resp.* 60 s). They are respectively referred to as RA$^-$ and RA$^+$. Their topography at the apex was characterized with an optical profilometer (Microsurf 3D, Fogale Nanotech) to extract the mean surface fraction ϕ covered by the asperities (Table 1) and the distributions of their heights h and radii of curvature R. Both distributions are found to be Gaussian (not shown) with means $\bar{h}$, $\bar{R}$ and standard deviations given in Table 1. For RA$^+$, h is found to be proportional to R (Fig. 2). This suggests that the spherical shape of the asperities is uniquely controlled by the contact angle θ of water droplets on the HMDS treated surface prior to molding. In this case, one expects, indeed, the relationship $h = R(1-\cos\theta)$. Fitting the data of Fig. 2 yields $\theta \sim 57°$, very close to 55° which is the value of the advancing contact angle we measured for water droplets on HMDS treated glass. For RA$^-$ however, no evident correlation has been observed, for which we have no clear explanation (Fig. 2, inset).

Table 1 RA's mean topographical characteristics

t_{exp}(s)	ϕ	$\bar{h}(\mu$m)	$\bar{R}(\mu$m)
15	0.34 ± 0.02	9.0 ± 2.4	49.6 ± 12.8 [a]
60	0.41 ± 0.05	29.6 ± 10.1	64.4 ± 19.6 [b]

[a] from 293 asperities.

[b] from 119 asperities.

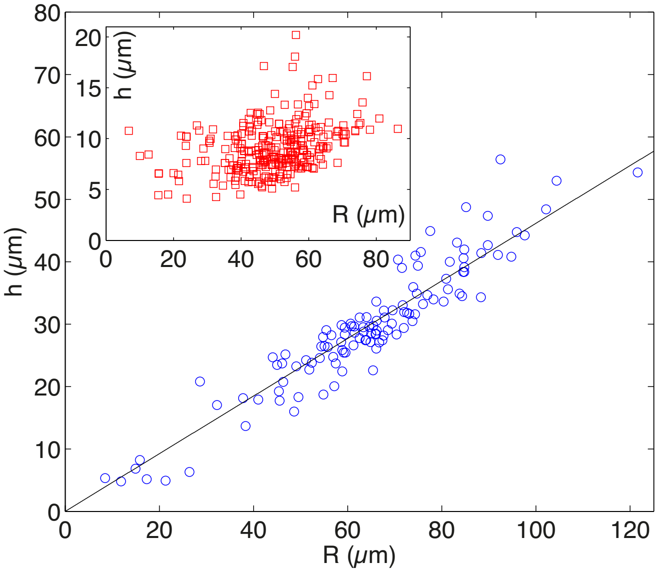

Fig. 2 (Color online) Height h of the spherical micro-asperities as a function of their radius of curvature R for the RA$^+$ lens ($\phi = 0.41$). Inset: Same for the RA$^-$ lens ($\phi = 0.34$). The solid line is a linear fit of the data.

SA samples

SA samples were obtained by cross-linking PDMS in molds (2.5 mm deep) fabricated with a desktop CNC Mini-Mill machine (Minitech Machinary Corp., USA) using ball end mills of radius 100 μm, allowing to design, with 1 μm resolution, patterns with controlled surface densities and height distributions (Fig. 1b). Spherical cavities were randomly distributed over 1 cm^2 with a non overlapping constraint with two different surface densities $\phi = 0.1$ and 0.4. Their heights as obtained from a uniform random distribution were in the range [30–60] μm. SA samples with $\phi = 0.1$ are thus referred to as SA$^-$ further down, and those with $\phi = 0.4$ as SA$^+$. Half of the bottom of the mold was kept smooth so that SA samples had both a patterned part and a smooth one. The smooth part was used in a JKR contact configuration[18], which allowed measurement of each sample Young's modulus E. Secondly, it provided means to locate accurately the center of the apparent contacts formed on the patterned part. Since contacts with the patterned part were obtained by a simple translation of the sample, the center within the contact images was taken as the center of the JKR circular contact, obtained using standard image analysis.

As detailed above, RA samples display spatial and height distributions of asperities set by both the evaporation and the sol-gel processes, which can only be characterized *a posteriori*. SA samples however, have a statistical roughness which can be finely tuned with any desired pattern, both in height and spacing. As a result, SA flat surfaces are very appropriate for the statistical investigation of contact pressure distribution as they can be produced at centimeter scales thus allowing for several realizations of the contact at different positions on the patterned surface. Nevertheless, contrary to SA asperities which always present a microscopic surface roughness inherent to the milling procedure, RA micro-asperities are very smooth. It thus makes them especially suitable for the investigation of frictional properties, as microcontacts obtained with a smooth rubber substrate can be assimilated to single asperity contacts.

Experimental setups

For RA lenses, normal contact experiments were performed by pressing the lenses against a thick flat PDMS slab under a constant normal load P. Its thickness ($\sim$ 15 mm) was chosen to ensure semi-infinite contact conditions (*i.e.* the ratio of the contact radius to the specimen thickness was more than ten[19]). For SA flat samples, sphere-on-plane contacts were obtained by pressing them against a clean BK7 spherical lens (LA1301, Thorlabs Inc.) with a radius of curvature of 128.8 mm, $\sim$ 10 times larger than the radius of curvature of the patterned RA lenses. To ensure comparable semi-infinite contact conditions, SA samples remained in adhesive contact against a $\sim$ 15 mm thick PDMS slab. The experiments were performed with a home made setup described in[20,21]. Using a combination of cantilevers and capacitive displacement sensors, both the normal (P) and interfacial lateral (Q) forces are monitored in the range [0–2.5] N with a resolution of 10^{-3} N. This setup also provides simultaneous imaging of the microcontacts with the combination of a high resolution CCD camera (Redlake ES2020M, 1600×1200 pixels^2, 8 bits) and a long–working distance Navitar objective. Once illuminated in transmission with a white LED diffusive panel, microcontacts appear as bright disks. Measuring their areas using standard image thresholding techniques provides a direct measure of their entire spatial distribution. The total true area of contact A is then obtained by summing all microcontact areas. In addition, assuming the validity of Hertzian contact theory at the scale of the asperity and knowing E, radii of curvature R of each asperity and $\nu = 0.5$ the Poisson's ratio[20,21], the disks radii a_i are a direct measure of the local normal forces p_i since

$$p_i = \frac{4Ea_i^3}{3(1-\nu^2)R} \quad (1)$$

As described previously[21], a linear relationship between the total normal load $P_c = \sum_i p_i$ and the measured P is systematically found for all SA samples, thus validating Hertz assumption. However, the slope of P_c versus P depends slightly on the optical threshold used to detect a_i. To recover a unit slope, we thus calibrated the optical threshold with a reference sample of known Young's modulus. For all other samples, we then kept the same optical threshold and tuned E for each sample within its measured uncertainties to recover a unit slope. For RA samples however, such a calibration method could not be applied as it requires knowing the radii of curvature of all asperities to evaluate p_i. Because of this limitation[*], we chose the threshold arbitrarily from the contact images between their two extremal values for which the change in total area was found to vary marginally. Consequently, it was not possible to measure any local normal force distribution for RA samples.

Friction experiments with RA patterned lenses were performed with another experimental setup described earlier[22]. RA lenses were rubbed against a smooth PDMS slab ($E = 3 \pm 0.1$ MPa) keeping both P and the driving velocity v constant. The setup allowed variation of v from a few μm s^{-1} up to 5 mm s^{-1} thus allowing simultaneous measurements of P and Q with a resolution of 10^{-2} N.

Multi-asperity contact models

To investigate quantitatively the effects of elastic interactions between micro-asperity contacts on the real contact area and related pressure distribution, two different multi-asperity contact models were considered, both of which include elastic interactions at different length scales. The first one was derived by Greenwood and Tripp (GT)[13] as an extension to the case of rough spheres of the seminal model of Greenwood and Williamson (GW) for the contact between nominally flat surfaces. The second one was developed more recently by Ciavarella *et al.*[14,15]. It consists in a modified form of GW's model, with elastic interactions between microcontacts incorporated in a first order-sense. Both models describe the contact mechanics of rough surfaces with random distributions of spherical asperities, which is what we investigate here experimentally. As a consequence of this simplified form of surface topography, it was not necessary to consider more refined contact models based on a spectral description of the surfaces such as Persson's model[8].

In GT's model, Hertz theory of elastic contact between a smooth sphere and a smooth plane is extended by adding roughness to the plane. As a starting point, the relationship between the local pressure and the local real contact area within an elementary portion of the rough contact is assumed to obey GW's theory. Accordingly, micro-asperity contacts are supposed to be Hertzian and to be independent, that is, the elastic displacements due to the normal force exerted on one asperity has negligible effect on any other asperity. However, use of GW's relationship requires that the separation of both surfaces at any location within the macroscopic contact is known, *i.e.* that the shape of nominal surfaces under deformation is determined. This requirement is deduced from linear elasticity theory (Green's tensor, see reference[23] for instance) that introduces long range elastic interactions at the scale of the apparent Hertzian contact. As opposed to GW's model, which can be derived analytically, in GT's model, calculation of the real contact area and pressure distribution can only be done with an iterative numerical integration of a set of coupled equations, as described in[13].

In Ciaravella *et al.*'s model, the approach includes in the first order-sense elastic interactions between Hertzian micro-asperity contacts, *i.e.* for every asperity a displacement is imposed which is sensitive to the effect of the spatial distribution of Hertzian pressures in the neighboring asperities. For each micro-asperity contact, a shift of the position of the deformable surface is introduced, which results from the vertical displacement caused by the neighboring ones. Accordingly, the indentation depth δ_i of the i^{th} micro-asperity contact is

$$\delta_i = \delta_i^0 + \sum_{j \neq i}^{N} \alpha_{ij} \delta_j^{3/2} , \quad (2)$$

where $\delta_i^0 > 0$ is the indentation depth in the absence of any elastic coupling between microcontacts, and α_{ij} are the elements of the interaction matrix. As shown in Fig. 3, δ_i^0 is a purely geometrical term simply given by the difference between the positions of the two undeformed surfaces for the prescribed indentation depth Δ. The sum in the rhs of eqn (2) represents the interaction term derived from Hertz contact theory. Our study slightly differs from Ciaravella *et al.*'s model as we take for α_{ij} an asymptotic expansion of the Hertz solution for the vertical displacement of the surface, instead of its exact expression. Elements α_{ij} of the interaction matrix thus read

$$[\alpha_{ij}] = -\frac{4\sqrt{R_j}}{3\pi}\frac{1}{r_{ij}} \ , i \neq j \ , \quad (3)$$

where r_{ij} is the distance between asperities i and j and R_j is the radius of curvature of the j^{th} asperity. This approximation avoids evaluating at each step of the calculation the interaction matrix $[\alpha_{ij}]$, which consequently depends only

---

[*] Measurements of radii of curvature were performed using profilometry images obtained at a high magnification. Identifying for a given asperity its radius of curvature would imply matching the position of this asperity with its position in a zoomed out image of the macroscopic apparent contact.

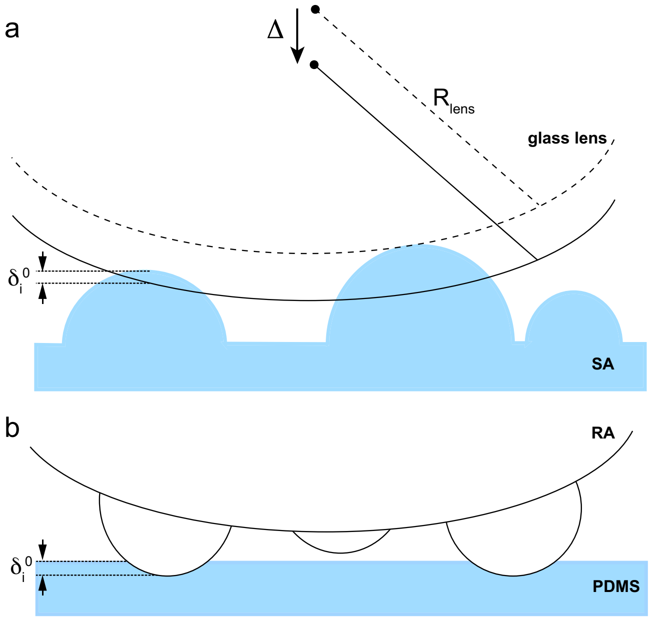

Fig. 3 Sketch of the geometric configuration for the indentation of (a) SA and (b) RA surface topography. For both configurations, Δ is the prescribed indentation depth taking as a reference for the vertical position of the indenting sphere the altitude at which the smooth surface is touching the uppermost asperity.

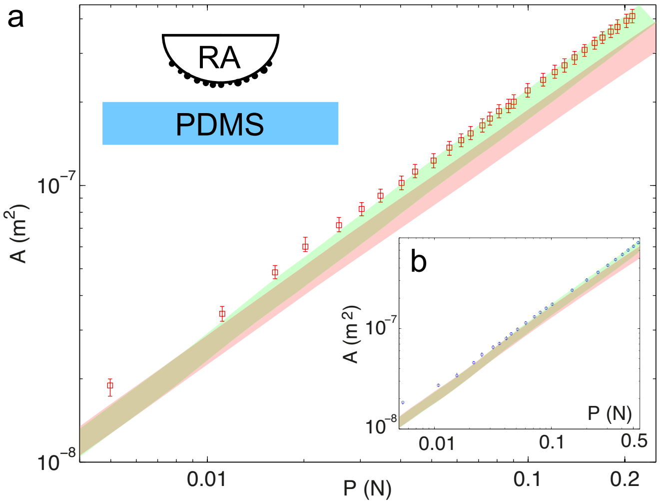

Fig. 4 Log-log plot of the real area of contact A versus P for both RA$^-$ (a) and RA$^+$ (b) lenses. The upper and lower limits of the error bars correspond to the total areas measured with the arbitrarily chosen extremal values of the optical threshold (see text). Red shaded areas correspond to the predictions of Ciavarella *et al.*'s model[14,15] by setting α_{ij} to 0 in eqn (2). Green areas correspond to $\alpha_{ij} \neq 0$. Areas extent characterizes the scatter in the simulations, arising from uncertainties in the experimental determination of the topography parameters.

on the surface topography. Such an approximation is valid as long as the average distance between asperities L is much larger than the average asperity microcontact radius a. For RA samples, optical measurements reveal that this criterion is satisfied as the ratio L/a, which is a decreasing function of P, remains between 6 and 8. For SA samples, one also measures that $L/a \approx 16-32$ for SA$^-$ and $L/a \approx 9-15$ for SA$^+$. The above detailed models are obviously valid as long as no contact occurs in regions between the top parts of the spherical caps.

Normal contacts

RA measurements

In order to stay consistent with the hypothesis of the contact models, true contact area measurements for RA lenses were performed for normal loads P for which only tops of the micro-asperities make contact with the PDMS slab. While for RA$^+$ lenses, this is observed for the entire range (up to 0.6 N) of P, for RA$^-$ lenses this occurs as long as $P \leq 0.2$ N. Figure 4 shows the total contact area A versus P for both RA lenses contacting a smooth PDMS substrate. $A(P)$ exhibits a non-linear power law behavior with the following exponents: 0.812 ± 0.009 for RA$^-$ and 0.737 ± 0.042 for RA$^+$.

To compare these results with Ciaravella *et al.*'s model, calculations were carried out using simulated lens topographies generated from Gaussian sets of asperity heights calculated using the experimental parameters reported in Table 1. The radii of curvature of the asperities were varied as a function of their heights using the experimentally measured $R(h)$ relationship. Asperities were spatially distributed according to a uniform distribution with a non-overlap constraint. In order to minimize bias in their spatial distribution, asperities were positioned by decreasing size order.

Figure 4 shows the results of such simulations using Ciavarella's model. Uncertainties in the experimental determination of surface parameters (mainly the $R(h)$ relationship) were found to result in some scatter in the simulated $A(P)$ response. In order to account for this scatter, the simulated curves are represented as colored areas in Fig. 4. A good agreement is observed between theory and experiments only when elastic interactions are accounted for. Without such interactions (*i.e.* when the term α_{ij} in eqn (2) is set to zero), the actual contact area at a given P is clearly underestimated.

SA measurements

For SA samples in contact with the glass lens of radius of curvature 128.8 mm, microcontacts always occur at the top of the asperities for the whole investigated P range up to 0.6 N. For each P, the real area of contact A was averaged over $N = 24$ different locations on the sample. This allowed us to probe statistically different contact configurations while reducing the error on A by a factor $\sqrt{N}$. Figure 5 shows the resulting A versus P for both SA$^-$ and SA$^+$ samples. As found with RA lenses, $A(P)$ curves are also sub-linear and are well fitted by power laws. For both tested surface densities, power law exponents are found to be density independent, with 0.945 ± 0.014 for SA$^-$ and 0.941 ± 0.005 for SA$^+$. Changing ϕ from 0.1 to 0.4 mainly results in an increase of $A(P)$ at all P (Fig. 5). As previously done with RA samples, both SA data sets are compared to Ciaravella *et al.*'s model[14,15] predictions, with both $\alpha_{ij} = 0$ and $\alpha_{ij} \neq 0$. Calculations were performed using the exact topography used to make SA samples, and A versus P curves were obtained with the exact same 24 contact configurations. Errors on the calculated A values were obtained by varying Young's modulus within its experimental uncertainties, yielding the shaded areas of Fig. 5. Red shaded areas correspond to α_{ij} to 0 in eqn (2), while green areas correspond to $\alpha_{ij} \neq 0$. At low normal loads ($P \leq 0.1$ N), the effect of the elastic interaction on A is almost negligible, but it becomes more pronounced at higher ones ($P > 0.1$ N), resulting in a larger true contact A. As shown on Fig. 5, our data at $P > 0.1$ N is clearly better captured by the interacting model rather than the non-interacting one for both surface densities.

These $A(P)$ measurements, together with those obtained with RA lenses, indicate that including an elastic interaction is thus essential to have a complete description of the contact mechanics of such systems. Yet, it remains unclear which of the short range (interaction between neighboring asperities) and/or long range (determined by the geometry of the macroscopic contact) parts of the elastic interaction predominate. We now address precisely this question in the following.

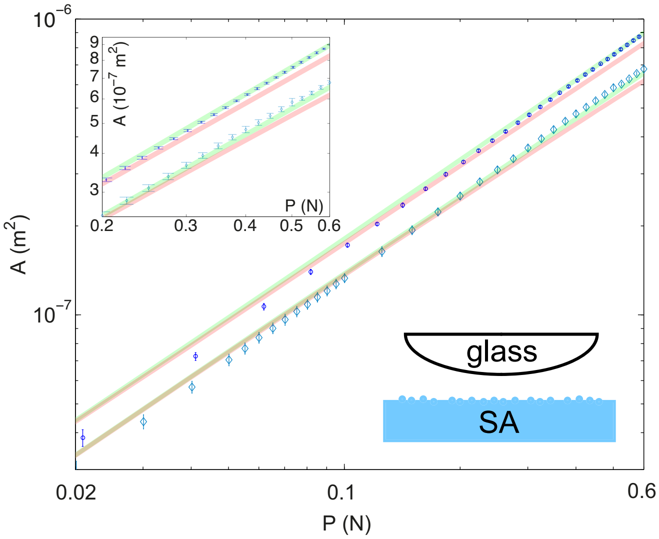

Fig. 5 Log-log plot of the real area of contact A versus P for both SA$^-$ ($\phi = 0.1$, blue diamonds) and SA$^+$ ($\phi = 0.4$, blue circles) samples. The inset is a close up for $0.2 \leq P \leq 0.6$ N. Error bars are given by the standard deviation of A on 24 different contact configurations. Red shaded areas correspond to the predictions of Ciavarella *et al.*'s model[14,15] by setting α_{ij} to 0 in eqn (2). Green areas correspond to $\alpha_{ij} \neq 0$. Areas extent characterizes the scatter in the simulations, arising from uncertainties in the experimental determination of E.

Role of elastic interactions

True contact area load dependence

Using contact imaging techniques, we were able to probe how the total true contact area varies with the applied load for contacts between a smooth surface and the different model rough surfaces decorated with spherical caps. For all sizes and spatial distributions of the micro-asperities tested here, we found that $A(P)$ curves could be satisfactorily described within the framework of a simple rough contact model with a classical assumption that Hertzian contact occurs at the scale of the micro-asperities. As opposed to both GW's and GT's models, our approach takes into account in an approximate manner the elastic coupling between asperities which is often neglected to fully describe the contact mechanics of rough interfaces.

For all investigated SA topographies, a nearly linear relationship is found for $A(P)$, which is consistent with the conclusions of the paper of Greenwood and Tripp[13] that states that $A(P)$ is "approximately" linear. More generally, our findings for SA surfaces do not depart from most of asymptotic development at low P of most current rough contact models for nominally flat surfaces[10]. Such models, indeed, also predict a linear $A(P)$ relationship. Conversely, for RA topographies, a non-linear power law like $A(P)$ relationship is found. Such deviations from linearity was actually pointed out in recent theoretical works by Carbone and Bottiglione[24] for nominally plane–plane rough contacts. These authors pointed out indeed that asperity contact models deviate very rapidly from the asymptotic linear relation even for very small, and in many cases, unrealistic vanishing applied loads. For our present sphere–on–plane contact, it is legitimate to wonder if the magnitude of the deviations arises either from the differences in the asperities height and size distributions and/or the macroscopic curvatures of the spherical indenter.

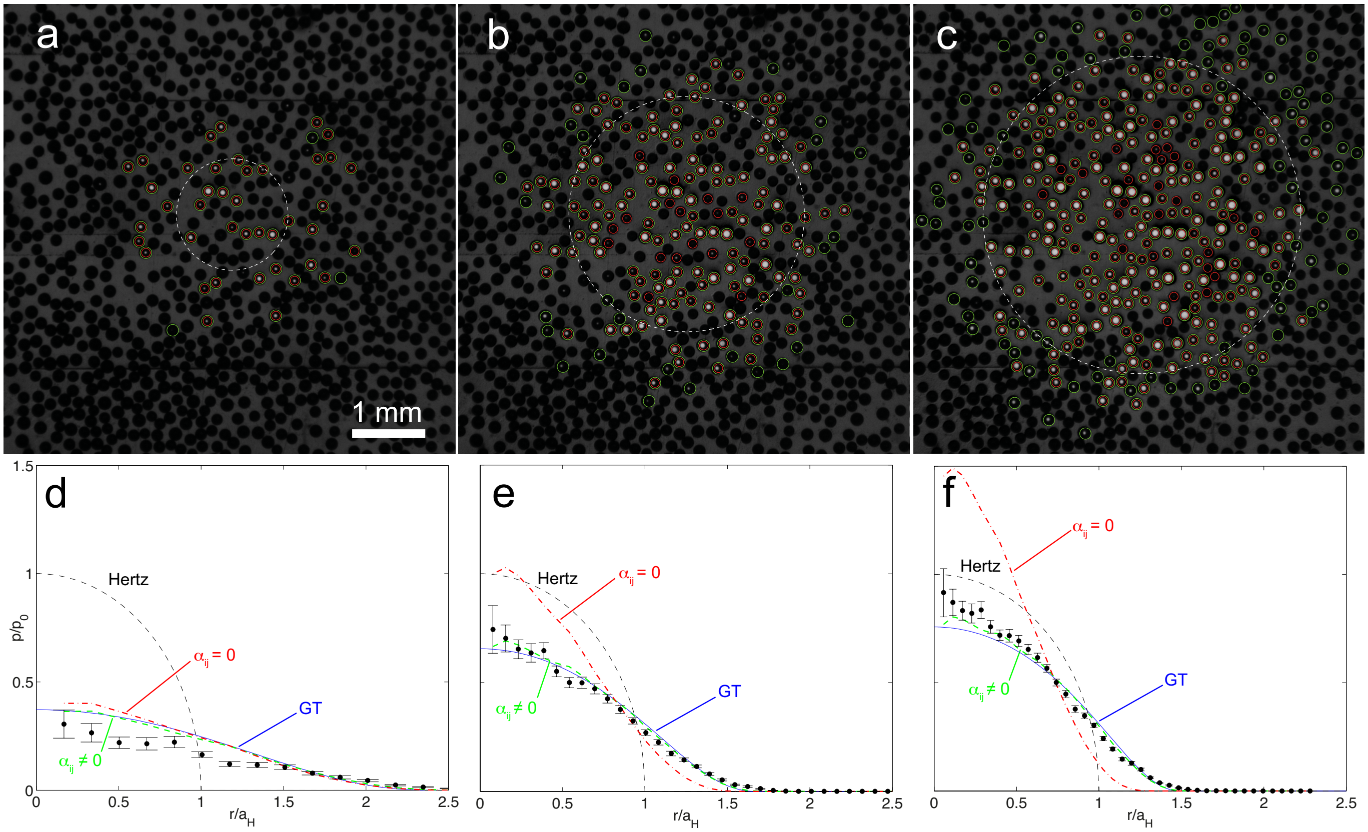

Fig. 6 (Color online) (a), (b), (c) Images of the interface at $P = 0.02, 0.2, 0.5$ N with the $\phi = 0.4$ SA sample. microcontacts appear as the white disks. Green (*resp.* red) circles indicate Ciaravella *et al.*'s model predicted microcontacts with $\alpha_{ij} \neq 0$ (*resp.* $\alpha_{ij} = 0$). On all images, the white dashed line circles delimit Hertz contacts for the corresponding P. (d),(e),(f) Angularly averaged pressure p distribution as a function of the distance to the center r on a SA sample with $\phi = 0.4$ at increasing normal loads P. Both p and r are normalized by respectively, Hertz' maximum pressure p_0 and Hertz contact radius a_H. The black dashed line corresponds to Hertz prediction. Blue solid lines are fits using Greenwood-Tripp model (GT) with a uniform asperity height density and same surface density ϕ. The red dot-dashed lines are predictions of Ciaravella *et al.*'s model[14,15] setting the interaction term $\alpha_{ij} = 0$, while the green dashed lines correspond to the full model with $\alpha_{ij} \neq 0$. Both latter predictions are statistical averages over 1000 independent pattern realizations with $\phi = 0.4$ and a uniform height distribution.

To provide an answer to this question, simulations using Ciaravella's *et al.*'s model, with the exact same asperities distribution (height, radius of curvature and lateral distribution) but different radii of curvature R_l of the macroscopic lens indenter ($R_l = 13$ mm and $R_l = 128.8$ mm, as in the experiments) were performed. In both cases, $A(P)$ curves are found to follow asymptotically (for $0.005 \leq P \leq 1$N) a power law, whose exponent is ~ 0.86 with $R_l = 13$ mm and ~ 0.93 with $R_l = 128.8$ mm. Decreasing R_l thus enhances the nonlinearity of the $A(P)$ relationship. It is likely that such effects simply result from the fact that the increase in the gap between both the PDMS and the lens from the edges of the contact is larger for a lens with a small radius of curvature. For a load increase δP, the increase in the number of microcontacts at the periphery of the apparent contact area is thus expected to be more pronounced with a large R_l. This should translate into a more linear $A(P)$ dependence for large R_l. This hypothesis is further supported by a simple calculation detailed in Appendix A. Assuming that the rough contact obeys Hertz law at the macroscopic length scale, one can express the gap height between surfaces at the periphery of the contact as a function of the Hertzian radius and the radius of curvature of the indenting lens. Equating this gap height to the standard deviation of the height distribution yields a characteristic length scale Δ which corresponds to the size of the annular region surrounding the Hertzian contact. This length is found to vary as $\Delta \propto R_l^{5/9} P^{-1/9}$. This confirms that for a given applied load, the extension of the contact area from its Hertzian value, as resulting from microasperities contacts, should be enhanced when R_l increases.

Of course, it is expected that the non-linearity of the $A(P)$ relationship could also depend on the statistical properties of the asperity distributions. This is indeed suggested by eqn. (A.9) which predicts that Δ scales as $\sigma^{2/3}$, where σ is the standard deviation of the height distribution of asperities. One can also mention the early theoretical work of Archard[3], based on hierarchical distribution of spherical asperities on a spherical indenter. This model predicts that $A(P)$ follows a power law whose exponent varies between 2/3 (*i.e.* the limit of the smooth Hertzian contact) and unity (when the number of hierarchical levels of asperities is increased).

Before addressing further the issue of the elastic interactions between microcontacts, some preliminary comments are warranted, regarding the sensitivity of the $A(P)$ relationship to the details of the spatial distribution of microasperities. For that purpose, one can consider a comparison between experimental and theoretical results for RA patterns. While the micro-asperities were distributed spatially according to a uniform random distribution in the simulations, such a distribution probably does not reproduce very accurately the features of the droplet pattern. As a result of droplet coalescence during condensation, some short distance order is probably achieved between asperities as suggested by a close examination of Fig. 1a. However, the good agreement between the experiments and the simulations in Fig. 4a shows that the load dependence of the actual contact area is not very sensitive to the details in the spatial distribution of asperities. As far as the normal load dependence of the real contact area is considered, the relevant features of surface topography are thus likely to be mainly the surface density of micro-asperities, and their size and height distributions.

Microcontacts and pressure spatial distributions

So far, we only considered the effect of the elastic interaction on the load dependence of A, and thus neglected any spatial dependence of the microcontacts distribution. Direct comparison of such data with Ciaravella *et al.*'s model calculations is not easily accessible for RA samples since it would require a knowledge of all asperities positions and respective radii of curvature. With SA samples however, this can be easily done, as positions and radii of curvature of asperities are known by design of the micromilled pattern. Figures 6a-b-c show such direct comparison at three increasing normal loads P ($P = 0.02, 0.2, 0.5$ N) for the case of the SA$^+$ sample. As expected, predicted microcontacts with $\alpha_{ij} \neq 0$ almost always match the measured microcontacts (see the green circles on the figure). For comparison, red circles at the predicted positions of the model without elastic interaction have been overlapped on the contact images. Clearly, the non-interacting model predicts contacts at locations within the apparent contact which are not seen in the experiment.

To perform a more quantitative comparison with theoretical predictions, we computed for both the experimental and calculated points, the local radial pressure profiles $p(r)$. The latter, which is expected to be radially symmetric for a sphere–on–plane normal contact, was obtained by summing up local forces p_i exerted on all microcontacts located within an annulus of width $dr = 0.25$ mm and radius r centered on the apparent contact center (obtained from JKR experiments). To reduce the statistical error, averaging of $p(r)$ for several contact configurations was then performed. For the experiment, 24 contact configurations (compatible with the size of the SA pattern) at different locations on the same SA pattern were used. For the calculated data (Ciaravella *et al.*'s model), 1000 statistically different SA patterns were used and normal loading was done at the center of the SA pattern. Both $\alpha_{ij} = 0$ and $\alpha_{ij} \neq 0$ data were computed. To test the effect of including an elastic interaction at different length scales, we also computed $p(r)$ as predicted by GT's model. As discussed earlier, this model indeed constitutes in some sense a 'zeroth order approximation' of Ciaravella *et al.*'s model, as it only takes into account long range elastic interactions whose extent is set by the size of the apparent contact. GT's calculation was implemented with Mathematica 9 (Wolfram Research Inc., USA), using a random asperities height distribution with heights chosen uniformly between 30 and 60 μm.

Figures 6d–e–f show the results on the example of SA$^+$ for the three increasing loads P of Figs. 6a–b–c. As already anticipated from Figs. 6a–b–c, Ciaravella *et al.*'s model with $\alpha_{ij} \neq 0$ gives a reasonably good fit of the measured data. Taking $\alpha_{ij} = 0$ yields larger discrepancy with the experimental points, revealing that, on average, the effect of the elastic interaction is to increase significantly the apparent radius of contact, the higher the normal load P. As pointed out by Greenwoood and Tripp in their original paper, the effect of roughness is to add a small tail to the Hertzian pressure distribution which corresponds to the annular region around the Hertzian contact in which the separation is comparable with the surface roughness. Indeed, as already mentioned earlier, an order of magnitude of this tail is provided by the characteristic length Δ which scales as $R^{5/9}\sigma^{2/3}$ (see Appendix A). It can be noted that this scaling is very close to that deduced from different arguments by Greenwood and Tripp (*i.e.* $\Delta \propto \sqrt{R\sigma}$).

Given the experimental error bars, it is difficult to clearly delineate which of Ciaravella *et al.*'s interacting model or GT's model fits best the measured data. Actually, to first order, both models fit equally well the experiments, and constitute, to our knowledge, the first direct experimental validation of both models. This suggests in particular, that if one needs to measure the spatial distribution of pressure $p(r)$, GT's model is a very good approximation. Second, it indicates that short range local elastic interactions effects cannot easily be caught when analyzing the radial pressure distribution, or that these effects are of second order.

The fact that $p(r)$ distributions are very similar for both models motivates a closer examination of the distributions of quantities from which $p(r)$ derives. For that purpose, the pressure dependence of surface density η and mean radius $\overline{a}$ of microcontacts was considered (where η is defined as the number of microcontacts per unit area). In Fig 7, theoretical (as calculated from Ciavarella's model with $\alpha_{ij} \neq 0$) and experimental values of η and $\overline{a}$ are reported in a log-log plot as function of the contact pressure p. Two different domains are clearly evidenced. When the pressure is greater than a critical value p^*, which is here of the order of 50 Pa, η and $\overline{a}$ exhibit with p a power law behavior whose exponents are found to be equal to 0.4 and 0.2, respectively, from the simulated data. As detailed in Appendix B, these exponents are identical to that predicted by the GW model for nominally flat surfaces in the case of a uniform distribution of asperities heights ($\eta \propto p^{2/5}$ and $\overline{a} \propto p^{1/5}$). This means that as long as $p > p^*$, the pressure dependence of η and $\overline{a}$ is insensitive to both the effects of the elastic coupling between micro-asperities contacts and to the curvature of the nominal surfaces. Below the critical pressure p^*, a power law dependence of η and $\overline{a}$ is still observed but with exponents, respectively 0.78 ± 0.11 and 0.37 ± 0.02, which depart from the GW predictions (Fig. 7). We do not yet have a definite explanation for these deviations which are systematically observed, irrespective of the number of surface realizations (up to 8000) considered. They could tentatively be attributed to some short range effects of the pair correlation function associated with asperity distribution. However, the important point is that p^* always corresponds to very low contact pressures. From an extended set of numerical simulations where parameters such as asperities density, radius of curvature and height distribution were varied by at least one order of magnitude, p^* was systematically found to be in the range $10^1 - 10^3$Pa. For the considered contact conditions, such a pressure range corresponds to a very narrow domain at the tail of the pressure distribution whose physical relevance is questionable. In other words, both the simulations and the experimental data indicate that the GW theory is able to describe accurately the microcontacts distribution over most of the investigated pressure range without a need to incorporate the effects of short range elastic interactions in the rough contact description.

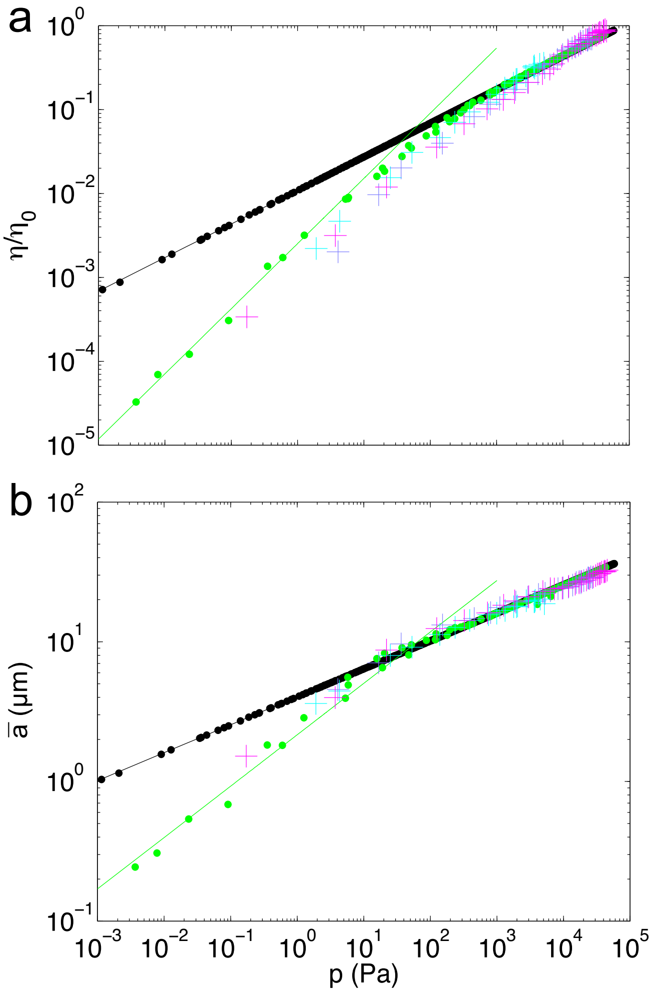

Fig. 7 (Color online) (a) Microcontacts density η, normalized by the mean number of micro-asperities per unit area η_0, versus local pressure p for the SA sample with $\phi = 0.4$. (b) Mean microcontacts area $\bar{a}$ versus local pressure p for the same sample. On both graphs, black disks are the results of GT's model predictions, the green disks are predictions of Ciaravella *et al.*'s model with $\alpha_{ij} \neq 0$ and crosses correspond to the experimental data at three different loads $P = 0.02, 0.2, 0.5$ N. Thick black lines are power law fits of GT's model predicted data, while green solid lines are power law fits of Ciaravella *et al.*'s model predicted data for $p < p^*$, with $p^* \approx 50$ Pa.

Frictional properties

We now turn onto the frictional behavior of RA lenses against a smooth PDMS slab. As mentioned above, RA asperities are very smooth which allows us to consider the associated micro-asperities contacts as single-asperity contacts. RA surfaces thus provide systems with a single roughness scale as opposed to SA surfaces which present an additional microscopic roughness. In what follows, we address from preliminary results the issue of the contribution of individual micro-asperities contact to the macroscopic friction force. For P within [0.01–0.6] N and driving velocities v up to 5 mm s^{-1}, both RA$^+$ and RA$^-$ lenses systematically exhibited smooth steady state friction with no evidence of contact instabilities such as stick-slip, nor strong changes in their frictional behavior. Thus, only results obtained at the intermediate velocity of $v = 0.5$ mm s^{-1} are reported here. Figure 8 shows the resulting lateral force Q versus normal force P curves for both RA$^-$ (Fig. 8a) and RA$^+$ (Fig. 8b) samples, as well as for a reference glass lens with the same radius of curvature and covered with a thin smooth layer of the same sol-gel material used for RA lenses (Fig. 8b, inset). In all cases, Q is found to vary non-linearly with P. In the simplest description, the total friction force Q is expected to be the sum of local friction forces q_i acting on all contacting micro-asperities. According to previous studies using glass/PDMS elastomer contacts[25,26], a constant, pressure independent, shear stress τ_0 can be assumed to prevail at the intimate contact interface between the asperities and the PDMS elastomer, yielding $q_i = \tau_0(\pi a_i^2)$. Within this framework, Q should thus write as

$$Q = \tau_0 A \tag{4}$$

with $A = \sum_i(\pi a_i^2)$ the real area of contact. In the calculation, we take for A the experimental values measured under normal indentation after verifying from optical contact observations that the microcontacts areas during sliding are not significantly different from that achieved under static loading [†]. As a first attempt, the frictional shear stress τ_0 was taken as the experimental value calculated from the ratio of the friction force to the actual contact area measured during steady state friction with the smooth lens. As shown by the dotted lines in Figs. 8a-b, choosing this shear stress value underestimates the experimental data for both small and large size asperities RA samples. Fitting the experimental data with eqn (4) using a least square method yields however $tau_0 = 0.4$ and 0.49 MPa for small and large size asperities respectively. There is thus some evidence of a dependence of the frictional shear stress on the contact length scale, the shear stress at the microcontacts scale being larger than that at the scale of a millimeter sized contact ($\sim$ 18% and $\sim$ 44% increase for RA- and RA+, respectively). Curvatures of the micro-asperity contacts being larger than that of the smooth contact with the glass lens, the increase in τ_0 at small length scales could be attributed to bulk viscoelastic dissipation as a result of the ploughing of the PDMS substrate by the micro-asperities. However, the fact that Q does not vary significantly when the sliding velocity is changed by nearly three orders of magnitude (from 0.01 to

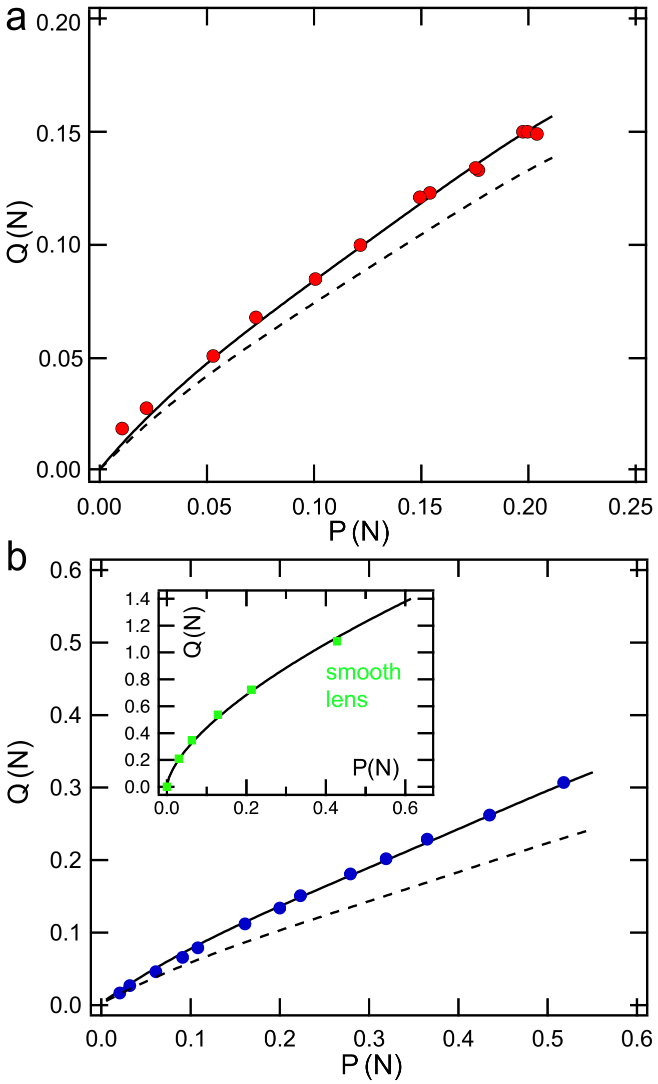

Fig. 8 Q versus P in steady sliding ($v = 0.5$ mm s^{-1}) for contacts between a smooth PDMS substrate and RA$^-$ (a) and RA$^+$ (b) lenses. On both graphs, dashed lines are the theoretical Q given by eqn (4), taking for A its measured values and for $\tau_0 = 0.34$ MPa the average shear stress obtained with the smooth lens. Solid lines are fits of the experimental data with eqn (4), yielding τ_0 =0.40 MPa for RA$^-$ and 0.49 MPa for RA$^+$. Inset: Q versus P for the smooth lens, in steady sliding. The solid line is a fit of the data using eqn (4), taking for A its measured value in steady sliding.

[†] When looking carefully, a slight decrease of individual areas of microcontacts can be seen between the static and sliding regime. This decrease remains however difficult to quantify.

5 $\mathrm{mm\,s^{-1}}$) does not support this assumption. Other effects, arising for example from non linearities in the highly strained microcontacts could be at play, which will be the scope of further investigations. However, these experimental results show that frictional stresses measured at macroscopic length scales may not be simply transposed to microscopic multicontact interfaces.

Conclusion

In this work, we have studied both normal contact and friction measurements of model multicontact interfaces formed between smooth surfaces and rough surfaces textured with a statistical distribution of spherical micro-asperities. Two complementary interfacial contacts were studied, namely a rigid sphere covered with rigid asperities against a smooth elastomer, and a smooth rigid sphere against a flat patterned elastomer. In both cases, experimental $A(P)$ relationships were found to be non-linear and well fitted by Ciaravella *et al.*'s model taking into account elastic interaction between asperities. Additional information regarding the nature of the elastic coupling between asperities was provided from the examination of the profiles of contact pressure, contact density and average radius of asperity contacts. While the long range elastic coupling arising from the curved profile of the indenter was found to be an essential ingredient in the description of the rough contacts, both experimental and simulation results demonstrate that, for the considered topographies, short range elastic interactions between neighboring asperities does not play any detectable role. As a consequence, the pressure dependence of both the density and the radius of asperity contacts within the macroscopic contact is very accurately described using GW model which neglects asperity interactions. To our best knowledge, these results constitute the first direct experimental validation of GW and GT models. The question arises as to what extent our conclusion regarding the elastic coupling could be extrapolated to more realistic surface roughnesses as theoretical simulations using, for example self affine fractal surfaces, indicate a significant contribution of such effects. From an experimental perspective, this issue could be addressed by considering more sophisticated patterned surfaces with hierarchical distributions of micro-asperities.

Acknowledgments

We acknowledge funding from ANR (DYNALO NT09-499845). Many thanks are also due to J.P. Gong (Hokkaido Univ., Japan) for her kind support to this study. We are indebted to J. Teisseire for his support in the fabrication of the sol-gel structures, and to F. Martin for the SEM images of both RA and SA samples, and thank E. Barthel for stimulating discussions. V. Romero is also grateful for a CONICYT financial support from Chile.

Appendix

A Gap between surfaces in Hertzian contact

In a Hertzian sphere–on–flat contact, the vertical displacement u_z of the free surface outside the contact can be expressed as[18]

$$u_z(r) = \frac{4}{3K}\frac{p_0}{2a}\Big[\left(2a^2 - r^2\right)\arcsin(a/r) + ra\left(1 - a^2/r^2\right)^{1/2}\Big] \;\; ; \; r \geq a \tag{A.1}$$

where p_0 is the maximum Hertzian pressure, a is the contact radius and K is the elastic constant defined by $K = 4/3E/(1-\nu^2)$. From the expression of the maximum contact pressure

$$p_0 = \frac{3}{2\pi}\frac{aK}{R_l} \tag{A.2}$$

where R_l is the radius of the spherical indenter, equation (A.1) can be rewritten as

$$u_z\left(r\right) = \frac{1}{\pi R_l}\Big[\left(2a^2 - r^2\right)\arcsin(a/r) + ra\left(1 - a^2/r^2\right)^{1/2}\Big] \;\; ; \; r \geq a \tag{A.3}$$

The profile of the sphere is given by

$$s(r) = \frac{1}{2R_l}\left(2a^2 - r^2\right) \tag{A.4}$$

The gap $[u]\left(r\right)$ between both surfaces is thus given by

$$[u]\left(r\right) = \frac{1}{\pi R_l}\Big[\left(2a^2 - r^2\right)\arcsin(a/r) + ra\left(1 - a^2/r^2\right)^{1/2}\Big] - \frac{1}{2R_l}\left(2a^2 - r^2\right) \tag{A.5}$$

A series expansion of eqn A.5 at $r = a$ yields

$$[u]\left(r\right) \sim \frac{8}{3}\frac{\sqrt{a}\sqrt{2}}{\pi R_l}\left(r-a\right)^{3/2} + O((r-a)^2) \tag{A.6}$$

For a rough contact, a characteristic length Δ can be defined as the length over which the above calculated gap between both surfaces is of the order of magnitude of some length characterizing the asperity distribution, like the standard deviation of the height distribution σ. From the condition $[u]\left(a + \Delta\right) = \sigma$,

$$\Delta \simeq \left(\frac{3\pi}{8\sqrt{2}}\right)^{2/3}\frac{R_l^{2/3}\sigma^{2/3}}{a^{1/3}} \tag{A.7}$$

or

$$\frac{\Delta}{a} \simeq \left(\frac{3\pi}{8\sqrt{2}}\right)^{2/3} \frac{R_l^{2/3}\sigma^{2/3}}{a^{4/3}} \tag{A.8}$$

which can also be expressed as a function of the applied normal load P

$$\begin{aligned} \Delta &\simeq \left(\frac{3\pi}{8\sqrt{2}}\right)^{2/3} R_l^{5/9}\sigma^{2/3}K^{1/9}P^{-1/9} \\ \frac{\Delta}{a} &\simeq \left(\frac{3\pi}{8\sqrt{2}}\right)^{2/3} \left(\frac{K^2R_l\sigma^3}{P^2}\right)^{\frac{2}{9}} \end{aligned} \tag{A.9}$$

B GW's model for a uniform height distribution of spherical asperities

In this Appendix, we formulate the classical GW's model for the contact between two nominally plane rough surfaces in the case of a uniform height distribution of the spherical asperities. Accordingly, non interacting Hertzian contacts are assumed to occur locally at the scale of the micro-asperities. The surface density of microcontacts is given by

$$\eta = \int_d^\infty \psi(z)dz \tag{B.1}$$

where d is the separation between the reference planes of the two surfaces and $\psi(z)$ is the expected number of contacts per unit area at a height between z and $z + dz$ above the reference plane. Similarly, the contact pressure p for a given approach d between the surfaces can be defined as

$$p = \int_d^\infty KR^{1/2}\left(z-d\right)^{3/2}\psi\left(z\right)dz \tag{B.2}$$

where p is defined as the ratio of the applied normal load to the nominal area of contact and $K = 4/3E/(1-\nu^2)$. In the case of a uniform distribution of asperity height with standard deviation σ, one can write

$$\int_{-\infty}^\infty \psi(z)dz = k\sigma = \eta_0 \tag{B.3}$$

where k is a constant and η_0 is the surface density of asperities. The surface density of contacts and the contact pressure can then be rewritten as

$$\eta = \int_0^{\Delta-d} kdx \tag{B.4}$$

$$p = \int_0^{\Delta-d} KR^{1/2}x^{3/2}dx \tag{B.5}$$

which gives

$$\eta = k\left(\Delta-d\right) = \frac{\eta_0}{\sigma}\left(\Delta-d\right) \tag{B.6}$$

$$p = \frac{2}{5}KR^{1/2}\left(\Delta-d\right)^{5/2}\frac{\eta}{\eta_0} \tag{B.7}$$

where Δ is the maximum asperity height above the reference plane. From eqns (B.6) and (B.7), the relationship between the surface density of contacts and the contact pressure can be expressed as

$$\frac{\eta}{\eta_0} = \left(\frac{5}{2}\right)^{2/5}\left[\frac{p}{\eta_0KR^{1/2}\sigma^{3/2}}\right]^{2/5} \tag{B.8}$$

According to the Hertzian behaviour of micro-asperity contacts, the relationship between the expected mean contact radius $\overline{a}$ and the contact pressure is given by

$$p = \frac{K}{R}\eta\overline{a}^3 \tag{B.9}$$

By inserting eqn (B.9) in eqn B.8), the expected mean contact radius may be expressed as

$$\overline{a} = \left(\frac{2}{5}\right)^{2/5}\left[\frac{pR^2\sigma^{2/3}}{K\eta_0}\right]^{1/5} \tag{B.10}$$

References

1 F. Bowden and D. Tabor, *The Friction and Lubrication of Solids*, Clarendon Press, Oxford, 1958.

2 J. Greenwood and J. Williamson, *Proceedings of the Royal Society of London. Series A*, 1966, **295**, 300–319.

3 J. F. Archard, *Proceedings of the Royal Society of London. Series A*, 1957, **243**, 190–205.

4 H. Westergaard, *Journal of Applied Mechanics Transactions of the ASME*, 1939, **6**, A49–A53.

5 K. Johnson, J. Greenwood and J. Higginson, *International Journal of Mechanical Sciences*, 1985, **27**, 383–396.

6 W. Manners, *International Journal of Mechanical Sciences*, 2003, **45**, 1181–1199.

7 W. Manners, *Proceedings of the Royal Society of London. Series A*, 1998, **454**, 3203–3221.

8 B. Persson, *Journal of Chemical Physics*, 2001, **115**, 3840–3861.

9 S. Hyun, L. Pei, J. F. Molinari and M. O. Robbins, *Physical Review E*, 2004, **70**, year.

10 C. Campana, M. Muser and M. Robbins, *Journal of Physics-Condensed Matter*, 2008, **20**, 354013.

11 S. Hyun and M. Robbins, *Tribology International*, 2007, **40**, 1413–1422.

12 J. H. Dieterich and B. D. Kilgore, *Tectonophysics*, 1996, **256**, 219–239.

13 J. A. Greenwood and J. H. Tripp, *Journal of Applied Mechanics*, 1967, **34**, 153.

14 M. Ciavarella, V. Delfine and G. Demelio, *Journal of the Mechanics and Physics of Solids*, 2006, **54**, 2569–2591.

15 M. Ciavarella, J. Greenwood and M. Paggi, *Wear*, 2008, **265**, 729–734.

16 G. Guidoni, D. Schillo, U. Hangen, G. Castellanos, E. Arzt, R. McMeeking and R. Bennewitz, *Journal of the Mechanics and Physics of Solids*, 2010, **58**, 1571–1581.

17 A. Letailleur, J. Teisseire, N. Chemin, E. Barthel and E. Sondergard, *Chemistry of Materials*, 2010, **22**, 3143–3151.

18 K. Johnson, *Contact Mechanics*, Cambridge University Press, Cambridge, 1985.

19 E. Gacoin, A. Chateauminois and C. Frétigny, *Tribology Letters*, 2006, **21**, 245–252.

20 A. Prevost, J. Scheibert and G. Debrégeas, *European Physical Journal E*, 2013, **36**, 13017.

21 V. Romero, E. Wandersman, G. Debrégeas and A. Prevost, *Physical Review Letters*, 2014, **112**, 094301.

22 M. Piccardo, A. Chateauminois, C. Frétigny, N. Pugno and M. Sitti, *Journal of the Royal Society Interface*, 2013, **10**, 20130182.

23 L. Landau and E. Lifshitz, *Theory of Elasticity. Third Edition*, Butterworth Heinemann, 1986.

24 G. Carbone and F. Bottiglione, *Journal of the Mechanics and Physics of Solids*, 2008, **56**, 2555–2572.

25 D. Nguyen, P. Paolino, M.-C. Audry, A. Chateauminois, C. Frétigny, Y. L. Chenadec, M. Portigliatti and E. Barthel, *Journal of Adhesion*, 2011, **87**, 235–250.

26 A. Chateauminois and C. Frétigny, *European Physical Journal E*, 2008, **27**, 221–227.

PROJET DE RECHERCHE

Je souhaite poursuivre mes recherches selon trois axes essentiels. Les deux premiers sont la continuation de projets déjà amorcés, tandis que le troisième axe constitue un nouvel axe de recherche.

Le premier axe est en effet tourné vers la mécanique du contact d'interfaces élastomère-verre en se focalisant sur l'étude des effets d'une texturation à des échelles mésoscopiques sur les propriétés de frottement. Quant au deuxième, il fait suite à mon activité autour de la perception tactile digitale humaine et étend l'approche biomimétique à celle de la perception tactile vibrissale chez les rongeurs.

Le troisième et nouvel axe correspond à une volonté de se rapprocher des thématiques biophysiques de plus en plus présentes au sein du LJP. Je compte y investir une part croissante de mon temps, et souhaite étudier les processus de mécano-transduction aux échelles cellulaires et moléculaires, en utilisant des systèmes biomimétiques de la paroi cellulaire ou d'une assemblée de cellules connectées.

A. Mécanique du contact et frottement solide de surfaces micro-texturées

J'étends actuellement mes travaux sur le frottement multi-contacts de surfaces texturées à des échelles mésoscopiques en tirant parti des deux types de systèmes que nous avons récemment mis au point.

Nous avons réalisé par micro-fraisage et moulage des surfaces constituées de quelques milliers d'aspérités sphériques de rayon de courbure typique 100 µm, réparties aléatoirement spatialement et en hauteur. Nous avons montré que ces surfaces, une fois en contact avec une surface de verre lisse, permettaient la mesure simultanée des forces locales, normales et tangentielles, sur chaque aspérité. Nous avons tiré parti de ces mesures pour analyser la dynamique de stick-slip de la topographie la plus simple possible, constituée d'un réseau hexagonal d'aspérités de même hauteur. Nous avons ainsi mis en évidence l'existence de fronts de détachement ou précurseurs de glissement, quasi-statiques et qui se propagent normalement aux lignes d'iso-pression.

Avec A. Chateauminois, C. Frétigny (SIMM-ESPCI) et M. Chaudhury (Lehigh University, USA), nous avons également développé un procédé alternatif pour fabriquer des surfaces similaires obtenues par moulage d'un élastomère contre une surface solide recouverte de microgouttelettes condensées. Bien que de telles surfaces ne permettent pas un aussi bon contrôle des distributions des aspérités que le permet le micro-usinage, elles demeurent néanmoins intéressantes car les aspérités obtenues sont parfaitement lisses, ce qui facilite la mesure optique.

Ces deux types de topographies offrent une perspective unique pour mesurer simultanément champs de contraintes normales et tangentielles dans un contact 2D et ainsi tester finement les modèles de mécanique du contact développés pour décrire la mise sous charge d'interfaces rugueuses et qui n'ont jusqu'à présent reçu que peu de confirmation expérimentale. En particulier, en faisant varier la densité d'aspérités ou l'épaisseur du bloc, nous testerons l'importance des effets de couplage élastique entre aspérités non pris en compte dans ces modèles, dans différentes géométries de contact.

En ce qui concerne la transition statique-dynamique, nous avons limité notre étude au cas de surfaces simples constituées d'un réseau hexagonal d'aspérités de même hauteur et essentiellement au régime de stick-slip. Je souhaite étendre notre étude à la mise en charge initiale et également au cas de surfaces dont les aspérités sont distribuées aléatoirement, spatialement et en hauteur. Cela permettra une meilleure comparaison avec notamment les travaux de l'équipe de J. Fineberg sur des interfaces rugueuses aléatoires. De plus, notre système met en jeu un contact entre deux surfaces (verre et PDMS) aux propriétés élastiques très différentes. On cherchera à savoir comment la transition statique-dynamique est changée si l'on remplace la surface de verre par un bloc de PDMS.

Jusqu'à présent, seule la dynamique de rupture au seuil de glissement a reçu une attention accrue. En revanche, la question de savoir comment l'interface « recolle » une fois que les fronts de détachement sont passés demeure entière. Nous étudierons ce problème en cherchant à corréler dynamique de recollement et mesures locales des contraintes dans le contact, dans deux types de géométrie, sphère-plan et plan-plan.

Enfin, par analogie avec le système à empreintes, nous étudierons la réponse mécanique de ces surfaces en régime de frottement établi, lorsqu'elles sont sollicitées par une rugosité microscopique ou des défauts chimiques hétérogènes. Il s'agira d'analyser le spectre des fluctuations de la force de frottement macroscopique en le corrélant à la dynamique locale des microcontacts. Plus généralement, on se posera la question de savoir si, de la mesure des caractéristiques spectrales des fluctuations de la force de frottement, il est possible d'inférer les caractéristiques topographiques de la surface rugueuse sondée.

B. Biomimétisme de la perception tactile : frottement de systèmes résonnants

Nos travaux antérieurs sur la perception tactile digitale humaine ont permis d'identifier les paramètres mécaniques pertinents (texturation de la peau, position des mécanorécepteurs dans la zone de contact, loi de frottement. . .) dont dépend la fonction de transfert texture/stimulus mécanique. Ces expériences ont été menées dans des régimes de frottement quasi-statique, caractérisés par des fréquences de modulation des contraintes de plusieurs ordres de grandeur inférieurs aux fréquences de résonance de l'organe tactile.

Dans le cadre de la thèse de N. Claverie, nous cherchons actuellement à comprendre comment les propriétés de transduction mécanique peuvent être modifiées lorsque ces deux fréquences caractéristiques deviennent proches. Chez l'humain, la peau peut être considérée, d'un point de vue mécanique et en première approximation, comme une membrane élastique faiblement tendue. Elle présente donc des propriétés de résonance dont on peut supposer qu'elles participent au mécanisme de transduction. Récemment, Bensmaia *et al.* **[1]** ont caractérisé la propagation d'ondes de vibration sur des doigts humains soumis à une indentation localisée, de fréquence et d'amplitude contrôlées. Ils ont établi que, pour des fréquences de stimulation proches des fréquences propres de résonance de la peau, la perturbation induite peut se propager sur des distances de l'ordre de la taille du doigt. Ce mécanisme pourrait avoir des conséquences importantes sur la perception tactile, car il permettrait un recrutement de mécanorécepteurs situés loin de la zone de contact.

Pour étudier ces questions chez l'humain, une approche biomimétique consisterait à modéliser la peau par une membrane d'élastomère gonflée que l'on vient frotter par exemple contre des textures bien caractérisées.

Nous avons préféré aborder cette question en reproduisant le fonctionnement d'un autre type de système frottant résonant qui a les avantages d'être unidimensionnel, *a priori* plus simple à modéliser qu'une membrane, et qui constitue un paradigme pour étudier les mécanismes de traitement de l'information tactile sensorielle. Il s'agit du système vibrissal des rongeurs.

Les rongeurs sont des mammifères pratiquement aveugles qui utilisent en effet comme organe tactile, leurs moustaches faciales ou vibrisses pour se localiser, détecter les formes et les textures des objets environnants **[2-5]**. Ces organes sont totalement dépourvus de mécanorecépteurs et transportent l'information tactile sous forme de déformations/vibrations mécaniques depuis l'endroit du contact vibrisse/substrat jusqu'au follicule où sont logés les mécanorécepteurs.

Deux modes d'exploration sont généralement observés, que les rongeurs utilisent indépendamment ou en combinaison pour détecter la présence d'obstacles ou discriminer des textures **[6, 7]**. On distingue un mode actif dit de "whisking" au cours duquel le rongeur se déplace peu et bouge activement dans un mouvement de va et vient ses vibrisses (5-25 Hz) et un mode passif où il se déplace rapidement tout en frottant ses vibrisses maintenues à une position fixe. Les études réalisées jusqu'à maintenant proposent essentiellement deux mécanismes que les rats utiliseraient pour obtenir une information sur la texture. Le premier mécanisme met en avant les propriétés de résonance des vibrisses. De par leur forme allongée, celles-ci se comportent des oscillateurs amortis, agissant comme des filtres passe-bande, dont la fréquence caractéristique est définie par la géométrie de chaque vibrisse. Ceci suggère un mécanisme de décomposition spectrale de l'information tactile par l'ensemble des vibrisses. On parle de codage résonant différentiel **[8]**. Le deuxième mécanisme est basé sur les résultats de récentes études qui semblent indiquer que dans la majorité des situations d'exploration, la dynamique des vibrisses est dominée par la séquence temporelle des événements de « stick-slip », dont la statistique serait directement reliée aux propriétés de rugosité de la surface sondée. On parle de codage cinétique **[9]**. Les deux mécanismes proposés s'appuient sur des expériences de comportement de rats à qui l'ont apprend à discriminer différents types de rugosités, comme des papiers de verre de différents grains, et leur importance relative est toujours discutée.

Pour aborder la question de la transduction mécanique de l'information tactile chez les rongeurs, nous avons récemment développé un système biomimétique de la vibrisse, qui consiste en une tige élastique conique, dont la conicité est obtenue en tirant d'un bain d'acide nitrique une tige cylindrique en laiton à vitesse constante. Cette tige conique peut être utilisée en tant que telle, et peut aussi être utilisée comme base de moulage pour fabriquer une tige en polyuréthane. Deux montages complémentaires ont été développés permettant de reproduire les deux modes d'exploration observés, respectivement passif et actif.

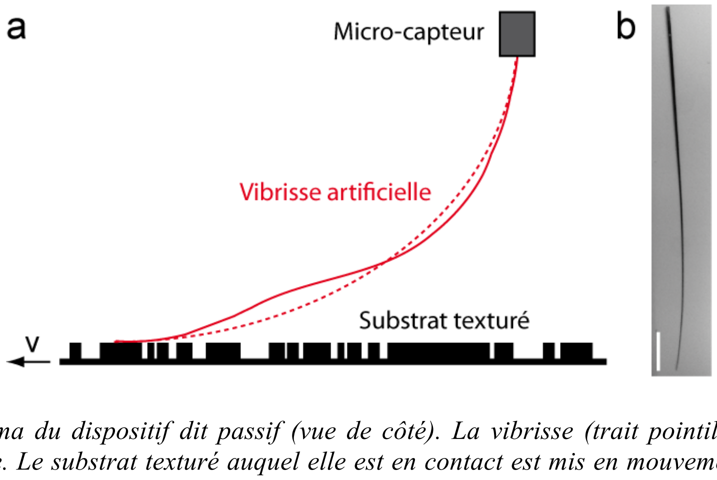

Figure 19 – **(a)** *Schéma du dispositif dit passif (vue de côté). La vibrisse (trait pointillé) est connectée à un micro-capteur de force. Le substrat texturé auquel elle est en contact est mis en mouvement à vitesse V à l'aide d'un moteur linéaire. La texture génère des oscillations de la vibrisse (trait plein) qui peuvent être détectées optiquement. Les forces et moments en base de vibrisse seront mesurés avec un micro-capteur de force.* **(b)** *Photo d'une vibrisse biomimétique en laiton obtenue au laboratoire par attaque chimique à l'acide nitrique. La barre a 1 cm de longueur.*

Le mode d'exploration passif est reproduit en considérant une vibrisse montée sur un capteur de force, maintenue à une position fixe et mise au contact de substrats texturés déplacés linéairement **(Fig. 19)**. Le mode actif de « whisking » est quant à lui obtenu avec une vibrisse montée sur une tête de rhéomètre qui peut osciller périodiquement avec une amplitude finie et une fréquence donnée. Pour les deux dispositifs, les mesures de forces et de moments sont complétées par des mesures en caméra rapide des déformations/vibrations de la vibrisse.

Jusqu'à présent, nous avons caractérisé les réponses statique et dynamique de vibrisses biomimétiques dans des situations de contact simples et contrôlées, comme la mise en contact avec un obstacle, obtenue en indentant à vitesse finie une vibrisse fixe, ou la rencontre avec des marches ou des creux, en mesurant notamment les moments en base de vibrisse.

Dans le cas du choc, une des questions à laquelle nous souhaiterions répondre est de savoir laquelle des deux mesures, statique (c'est-à-dire déformation quasi-statique de la vibrisse) ou dynamique (c'est-à-dire mettant en jeu la propagation rapide depuis l'endroit du contact jusqu'au follicule de vibrations), est la plus adaptée pour une détection rapide de la présence d'un obstacle. Des expériences consistant à enregistrer la réponse corticale montrent en effet que les rongeurs détectent la présence d'un obstacle en quelques dizaines de millisecondes, ce qui suggère qu'un mécanisme dynamique serait beaucoup plus efficace.

Dans le cas de marches et de creux élémentaires, il s'agit essentiellement de relier déformations en base de la vibrisse à leurs caractéristiques topographiques (hauteur, largeur, rapport d'aspect) afin d'identifier la limite mécanique de détection et discuter, comme dans le cas du choc, l'apport d'un mécanisme de détection dynamique comparé à une détection purement quasi-statique. En effet, au passage d'une marche, on s'attend à qu'une onde de vibration soit également déclenchée.

Nous disposons actuellement de deux dispositifs de mesure complémentaires, ainsi que d'un modèle biomécanique de vibrisse en interaction développé par G. Debrégeas au LJP **[10]** dont on peut tester en détail les prédictions sur notre système biomimétique. Ces trois outils devraient permettre de répondre à plusieurs des questions suivantes.

Nous utiliserons le dispositif actif pour reproduire les conditions exploratoires réelles de « whisking » utilisées par les rongeurs pour détecter les obstacles. Au cours de ce mouvement, les vibrisses des rongeurs vibrent à leur fréquence propre. En revanche, lors du contact avec un obstacle, le changement des conditions aux limites modifiera leurs fréquences de vibration. La détection d'un obstacle pourrait donc reposer sur ce changement de fréquence, dont nous testerons l'efficacité avec notre système biomimétique.

Nous chercherons également à mieux caractériser les événements individuels de « stick/slip » qui peuvent exister à l'interface entre les vibrisses et la surface explorée, en étudiant le décrochement d'une vibrisse en rotation, initialement au contact d'une surface plane. Nous identifierons quel angle/moment critique conduit à son décrochement et comment celui-ci dépend des conditions de chargement et de la topographie du substrat.

Nous caractériserons ensuite le signal vibratoire produit par une succession de ces événements de « stick/slip » obtenus par exemple, en frottant la vibrisse contre des textures micro-fabriquées ou des surfaces réelles de rugosité bien caractérisée. Nous utiliserons pour cela le dispositif passif. Il s'agira ici de caractériser les propriétés statistiques des fluctuations du signal de moment, et d'inférer de ces mesures les caractéristiques spectrales de la topographie sondée.

Nous souhaitons également fabriquer des systèmes à plusieurs vibrisses (jusqu'à 4 vibrisses) qui permettront notamment de déterminer si la séquence temporelle des événements de « stick-slip » mesurés en base de chaque vibrisse permet une discrimination rapide des textures sur des temps beaucoup plus courts que la durée typique entre deux événements successifs de « stick-slip » **[11]**. Ce type de mécanisme pourrait expliquer la célérité avec laquelle les rongeurs parviennent à discriminer des textures. Nous pourrons explorer ces différents aspects indépendamment avec le dispositif actif ou passif.

Enfin, nous avons récemment entamé des discussions avec T. Celikel (Faculty of Science, Department of Neurophysiology, Nijmegen, Pays-Bas). Son groupe étudie les stratégies de codage de l'information somatosensorielle chez le rat. Pour cela, ils combinent mesures optiques des déformations des vibrisses de rats anesthésiés ou éveillés et enregistrement de l'activité neuronale au niveau des ganglions trigéminaux, qui constituent le premier relai avant tout traitement par le cortex somatosensoriel. Nous souhaitons reproduire avec eux des conditions exploratoires simples (contact quasi-statique ou dynamique d'une ou plusieurs vibrisses, passage de topographies élémentaires comme des creux ou des marches) sur des rats anesthésiés ou éveillés et confronter enregistrements neuronaux, expériences biomimétiques et prédictions théoriques. Ces confrontations devraient permettre d'avoir une meilleure compréhension des mécanismes de codage à l'œuvre.

C. Etude de réseaux mécano-sensibles

Pour ce projet, je souhaite étudier le problème général de la transduction mécanique, c'est-à-dire la manière dont tous les êtres vivants (depuis la cellule unique à une collection de cellules) convertissent un stimulus mécanique en une réponse biologique de nature chimique et/ou électrique. Ces mécanismes ont reçu ces dernières années une attention accrue, notamment avec l'étude du système auditif **[12]**, et suscitent depuis un engouement particulier à l'interface physique-biologie **[13-15]**. Plus précisément, il s'agira pour ce projet d'utiliser une approche biomimétique pour caractériser la mécano-transduction à des échelles cellulaires et moléculaires.

La détection des contraintes mécaniques repose sur la capacité de cellules neuronales spécialisées (mécanorécepteurs) à convertir en impulsions électriques toute fluctuation de contrainte mécanique. On sait que cette capacité dépend de la présence sur leur membrane extérieure, de canaux ioniques – des pores protéiques de taille nanométrique – qui s'ouvrent et se ferment sous l'effet d'une perturbation mécanique **[13, 16, 17]**, créant un flux d'espèces ioniques qui change la perméabilité ionique de la membrane et permet *in fine* de générer un potentiel d'action. La dynamique précise d'ouverture et de fermeture de ces pores sous l'action d'une stimulation mécanique et notamment l'existence d'un seuil de réponse, sont en revanche bien moins comprises **[13]**. Récemment, des techniques consistant à stimuler à l'aide de micropipettes des mécanorécepteurs extraits et cultivés *in vitro* et à mesurer les courants ioniques résultants (techniques de « patch-clamp ») ont été développées **[13]**. Ces mesures sont cependant particulièrement invasives et la méthode de stimulation est peu réaliste. La stimulation est en effet localisée sur la membrane, bien loin des conditions de stimulation qui existent *in vivo* où l'ensemble du tissu environnant transmet les contraintes mécaniques. De plus, les stimulations mécaniques généralement utilisées restent localisées sur la membrane cellulaire et vraisemblablement donnent lieu à une réponse hétérogène d'un nombre inconnu de canaux ioniques **[18]**. Enfin, les réponses rhéologiques et mécaniques des cellules sont connues pour être complexes et sont encore loin d'être bien caractérisées.

Pour surmonter cette complexité inhérente aux systèmes cellulaires naturels, de récents développements ont vu le jour, consistant à fabriquer des systèmes de bicouches lipidiques synthétiques dans lesquelles différents complexes protéiques peuvent être insérés en vue d'étudier leur réponse à des sollicitations contrôlées. En particulier, une approche récente très prometteuse a consisté à utiliser des hydrogels recouverts de lipides (LCH = Lipid Coated Hydrogels) en contact avec des gouttelettes aqueuses ou formées du même hydrogel dans un bain d'huile contenant des lipides. A l'interface de contact se forme une bicouche lipidique dans laquelle différentes protéines transmembranaires, comme des canaux ioniques, ont pu être insérées **[19, 20]**. Comme la bicouche résultante est planaire, il est possible de l'imager avec des méthodes optiques standard de fluorescence, en complément de mesures de courant ionique global à travers la membrane. Des expériences récentes ont principalement étudié l'inclusion de nanopores inertes comme l'alpha-hemolysin (αHL) obtenue à partir de Staphylococcus Aureus.

Pour ce projet, nous chercherons dans un premier temps à insérer des canaux ioniques mécano-sensibles dans cette bicouche et étudierons la réponse mécanique de ces objets à une stimulation mécanique contrôlée en sollicitant directement l'hydrogel. Il s'agira de mesurer comment le transport ionique à travers la membrane est modifié par des perturbations statique ou dynamique. Cela devrait permettre de mieux comprendre comment une membrane biologique convertit une information de type mécanique en un flux d'espèces chimiques. Dans un deuxième temps, nous étendrons ces études à la réponse chimique d'assemblées de gouttelettes LCH connectées par des nanopores mécano-sensibles et soumises à des déformations mécaniques contrôlées.

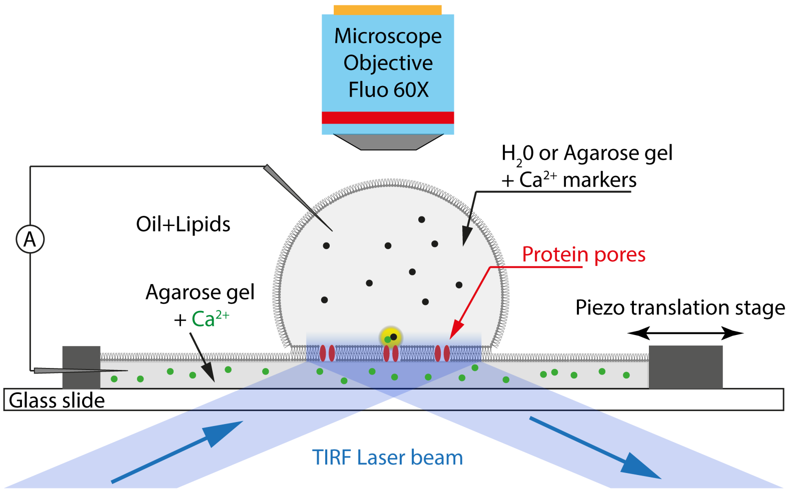

Figure 20 – *Montage expérimental pour imager le flux d'ions à travers les nanopores protéiques en réponse à un stimulus mécanique. Une bicouche lipidique est formée à l'interface de contact entre une gouttelette aqueuse immergée dans un bain d'huile-lipides et un film d'hydrogel contenant des ions* Ca^{2+}*. Le film est solidaire d'un transducteur piézo-électrique permettant d'appliquer des contraintes d'étirement contrôlées sur la bicouche. Les courants ioniques seront mesurés d'une part en imageant la fluorescence induite quand les ions* Ca^{2+} *se lient aux marqueurs, par épifluorescence ou TIRF, d'autre part à l'aide d'une paire de deux électrodes.*

Nous étudierons d'abord les propriétés de mécano-transduction d'une unique bicouche lipidique. Ces membranes seront produites en suivant des protocoles bien établis **[21]**. Comme indiqué sur la **Fig. 20**, une goutte aqueuse (eau ou gel d'agarose) qui contient une marqueur fluorescent sensible au calcium (Fluo 4 ou Oregon Green BAPTA-1 par exemple) sera mise en contact avec un film d'agarose contenant des ions Ca^{2+}. La membrane obtenue sera décorée de pores protéiques qui ne sont pas mécano-sensibles (αHL), puis de pores mécano-sensibles comme les protéines MscS ou MscL qui sont présentes chez la bactérie E. Coli **[22,23]** et dont on sait qu'elles sont importantes pour la protéger contre des chocs hypo-

osmotiques **[24]**. En plus de mesures électriques standard, le transport trans-membranaire sera sondé par imagerie calcique soit en épifluorescence, soit en microcopie TIRF (Total Internal Reflection Fluorescence).
La stimulation mécanique du système bicouche sera faite de deux manières différentes. D'abord, en appliquant une contrainte de compression/étirement à l'aide d'un transducteur piézo-électrique connecté à un des bords du film d'agarose. Ensuite, en cisaillement en déplaçant la gouttelette d'hydrogel du dessus **[25]**. Ce deuxième mode d'excitation permettra d'étudier plus précisément l'effet d'une contrainte de cisaillement sur la cinétique d'ouverture des nanopores mécano-sensibles et de le comparer à un effet purement extensionnel.

Nous étudierons ensuite les propriétés de mécano-transduction d'un réseau connecté de gouttelettes LCH. Nous étudierons en particulier comment la distribution spatiale et temporelle d'espèces chimiques diffusant à travers le réseau est modifiée lorsqu'on la soumet à une contrainte mécanique contrôlée. Chez les êtres vivants, il est bien connu que les gradients de concentration de morphogènes sont essentiels au mécanisme de la morphogenèse **[26]**. Notre système pourrait constituer un cadre simple pour étudier comment les processus de mécano-transduction affectent les conditions d'apparition des motifs morphogénétiques. Nous utiliserons pour cela des réseaux 1D et 2D de quelques centaines de gouttelettes LCH produites par microfluidique (diamètre 10 à 100 µm) **[27]**. Chaque gouttelette sera connectée à ses voisines par des nanopores, d'abord inertes (αHL), puis mécano-sensibles.

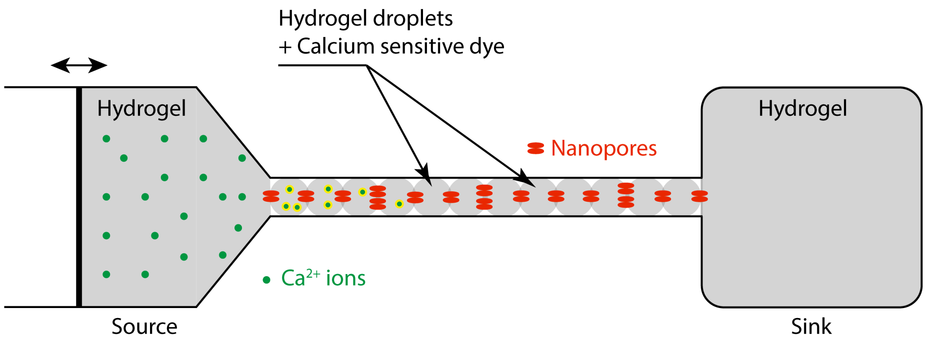

Figure 21 – *Schéma de l'expérience pour étudier les mécanismes de mécano-transduction dans un réseau 1D de gouttelettes LCH.*

Nous considérerons dans un premier temps, le cas 1D en réalisant le montage de la **Fig. 21**. Un canal contenant des gouttelettes LCH sera relié à ses extrémités à deux réservoirs de grande taille dont l'un servira de source d'ions Ca^{2+}. Les gouttelettes contiendront un marqueur calcique fluorescent permettant de visualiser en épifluorescence le transport des ions Ca^{2+} à travers le réseau. La stimulation mécanique du réseau sera obtenue en déplaçant une des parois du réservoir source. Nous étudierons en particulier comment l'ajout d'une contrainte mécanique modifie les propriétés de diffusion du réseau, à savoir comment le profil de concentration des ions Ca^{2+} est modifié spatialement et temporellement. On peut s'attendre notamment à un transport intermittent du à la cinétique d'ouverture/fermeture des nanopores.

Nous généraliserons notre approche au cas 2D. Cette configuration permettra d'exciter en cisaillement le système et de tester l'existence de chemins de transport privilégiés des espèces chimiques. Nous chercherons à quantifier l'effet d'un changement de connectivité chimique sur les propriétés de transport du réseau, soit en variant le nombre moyen de nanopores, soit en jouant sur le désordre géométrique (distributions de tailles de gouttelettes) pour modifier localement le nombre de contacts.

Références :

[1]. L. R. Manfredi *et. al.*, *PLoS ONE* **7**, e31203 (2012).

[2]. D. H. O'Connor *et. al.*, *J. Neurosc.* **30**, 1503 (2009).

[3]. D. B. Polley *et. al.*, *Neurobiol Learn. Mem* **83**, 134 (2005).

[4]. T. Morita *et. al.*, *PloS One* **6**, e20437 (2011).

[5]. M. A. Neimark *et. al.*, *J. Neurosc.* **23**, 6499 (2003).

[6]. S.A. Hires, L. Pammer, K. Svoboda et D. Golomb, *eLife* (2013).

[7]. J.T. Ritt, M.L. Andermann et C.I. Moore. *Neuron* **57**, 599 (2008).

[8]. M.A. Neimark, M.L. Andersmann, J.J. Hopfield et C.I. Moore, *J. Neurosci.* **23**, 6499 (2003).

[9]. J. Wolfe, D.N. Hill, S. Pahlavan, P.K. Drew, D. Kleinfeld et D.E. Feldmann, *PLoS Biol.* **6**, e215 (2008).

[10]. Y. Boubenec, D. Schultz, G. Debrégeas, *Front. Behav. Neurosci.* **6**, 74 (2012).

[11]. R. S. Johansson, J. R. Flanagan, *Nature Review Neuroscience* **10**, 345 (2009).

[12]. F. Nin *et al., PNAS* **109** (51) 21076 (2013).

[13]. P. Delmas *et al., Nat. Rev. Neuroscience* **12**, 139 (2011).

[14]. C. Lucarotti *et al., Sensors* **13**, 1435 (2013).

[15]. S. Aimont *et al., PlosOne* **6** (10), e25529 (2011).

[16]. S. L. Geffeney, M. B. Goodman, *Neuron* **74**, 609 (2012).

[17]. W. C. Ruder *et al., Nature: Sci. Rep.* **2**, 554 (2012).

[18]. C.-M. Cheng *et al., Nature Protocols* **4**, 714 (2010).

[19]. H. Bayley *et al., Mol Biosyst.* **4**(12), 1191 (2008).

[20]. A.J. Heron *et al., J. Am. Chem. Soc.* **131**, 1652 (2009).

[21]. S. Leptihn *et al., Nature Protocols* **8**(6), 1048 (2013).

[22]. C. C. Häse *et al., J. Bio. Chem* **270**(32), 18329 (1995).

[23]. H.M.G. Barriga *et al., J. R. Soc. Int.* **11**, 20140404 (2014).

[24]. I.R. Booth, P. Louis, *Curr. Opin. Microbiol.* **2**, 116 (1999).

[25]. A. J. Heron *et al., JACS* **129**, 16042 (2007).

[26]. N. Tompkins *et al., PNAS* **111**(12), 4397 (2014).

[27]. X. Leng *et al., Lab Chip.* **10**, 2841 (2010).

Publications, conférences et séminaires

A. Publications

Revues à comité de lecture

1. "Galileo Flybys of Earth: The Nature of the Distant Shock" M.G. Kivelson, A. Prevost, F.V. Coroniti, K.K. Khurana et D.J. Southwood, *Adv. Space Res.* **16**, No.4, 197-204 (1995).
2. "Depinning of the superfluid 4He-Cs contact line" E. Rolley, A. Prevost, C. Guthmann, *JLTP* **113**, 787 (1998).
3. "Thermally Activated Motion of the Contact Line of a Liquid 4He Meniscus on a Cesium Substrate" A. Prevost, E.Rolley, C. Guthmann, *Phys. Rev. Lett.* **83**, 348 (1999).
4. "Wetting of helium-4 on rough cesium substrates" A. Prevost, M. Poujade, E. Rolley, C. Guthmann, *Physica B* **280**, 80 (2000).
5. "Dynamics of the contact line on rough substrates" A. Prevost, E. Rolley, C. Guhtmann, M. Poujade, *Physica B* **284-288**, 145 (2000).
6. "An easy to build long working distance microscope" D. Douillet, E. Rolley, C. Guthmann, A. Prevost, *Physica B* **284-288**, 2059 (2000).
7. "Dynamics of a Helium-4 Meniscus on a Strongly Disordered Cesium Substrate" A. Prevost, E. Rolley et C. Guthmann, *Phys. Rev. B* **65**, 064517 (2002).
8. "Forcing and velocity correlations in a vibrated granular monolayer", A. Prevost, D.A. Egolf et J.S. Urbach, , *Phys. Rev. Lett.* **89**, 084301 (2002).
9. "Nonequilibrium two-phase coexistence in a confined granular layer", A. Prevost, P. Melby, D.A. Egolf et J.S. Urbach, *Phys Rev E*, **70**, 050301(R) (2004).
10. "The dynamics of thin vibrated granular layers", P. Melby, F. Vega Reyes, A. Prevost, R. Robertson, P. Kumar, D. A. Egolf, J. S. Urbach, *J. Phys.: Condens. Matter* **17** S2689-S2704, (2005).
11. "Depletion force in a bidisperse granular layer", P. Melby, A. Prevost, D. A. Egolf, J. S. Urbach, , *Phys. Rev. E.* **76**, 051307 (2007).
12. "Experimental evidence of non-Amontons behaviour at a multi-contact interface", J. Scheibert, A. Prevost, J. Frelat, P. Rey, G. Debrégeas, , *Euro. Phys. Lett.* **83**, 34003 (2008).
13. "The Role of Fingerprints in the Coding of Tactile Information Probed with a Biomimetic Sensor", J. Scheibert, S. Leurent, A. Prevost, G. Debrégeas, *Science,* Vol. **323** Issue 5920, pages 1503-1506 (2009).
14. "Effect of fingerprints orientation on skin vibrations during tactileexploration of textured surfaces", A. Prevost, J. Scheibert et G. Debrégeas, *Communicative & Integrative Biology* **2:5**, 1-3 (2009).
15. "Stress Field at a Sliding Frictional Contact: Experiments and Calculations", J. Scheibert, A. Prevost, G. Debrégeas, E. Katzav, M. Adda-Bedia, *J. Mech. Phys. Solids*, **57**, 1921-1933 (2009).
16. "The Role of Exploratory Conditions in Bio-Inspired Tactile Sensing of Single

Topogical Features", R. Candelier, A. Prevost, G. Debrégeas, *Sensors* **11**(8), 7934-7953 (2011).

17. "Texture-Induced Modulations of Friction Force: The Fingerprint Effect", E. Wandersman, R. Candelier, G. Debrégeas, A. Prevost, *Phys. Rev. Lett.* **107**, 164301 (2011).
18. "Crack Front Dynamics across a Single Heterogeneity", J. Chopin, A. Prevost, A. Boudaoud, M. Adda-Bedia, *Phys. Rev. Lett.* **107**, 144301 (2011).
19. "Probing the micromechanics of a multi-contact interface at the onset of frictional sliding", A. Prevost, J. Scheibert, G. Debrégeas, *Euro. Phys. J. E* **36**, 13017 (2013).
20. "Non Amontons-Coulomb local friction law of randomly rough contact interfaces with rubber", D. T. Nguyen, E. Wandersman, A. Prevost, Y. Le Chenadec, C. Frétigny, A. Chateauminois, *Euro. Phys. Lett.* **104**, 64001 (2013).
21. "Probing Locally the Onset of Slippage at a Model Multicontact Interface", V. Romero, E. Wandersman, G. Debrégeas, A. Prevost, *Phys. Rev. Lett.* **112**, 094301 (2014).

Articles de synthèse

22. "Vers des senseurs tactiles biomimétiques", A. Prevost, G. Debrégeas, *Biofutur* **326**, 34 (2011).
23. "Mécanique du contact rugueux et perception tactile", J. Scheibert, G. Debrégeas, A. Prevost, *Reflets de la physique* n°**16**, octobre 2009, pp. 17-19
24. G. Debrégeas, A. Prevost, J. Scheibert, "Toucher digital humain : transduction mécanique de l'information tactile et rôle des empreintes digitales", pp. 11−17, *Images de la Physique* (2009).

Actes de congrès

25. "A Novel Biomimetic Haptic Sensor to study the Physics of Touch", J. Scheibert, A. Prevost, G. Debrégeas, R. Rousier, P. Rey, *Actes Mécano−Transduction* (2004).
26. "A MEMS-based tactile sensor to study human digital touch: mechanical transduction of the tactile information and role of fingerprints", J. Scheibert, G. Debrégeas, A. Prevost, *ICEM 14: 14th International Conference on Experimental Mechanics*, **6**, 21006 (2010).
27. "MEMS-based contact stress field measurements at a rough elastomeric layer: local test of Amontons' friction law in static and steady sliding regimes" J. Scheibert, E. Katzav, M. Adda-Bedia, J. Frelat, A. Prevost, G. Debrégeas, *ICEM 14: 14th International Conference on Experimental Mechanics*, **6**, 26006 (2010).

Articles soumis ou en préparation

28. "Normal contact and friction of rubber with model randomly rough surfaces", S. Yashima, V. Romero, E. Wandersman, C. Frétigny, M. Chaudhury, A. Chateauminois, A. Prevost, soumis à *Soft Matter* (2014).

B. Conférences et séminaires

1. Séminaire invité à Unilever Research and Development, Port Sunlight, Grande-Bretagne, 24 Janvier 2005.
2. Conférence invitée, GDR 2796 “Dynamique Interfaciale Des Milieux Confinés sous Contrainte Mécanique“, Obernai, France, 07 Avril 2005.
3. Conférence invitée, 11ièmes Journées de la Matière Condensée JMC11, Strasbourg, France, 26 Août 2008.
4. Conférence invitée, GDR 3588 - MePhy (MEcanique et PHYsique multi−échelles, mixte INSIS/INP), 03 Juin 2008.
5. Séminaire invité, Université de Leiden, Pays-Bas sur « Contact mechanics at a rough glass−elastomer interface », 06 Juin 2008.
6. Séminaire invité, Institut Jean−Rond d'Alembert, 22 Octobre 2009.
7. Séminaire invité, Gulliver PCT−MMN−NBP−ESPCI, 22 Février 2010.
8. Séminaire invité, INM−Saarbrücken, Allemagne, 06 Octobre 2010.
9. Séminaire invité, ENS Cachan, 14 Décembre 2010.
10. Séminaire invité, Laboratoire MSC, 26 Septembre 2011.
11. Conférence invitée, 26th Conference on Surface Modification Technologies SMT26, Lyon, 20-22 Juin 2012.
12. Communication orale GDR 3588 - MePhy, Workshop Adhésion-Friction, « Probing locally the onset of slippage at a model multicontact interface », 29 Septembre 2014.
13. Conférence invitée, CECAM-COST « Friction and Interface Dynamics at Nano- and Mesoscales », Tel-Aviv University, Tel Aviv, Israël, 27-31 Octobre 2014.

Encadrement

- **Doctorants**
  - Julien Scheibert (2003-2007), Mécanique du contact aux échelles mésoscopiques (récompensé par le prix Edouard Branly 2008).
  - Laure Nayélie Claverie (depuis Octobre 2012).
- **Postdoctorants**
  - Raphaël Candelier (depuis Octobre 2009).
  - Elie Wandersman (Novembre 2010 à Septembre 2011).
  - Victor Romero (Octobre 2011 à Décembre 2013).
- **Jeunes chercheurs**
  - Elie Wandersman (Maître de Conférences des Universités, depuis Janvier 2012).
- **DEA, Master 2**
  - Sébastien Leurent (de Janvier à Février 2008).
  - Flavien Kiefer (de Janvier à Février 2008).
  - Frederico Zalamea (de Janvier à Février 2010).
- **License/Maitrise (M1)/Ecole d’ingénieur**
  - Maxime Deforet (de Avril à Juin 2007).

- Julien Dupas (de Avril à Juillet 2008).
- Adrien Bouty (de Avril à Juillet 2009).
- Renaud Béziat (Juillet 2009).
- Laure Nayélie Claverie (Avril 2010 à Juillet 2010).
- Antoine Allard (Juin 2013).
- Christophe Raynaud (Avril 2014 à Juillet 2014).
- Tiphaine Paiik (Juin 2014).

Responsabilités d’enseignement et administratives

- Cours d’option sur la « Théorie Cinétique des Gaz Granulaires et Milieux Granulaires Vibrés », dans le cadre du parcours recherche "Physique des Fluides Complexes et des Milieux Structurés », Master 2 de Physique à Paris 7 (3 heures en 2005 et 3 heures en 2006).

- Fête de la Science 2007, démonstration autour du toucher (Lycée Chaptal, Paris).

- \- Examinateur du travail de thèse de Cécile Breugnot, « Contribution à la caractérisation mécanique du toucher des surfaces textiles à partir de critères neurosensoriels », (12 juillet 2005), Université de Haute Alsace, Mulhouse.
  \- Examinateur du travail de thèse d'Alexis Burdeau, "Propriétés cinétiques de milieux granulaires vibrés", (17 septembre 2009), Université de Paris 6.
  \- Examinateur du travail de thèse de Florian de Boissieu, "Toucher artificiel à base d'un micro−capteur d'effort: traitement du signal et des informations associées", (07 mai 2010).

- Rapporteur pour stages L3/M1 d’étudiants du Magistère de l’ENS (FIP), et M2 Physique Macroscopique et Complexité de l’UPMC.

- Tuteur de Maxime Deforet au cours de sa thèse à l’Institut Curie avec P. Silberzan ().

- Rapporteur pour Physics of Fluids, Physical Review E, IEEE Transactions on Robotics, Sensors…

- Co-organisateur du séminaire du LPS (Janvier 2006 à Juillet 2007).

- Membre de la commission de spécialistes Université Paris 6 - Section 28 (2008-2012).

- Membre élu du Conseil de la Faculté de Physique de l’UPMC (depuis Février 2013).

- Responsable Communication du Laboratoire Jean Perrin (en charge notamment de la mise à jour du site web du laboratoire) jusque Septembre 2014.

Financements

- Projet européen NEST-MONAT « Measurement Of NATuralness » (2006-2009). Responsable pour le LPS.

- Projet ANR-DYNALO « Dynamique locale d’une interface frottante : de l’aspérité au contact macroscopique » (2009-2013). Responsable pour le LPS-LJP.

- Projet ANR-TRANSTACT « Transduction et représentation tactile des textures par les vibrisses de rat et le doigt humain » (2009-2013).

- Projet C’Nano Ile de France BIOSTAR « Biomimétisme des systèmes tactiles résonnants » (2014-2017).

- Projet Emergence de la Ville de Paris SYTARES « Biomimétisme de la perception tactile : Systèmes Tactiles Résonants » (2014-2018).

- Projet financé par Nestec Ltd (Nestlé Research Center) « Using a biomimetic approach to study in-mouth texture perception » (2015-2016).